Diss. ETH No. 22503

Tip-Enhanced Raman Spectroscopic Imaging of Molecular Monolayers

A thesis submitted to attain the degree of

DOCTOR OF SCIENCES of ETH ZURICH

(Dr. sc. ETH Zurich)

presented by

LOTHAR JOHANNES OPILIK

MSc ETH in Chemistry, ETH Zurich, Switzerland

born on 16.02.1985

citizen of
Schwyz (SZ)

accepted on the recommendation of

Prof. Dr. Renato Zenobi, examiner
Prof. Dr. Lukas Novotny, co-examiner

2015

Acknowledgments

I would like to thank Prof. Dr. Renato Zenobi for giving me the opportunity to do my doctoral studies in his research group. I also thank Prof. Dr. Lukas Novotny for agreeing on being my co-examiner.

Thanks to Brigitte Bräm for taking care of all the administrative work in the background.

Thanks to Christian Marro and Christoph Bärtschi from the mechanical workshop as well as Heinz Benz from electronics for all the things they built and repaired for me.

Many thanks go to my coworkers in the TERS team: Thomas Schmid, Johannes Stadler, Carolin Blum, Bruno Stephanidis, Jacek Szczerbiński, Üzeyir Dogan, Feng Shao, Wan-Ing Lin, Jianfeng Li, Ludovic Roussille and Melissa Paulite. My projects would not have been possible without your help! Furthermore, I had the pleasure to supervise three excellent students: Idlir Liko, Martin Spergl and Lorenzo Querci. Thank you very much for your effort. You did an awesome job!

Thanks to my collaboration partners at ETH Zurich and the University of Bielefeld: Thomas Bauer, Zhikun Zheng, Payam Payamyar, Xianghui Zhang and Daniel Emmrich. It was great to work with you. Thanks as well to Prof. Dr. A. Dieter Schlüter and Prof. Dr. Armin Gölzhäuser for supporting our collaborative works.

Thanks to Igor Arkov, Sergey Lemeshko and Pavel Dorozhkin from NT-MDT for their great support with the instrumentation.

Thanks to Eszter Barthazy, Alla Sologubenko and Falk Lucas from EMEZ for taking numerous electron microscope images of my tips and sharing some of their expertise in electron microscopy with me.

I want to thank the members of the office D330: Jasmin Krismer, Simon Weidmann, Jan-Christoph Wolf, Agni Gavriilidou, Guido Zeegers, Martin Pabst, Martin Köhler, Katharina Root and Ross Farrell. Thanks for the discussions and distractions in the office. Thanks also to the other group members I got to know during my PhD, in particluar Robert Steinhoff, Volker Neu, Stephan Fagerer, Rob Nieckarz, Stefanie

Mädler, Fan Chen, Kostya Barylyuk, Christian Berchtold, Stefan Schmid and Amy Lee. Thanks for all the activities we did together besides work.

Special thanks also to Jason Yeo, who was the first to show me the beauty of tip-enhanced Raman spectroscopy.

Thanks also to Jonas Halter, Leo Betschart, Oliver Jeker, Sam Fux, Nikolas Huwyler, Bastian Brand, Nora Hild and Barbara Czarniecki, who accompanied me almost during my whole time at ETH Zurich. I very much enjoyed the lunches and all the other times we spent together.

Finally, I would like to thank my family. I am grateful to my parents, Ursula and Klaus Opilik, for the moral and financial support during my studies. This thesis would not have been possible without you. Many thanks also to my siblings, Lydia and Alex, for their support and interest in my work.

Contents

Zusammenfassung

Seit den ersten Veröffentlichungen im Jahr 2000 wurde die spitzenverstärkte Raman Spektroskopie (engl. *tip-enhanced Raman spectroscopy*, TERS) in verschiedenen Forschungsbereichen angewendet, um die chemische/molekulare Zusammensetzung zahlreicher Materialien auf der Nanometerskala zu bestimmen. Dabei handelt es sich hauptsächlich um auf Kohlenstoff basierende Materialien (Graphen, Nanoröhren, Fullerene, und Nanodiamanten) sowie Farbstoffmoleküle, aber auch Biomoleküle, Polymere und Halbleiteroberflächen. Trotzdem wird die Methode immer noch nur in spezialisierten Forschungslaboren angewendet und ist noch weit davon entfernt ein gängiges Analyseverfahren zu sein. Dies kann auf die komplexe und teure Instrumentierung sowie die hohe Variabilität und Anfälligkeit der notwendigen Spitzen zurückgeführt werden. Dies macht sich vor allem bemerkbar, wenn die Methode nicht nur für Punktspektroskopie, sondern auch als hochauflösende bildgebende Methode verwendet wird.

Im ersten Teil dieser Dissertation werden Methoden zur Spitzenproduktion eingeführt. Diese beinhalten auch einen neuen Ansatz, der es erlaubt besonders verstärkende geätzte Silberspitzen, welche oft für Rastertunnelmikroskop-TERS verwendet werden, mit dem breiter einsetzbaren intermittierenden Modus der Rasterkraftmikroskopie zu verwenden. Dies ist ausserdem mit jeder der normalerweise eingesetzten Beleuchtungsgeometrien möglich. Mit dem Fokus auf Silberspitzen wurde eine erste umfangreiche Studie über den Einfluss der atmosphärischen Korrosion auf deren verstärkenden Effekt durchgeführt. Es hat sich gezeigt, dass Korrosion im Frühstadium bereits Stunden nach der Spitzenproduktion in spitzenverstärkten Raman-Spektren sichtbar war, was während bildgebenden Messungen über einen längeren Zeitraum berücksichtigt werden muss. Ausserdem wurde ein signifikanter Rückgang des Verstärkungseffekt während der ersten Tage nach der Produktion festgestellt. Deshalb wurde eine einfache Methode entwickelt, um den Korrosionsprozess rückgängig zu machen. In einer leicht abgeänderten Form kann die Methode zur Langezeitlagerung von TERS Spitzen eingesetzt werden. Eine andere Strategie ist, die Korrosion von vorneherein durch die Verwendung von dünnen künstlichen Passivierungsschichten zu verhindern. Verschiedene Methoden, dies zu bewerkstelligen, wurden entwickelt, welche nicht nur als effektiver Korrosionsschutz fungieren, sondern auch vor ungewollter Chemisorption schützen. Ausserdem ergab sich die Notwendigkeit für eine Testprobe, um die effektive TERS-Auflösung zu bestimmen und um die Stabilität während bildgebenden TERS Experimenten zu überprüfen. Ein erster Vorstoss in diese Richtung wurde unternommen durch die Einführung einer Nanometer-grossen Auflösungstesttafel mit einem klaren TERS Kontrast und nur minimalem bis keinem topografischen Kontrast.

Im zweiten Teil der Dissertation, wird TERS als bildgebendes Verfahren auf verschiedene gemischte (nicht-resonante) molekulare Dünnfilme, hergestellt mittels Langmuir-Blodgett Technik, angewendet. Konkret handelt es sich dabei um segregierte Lipid Monolagen und kovalente Monolagen/zweidimensionale Polymere. Im Fall der Lipidschichten wurde bildgebendes TERS auf binären Mischungen vorgestellt. Zum ersten Mal waren aufeinanderfolgende Messungen auf derselben Probenposition möglich, was die Nicht-Invasivität der Methode zeigt. Ausserdem wurde gezeigt, dass TERS Messartefakte (z.B. plötzliche Änderungen in der Verstärkung von einer Linie zur nächsten) eliminiert werden können, indem Signalverhältnisse von den zwei Komponenten der Mischung dargestellt werden. Ausserdem wurden erste TERS Messungen auf ternären Lipid Mischungen durchgeführt. In diesem Experiment war es möglich, das sonst versteckte Cholesterin in gemischten Lipidschichten zu lokalisieren. Im Fall der kovalenten Monolagen/zweidimensionalen Polymere wurde zum ersten Mal demonstriert, dass TERS verwendet werden kann, um qualitativ hochwertige Raman-Spektren von einzelnen Lagen dieser neuen Materialien zu erhalten, wodurch deren Zusammensetzung teilweise aufgedeckt werden konnte. Es wurde gezeigt, dass die signifikant kürzeren Aufnahmezeiten im Vergleich zur konfokalen Raman Mikroskopie es erlauben, weniger invasive Untersuchungen auf diesen lichtempfindlichen Proben durchzuführen. Ausserdem ermöglichen bildgebende Experimente erste Schussfolgerungen bezüglich des Polymerisierungsmechanismus, welcher für diese neuartigen Materialien noch gänzlich unerforscht ist.

Abstract

Since its first demonstration in 2000, tip-enhanced Raman spectroscopy (TERS) has been applied in different fields of research to elucidate the chemical/molecular composition of various materials on the nanometer length scale. These include mainly carbon-based materials (nanotubes, fullerenes, graphene, and nanodiamonds) and dye molecules, but also biomolecules, polymers and semiconductor surfaces. However, the method is still only used by dedicated research labs and far from being a routine analytical technique. This can be attributed to the rather complex and expensive instrumentation and the high variability and vulnerability of the required tips. This is noticeable especially when the method is not only used for point spectroscopy, but for high-resolution spectroscopic imaging.

In the first part of this thesis, methods for tip production are introduced, including a novel approach, which allows to use highly enhancing etched silver tips commonly used for TERS in scanning tunnelling microscopy (STM) feedback in the more widely applicable tapping-mode atomic force microscopy (AFM) feedback in combination with any of the common illumination geometries. With a focus on silver tips, a first thorough study of the influence of atmospheric corrosion on their enhancing effect was conducted. It was found that early stage corrosion products were already visible in tip-enhanced Raman spectra hours after tip preparation, which has to be taken into account for long imaging experiments. Moreover, a significant decrease in enhancement during the first days after production was found and a simple method to reverse this process is presented, which in a slightly modified version can be used for long-term storage of TERS tips. Another strategy is to prevent corrosion of the silver tips in the first place, by introducing thin artificial passivation layers. Different approaches for achieving this were developed, not only leading to an effective protection against atmospheric corrosion, but also against unwanted chemisorption. There is also an urgent need for a test sample to determine the effective TERS resolution and to check tip stability during TERS imaging experiments. The first attempt in this direction was made by introducing a nanometers sized resolution test target with a clear TERS contrast, but little or no topographic contrast.

In the second part of this thesis, tip-enhanced Raman imaging is applied to various mixed (non-resonanant) molecular thin films prepared by the Langmuir-Blodgett technique, specifically, segregated lipid monolayers and covalent monolayers/two-dimensional polymers. In the case of the lipid layers, spectroscopic imaging on a binary mixture was demonstrated. For the first time, subsequent mapping on the same sample region was possible, demonstrating the non-invasiveness of the technique. Moreover, it was shown that TERS measurement artefacts (e.g., a sudden change in enhancement from one line to another) can be eliminated by plotting peak ratios of the two constituents of the mixture. Moreover, first TERS measurements on a ternary lipid mixture were performed. In this experiment, it was possible to locate the otherwise hidden cholesterol in mixed lipid layers. In the case of covalent monolayers/two-dimensional polymers, it was demonstrated for the first time that TERS can be used to obtain high quality Raman spectra from single layers of these novel materials, shining light on their composition. It was shown, that the significantly shorter acquisition times compared to confocal Raman microscopy, allow for less-invasive investigation of these light sensitive samples. Moreover, imaging experiments give first insights into the polymerization mechanism, which is still largely unknown for these novel materials.

Chapter 1

Introduction

This chapter gives a general introduction to the concept of tip-enhanced Raman spectroscopic imaging with a strong focus on optical resolution. The first formulation of the optical resolution limit given by Abbe and Helmholtz leads to near-field optical methods, which successfully circumvent this limit, although with some restrictions. Then, the current status of tip-enhanced Raman imaging is shortly reviewed, followed by a brief outline of the projects realized in this thesis.

1.1 Motivation

Optical imaging systems (cameras, telescopes and microscopes) strongly influence how we perceive our surroundings. Consumer digital cameras are commonly used to document our everyday lives and are nowadays built into every smartphone. Advanced telescopes (e.g., the Hubble space telescope) provide impressive pictures from far away galaxies and essentially influenced our perception of the universe surrounding us. The microscope also opened up a new world by giving us the possibility to look at very small things that are typically not observable by the naked eye. The human eye is at best capable of differentiating objects spaced by approx. 100 µm under close inspection. A resolution limit exists for every optical imaging system and it can be caused by different effects.

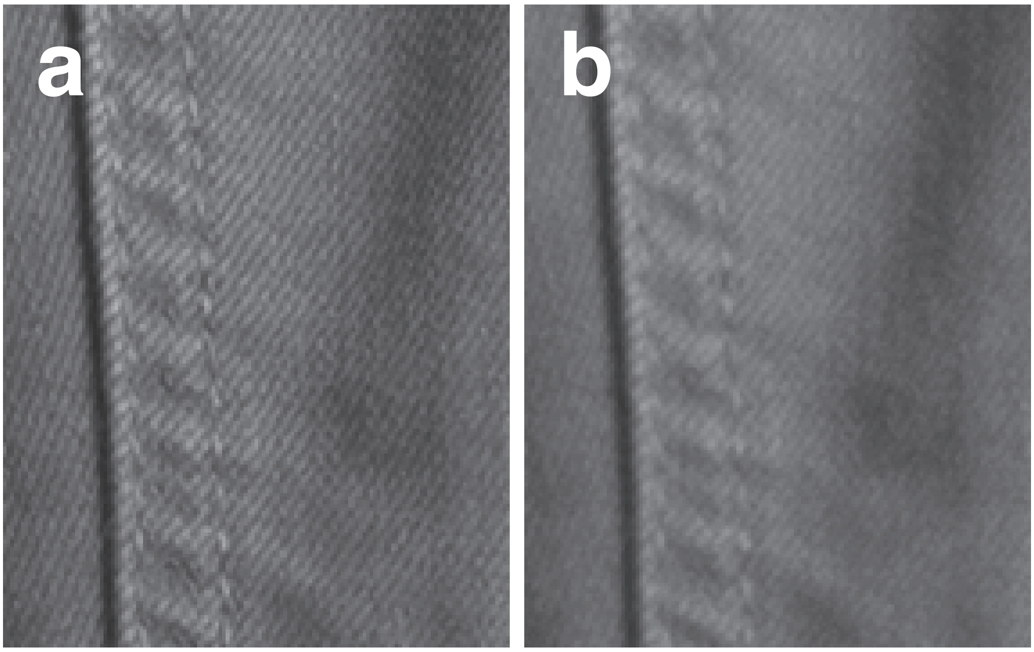

Figure 1.1: Comparison of photos taken from a denim fabric at different camera apertures. At an aperture of f/4 (a) the lines of the fabric can be clearly distinguished. When stopped down to f/22 (b), the line structure appears blurry. The loss in resolution can be attributed to diffraction.

When comparing the digital photographs in Figure 1.1 one can notice the difference in resolution between image a and b. The two images only differ in the camera's aperture size during shutter release. The significantly smaller aperture chosen for the acquisition of image b leads to a deterioration of resolution caused by Fraunhofer diffraction at the camera's circular aperture. The effect is noticeable because the diffraction pattern (Airy pattern[1]) extends over the sensor pixel size. Other effects that limit the resolution are so-called lens aberrations which are more noticeable at wider apertures, but can in generally be avoided by using high quality optics. Diffraction effects, however, set an ultimate resolution limit to every optical imaging system. An ultimate resolution limit in the context of microscopy was first described by Abbe in 1873,[2] and shortly thereafter by Helmholtz[3] who also gave a mathematical derivation. Their findings are reflected in the following formula for the diffraction limit of an optical imaging system in air:

$$d_{min} = \frac{\lambda}{2sin(\alpha)} \tag{1.1}$$

where λ is the wavelength of the light and α is the half-angle of the maximum cone of light that can enter the microscope objective. Both, Abbe and Helmholtz did not specifically discuss the influence of the refractive index n and in a more generalized form of the formula, $sin(\alpha)$ is typically substituted by the numerical aperture ($NA = nsin(\alpha)$). Around the same time, Rayleigh[4] describes a criterion for the resolution of an optical system as the minimal distance r of two Airy patterns to be still distinguishable from each other:

$$r = \frac{0.61\lambda f}{R} \tag{1.2}$$

where f is the focal length and R the radius of the lens. The formula can again be expressed using the numerical aperture NA:

$$r = \frac{0.61\lambda}{NA} \tag{1.3}$$

Nowadays, a numerical aperture of approx. 1.5 can be reached with oil-immersion objectives, resulting in a diffraction-limited resolution of 200-300 nm using visible light. This is where a practical limit is reached. However, new methods have been developed that can achieve a significantly higher spatial resolution by making use of the fact that a light source (e.g., a molecule) can be localized with very high precision, if there is no overlap with neighbouring Airy discs. This can, e.g., be achieved in fluorescence microscopy where photoswitchable fluorophores are located using deterministic (e.g., stimulated emission depletion, STED) or stochastic techniques (e.g., stochastic optical reconstruction microscopy, STORM).[5][1] However, these methods do not allow true optical resolution below the diffraction limit. This is where near-field optical

---

[1] The Nobel Prize in Chemistry was awarded to the developers of these techniques in 2014.

techniques come into play. For these techniques, the abovementioned diffraction limit does not apply. How this is possible will be explained in the following.

The first reports on the ultimate resolution limit of a microscope were used by Heisenberg to illustrate his famous uncertainty principe in 1927.[6] If we formulate Heisenberg's uncertainty principe for the photon using the dispersion relation for free space propagation, we get:[2]

$$\hbar \Delta k_x \cdot \Delta x \geq \hbar \tag{1.4}$$

where k_x is the wave vector component in x direction. Rearranging the formula results in the following expression, where the upper limit of Δk_x is set by the total length of the wave vector for free space propagation ($k = 2n\pi/\lambda$) corrected by the numerical aperture of the optical imaging system, resulting in an expression similar to (but more optimistic than) the Rayleigh criterion:

$$\Delta x \geq \frac{1}{\Delta k_x} = \frac{\lambda}{2\pi NA} \tag{1.5}$$

The significant deviation from the Rayleigh criterion can be explained by the fact that there is some ambiguity with respect to the chosen distance at which the two Airy discs cannot be distinguished from each other anymore.

According to Fourier optics, the optical fields in a homogeneous medium propagating along z can be described as follows:

$$\mathbf{E}(x, y, z) = \iint\limits_{-\infty}^{\infty} \hat{\mathbf{E}}(k_x, k_y, z = 0) e^{i(k_x x + k_y y)} e^{\pm i k_z z} dk_x dk_y \tag{1.6}$$

The field is expressed as a spectrum of spatial frequencies. For the case of propagating plane waves, the spectrum of spatial frequencies is limited to $k_x^2 + k_y^2 \leq k^2$. These frequencies can be used to recover the original scene in an optical imaging system (e.g., a camera). This can be illustrated using the photograph of the denim fabric (Figure 1.2a), by applying a low-pass filter (Figure 1.2b) and a high-pass filter (Figure 1.2c) to the original image. Folds are only visible in the low frequency image, whereas the narrow line structure of the fabric is only visible in the high frequency image.

Consequently, if it were possible to extend the spectrum of angular frequency to the range $k_x^2 + k_y^2 > k^2$, it would be possible to resolve even smaller structures.

---

[2] The following derivation was adapted from Novotny et al.[7]

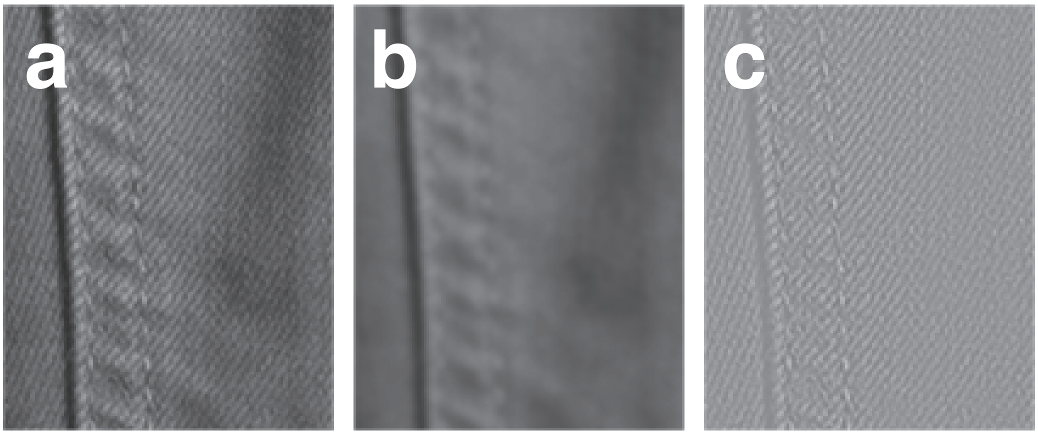

Figure 1.2: The original image of denim fabric (a) after applying a low-pass filter (b) and a high-pass filter(c)

This is feasible if k_z is purely imaginary. Unfortunately, the resulting (evanescent) waves decay exponentially in space and do not reach the optical imaging system. This is because the propagator $exp \pm ik_z z$ in equation 1.6 becomes an exponentially decaying function. The free space therefore somehow acts as a kind of low-pass filter. However, evanescent waves exist at interfaces and methods to access their valuable information have been developed (near-field optics) and allow for optical imaging not restricted by the diffraction limit. One possible way to practically realize this is called tip-enhanced near-field optical microscopy.[8] In this method, a laser illuminated metal or metallized tip is brought close enough (a few nanometers) to a light source or scatterer to probe the short-range (evanescent) electromagnetic field. This requires a very accurate feedback mechanism, which can be borrowed from scanning probe microscopy techniques. A great advantage of this technique is that it not only allows imaging below the optical diffraction limit, but is also accompanied by a considerable field enhancement. This is particularly useful, when the technique is used for Raman spectroscopic imaging below the optical diffraction limit, because the Raman scattering of a small number of molecules is typically too weak to be probed. This variant of the technique is called tip-enhanced Raman spectroscopy (TERS) and was pioneered in 2000 by different research groups independently.[9–11] Since then, the technique has proven powerful as an imaging tool for various carbon materials,[12,13] and a sensitivity down to the molecular[14] and even submolecular[15] level has been demonstrated. However, important limitations still prevent the method from becoming more widespread. These include, for example, high costs, sophisticated instrumentation, and the existence of some artefacts. Tip-enhanced Raman microscopes are therefore still only used in dedicated research labs. One of the most challenging aspects of the method is the reproducible production of TERS active tips with a long lifetime. Moreover, the close proximity of the tip to the sample can lead to unwanted interactions with the analyte molecules, which promotes tip contamination.

1.2 Outline of This Work

This thesis is structured as follows: Chapter 2 gives a fundamental introduction to Raman imaging, starting with the basic principles of spontaneous Raman scattering and related methods, in particular near-field Raman scattering. This is then followed by an introduction to the typically used instrumentation for Raman and tip-enhanced Raman imaging. After that, an introduction to optical probes, common illumination geometries and often used metallic substrates for tip-enhanced Raman spectroscopy are discussed before introducing some technical aspects that have to be taking into consideration when performing tip-enhanced Raman imaging experiments.

Chapter 3 introduces the instrumentation and important procedures used throughout the work. This is followed by a chapter on the corrosion of silver TERS tips, which also introduces a simple method for tip restoration and long-term storage. The two subsequent chapters introduce new methods to cover TERS tips with a thin protective coating.

Chapter 6 introduces tip-enhanced Raman spectroscopic imaging on simple binary mixed molecular layers in the form of segregated lipid monolayers followed by a chapter on the TERS investigation of ternary lipid mixtures. Chapter 8 introduces tip-enhanced Raman imaging on covalent monolayers prepared by light-induced cross-linking in two dimensions. These experiments shine light on the structural changes during the polymerization event and give a fist indication on the mechanism of two-dimensional polymerization. In the last chapter, in-situ resonance Raman measurements of the transmetalation within a two-dimensional coordination polymer is shown and possible reasons, why tip-enhanced Raman spectroscopy is difficult on these films, are discussed.

Chapter 2

Theoretical Background and State of the Art

This chapter gives a short introduction to modern Raman imaging techniques, including the basic principles of Raman scattering and state-of-the-art instrumentation. Moreover, sections on near-field optical probes, commonly used illumination geometries and practical aspects of tip-enhanced Raman spectroscopic imaging lead over to the experimental part of the thesis.

Parts of this chapter are reproduced with permission from L. Opilik, T. Schmid, R. Zenobi: 'Modern Raman Imaging: Vibrational Spectroscopy on the Micrometer and Nanometer Scales', *Annual Reviews of Analytical Chemistry*, **2013**, 6, pp. 379–398.

Parts of this chapter are reproduced with permission from T. Schmid, L. Opilik, C. Blum, R. Zenobi: 'Nanoscale Chemical Imaging Using Tip-Enhanced Raman Spectroscopy: A Critical Review', *Angewandte Chemie International Edition*, **2013**, 52, pp. 5940–5954.

2.1 Introduction to Raman Imaging

Optical microscopy plays an important role in various fields of research because it allows for non-invasive and non-destructive sample investigation with high spatial resolution under ambient conditions. Inventions like the confocal microscope in 1957[16] as well as the discovery of the green fluorescent protein (GFP)[17] and its use for fluorescence imaging[18] led to optical microscopy being widely used in the life sciences. However, despite the high impact of fluorescence microscopy, it has some major drawbacks, limiting its use: prior knowledge of the system under investigation is usually necessary, because a suitable target has to be chosen for labeling. In addition, the use of multiple fluorescent labels is limited by the width of their emission bands, such that only a few targets can be imaged at the same time. Moreover, common fluorescent labels (antibodies, proteins or small molecules) can alter the system under investigation and, for complex biological systems, time consuming and elaborate tests are necessary to exclude that the introduction of a fluorescent label has no effect.[19] Photobleaching can also limit the applicability due to the loss of signal for long measurement times and/or high laser powers. Because vibrational spectroscopy techniques probe intrinsic properties of the molecules under investigation, limitations arising from the required external labels do not exist. Raman spectroscopy is a powerful technique, which is readily combined with optical microscopy. It yields spectroscopic fingerprints from the molecules under investigation and can even give much more detailed information on the specific state the molecules are in at the moment of investigation. However, the absence of labels can render data evaluation challenging, because for complex systems with a lot of different chemical entities, the collected spectra are so rich in information that it is not straightforward to extract the relevant information. Therefore, in some studies minor labeling (e.g., isotopes, ethynyl groups) is used to improve specificity for vibrational spectroscopic imaging.[20–23] These labeling techniques are considered less invasive compared to typical labels for fluorescent microscopy and are not prone to photobleaching. However, despite the high information content of Raman spectra, the main restriction of confocal Raman microscopy is the low yield of Raman scattered photons, limiting the achievable image contrast at reasonable measurement times. The introduction of coherent anti-Stokes Raman scattering (CARS) microscopy, stimulated Raman scattering (SRS) microscopy and techniques, which rely on the scattering enhancement close to rough metal structures (surface enhanced Raman scattering, SERS) led to a huge improvement, and image contrasts as well as measurement speeds not much different from confocal fluorescence microscopes can be reached.[24]

Because of advances in nanoscale fabrication methods in the materials sciences and semiconductor industries as well as the recognition that important processes in cell biology rely on interactions on the molecular level, the intrinsically restricted resolution of optical microscopy (see chapter 1) became another key limitation. However, new microscopy techniques have been developed that circumvent or even break the diffraction limit to allow optical microscopy and spectroscopy on the nanometer length scale. These include high resolution fluorescence techniques (STED, STORM,...)[5] as well as near-field optical microscopy techniques, such as tip-enhanced Raman spectroscopy (TERS).

2.2 Spontaneous Raman Scattering and Related Phenomena

The phenomenon of Raman scattering was first described by Raman and Krishnan in 1928.[25] Details on the physics of Raman scattering can be found in various textbooks.[26–29] This section will only cover some fundamental aspects following the theoretical derivation by Ferraro et al.,[27] and will then lead over to nonlinear and enhanced Raman scattering phenomena.

2.2.1 Spontaneous Raman Scattering

If electromagnetic radiation interacts with a molecule, it can be absorbed if the energy of the incident photon matches the energy difference ΔE between the ground and an excited state, and thus fulfills the Bohr criterion $\Delta E = h\nu$, with h denoting the Planck constant and ν the frequency of the incident radiation. Vibrational transitions, for example, require infrared (IR) radiation with typical wavenumbers between 400 and 4000 cm^{-1}. However, when considering the whole electromagnetic spectrum, it happens much more often, that the incoming radiation does not match any molecular transition, and is scattered upon interaction with the molecule. Most scattered photons have the same energy as the incoming photons. This elastic scattering process is called Rayleigh scattering. In a few cases, the molecule changes its vibrational or rotational state upon interaction with the incoming photon and the energy of the scattered photon differs by an amount corresponding to a vibrational transition (see figure 2.1). This inelastic scattering process is called Raman scattering. In Stokes scattering, the initial state is the ground state and after the scattering process, the molecule is in an excited vibrational state (the scattered photon has lower energy compared to the incoming photon). In the anti-Stokes case, the molecule is already in an excited vibrational state and returns to the ground state during the scattering process (the scattered photon has higher energy compared to the incoming photon). At room temperature the majority of molecules is in the ground state, as can be derived from the Maxwell-Boltzmann distribution. As a consequence, the intensity of the Stokes and anti-Stokes lines typically differ by approximately one order of magnitude.[30]

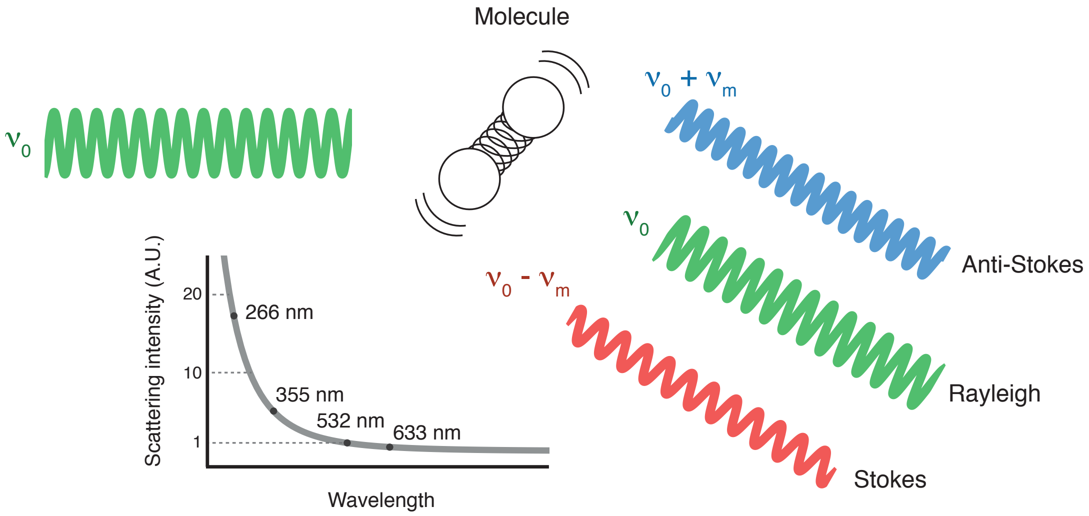

Figure 2.1: Rayleigh (elastic) and Raman (inelastic) scattering at a molecule and scattering intensity dependence on the wavelength of the scattered light (for better comparabiliy, the scattering intensity is arbitrarily set to 1 at a wavelength of 532 nm).

When light is scattered by a molecule, the time-dependent electric field component of the incoming electromagnetic wave distorts the electron cloud of the molecule, which induces an electric dipole moment. This is the case because the molecule experiences the incoming electromagnetic wave as an oscillating electric field due to the considerably smaller size of the molecule compared to the typical wavelength of Raman excitation in the visible part of the electromagnetic spectrum (400–700 nm).

The extent of the electron cloud distortion depends on its polarizability α. In a classical description, the induced electric dipole moment P can be written as follows:

$$P = \alpha E = \alpha E_0 cos(2\pi\nu_0 t) \tag{2.1}$$

where E_0 is the amplitude and ν_0 the frequency of the electric field component of the incoming electromagnetic wave. In the simplest case of a diatomic molecule (harmonic oscillator) vibrating with a frequency ν_m the nuclear displacement q is as follows:

$$q = q_0 cos(2\pi\nu_m t) \tag{2.2}$$

where q_0 is the amplitude (maximum displacement) of the molecular vibration. For small amplitudes of the molecular vibration, α can be approximated by a linear function of q (linear term of the Taylor series):

$$\alpha = \alpha_0 + \left(\frac{\delta\alpha}{\delta q}\right)_0 q + ... \tag{2.3}$$

where α_0 is the polarizability at the equilibrium position and $\left(\frac{\delta\alpha}{\delta q}\right)_0$ is the derivative of α with respect to the change in q, evaluated at the equilibrium position. The expression for the induced dipole moment can then be written as follows:

$$P = \alpha_0 E_0 cos(2\pi\nu_0 t) + \frac{1}{2}\left(\frac{\delta\alpha}{\delta q}\right)_0 q_0 E_0 \{cos[2\pi(\nu_0 + \nu_m)t] + cos[2\pi(\nu_0 - \nu_m)t]\} \tag{2.4}$$

The three contributions to the scattered radiation appear as separate terms with ν_0 for Rayleigh scattering, $\nu_0 - \nu_m$ for Stokes Raman scattering and $\nu_0 + \nu_m$ for anti-Stokes Raman scattering. The expression implies that if the derivative $\left(\frac{\delta\alpha}{\delta q}\right)_0$ is zero, or in other words, if the polarizability does not change during a vibration, the corresponding transition is not Raman active.

Considering an oscillating induced dipole as the source of radiation, the resulting intensity of the Stokes Raman scattered light can be described with the following expression:[29,31]

$$I \propto \left(\frac{\delta\alpha}{\delta q}\right)_0^2 I_0(\nu_0 - \nu_m)^4 \tag{2.5}$$

Therefore, the intensity depends on the derivative of the polarizability, the intensity of the incident radiation I_0 as well as the frequency of the scattered light. Note the 4th-power dependence of the signal intensity on the frequency of the scattered radiation (see figure 2.1). This frequency dependence is, however, not valid if ν_0 is close to the frequency of an electronic transition of the molecule. In this case, significantly higher Raman scattering intensities are observed (resonance Raman scattering). This effect is sometimes used to selectively enhance the Raman response of a particular class of molecules.

2.2.2 Nonlinear Raman Scattering

In the previous section, only scattering events where one photon at a time interacts with a molecule were considered (scattering intensity is linearly related to the laser intensity as shown in equation 2.5). However, at high power densities, multiple photons can be involved in the scattering process at the same time, i.e., the scattering intensity is no longer linearly related to the laser intensity.[32] Advances in optics (mainly in the form of fast pulsed laser sources) made techniques relying on nonlinear scattering more accessible. Two prominent examples are CARS and SRS.

SRS was discovered earlier than CARS. It was actually discovered accidently right after the laser was invented in 1962.[33] CARS was first reported in 1965 by Maker & Terhune[34] and rediscovered by Zumbusch et al. in 1999 for imaging experiments.[35] These nonlinear Raman techniques are particularly interesting for (three dimensional) imaging experiments, because of the enhanced signal intensity (and improved z-resolution[1]) compared to conventional Raman microscopy. The two methods are very similar and mainly differ in the extracted information.

When the frequency difference of a pump and a Stokes beam is tuned to a Raman active molecular vibration, the oscillators within the laser focus are coherently driven in phase (see figure 2.2). After another scattering event of the pump beam, coherent radiation at the anti-Stokes frequency $\nu_{as} = 2\nu_p - \nu_s$ is generated (probed in CARS microscopy), leaving the molecule in its ground state.[36,37] The more efficient excitation of the Raman active molecular vibration due to the combined interaction of the incident pump and Stokes beam requires energy. This results in an intensity loss of the pump beam (Raman loss) and an intensity gain of the Stokes beam (Raman gain).[36] These small changes in intensity are probed in SRS microscopy.

---

[1] Nonlinear effects only take place in the center of the focus where the peak powers of two excitation lasers interact resulting in a three-dimensionally well-confined excitation source that makes the use of a confocal pinhole obsolete.

The anti-Stokes Raman scattering probed in CARS microscopy is always accompanied by a non-resonant background, leading to a distortion of the resulting spectra.[37] This is not the case for SRS, which makes spectra interpretation much easier.

Methods based on nonlinear Raman scattering are the topic of various publications and especially their use for the analysis of tissue and living cells is worth mentioning.[21,24,38,39] However, this topic is not within the scope of this thesis and the interested reader is referred to works by Xie et al.[24,40,41]

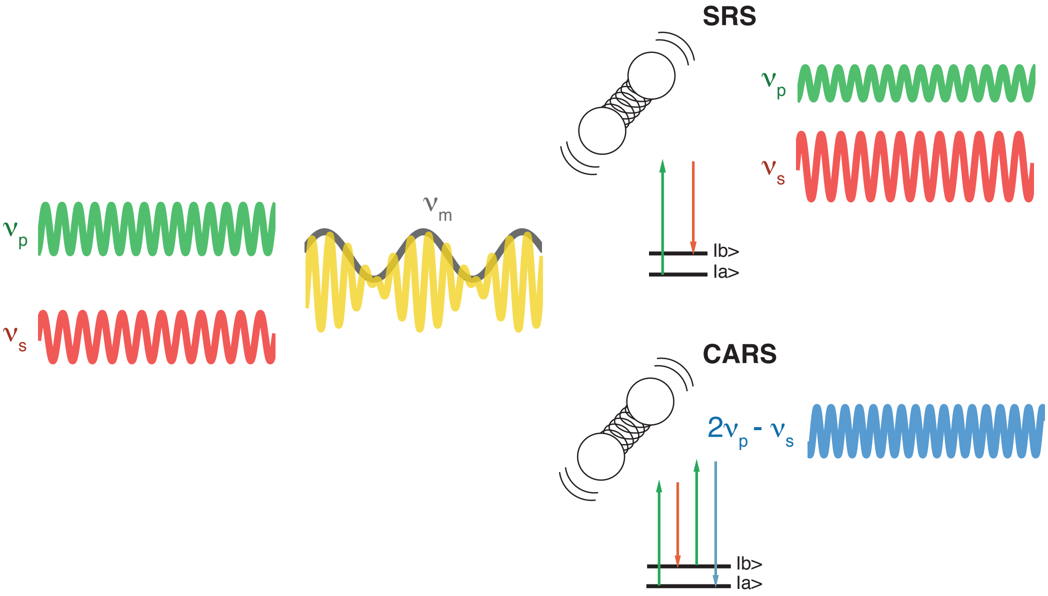

Figure 2.2: Comparison of coherent anti-Stokes Raman scattering (CARS) and stimulated Raman scattering (SRS).

2.2.3 Near-Field Raman Scattering

SERS relies on the enhancement of Raman signals from molecules in close proximity of silver or gold nanostructures and was first described in the 1970s.[42,43] In 1985, Wessel suggested to use the effect for optical microscopy to achive sub-diffraction spatial resolution by scanning a single enhancing particle across a sample surface.[44] The experimental realization followed in 2000 from three research groups independently.[9–11] Nowadays, TERS has become a powerful spectroscopic imaging technique used in various fields of research. In the following, the origin of the underlying signal enhancement is shortly reviewed. For a more detailed discussion, we refer to various review articles and textbooks.[7,8,45–47]

Metal nanostructures with dimensions smaller than the wavelength of the incident light can exhibit so-called surface plasmons.[46] These plasmons are collective oscillations of the conduction electrons in relation to the ionic metal cores caused by the electric field vector of the incident light which varies with time. In the simplest case of a very small sphere, only dipolar plasmons are of relevance (dipolar approximation). The strength as well as the sharpness of the dipole plasmon resonance depends on the mobility of the conduction electrons.[48] The incident electromagnetic field can be strongly modified (in magnitude and orientation) in close vicinity of the metal nanostructure especially if the incident wavelength is close to a plasmon resonance. The amplitude of the (averaged) local field strength $E_{loc}(\nu_0)$ is described as follows,[46,48]

$$E_{loc}(\nu_0) = gE_0 \tag{2.6}$$

where E_0 is the magnitude of the incident field and g is the field enhancement averaged over the surface of the particle. The induced electric dipole moment of a molecule in close proximity of the surface of the nanostructure can therefore be written as follows,

$$P = \alpha E_{loc} = \alpha g E_0 \tag{2.7}$$

In most cases it is sufficient to assume that the Raman scattered light does get enhanced the same way as the incoming light. However, the corresponding field enhancement factor g' differs from the g mentioned above, because of the difference in wavelength of the Raman scattered radiation. The overall Raman scattering intensity (proportional to $|P|^2$) can therefore be written as follows:[48]

$$I \propto |\alpha|^2 |gg\prime|^2 I_0 \tag{2.8}$$

For small Raman shifts, where g' is very similar to g, the intensity scales with the fourth power of the local field enhancement. This relation is the reason for the extraordinary enhancement in Raman intensity, which can reach several orders of magnitude, as commonly observed in SERS and TERS experiments. A schematic of the process is shown in Figure 2.3. The SERS enhancement decays with $(1 + d/r)^{-12}$ for a nanoparticle with radius r and the distance d of the molecule to the particles surface.[49]

Most studies support the theory of electromagnetic enhancement and there is no evidence that the increase in Raman intensity is related to a change in scattering cross-section. In this model, an overall increase in scattering intensity is only caused by more effective illumination of the scattering molecule in the optical near-field surrounding the metallic sphere. Another proposed enhancement mechanism was formulated for chemisorbed analyte molecules, and is called chemical enhancement.[49] If the Fermi level of the metal is somewhere between the highest occupied molecular orbital (HOMO) and the lowest unoccupied molecular orbital (LUMO) of the molecule chemisorbed on the particles surface, charge transfer from the HOMO to the Fermi level or from the Fermi level to the LUMO is possible. These transitions require less energy than intramolecular transitions of the free molecule and may lay in the visible part of the electromagnetic spectrum. The expected contribution to the signal enhancement (10-100) is therefore similar to the observed intensity increase in resonance Raman spectroscopy.[49]

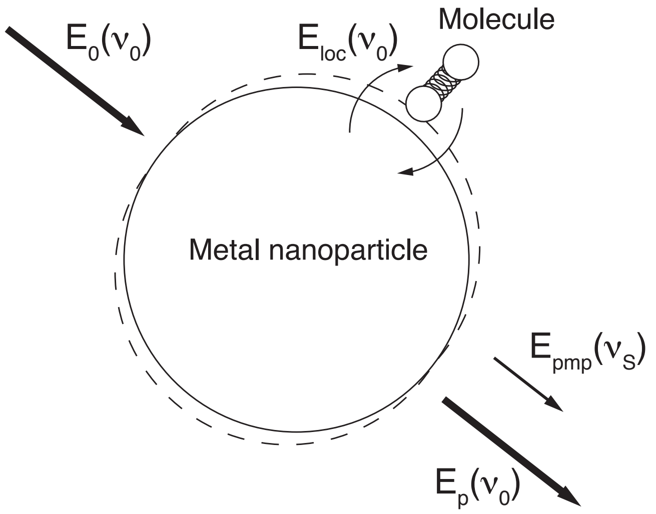

Figure 2.3: Scheme of the electromagnetic enhancement in surface enhanced Raman scattering. The incoming light polarizes the metal nanoparticle and the local field E_{loc} is inelastically scattered at the molecule and transferred back to the nanoparticle, which reradiates the frequency shifted field E_{pmp}. E_p is the field directly scattered by the metal nanoparticle.

2.3 Instrumentation

2.3.1 Raman Microscopy

In Raman spectroscopy, excitation with one fixed (laser) wavelength induces inelastic scattering related to all vibrational Raman-active modes of the sample molecules simultaneously. Thus, scanning of a focused continuous-wave laser beam through a sample allows imaging with the full spectroscopic information collected in every pixel.[50] This common approach for Raman imaging is realized by either laser scanning using mirrors and motorized objectives, or sample scanning by piezoelectrically driven stages. This is schematically depicted in Figure 2.4. A microscope objective focuses a laser beam onto a sample and the Raman scattered light is typically collected with the same objective.[2] This part of the instrument corresponds to the excitation configuration in laser-scanning fluorescence microscopes. Typical for Raman microscopes is a possibility to very efficiently suppress the back-reflected and Rayleigh-scattered light that has the same wavelength as the excitation laser and is orders of magnitude stronger than the Raman scattered light. In the visible and near-IR ranges, optical filters are employed for this purpose. Notch filters selectively suppress the laser wavelength allowing for detection of both, Stokes and anti-Stokes Raman spectra. As in most applications only the stronger Stokes lines are of interest, less expensive edge filters are more frequently used. Some notch or edge filters are designed to work at a certain angle (e.g., 45°) and can thus be used as beam splitters (see Figure 2.4). For analysis and detection of the collected light, spectrometers with (interchangeable) gratings and charge-coupled device (CCD) detectors are used most frequently. The newest generation of electron-multiplying CCDs (EMCCDs) offers high sensitivity, down to single-photon counting, and fast read-out rates (in the millisecond range). Alternatively, there are other illumination techniques available. Wide-field illumination, for example, has the advantage of collecting the full image, not only one pixel, during one acquisition. The price one has to pay is that the full spectroscopic information is lost because filters are used to select the scattering intensity at one specific Raman band that is projected onto a CCD camera employed for imaging. A comparison of different scanning and wide-field techniques was given by Schlücker et al. in 2003.[51]

Most of the commercially available Raman microscopes include spatial filtering of

---

[2] Only one possible configuration is shown here and both, inverted and upright microscopes equipped for Raman measurements are commercially available nowadays.

the collected light like in confocal microscopy. Here, the classical approach is to place an adjustable pinhole in front of the spectrometer entrance to reject out-of-focus contributions to the signal (see Figure 2.4). Nowadays alternative approaches are also available, which, for example, use arrays of apertures and slits that can be inserted individually into the beam,[52] or a spectrometer entrance slit for spatial filtering in one dimension and binning of only a few rows on the CCD for spatial filtering in the perpendicular direction.[53] Confocal Raman microscopes provide diffraction-limited resolution laterally, which ranges typically from 300 nm to 2 µm, depending on the laser wavelength and numerical aperture of the objective lens used. In axial direction, the confocal resolution is 1–6 µm.[54]

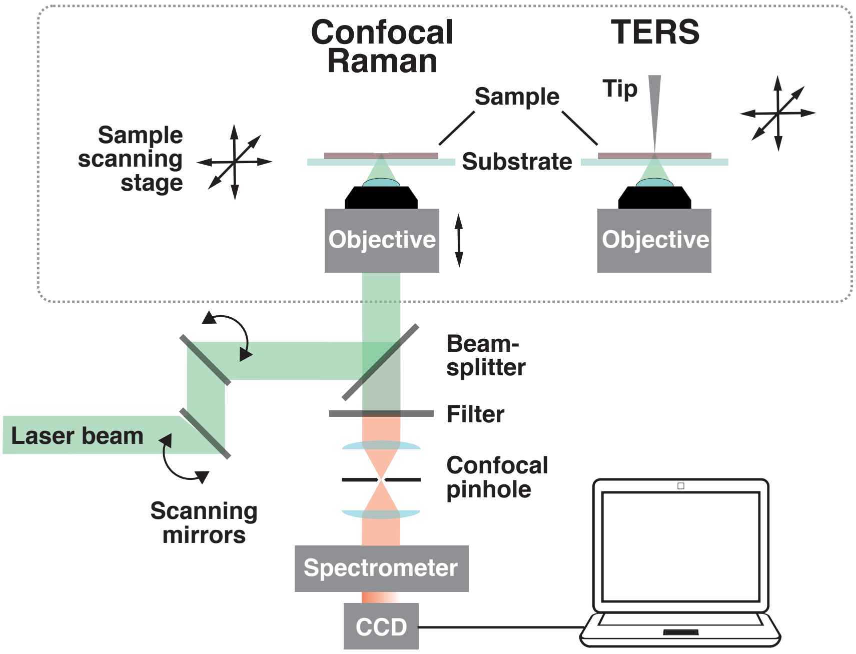

Figure 2.4: Schematic of an inverted laser-scanning confocal Raman microscope (left) and a TERS setup (right) based on inverted-microscope bottom-illumination of the tip.

2.3.2 TERS

As opposed to confocal Raman microscopy, which has been commercially available for years and has become a routine technique for some applications, TERS is still only done in specialized research labs. However, combinations of scanning probe microscopy (SPM) with Raman microscopy have become commercially available and the number of TERS groups has begun to grow in recent years. Users of such commercial SPM-Raman combinations have to produce the enhancing tips by themselves. There are many different recipes for probe fabrication in use, all of them being limited in terms of yield and reproducibility (see section 2.4). TERS is presently neither routine nor commercially available.

2.4 Near-Field Optical Probes

Since the very beginning of scanning near-field optical microscopy (SNOM), the production and characterization of tips/probes for near-field optical methods have always been key factors in deciding the success or failure of such experiments. SNOM first existed as a thought experiment by Synge, who in 1928 proposed to bring a very small aperture (with a size well below the optical diffraction limit) very close to a sample surface.[55] The illuminated aperture would thus act as a near-field light source to obtain images with subdiffraction spatial resolution when scanning it across the sample surface. 56 years after publication of this general idea, the experimental realization with visible light was accomplished by using a metal-coated glass-fiber tip with a small aperture at its apex.[56,57] However, because the light intensity decreases significantly when reducing the physical size of the aperture, the best spatial resolution obtained so far with this approach is in the range of 50 nm.[58] A spatial resolution higher than that is desirable in many different areas of research and technology. With apertureless SNOM (called TERS when used for Raman spectroscopic measurements) a spatial resolution down to 4 nm has been demonstrated experimentally.[59] The key difference compared to aperture SNOM is that instead of a subdiffraction aperture, a nanometer-sized scatterer illuminated with a diffraction-limited light source is scanned across the sample surface (see Figure 2.5). The tiny scatterer can lead to an enhanced optical field in its proximity (mainly arising from localized surface plasmon resonances), and thereby acts as a near-field light source. The main drawback accompanying this approach is the background signal resulting from the necessary far-field illumination. However, different approaches have been presented in the literature to remove or suppress this far-field contribution.[60–63] Another issue of TERS that has not been solved so far is that suitable optical probes cannot yet be fabricated reproducibly. Etched metal wires or metal-coated SPM probes are easy to produce and are commonly used, but lack reproducibility.

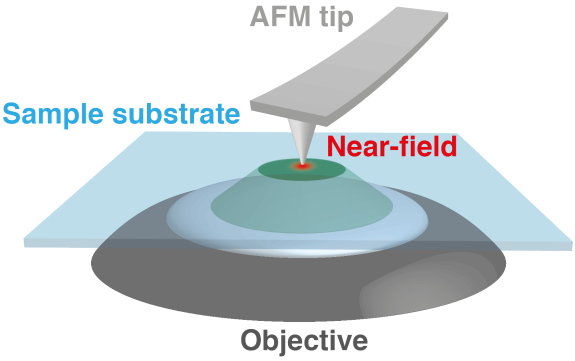

Figure 2.5: Scheme of a possible configuration for apertureless SNOM, using the apex of an AFM tip as nanometer-sized scatterer.

The main factors that influence the efficient coupling of light to an optical probe are the tip geometry, its material and dielectric function $\varepsilon(\omega)$, the dielectric constant ε_M of the materials surrounding the tip, as well as the angle of incidence and the polarization of the incident light. As a very simple first approximation, the tip apex can be considered a small sphere with a size much smaller than the excitation wavelength (and smaller than the skin depth of the metal). In this case, the electrostatic (or quasistatic) approximation is valid and the internal electric field E_{in} is described by an electric dipole in the center of the sphere.[7] The ratio of the internal electric field E_{in} to the incident field strength E_0 becomes very large if $\varepsilon(\omega) \approx -2\varepsilon_M$, i.e., when $\mathrm{Im}(\varepsilon(\omega))$ is close to zero and $\mathrm{Re}(\varepsilon(\omega))$ is close to $-2\varepsilon_M$.[46] This is only possible for materials having values of $\mathrm{Re}(\varepsilon(\omega))$ between -1 and -20 in the frequency range of interest.[46] The condition $\varepsilon(\omega) \approx -2\varepsilon_M$ leads to a strong optical response only at a certain (resonance) frequency ω. This is a simple example of a localized surface plasmon resonance that specifies the required wavelength at which the most efficient coupling to the optical probe will occur. Materials with the required optical properties exist and can be identified after evaluation of their dielectric functions. Figure 2.6 shows the dielectric function of a selection of materials (Si, Au, Ag, Pt and Al). When comparing the real part of the dielectric functions, the semiconductor Si (no plasmon resonances in the visible part of the electromagnetic spectrum) can clearly be differentiated from the metals, which show an overall decrease from small positive values (below 1) in the ultraviolet (UV) to negative values in the visible and infrared part of the electromagnetic spectrum. This behavior of the real part of the dielectric function is common to all metals and is simply predicted by the optical response of the free electrons in the conduction band (classical Drude model).[46,64,65] As mentioned above, this allows for plasmon resonances to occur at frequencies that are specific for each metal [depending on $\mathrm{Re}(\varepsilon(\omega))$]. The actual magnitude of the polariton resonance is determined by $\mathrm{Im}(\varepsilon(\omega))$, which ideally should have a value close to zero (see above), because then dissipation losses are minimal.[46] The dielectric function of different metals can be found in various textbooks[46,66,67] and their evaluation leads to the conclusion that the highest resonances can be expected for Ag and Au in the visible range (typical wavelength range for Raman spectroscopic measurements). Silver and gold are indeed most frequently used as materials for optical probes.[68] Interband transitions stretching from the near-UV to the visible region are the most pronounced difference between the dielectric function of Au compared to the one from Ag. Consequently, Au (similar to Cu) has a significant optical absorption below about 600 nm (high value for the imaginary part of the dielectric function in this range), but can exhibit strong resonances above 600 nm. In contrast, Ag is suitable for plasmonics over the whole visible range. Other metals such as platinum, palladium, and aluminum strongly absorb in the whole visible range. Aluminum, for example, is suitable for applications with UV excitation.[69,70] The above-mentioned condition and the trend of the real part of the metals dielectric function also implies that an increase in the dielectric constant ε_M of the surrounding medium leads to a red-shift of the localized surface plasmon resonance. This effect was used by Yeo et al.[71] and recently also by Hayazawa et al.[72] to tune the resonance frequency of a near-field optical probe to the blue/green spectral range by changing the underlying tip material in direct contact with the enhancing silver structure to a low-refractive-index material (e.g., $\mathrm{SiO_x}$, $\mathrm{AlF_3}$).

The frequency of the localized surface plasmon resonance is independent of the size of the sphere as long as the electrostatic approximation holds true. For larger spheres (best described by the Mie solution to the Maxwell equations), a red-shift of the resonance is observed as the particle size increases. The resonance condition can become very complicated when particle geometries other than a perfect sphere are considered. Extending the above theory for small spherical particles to small ellipsoidal particles leads to a modified resonance condition with the possibility of up to three distinct extinction peaks (the absorption depends on the incident polarization).[67] In the case of polarization along the longer axis of a spheroid, a red-shift of the resonance is expected with increasing aspect ratio. One approach which uses this phenomenon in the design of a tunable near-field probe was recently

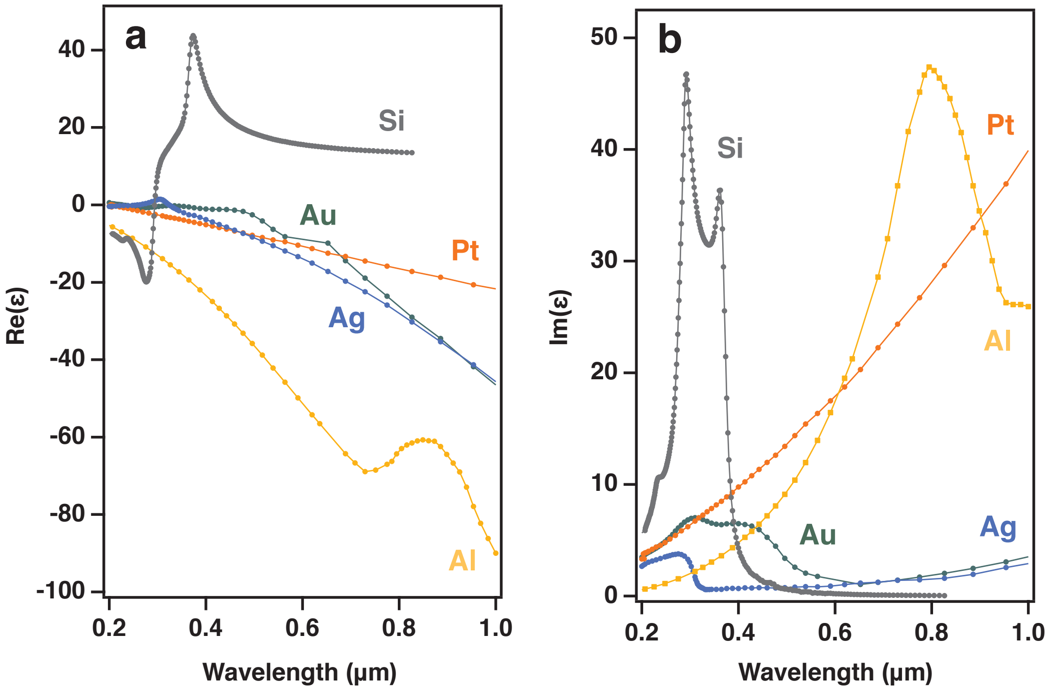

Figure 2.6: Real and imaginary part of the complex dielectric function of Si , Ag , Au , Pt and Al plotted against the wavelength. The plots are based on data from Palik.[66]

reported in the literature.[73] Fleischer et al. placed gold nanocones on AFM cantilevers as efficient optical probes. By varying the height of the gold cones (accompanied by a shift in their resonance wavelength), Fleischer et al. were able to adapt their optical probes to a large part of the visible spectrum (500–700 nm). Despite the large range of necessary heights (10–170 nm), the tip radius at the apex stayed the same, thus allowing for highly localized fields over the whole spectral range. For further details on the concentration of light by plasmonic structures, we refer to the recent review by Schuller et al.[74]

Localized surface plasmon resonances are considered to be the main contribution to the observed field enhancement, but other effects (mainly geometrical) can also contribute to the field enhancement. For example, “field line crowding” at any sharp tip apex can lead to a nonresonant local field enhancement independent of the excitation wavelength (lightning rod effect).[75] Correlations of the local field enhancement with, for example, the tip length and the apex radius of a silicon probe (to have no contribution from polaritons) were presented in a theoretical study by Esteban et al.[76] It was shown that a smaller apex radius leads to a more confined field and increased scattering. Furthermore, it was pointed out that very small tips (or even spheres) produce more confined fields than the long tips typically used for apertureless SNOM studies. Esteban et al. also discussed antenna-like resonances, which have to be considered when evaluating the tip length. This effect, known from traditional antenna theory, can also be used to specifically design efficient near-field optical probes.[77]

2.5 Practical Aspects of TERS

2.5.1 Tip–Sample Distance

An STM or AFM feedback scheme is normally used to control the tip-sample separation during TERS imaging experiments. When an STM technique is used, the distance control is based on the tunneling current between the tip and a conductive substrate, which is a strictly monotonic (decreasing) function of the tip-sample distance. The insulating gap is typically in the range of 0.5–1 nm. When an AFM technique is used, the distance control is based on forces acting between tip and sample surface, which cannot be described by a monotonic function (depending on the distance, repulsive or attractive forces dominate). When operated in contact mode, the tip-sample separation is typically smaller than in STM feedback control (<0.5 nm), which can be a considerable advantage (higher field enhancement), but can also lead, for example, to displacement or pick-up of sample molecules. Other feedback schemes sometimes used for TERS are tapping/semicontact mode AFM[78–81] and shear force feedback using a tuning fork.[82–84] Typically used tuning forks for this purpose are made of quartz (like those used in wristwatches). These oscillators are much stiffer (1800 N/m) than the silicon cantilevers used for tapping mode AFM and have a very defined resonance frequency of 32768 Hz (without the tip attached).[3]

The local field strength at the sample surface decays rapidly with increasing tip-sample separation. This phenomenon is a very good indicator of a true near-field effect. A recent study by Yano et al.[85] evaluated the effect of varying the tip-sample distance in tip-enhanced Raman experiments. They used a silver-coated silicon AFM probe in tapping-mode feedback. By using a time-gated photon-counting scheme, the detected Raman signal could be correlated with the vertical distance between

---

[3] This is accomplished by adding gold deposits at the end of the tines of the tuning fork, which makes the vibration frequency of the tuning forks too low. Precise removal of parts if the gold layer allows to precisely tune to the final resonance frequency of 32768 Hz.

the tip and the sample surface over the range of the tapping amplitude. They found an exponential decay of the near-field Raman intensity with increasing tip-sample separation, with typical values at $1/e$ between 10 and 25 nm depending on the tip used. Other studies state that the TER intensity (and the TER background intensity) is inversely proportional to the tenth power of the tip-sample distance. In most cases, no near-field contribution was observed for distances larger than 20 nm.[86–93]

2.5.2 Illumination Geometries

Various illumination geometries have been used for TERS so far. They can roughly be divided into bottom-, side- and top-illumination geometries (see Figure 2.7). Often, the same objective is used for excitation and detection, but the geometries can also be mixed (e.g., top-illumination with bottom-detection). In order for the bottom-illumination scheme to be applicable, the sample has to be transparent. However, bottom-illumination allows for the use of oil-immersion objectives with numerical apertures >1 by having a very short working distance and oil to match the refractive index of the glass substrate and the objective lens. In the case of opaque samples, restrictions for the objectives working distance are evident. Unfortunately, an increase in working distance typically comes with a decrease in the objectives numerical aperture. The spatial constraints in side illumination setups restrict the objectives numerical apertures to approx. 0.5. The different arrangement used in top-illumination schemes allows to bring the objective slightly closer to the sample and numerical apertures of 0.7 are possible. Even higher numerical apertures (NA ≈ 1) are achieved when instead of an objective, a parabolic mirror is used to focus the excitation beam and collect the scattered light.

Bottom-illumination

The first TERS experiments were done in a bottom-illumination configuration,[9–11] probably because it is readily implemented using an inverted optical microscope and because it promises the highest excitation and detection efficiency. The use of oil-immersion objectives results in the smallest possible focus at a certain excitation wavelength and collection of light from a solid angle of up to approx. 140° is practically possible. However, this configuration comes with the major restriction that it is only applicable for transparent samples.

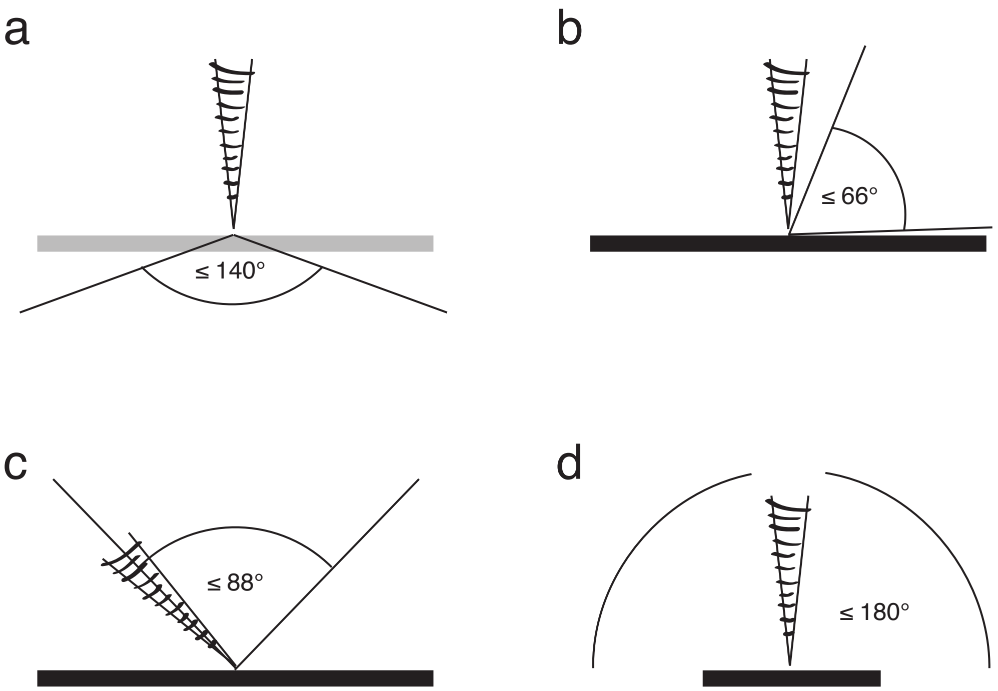

Figure 2.7: Schemes of commonly used TERS illumination geometries: Bottom-illumination (a), side-illumination (b), top-illumination (c), parabolic mirror illumination (d). The maximum illumination/collection angles are indicated.

Side-illumination

Side-illumination TERS was introduced by Pettinger et al. shortly after the first bottom-illumination TERS experiments.[94] It widened the scope of suitable samples, because side-illumination allowed measurements on opaque samples and was readily implemented using a metallic tip in STM feedback. Angles of incidence between 45° and 87° have so far been used for side-illumination.[95–102] Spatial restrictions require the use of long working distance objectives. This limits the objective's numerical aperture to values between 0.28 and 0.5, which leads to relatively large focus sizes. Especially when high angles of incidence are used, the effective size of the (asymmetric) focal spot is additionally increased. This requires the use of relatively high laser powers, compared to the other illumination schemes. If the same objective is used for detection of the scattered light, an additional loss in sensitivity is caused by the comparably low collection angles.

Top-illumination

The top-illumination scheme is rather intuitive, since epi-illumination confocal microscopes are widely used. However, a difficulty with this geometry is the fact that the tip has to be placed between objective and sample surface. This necessitates the use of long working distance objectives, which still maintain a rather wide illumination/collection angle to prevent shadowing effects. Top-illumination TERS was first reported in 2001 using a NA 0.45 objective and bent AFM tips.[103] The enhancement obtained on silicon was rather weak. A more successful approach using a NA 0.7 objective and etched full-metal STM tips followed in 2010.[104] The tip is typically introduced at an angle of approx. 45°. The symmetric scheme allows for tighter focusing compared to side-illumination.

Parabolic mirror illumination

All the illumination schemes mentioned above use refractive optical elements (lenses) to focus the excitation light on the sample and to collect the scattered light. Another possibility is to use one reflective element (parabolic mirror) to achieve practically the same thing.[4] The first experimental realization for TERS in ultrahigh vacuum was presented in 2007.[105] With such an illumination scheme, numerical apertures close to 1 can be reached allowing illumination/collection angles of almost 180° in air. Moreover, because refractive elements are eliminated, no chromatic aberrations arise. However, these setups are difficult to align, prone to coma aberrations and strongly restrict the sample size.[106,107]

2.5.3 Metallic Substrates

Scattering SNOM is a method where a tip with a nanometer sized apex is brought in close proximity to a sample substrate and illuminated with a focused laser beam (see section 2.4). The scattering response gives information on the surface morphology on a nanometer length scale. If the tip is placed on a thin metallic film, its scattering response scales with the thickness of the film, reaching a maximum intensity for thicknesses greater than the skin depth of the metal (32 nm at $\lambda = 633$ nm for gold).[62] If such substrates are used for TERS to enhance the overall Raman scattering one typically refers to this measurement configuration as gap-mode TERS.[108]

---

[4] Compared to a lens, the parabolic mirror has a focal point and not a focal plane.

For a free standing metal sphere of radius r ($r << \lambda$) in close proximity to a metal surface, the electric field from the dipole induced in the sphere considering a perpendicular electric field of the incoming radiation is as follows:[5][109]

$$E_{dipole}(d) = \frac{p}{2\pi d^3}, \tag{2.9}$$

with the distance d from the center of the sphere to the surface and the spheres dipole $p = \alpha E = 4\pi r^3 E(\varepsilon_p - 1)/(\varepsilon_p + 2)$ with the dielectic constant ε_s. As a result, an image dipole in the substrate is induced (manifests itself in the form of surface charges). The image dipole moment can be expressed as $p' = \beta p$ with $\beta = (\varepsilon_s - 1)/(\varepsilon_s + 1)$ (with the metal surfaces dielectric constant ε_s) and is located at a distance $2d$ from the dipole of the metallic sphere. The induced image dipole is also accompanied by an electric field, which will change the effective 'enhanced' electric field at the metal surface:

$$E_{eff}(d) = \frac{\alpha}{2\pi d^3}\left(E + \frac{p'}{16\pi d^3}\right) = \frac{\alpha}{2\pi d^3 - \frac{\alpha\beta}{8}} E. \tag{2.10}$$

The gain in TERS enhancement originating from different metallic substrates was recently studied by Stadler et al.[108] To also profit from this effect when using a bottom-illumination TERS setup, the use of gold and silver nanoplates has been introduced.[110,111] Another possibility is to use glass slides with a very thin (semi-transparent) metallic coating.[112] However, the effect is expected to be less pronounced, because in order to be transparent, these films have thicknesses below the metals skin depth.

2.5.4 Contrast, Enhancement Factor, and Field Confinement

The so-called enhancement factor is regularly used to compare different TERS studies, despite the high variability of enhancement factors cited in the literature.[47,113] The motivation to use an enhancement factor mainly stems from single-molecule TERS, where it is applied to estimate whether the enhancement is sufficient to detect single molecules at all. In TERS imaging experiments, however, reducing the near-field enhancement effects to a single number does not have much practical value. Characteristics such as spectroscopic contrast, field confinement, and the far-field-illuminated area/volume are of much higher practical relevance when considering TERS imaging

---

[5] for a parallel electric field of the incoming radiation the induced dipole is $E_{dipole}(d) = -\frac{p}{4\pi d^3}$ and the image dipole moment $p' = -\beta p$

experiments, because they give a direct measure of the achievable image quality (resolution, contrast) and the necessary collection time. The spectroscopic contrast can be determined by performing a 'tip-in-tip-out experiment' (Figure 2.8a), where the Raman peak intensity with the enhancing tip in contact with the sample surface is directly compared to the peak intensity on the sample surface with the tip in a retracted position. The most common definition is given by Equation 2.11:[47,68,114,115]

$$\gamma = \frac{I_{nf}}{I_{ff}} = \frac{I_{tip-in} - I_{tip-out}}{I_{tip-out}} = \frac{I_{tip-in}}{I_{tip-out}} - 1 \tag{2.11}$$

where I_{tip-in} is the Raman signal intensity when the near-field probe is in contact with the sample, $I_{tip-out}$ is the Raman signal intensity at the same sample position with the tip retracted, I_{nf} is the pure near-field signal intensity, and I_{ff} the (pure) far-field signal intensity.

The field confinement mainly depends on the probe dimensions, and distance curves give a good idea of the near-field nature of the enhancement and the field confinement in the z direction (see Section 2.5.1). The lateral field confinement can in practice be determined by a line scan across a sharp edge of a thin film of a strong Raman scatterer (e.g., graphene): the resolution is directly connected to the distance Δx (Figure 2.8b) over which the intensity increases from 10% to 90% of the final Raman intensity (on the film), which simply corresponds to the full width at half maximum (FWHM) of the line-spread function (first derivative of the edge response). A one-dimensional structure such as a single-walled carbon nanotube can also be used, where the near-field confinement directly corresponds to the measured intensity profile across the tube.[116]

The far-field illuminated area can have a considerable impact on the outcome of a tip-enhanced Raman imaging experiment. Continuous irradiation of a large sample area should be avoided to prevent photo-induced sample decomposition or bleaching. Considering a 128x128 pixels near-field image with a pixel size of 10 nm for a typical TERS imaging experiment, the investigated area of 1.64 μm^2 is almost seven times larger than the area illuminated by a tightly focused excitation laser beam in a bottom-illumination TERS experiment, when an oil-immersion objective can be used. In a typical side-illumination TERS experiment, the area that is continuously illuminated by the excitation laser is, e.g., close to 2 μm^2, which may lead to much more sample damage if the same power density is used. Recent TERS approaches without direct far-field illumination of the sample are therefore of particular interest for imaging experiments.[60,63]

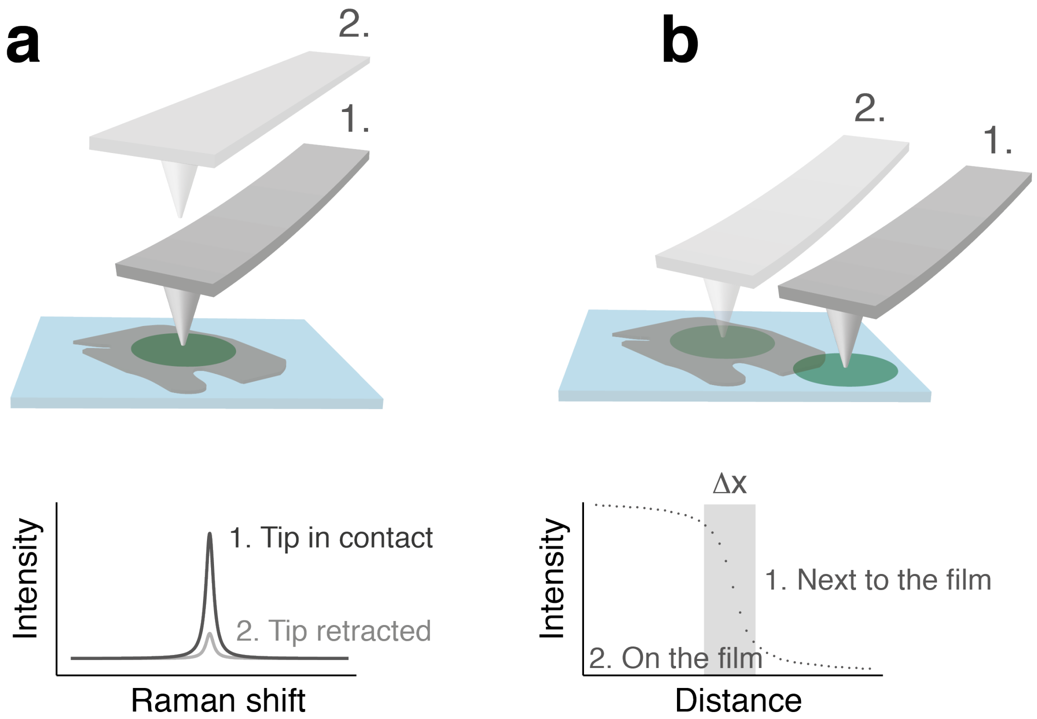

Figure 2.8: Schematic illustration of the experimental procedure for determining the contrast (a) and the lateral field confinement (b). To determine the spectroscopic contrast, the Raman band intensity with the enhancing tip in contact with the sample surface (a, 1) is directly compared to the peak intensity on the sample surface with the tip in a retracted position (a, 2). A line scan across the edge of a thin film (e.g., graphene) from a position next to the film (b, 1) to a position on the film (b, 2) shows an intensity slope, where Δx is a direct measure for the lateral extent of the near-field contribution (if the far-field contribution is negligible). The green circle symbolizes the size of the laser focus spot.

2.5.5 TERS Imaging

TERS imaging provides spectroscopic contrast, for example, to visualize the distribution of organic molecules on a sample surface[104] or to map physical stress on inorganic crystal lattices[81] on the nanometer scale. It delivers basically the same spectroscopic information as confocal Raman imaging; however, by introducing a near-field optical probe a considerably higher spatial resolution can be achieved. Some additional restrictions arising from the presence of the SPM probe are added: because the enhanced electromagnetic field at the tip apex decreases rapidly with increasing tip-sample distance (see Section 2.5.1), TERS imaging is restricted to the uppermost layer of a sample surface. Furthermore, as the tip's position is normally fixed relative to the focused laser beam, and only the sample is moved during an imaging experiment, the maximum grid size and scan speed for a TERS imaging experiment is determined by the positioning system of the sample stage (typically piezoelectric scanners).

It is known from confocal Raman imaging that, as a consequence of the inherently low Raman cross-section of most sample molecules, the collection, transfer, and detection of the scattered light has to be as efficient as possible to allow short acquisition times. The same holds true for TERS imaging. One aspect that contributes to the overall efficiency of a TERS imaging experiment is the detector used. However, since EMCCD cameras with single-photon detection capabilities are available, sufficient detector sensitivity is often not a big issue anymore.

Recent TERS imaging studies with acquisition of full spectra in every pixel demonstrated that a spatial resolution of about 10 nm can be achieved and acquisition times of 50 ms/pixel are possible for strong Raman scatterers[104,117] and 500 ms/pixel for weak Raman scatterers.[101] These studies include images with up to 256x256 pixels. If a pixel size of 5 nm (chosen below the expected spatial resolution of 10–20 nm) is used, the largest area that can be scanned at 50 ms/pixel in 1 h has a size of 1.34x1.34 μm^2. Typical values for the thermal drift of a state-of-the-art atomic force microscope are in the range of 0.01–0.1 nm/s, i.e., the total drift during a 1 h imaging experiment is between 36 and 360 nm. Direct comparison of these values to the estimated maximum scan area of 1.34x1.34μm^2 immediately shows that thermal drift can have a significant influence on the resulting image quality. Additionally, when the excitation laser has a typical focal spot diameter in the range of 300 to 2000 nm (depending on the laser wavelength and the used objective), the whole imaged sample area or a large fraction of it is illuminated during the entire experiment. This can limit the total imaging time because of possible photo-degradation of sample molecules.

As the Raman signal intensity is proportional to the amount of analyte inside the measurement volume, quantitative measurements with TERS are theoretically possible, but they are hampered by the effects that other parameters have on the signal intensity, such as fluctuations in the laser power and TERS contrast during a measurement (for example, because of instabilities in the tip-sample distance). Temporal changes in the AFM or STM feedback lead to fluctuations of the TERS contrast, which in TERS images manifest themselves as lines of higher or lower enhancement that are parallel to the scan direction of the tip, and thus are very similar to artefacts known from AFM and STM. A simple way to correct for that is to take the ratio between two characteristic marker bands (from two different compounds) instead of their absolute values to obtain the corresponding image.[118,119] Another approach is to use an internal standard such as, for example, the tip material itself (Ichimura et al. used the Si peak of their tip as an internal standard)[120] or an additional coating (e.g., a self-assembled monolayer of a thiol) whose Raman signal intensity is used to monitor changes in the enhancement and/or laser power during a TERS experiment.[121,122]

2.5.6 Common Artifacts in TERS Imaging

Spectral features originating from amorphous carbon are a well-known problem in SERS,[123] but are often neglected in TERS. Amorphous carbon has a four orders of magnitude higher scattering cross-section than benzene in the visible range of the electromagnetic spectrum.[124] Amorphous carbon appears as two broad bands at 1360 cm^{-1} (D band) and 1580 cm^{-1} (G band) or as fluctuating peaks,[125–127] depending on the integration times used. A study by Domke et al. formulated guidelines for how these spurious spectral features can be recognized and avoided for point measurements and measurement sequences.[128]

TERS imaging is also prone to spectral artefacts. However, intuitive guidelines can help to identify them to some extent. Let us consider the following example: a persistent spectral pattern is observed for a number of subsequent points during an imaging experiment. In a first assumption, this consistent sequence reflects the spatial distribution of a compound (analyte or contaminant) on the sample surface. However, on a second thought, it is just as well possible that this sequence is rather caused by a temporal artefact. In contrast, if one finds a recurring spectral pattern at adjacent positions perpendicular to the scan direction, a spatial correlation is more evident.

Because a metallic tip is brought very close to the sample surface, direct interaction of the analyte molecules with the tip surface are very likely. This can lead to an additional signal enhancement (see section 2.2.3), but especially for TERS imaging should be prevented, because the covalent bonds formed can be very stable and lead to permanent contamination of the tip, rendering it unusable. Particularly, molecules containing sulfur or nitrogen atoms show strong affinity to the commonly used nobel metals. Moreover, aromatic compound can have strong π-interaction with the metallic surfaces. Adsorption of analyte molecules can lead to shifts in vibrational modes of the molecules. This was, for example, shown for the analysis of adenine crystals, where Raman bands for different Adenine-Ag isomers were observed.[129]

2.5.7 Tip Lifetime

Silver is particularly prone to corrosion under atmospheric conditions (mainly due to the reaction with sulfur compounds). It has been shown that the corrosion happens particularly fast for silver nanostructures and strongly affects their plasmon resonance.[130]

Another factor limiting the tips lifetime is their mechanical instability. It is known form atomic force microscopy that even hard silicon tips can get blunt during an imaging experiment.[131] The more ductile materials used for TERS tips are even more prone to deformation. Coated tips can lose part of the coating, because the metals used adhere poorly to the underlying tip material. It was recently shown that the mechanical stability of silver coated AFM tips can be improved with a thin (2–3 nm) Al_2O_3 overcoating.[132] As mentioned in section 2.5.6, also contamination (e.g., with amorphous carbon) can limit the tip lifetime. A method for effective removal of carbon contaminants from SERS surfaces based on the much higher affinity of thiols to metallic surfaces was presented in 1998.[133]

Chapter 3

Experimental Setups and Procedures

This chapter introduces the instrumentation as well as the most important experimental procedures used throughout the thesis. Starting with the description of the top-illumination setup used most frequently throughout the work, another experimental setup based on an inverted optical microscope is described. This second setup was modified considerably during the course of the thesis, with the aim to allow TERS imaging on transparent samples using AFM feedback control in an aqueous environment. Moreover, improved and newly introduced tip preparation methods are presented. These include coated high aspect ratio Si AFM tips, which allow top-illumination AFM-TERS with high contrast factors, and self-made full-metal AFM-TERS tips, which are believed to be more mechanically stable than the coated AFM tips.

3.1 Instrumentation

3.1.1 Top-Illumination Setup

Opaque samples were investigated on a NTEGRA Spectra Upright (NT-MDT, Zelenograd, Russia). A scheme of the instruments optics is shown in Figure 3.1. The instrument is equipped with an xyz sample scanner (100x100x10 µm) based on a piezo-ceramic tube and capacitance sensors for closed-loop operation. The sample scanner can be roughly positioned in all three dimensions by means of manual micrometer drives. A measuring head with an incorporated objective (NA 0.7, W.D. 6 mm, 100x, Mitutoyo, Japan) and an attached AFM laser registration unit allows for easy exchange of tip holders for AFM and STM tips, respectively. Two visible lasers are coupled to the instrument by means of fiber optical cables. One of them is a Helium-Neon laser with a wavelength of 632.8 nm ($3s_2 \rightarrow 2p_4$ transition of neon) and an output power of 10 mW (LGK 7627, Siemens, Germany). The other one is a diode-pumped solid-state laser (DPSS, MLL532, CNILaser, China) with a wavelength of 532 nm and an output power of 50 mW. Both laser beams are sent through a plasma line rejection filter and brought to the same optical axis by means of beamsplitters. Motorized rotation of a circular variable neutral density filter (optical density gradient of 0–3.1) allows for continuous attenuation of the laser power on the sample stage. A manually revolvable Glan-Thompson prism can be introduced into the beam path to obtain a linearly polarized excitation beam. A motorized half-wave plate gives an additional means of rotating the polarization axis by up to 90°. The beam diameter can be adjusted to fill the back aperture of the microscope objective used by means of a motorized beam expander (1.78–7.19x, based on a Galilean telescope). A movable mirror (equipped with a piezo-ceramic tube) allows for scanning of the focused laser beam on the sample stage with high precision. Edge filters are used to separate back-reflected/elastically and inelastically scattered light. The inelastically scattered light can be sent through another revolvable Glan-Thompson prism for polarization analysis of the scattered light and is then directed through a confocal pinhole (double-crossed slits adjustable between 0 and 1.5 mm (80 µm for optimal confocality with the HeNe laser) right in front of a Czerny-Turner type monochromator (f = 520 mm) with four exchangeable diffraction gratings (one echelle grating and three conventional gratings with 150, 600 and 1800 l/mm) on a turnable turret. The two detector ports of the monochromator are equipped with a back-illuminated EMCCD (1600x400 array of 16 µm pixels, Newton 971 UVB, Andor, UK) and a photon counting head (GaAsP photocathode, H7421-40, Hamamatsu Photonics, Hamamatsu, Japan). The system is equipped with an additional detection unit comprised of a adjustable pinhole, a neutral density filter unit and a photomultiplier tube (PMT) for detection of the back-reflected/elastically scattered light in a confocal laser scanning microscope configuration. An integrated software allows for quick and accurate positioning of most optical elements. It allows for the acquisition of AFM and STM images and the dedicated tab for spectroscopic measurements differentiates between so-called slave (scanning mirror control) and master (sample scanner control) scanning. Full-spectral imaging times can be rather short by taking advantage of the cropped sensor mode and the internal memory of the EMCCD camera. This allows to scan a 64x64 pixels image in as little as 25 seconds. This is not as fast as can be achieved with the photon counting head, but is in most cases below the speed limit set by the Raman scattering properties of the analyzed sample. The instrument design allows to exchange tips without losing the current sample position. This gives the possibility to test different TERS active tips on the same sample position and to topographically image the area of interest with conventional AFM/STM tips.

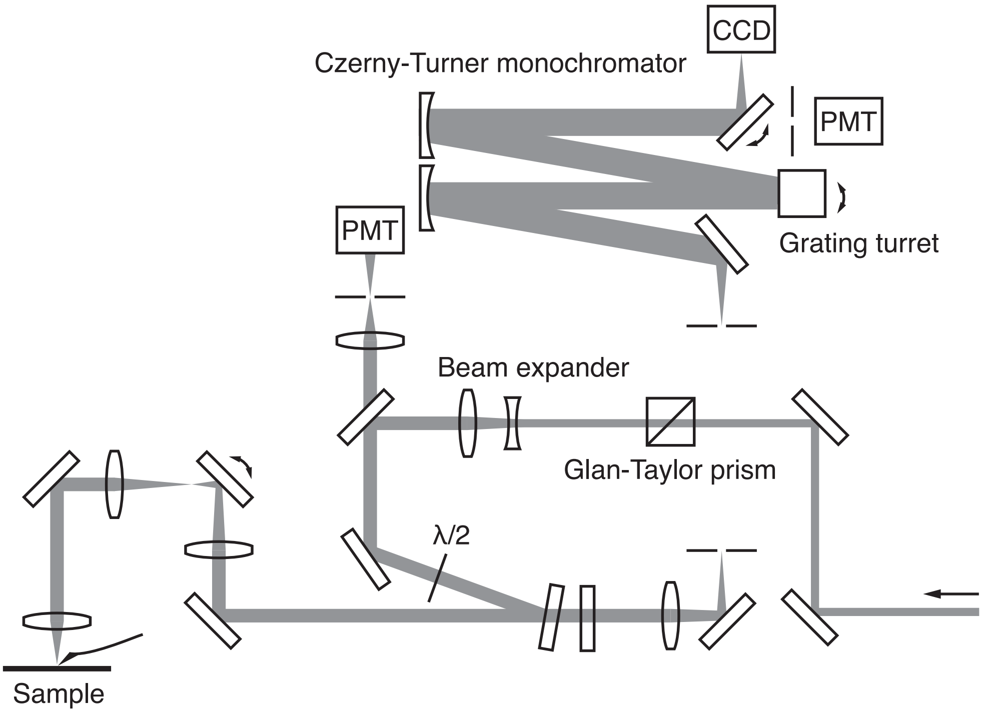

Figure 3.1: Optical scheme of the top-illumination TERS setup.

A typical STM-TERS experiment with the upright microscope goes as follows: A freshly etched TERS tip is mounted in the STM holder, where it is held in position by a mechanical spring that also enables electrical contact (see Figure 3.2). The tip is then manually brought into close proximity to the sample surface (at an angle of approx. 45° with respect to the surface normal) by means of manual z-movement of the stage. The distance to the sample surface can be monitored on a live camera image recorded though the measurement objective (field of view of approx. 115x85 μm^2). The last approx. 5 µm to the sample surface are then moved by carefully extending the piezoelectric tube of the sample stage until tunnelling feedback (constant current mode) is reached. Electrical contact to the sample surface is achieved with a contact clamp placed on the substrate (positive sample bias). A slave scan of the focused laser across the tip apex with simultaneous acquisition of Raman spectra and back-reflected light intensity reveals the position of the TERS hot spot at the tips apex. The laser focus is then manually positioned on the most enhancing spot and TERS point measurements at different positions or raster scans can be performed in master scan mode.

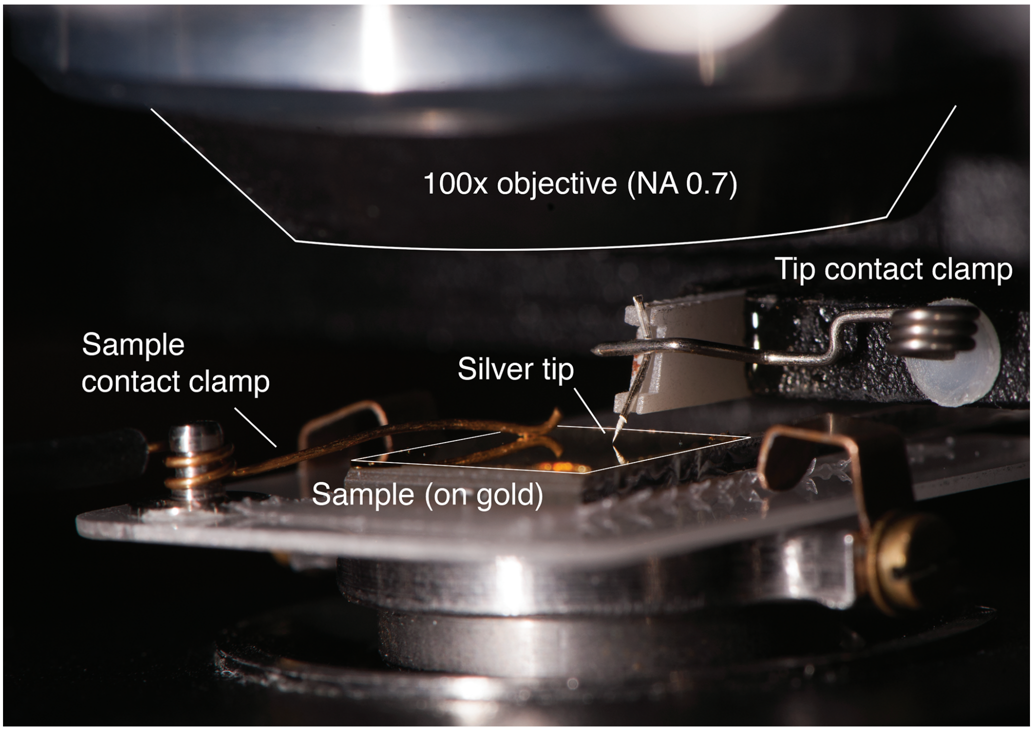

Figure 3.2: Photograph of the NT-MDT sample stage taken during an STM-TERS experiment.

3.1.2 Bottom-Illumination Setup

First Generation Setup

The first generation of the TERS instrument in our laboratory for transparent samples (see Figure 3.3) was based on a commercial inverted optical microscope (IX70, Olympus, Tokyo, Japan) in combination with a confocal laser scanning unit for fluorescence microscopy (FV500, Olympus, Tokyo, Japan). A 532 nm diode-pumped solid state laser with 70 mW output power (Ventus, Laser Quantum, Stockport, UK) is coupled to the system by means of a fiber optical cable and sent through a plasma line rejection filter (MaxLine LL01-532, Semrock, Rochester, USA). The beam is then sent through a combination of a linear polarizer and a removable radial polarizer (6 mm clear aperture, RPC-515-06, Workshop of Photonics, Vilnius, Lithuania) before it reaches the two-axis galvanometer mirror scanner. A series of pupil lenses link the FV500 unit with the inverted microscope. A tube lens (f = 180 mm) collimates the beam before sending it through one of the infinity-corrected microscope objectives: a 60x oil immersion objective (NA 1.4, PlanApo, Olympus, Tokyo, Japan) or a 20x air objective (NA 0.7, UPlanApo, Olympus, Tokyo, Japan). The scattered light is collected through the same objective and the inelastically scattered light is separated from the back reflected and elastically scattered light by means of a 45° dichroic beamsplitter (186 cm^{-1} transition, Semrock, Rochester, USA). A motorized filter wheel allows three possible scenarios: to leave the scattered light unaltered, to reflect it towards a PMT detector (R7862, Hamamatsu Photonics, Hamamatsu, Japan) behind an adjustable confocal pinhole, or to split the light once more by means of another 45° dichroic beamsplitter. Behind the motorized wheel, an edge filter removes any residual laser light before the Raman scattered light is coupled into a multimode fiber. The entrance of the fiber acts as the confocal pinhole. The fiber is directly connected to an axial transmissive spectrograph (HoloSpec f/1.8i, Kaiser Optical Systems, Ann Arbor, USA) equipped with a volume-phase holographic transmission grating. The spectrograph is equipped with a back-illuminated CCD camera (1024x255 array of 26 µm pixels, DU420-BV, Andor, UK). A baseplate on the inverted microscope is equipped for manual coarse positioning of a commercial tripod AFM scanner head (BioScope Catalyst, Bruker, Santa Barbara, USA) and motorized coarse position of the sample above the microscope objective. The scanner head is equipped with a piezo tube for accurate z positioning of the tip. Additionally the sample stage is equipped with a 2-axis piezoelectric scanner for accurate sample positioning (100x100 µm closed-loop scan range).

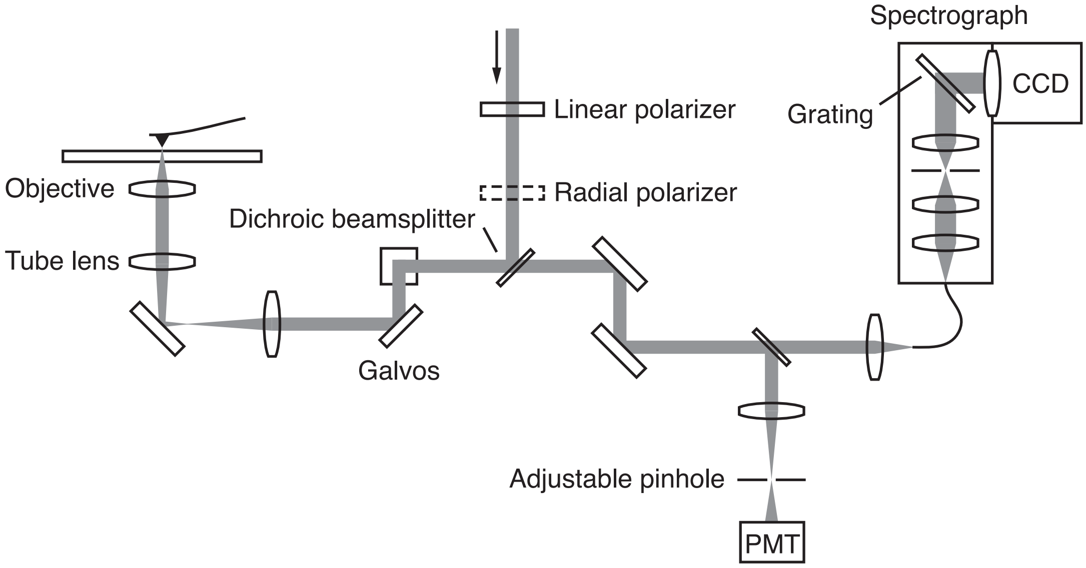

Figure 3.3: Scheme of the first generation bottom-illumination setup.

Positioning and scanning of the excitation laser beam is accomplished with the galvanometer mirror scanners and motorized z positioning of the objective. Software control (Fluoview software, Olympus) allows point measurements as well as line and rectangular area scanning with direct readout of the PMT detector. Acquisition of Raman spectra is done separately with an in-house written LabView software. Communication of the Raman microscope and the AFM is possible through an intermediate software (IRIS software, Bruker, Santa Barbara, USA).

A typical AFM-TERS experiment goes as follows: A freshly prepared TERS tip is mounted in the AFM holder and the AFM laser is reflected from the back of the cantilever toward the quadrant detector. First, tip approach toward the sample surface is done by means of motorized retraction of the two front tripod feet of the scanner head. Additionally the lateral position of the scanner head has to be adjusted (by moving the whole stage) in order to position the tip sufficiently close to the optical axis of the microscope objective (see Figure 3.4a). After this rough alignment the tip is automatically approached ('woodpecker' approach) using the Nanoscope software. Afterwards the tip is brought into AFM feedback with the sample surface. The tip is then imaged by confocal laser scanning and detection of the back reflected light with the PMT (see Figure 3.4b). The laser focus can be manually fixed on the tip apex before acquiring a tip-enhanced Raman spectrum using the custom LabView software.

In order to perform tip-enhanced Raman spectroscopic imaging, a previously recorded AFM image can be loaded into the IRIS software, where a grid for the TERS map can be defined. After starting the scan, the tip moves to the desired positions and spectra acquisition in the LabView software is triggered. The software then safes the resulting matrix of spectra together with the sample coordinates provided. The same approach can also be used for colocalized AFM/Raman measurements.

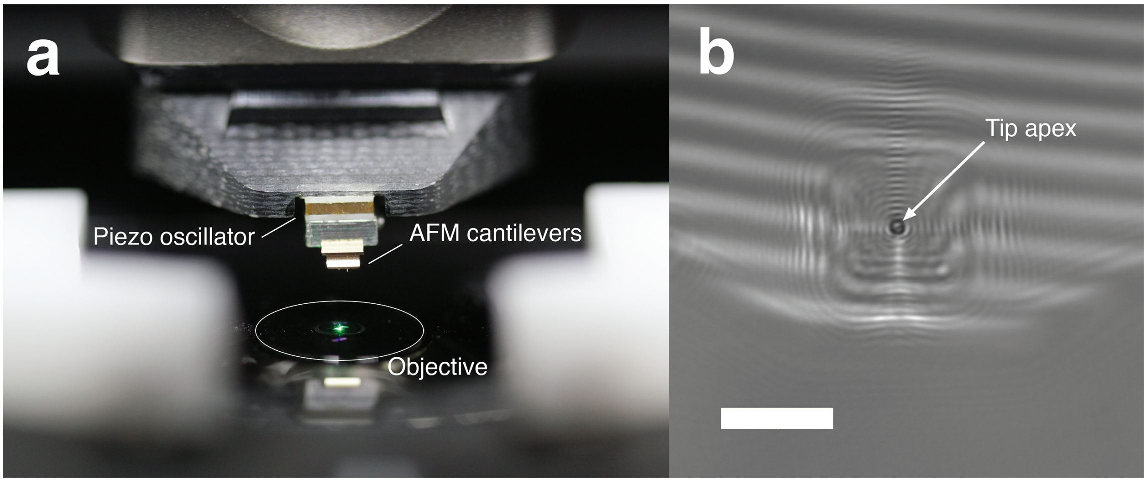

Figure 3.4: Photograph of the Catalyst sample stage (a) and reflected light image of an AFM tip collected with the PMT detector during confocal laser scanning. The scale bar indicates 5 µm.

Second Generation Setup

A second generation bottom-illumination TERS system was set up to overcome limitations of the laser positioning system of the first generation system and to increase atomation and flexibility for TERS imaging. The second generation system (see Figure 3.5) is equipped with a confocal Raman microscope (inVia, Renishaw, Gloucestershire, UK) with an additional laser port and mostly motorized optics. A home-built coupling to the existing inverted microscope allows for accurate positioning of the excitation laser on the sample and tip, respectively. The previously used 532 nm diode-pumped solid state laser and a new 632.8 nm Helium-Neon laser with 17 mW output power (R-30995, 500:1 polarization, Newport, Irvine, USA) are sent through plasma line rejection filters and reflected towards the spectrometer inlet, where the power can be reduced by means of motorized neutral density filters (16 possible power levels). A motorized Galilean telescope beam expander allows to adjust the beam diameter to fill the whole clear aperture of the optional radial polarizer (6 mm clear aperture, RPC-515-06, Workshop of Photonics, Vilnius, Lithuania). The excitation beam is directed towards the inverted microscope inlet by means of a periscope with a piezo tip/tilt mirror (S-334.1SD, Physik Instrumente, Karlsruhe, Germany) at the bottom position. This scan mirror is part of a 4f-imaging system, which also includes the inverted microscopes tube lens. Both abovementioned infinity-corrected objectives can be used. The scattered light is collected through the same objective and directed back to the spectrometer where the laser line is filtered out by means of edge filters. The inelastically scattered light is then focused through an adjustable spectrometer slit before entering a Czerny-Turner type monochromator (f = 250 mm) with the possibility to switch between three diffraction gratings (1800 l/mm, 1200 l/mm and 600 l/mm). A lens focuses the diffracted light onto a back-illuminated CCD camera (1024x255 array of 26 µm pixels, DU420-BV, Andor, UK) or a front-illuminated CCD camera (1024x256 array of 26 µm pixels, RenCam, Renishaw, Gloucestershire, UK).

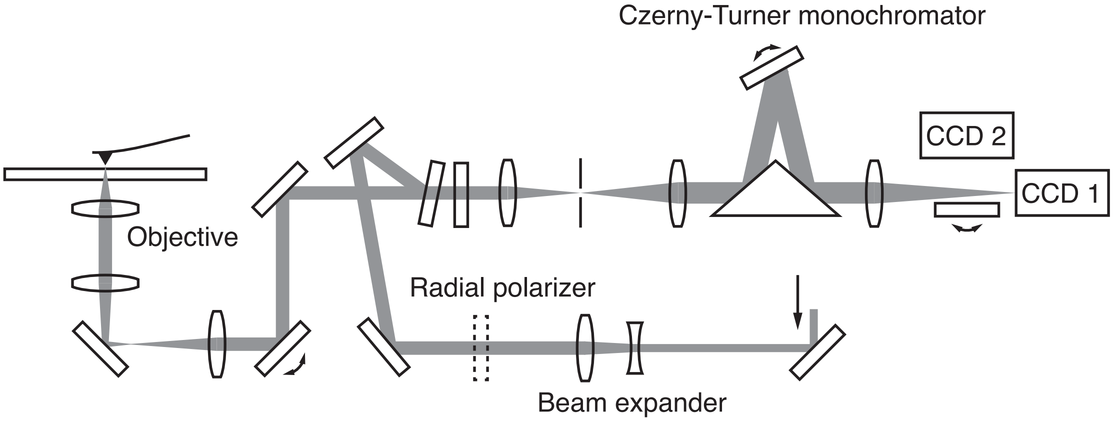

Figure 3.5: Scheme of the second generation bottom-illumination setup.

As mentioned above, the piezo tip/tilt mirror used for beam scanning is positioned at the lower periscope position at an angle of 45° with respect to the incoming beam when centered. The piezo mirror has a fixed pivot point and high angular accuracy in closed-loop operation. The mirror position is chosen such that the tipping motion is aligned with the optical axis and the tilting motion happens perpendicular to it. Tipping along the optical axis by α leads to a change in beam deflection of 2α (law of reflection), whereas tilting of the mirror perpendicular to the optical axis by β leads to a beam deflection of only $\sqrt{2}\beta$. Figure 3.6 illustrates the angular dependencies during mirror tilting. The resulting beam deflection θ is shown in the following.

Using the law of cosines for the two isosceles triangles in Figure 3.6 results in the following expressions:

$$c^2 = 2a^2(1 - cos(\beta)) \tag{3.1}$$

$$c^2 = 2b^2(1 - cos(\theta)) = a^2(1 - cos(\theta)) \tag{3.2}$$

The two formulae can be combined, which results in an expression that only depends on the two angular quantities, the tilting angle of the mirror β and the beam deflection θ.

$$2cos(\beta) - cos(\theta) = 1 \tag{3.3}$$

Because the applied tilt angles are small, the small-angle approximation ($cos(\theta) \approx 1 - \theta^2/2$) can be applied and the aforementioned relation $\theta = \sqrt{2}\beta$ results.

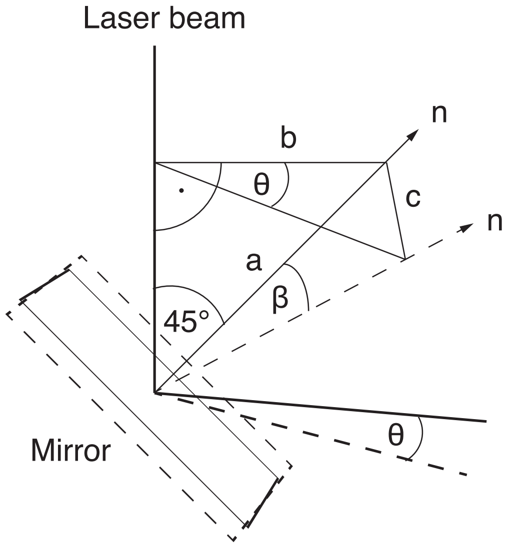

Figure 3.6: Scheme of the relevant angles for the tilting motion of the tip/tilt mirror.

The high voltages for the piezo tubes are supplied by a multichannel servo-controller (E-616.SS0G, Physik Instrumente, Karlsruhe, Germany). The control input voltages are supplied by an analog output module (NI 9263, +/-10V, 16-bit, National Instruments) in an ethernet data acquisition chassis (cDAQ-9184, National Instruments) and can be specified in the previously mentioned self-written LabView software for the acquisition of Raman spectra. The scanning of the laser focus on the sample surface can be visualized using a glass cover slip covered with a thin layer of ink deposited wit a felt-tipped pen. The laser focus is scanned across the surface after adjusting laser flux and dwell time in order to obtain small holes in the ink layer. An optical microscope image of such a grid of holes (32x32 pixels, scan range of 210x210 µm^2) is shown in Figure 3.7 shot using the 20x air objective. Almost no distortion is observed for this large scan range. The maximum scan range with the 60x oil-immersion objective is 70x70 µm^2. The laser focus scanning option allows confocal Raman scans as well as scanning during a single acquisition to reduce laser induced sample decomposition. Moreover, it allows to acquire scans across the tip apex to determine the location of the most enhancing spot (similar to the slave scanning option available on the top-illumination instrument (see section 3.1.1).

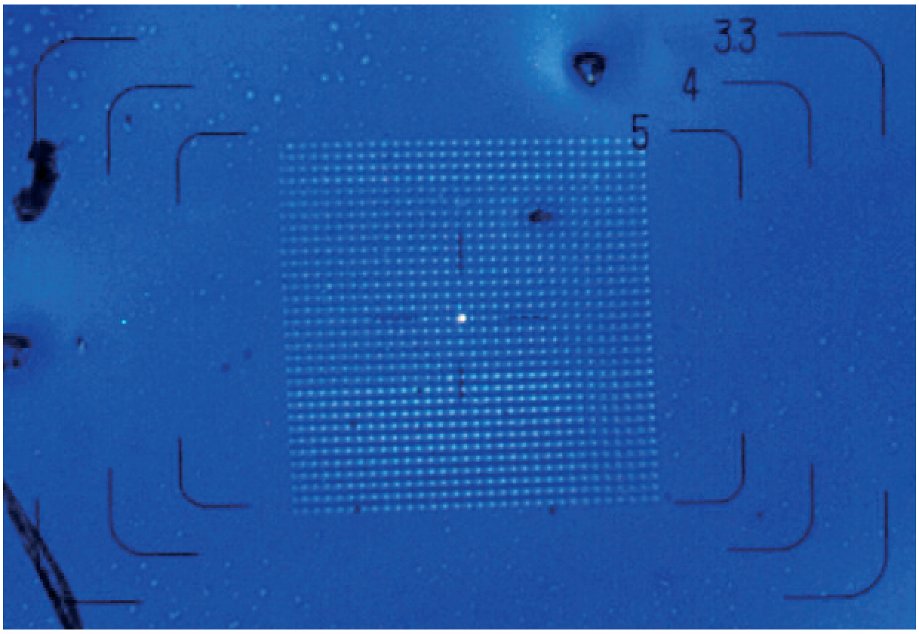

Figure 3.7: Visualisation of a 32x32 pixels laser beam raster scan of a 210x210 µm^2 area using the piezo tip/tilt mirror in combination with a 20x air objective.

3.2 Fabrication of TERS Tips

The development of methods for the preparation of full metal tips has mainly been driven by the field of scanning tunnelling microscopy (STM). The suitability of the prepared tip is then mainly defined by its foremost structure, which in the best case should comprise of only one atom. The morphology and cone angle of the tip shaft does not have any influence on the performance of the tip for scanning tunnelling applications. However, when the tip is used for optical applications, the surface roughness, cone angle, radius of curvature and crystallinity can have a major impact on the measurement. Ideally, the tips should have a particularly small radius of curvature and a conical shape.[1] Such tips can be prepared by electrochemical etching of silver and gold wires. The preparation of TERS tips to be used in contact-mode or tapping-mode AFM feedback is more elaborate, because a reflective cantilever is required for feedback control. These tips are typically prepared by deposition of the enhancing metals on the tips of commercial AFM probes. However, it is also possible to prepare working full-metal AFM-TERS tips from etched metal wires (see section 3.2.4).

3.2.1 Silver Tip Etching Procedure

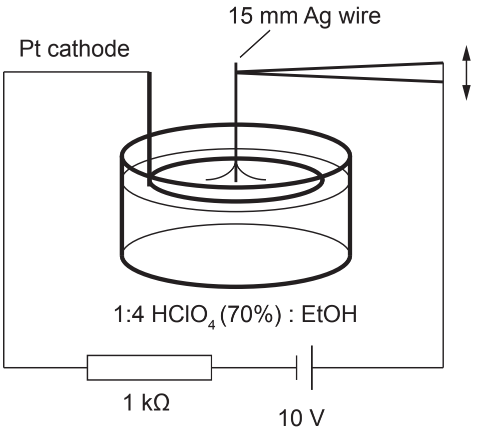

Figure 3.8: Scheme of the Ag tip etching setup.

Figure 3.8 shows a scheme of the silver tip etching setup. Slightly different etching recipes have been used throughout this thesis and are described separately, when necessary. In the following, only the optimized procedure developed during the thesis is describes: The etchant is premixed in a glass beaker. It consists of perchloric acid ($HClO_4$, 70%) and ethanol in a ratio of 1:4 (v/v). The ethanol is added to prevent bubble formation. A platinum wire (Ø 0.5 mm) ring electrode with an inner diameter of approx. 13 mm is immersed into the etchant. It should be fully immersed in the etchant, however, close to its surface. An Ag wire (Ø 0.25 mm) with a length of

---

[1] A recent work by Johnson et al. demonstrated the high effectiveness of tips with a smooth pyramidal shape.[134]

15 mm is immersed into the etchant by 2 mm at the center of the ring electrode. Then, the etching voltage is turned on. A voltage of 10 V is applied and a 1 kΩ resistance defines the etching current of approx. 10 mA. The etching happens most rapidly at the meniscus and it continues until the lower (immersed) part of the wire drops to the bottom of the beaker. Because this leads to a sudden drop in the current, an in-house built control device can be used to immediately interrupt the circuit to prevent overetching of the tip. The formed tip is then carefully retracted from the etchant surface and rinsed with water and ethanol.

3.2.2 Gold Tip Etching Procedure

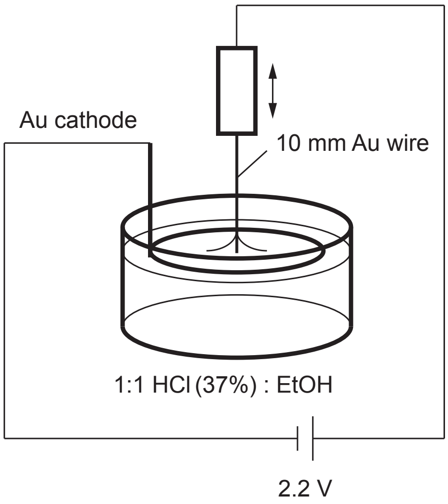

Figure 3.9: Scheme of the Au tip etching setup.

Figure 3.9 shows a scheme of the gold tip etching setup. The etchant is premixed in a glass beaker. It consists of hydrochloric acid (HCl, 37%) and ethanol in a ratio of 1:1 (v/v). A gold wire (Ø 0.5 mm) ring electrode with an inner diameter of 30–40 mm is immersed into the etchant (5–10 mm below the surface of the etchant). A gold wire (Ø 0.25 mm) with a length of 10 mm is fixed in a conductive holder, which is put in place above the etchant beaker. The holder is then carefully lowered until the gold wire is immersed into the etchant by approx. 3 mm. The etching circuit with an applied constant voltage of 2.2 V is then closed by attaching the clamp wire to the tip holder. During the etching the etchant slowly starts to turn yellow, which can be explained by the formation of $AuCl_4^-$ ions:[135]

$$\mathrm{Au} + 4\mathrm{Cl}^- \rightleftharpoons \mathrm{AuCl_4}^- + 3\,\mathrm{e}^-, E^0 = -1.002\ V \tag{3.4}$$

Oscillations of the current during the etching procedure is normal and is caused by passivation of the gold surface due to oxidation (decrease in current) and dissolution of the oxide (increase in current).[136] The etching is finished when the lower (immersed) part of the wire drops to the bottom of the beaker. The formed tip is than carefully rinsed with water and ethanol.

3.2.3 Coated AFM Tips

Commercial pyramidal silicon nitride contact-mode tips (RC800PSA, Olympus, Tokyo, Japan), high aspect ratio Si tapping-mode tips (AC160BN, Olympus, Tokyo, Japan), conical Si tapping-mode tips (CT300, Nanoscience Instruments, Phoenix, USA) and Concorde-shaped Si tips (ATEC-NC/CONT, Nanosensors, Neuchatel, Switzerland) were coated with a 30–50 nm thin metal layer using a vapor coating chamber (MED 020, Bal-Tec, Liechtenstein) at a pressure of 10^{-6} mbar. The tips were mounted approx. 15 cm above the evaporation source. The material placed in a molybdenum boat or a tungsten coil can be evaporated by resistive heating. The film thickness obtained is monitored using a quartz crystal microbalance (SG 060, Bal-Tec, Liechtenstein). In some cases precoatings of $\mathrm{AlF_3}$ or $\mathrm{SiO_x}$ were used to tune the optical responds of the TERS tips.[71]

Figure 3.10a shows the bottom side of a coated pyramidal silicon nitride contact-mode cantilever and reveals a square pyramid with a side length of approx. 5 µm. A close-up image of the apex of the pyramid (Figure 3.10b) reveals the grainy structure of the silver coating. The tip radius of the uncoated tip is specified to be less than 20 nm. The close-up SEM image reveals an increase in the tip radius due to the coating with a single silver nanoparticle (Ø $\approx$ 70 nm) at the apex.

Because the tip is 'hidden' under the cantilever, the AFM probes shown above are not compatible with top-illumination TERS. Concorde-shaped silicon tips are a good alternative, because the tip is protruding from the cantilever, making it visible from the top. However, it was found that these tips give almost no signal enhancement when illuminated from the top, whereas they worked fine with bottom illumination.[137] The reason was ascribed to the fairly low aspect ratio of the tips leading to shadowing of the incoming laser light and the Raman scattered light. In order to solve this problem, high aspect ratio (typically 7:1) silicon tips were used

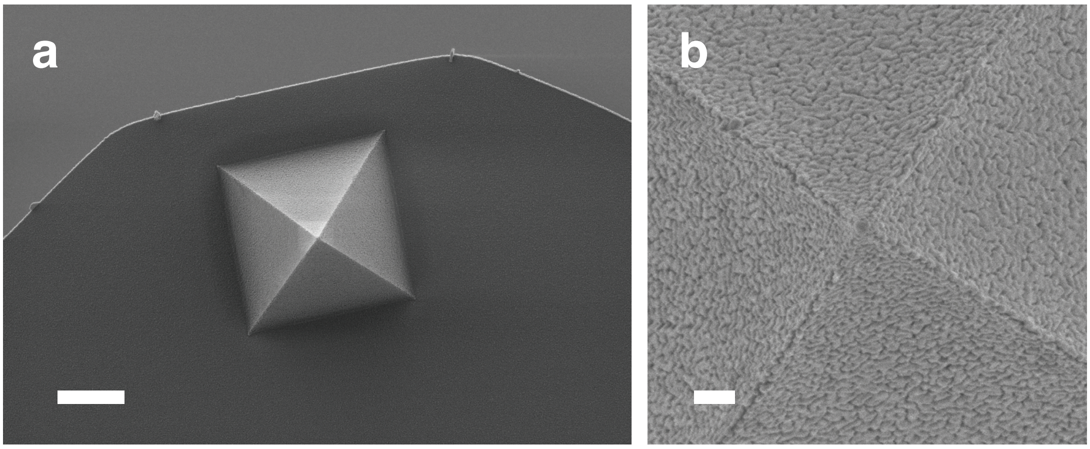

Figure 3.10: SEM overview image of a silicon nitride AFM tip coated with a 30 nm Ag layer (a) and a close-up image of the tip (b). A particulate structure of the silver is observed with a single particle (Ø ≈ 70 nm) at the apex. The scale bars indicate 2 µm and 200 nm, respectively.

instead. SEM images from a used high-aspect ratio tip after coating it with 20 nm AlF_3 and 30 nm silver is shown in Figure 3.11. The overview image of the bottom side of the cantilever (Figure 3.11a) illustrates the high-aspect ratio of these tips. The close-up image in Figure 3.11b shows the particulate structure of the coating, which has been removed at the tip apex, probably due to mechanical interaction with the sample surface.

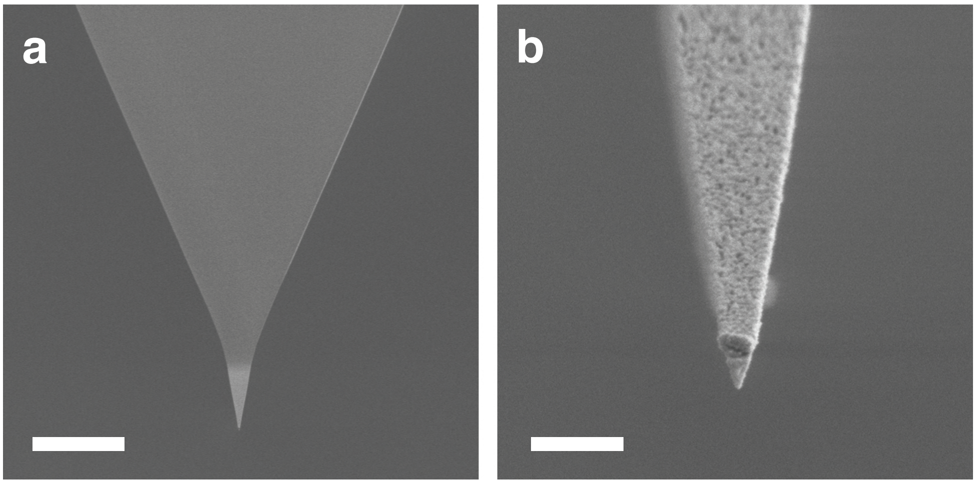

Figure 3.11: SEM image of a used high aspect ratio silicon AFM cantilever coated with 20 nm AlF_3 and 30 nm silver (a). The close-up image of the tip apex (b) reveals the grainy structure of the silver layer and shows that part of the coating was removed at the very end of the tip. The scale bars indicate 10 µm and 500 nm, respectively.

Figure 3.12 shows a tip-enhanced Raman spectrum collected with a silver coated high-aspect ratio tip in tapping-mode feedback. The high contrast factor (>150) obtained with this tip indicates that the previously stated hypothesis of a shadowing effect of the low aspect ratio tips is very likely and can be avoided by changing to high aspect ratio tips. However, the apparent low adhesion of the coating to the underlying silicon surface (see Figure 3.11b) does not make these tips suitable candidates for TERS imaging experiments. Not using an AlF_3 precoating, as well as prior oxidation of the silicon cantilevers could improve silver adhesion.[72,138]

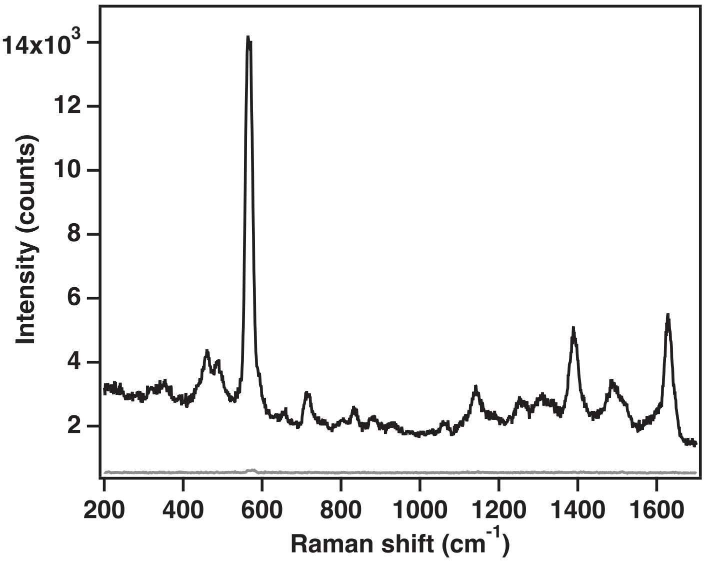

Figure 3.12: Raman spectrum of spin-coated BCB on TS gold (230 µW, 0.5 s acquisition time) right at the tip apex (black) and next to the tip (gray).

3.2.4 Full Metal AFM Tips

In order to produce more robust AFM-TERS tips, the know-how for the preparation of full metal tips typically used for STM measurements was adapted to prepare an equivalent version compatible with AFM feedback. This approach is inspired by recently reported methods with etched gold tips and cut silver wires.[115,139]

The preparation procedure of these full-metal AFM-TERS tips is as follows: Silver microwires (Ø 0.05 mm, 99.99%, Alfa Aesar) were electrochemically etched using the method described in section 3.2.1. The etched wires were then flattened between two borosilicate glass coverslips and attached to a used silicon chip after the original cantilever had been broken off. An electrically conductive silver-filled epoxy paste

(E4110, Epoxy Technology, Billerica, USA) was used for this purpose. In a last step the apex of the cantilever tip is mechanically bent. This is the most critical step and an exact control of the bending angle is rather difficult. One rather intuitive method requires a pair of fine tweezers and a steady hand. Another possibility is to cover the cantilever all the way down to the tip with a glass cover slip and use careful upwards tilting of another coverslip positioned underneath the cantilever to bend the tip. Figure 3.13 shows scanning electron microscopy images of a silver cantilever made by the second procedure. The top view image of the cantilever (Figure 3.13b) shows that since the wire was flattened after the etching procedure, the conical part of the tip is also flattened, which allows to reflect the AFM laser very close to the tip apex. This property is essential, since in our top-illumination setup, the AFM laser runs through the same objective as the Raman laser.

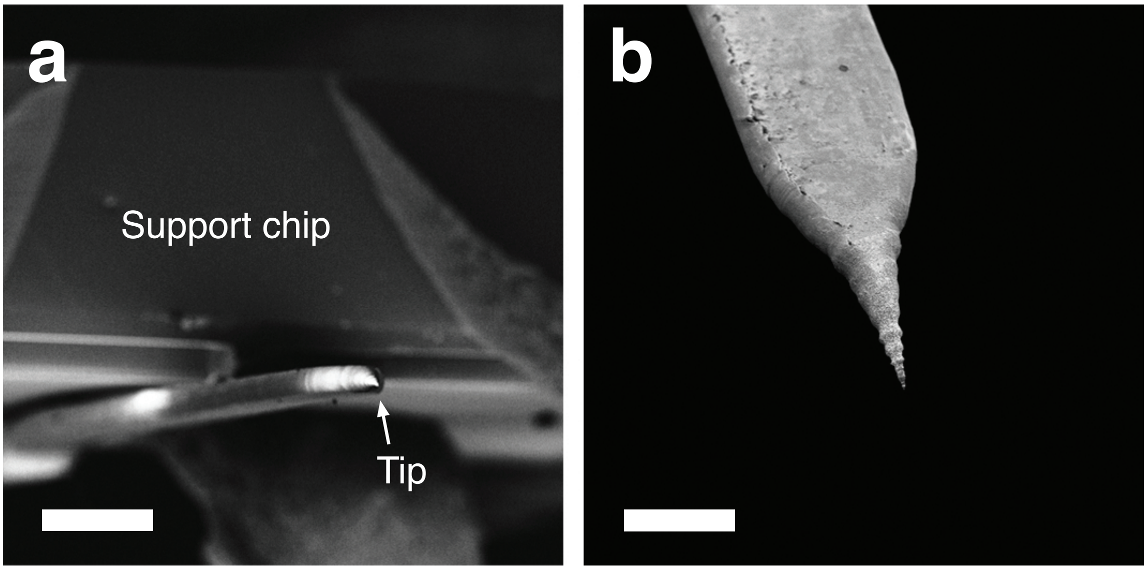

Figure 3.13: SEM image of a self made tapping mode AFM probe with full-metal Ag cantilever. The overview image (a) shows the front of the silicon chip with the attached Ag cantilever, which extends by approx. 580 µm from the silicon chip. The tip is slightly bent downwards to ensure that the apex touches the sample surface first (the used holder already positions the chip at an angle of 15° with respect to the sample surface). The scale bar indicates 100 µm. The top view image (b) of the etched cantilever end shows that the conical part of the cantilever is also flattened to ensure that the AFM laser can be reflected very close to the tip end. The scale bar indicates 50 µm.

Figure 3.14a shows the resonance spectrum of one of the self-made silver cantilevers. The resonance frequency f_0 of approx. 145 kHz is in a similar range as those of commercial silicon tapping mode cantilevers and could be tuned by controlling the cantilever's length l and thickness t ($f_0 \propto t/l^2$).[140] The force constant of the cantilever was not measured. After determining the resonance frequency of the cantilever, it was used for a tapping-mode AFM scan on a silicon test grid to demonstrate its stability for AFM scanning. The square elevations of the test grid are clearly visible.

First TERS experiments on a thiophenol self-assembled monolayer (SAM) on gold using one of these full-metal AFM cantilevers in tapping mode feedback and top illumination were performed, however, so far only with moderate signal enhancement. Since the bending of the tip apex cannot be done in a very reproducible manner (see above), different effective angles with respect to the incident excitation laser result. This could have a strong influence on the obtainable signal enhancement.

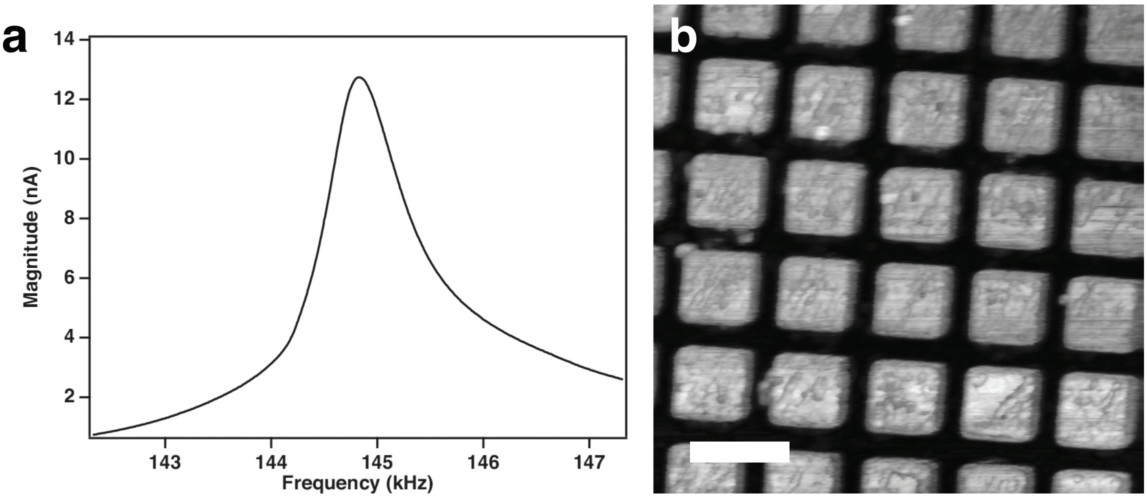

Figure 3.14: Resonance spectrum of a self-made Ag AFM cantilever (a) and a tapping-mode AFM topography image of a silicon test grid (b) The scale bar indicates 10 µm

3.3 Gold Substrates

Flat gold films can be prepared by means of a template stripping method:[141] silicon wafers are cleaned in piranha solution before they are vapor coated with a 200 nm gold film. This was done with the same coating chamber used for tip coating described in section 3.2.3. A glass support (cut from a microscope slide) is then glued onto the gold covered side with an optical adhesive (NOA 61, Norland, Cranberry, USA). Curing under UV light (365 nm) and thermal aging on a heating plate at 50°C results in a ‘sandwich structure’ consisting of the template (silicon wafer), the gold film and a mechanical support (glass). Mechanical cleavage releases a flat gold surface. The ‘sandwich structure’ can be stored for long periods of time without contamination of the gold surface. Before use it can directly be mechanically cleaved.

Semi-transparent gold substrates were prepared as follows: borosilicate glass slides (D263, Marienfeld, Germany) were cleaned in piranha solution and vapor coated with a 2 nm titanium (99.7% purity, ABCR, Germany) adhesion layer and a 10 nm gold layer. These substrates have a transmission of >50% at 532 and 633 nm.

Gold nanoplatelets were prepared in piranha cleaned glass ware. A 7.4 mM solution of cetyltrimethylammoniumbromide (CTAB, ≥99%, Sigma Aldrich) was added to 20 ml of a 1.5 mM $HAuCl_4$ solution (≥99.99%, Alfa Aesar) in a round bottom flask and the mixture was heated to 50°C. A sudden change to a dark orange color suggests the formation of $AuBr_4^-$. 30 ml of an aqueous solution of 0.9 mM sodium citrate dihydrate (≥99%, Sigma Aldrich) was heated to 50°C and the mixed CTAB, $HAuCl_4$ solution was injected into the sodium citrate solution. Gradual increase of the temperature (5°C every 5 minutes) up to 80°C was done under reflux. The solution was left at the final temperature for another 60 minutes. After cooling, suspended shiny flakes were visible by eye. Before deposition, 3 ml of the final solution were diluted with 17 ml milliQ water. Droplet deposition, vacuum drying in a deccicator and washing in a 70°C milliQ water bath was repeated up to three times to increase the surface coverage. Finally, the samples were dried in an oven for 30 min at 140°C. An AFM topography image of a hexagonal gold nanoplatelet is shown in Figure 3.15. Deposition of these nanoplatelets on ultraflat ITO glass (Balzers) allows to use these substrates for STM-TERS measurements.

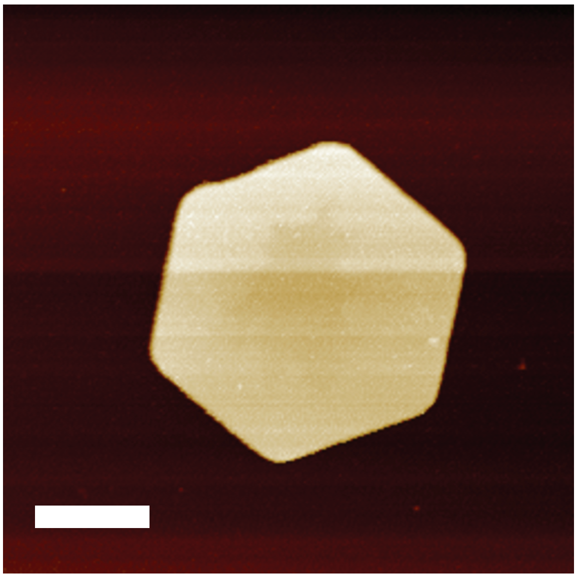

Figure 3.15: AFM topography image of a gold nanoplatelet with a thickness of approx. 80 nm on glass. The scale bar indicates 1 µm.

3.4 Control of Polarization

In side-illumination TERS, the polarization of the excitation beam is crucial to obtain high contrast factors. When the tip axis is perpendicular to the surface, p-polarization (polarisation parallel to the surface normal) works best.[95,142,143] In the case of top illumination with the tip tilted sideways, the situation becomes slightly more complex, especially if measurements are performed on a gold surface (see section 2.5.3). Figure 3.16 shows the resulting enhancement (of the ring breathing mode of thiophenol) using different linear polarization directions with respect to the tip axis. The enhancement with the polarization direction along the tip axis was slightly higher compared to the cases, where the polarization was turned by 45° and 90° with respect to the tip axis. However, the effect is not very pronounced and mixed polarization was used for most experiments.[2]

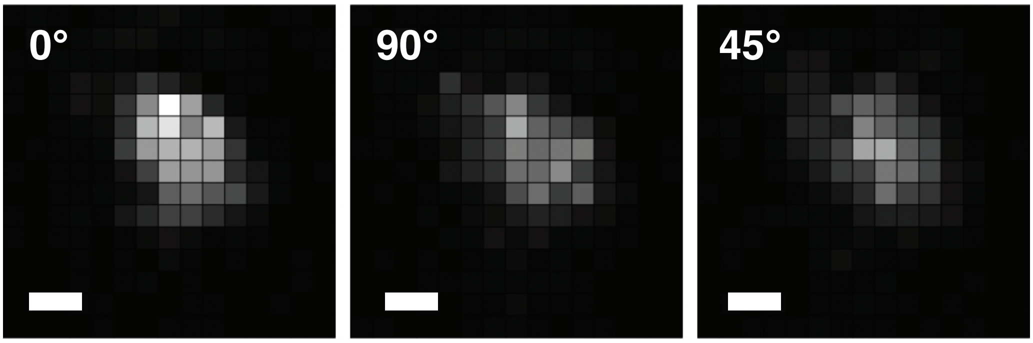

Figure 3.16: Slave scan across the tip apex in close proximity of a thiophenol SAM on gold using different linear polarization directions. The pixel brightness represents the peak height of the ring breathing mode of thiophenol. The brightness scale is the same for all three images and spans from 0 counts (dark) to 820 counts (bright). The indicated angles are with respect to the tip axis. The tip enters the image from the bottom and the scale bar indicates 500 nm.

In the case of bottom illumination, where the tip is typically introduced perpendicular to the sample surface, the focusing of linearly polarized beams with high numerical aperture objectives leads to two pronounced longitudinal (along the direction of propagation) field lobes slightly displaced from the optical axis, which can effectively couple to the tip. A more abundant longitudinal field component in the center of the focus can be obtained, when radially polarised beams are used.[12] Radially polarized beams have the characteristic that the polarization vector at any position on the

---

[2] The mixed polarization is most probably caused by polarization mode dispersion in the optical fiber.

beam points towards the center. Focused with a high numerical aperture objective, these beams have strong longitudinal, non-propagating fields in the center (magnetic field is zero and therefore also the poynting vector). A radially polarized beam can be obtained by sending a linearly polarized beam through a mode converter that gradually turns the polarization by an increasing angle using, e.g., arrays of wave plates. Besides the pronounced longitudinal field component, the rotational symmetric superposition in the focus allows to focus radially polarized beams more tightly than linear polarized Gauss beams (at the same numerical aperture). Dorn et al. demonstrated the possibility to focus a radially polarized beam down to a spot size of 0.16 λ^2 using an objective with a numerical aperture of 0.9.[144]

The bottom-illumination setup described above is equipped with a commercial radial polarizer (see section 3.1.2), allowing to use radially polarized beams for improved coupling to the TERS tip. A home-made beamprofiler (modified Logitec webcam) was used to show the quality of the radially polarized beam. Figure 3.17a shows the doughnut shape of the beam obtained. By sending the doughnut beam through a linear polarizer, a bow tie shape results. In the case of a radially polarized beam, the bow tie is oriented along the direction of polarization specified on the linear polarizer and allows to clearly differentiate it from azimuthally polarized beams, which would result in a bow tie turned by 90° with respect to the direction of polarization.

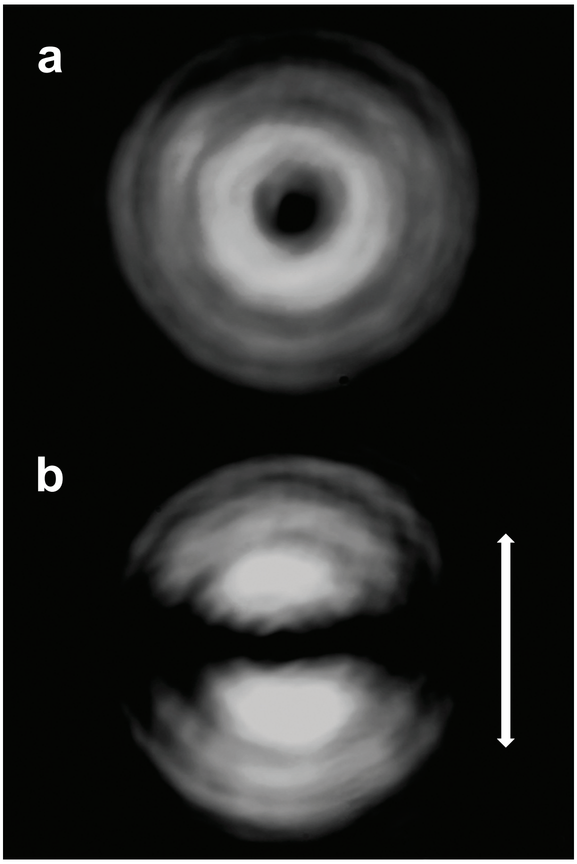

Figure 3.17: Beam profile of a radially polarized doughnut beam before (a) and after (b) sending it through a linear polarizer. The two sides arrow indicates the direction of poarization of the used linear polarizer.

Chapter 4

Chemical Degradation of Silver Near-field Optical Probes and Its Electrochemical Reversal

Elemental silver suffers from corrosion caused by the reaction with sulfides, sulfates, oxides and chlorides in the atmosphere. This limits its application in the field of plasmonics and nanoelectronics, where its outstanding optical and electrical properties could otherwise be fully exploited. Corrosion of plasmonic silver tips renders them unusable for TERS within a few days after production. This makes a commercialization impossible and only specialized laboratories with in-house tip production are using these highly enhancing tips. We present a simple method to recover the enhancing effect of corroded silver tips as well as to store fresh tips, for example, for easy shipment.

This chapter is adapted from:
L. Opilik, Ü. Dogan, J. Szczerbiński, R. Zenobi: 'Chemical Degradation of Silver Near-field Optical Probes and Its Electrochemical Reversal', in preparation.

4.1 Introduction

TERS has gained significant attention in recent years because it allows for spectroscopic imaging under atmospheric conditions with a lateral resolution down to a few nanometers[13,145,146] and a sensitivity on the single molecule level.[14] The main difficulty that prevents TERS form being used as a routine analytical method is that the reproducible production of long-term stable and strongly TERS active tips is very challenging. Silver is known as excellent plasmonic material because, compared to other commonly used metals, silver is cheap and exhibits the lowest losses at visible and near-IR frequencies.[147] Gold is more commonly used despite its inferior optical properties (high losses due to interband transition below 600 nm). This is mainly due to the low chemical stability of silver, which corrodes under ambient conditions due to reactions with sulfides, sulfates, chlorides and oxides from the atmosphere mediated by the surface water layer.[148] The most abundant corrosion product is acanthite (Ag_2S) and the dominant reaction pathways of sulfur-containing compounds are understood to a great extent (see Figure 4.1).[148] It was found that the corrosion products formed lead to broadening and redshifting of the localised surface plasmon resonance peak of silver nanostructures.[130,149] Because of this and the fact that the corrosion processes do not lead to a passivating layer, but extend deep into the material, the use of bare silver for plasmonic applications is very limited.

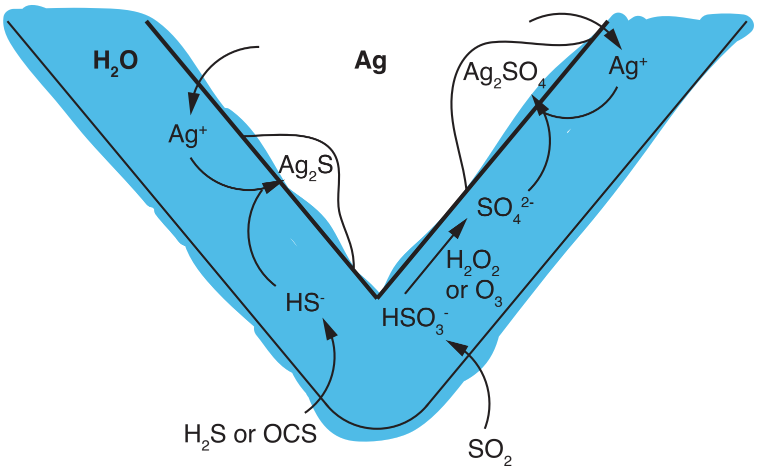

Figure 4.1: Reactions with atmospheric sulfur-containing compounds occurring during silver corrosion within the surface water layer at the silver tip apex.

A widely used strategy to cope with the low chemical stability of silver is the use of thin protective coatings that do not strongly interfere with the desired optical properties. Commonly used coatings include alumina,[114,150–152] silica,[153–155] self-assembled monolayers of thiols[156–159] and graphene.[149,160] All of these materials prevent direct access, e.g., of H_2S to the silver surface and can be considered artificial passivation layers. It was found that these coatings also lead to increased mechanical and thermal stability as well as changes in adsorption characteristics.[132,151,152] However, for surface-enhanced and tip-enhanced Raman techniques, even a very thin passivation layer can lead to a considerable decrease in signal intensity.[161]

Another strategy to deal with the corrosion of silver is based on the fact that the reaction with sulfur compounds can be reversed in a galvanic cell like configuration, using an anode (e.g., aluminum) with a lower reduction potential than the ones of the typical products of silver corrosion. Two relevant half reactions with their corresponding standard reduction potentials are[135]

$$\mathrm{Ag_2S} + 2\,\mathrm{e^-} \rightleftharpoons 2\,\mathrm{Ag} + \mathrm{S^{2-}}, E^0 = -0.691\ V \tag{4.1}$$

$$\mathrm{Al^{3+}} + 3\,\mathrm{e^-} \rightleftharpoons \mathrm{Al}, E^0 = -1.676\ V \tag{4.2}$$

This method is commonly used to restore the shiny appearance of silverware and has, to our knowledge, not been used so far for the restoration of plasmonic nanostructures. In this chapter, successful “revival” of plasmonic silver tips is demonstrated and it is shown that similar conditions can be used to safely store the plasmonic tips for extended periods of time (≥54 days).

4.2 Experimental Methods

Silver tips were produced by electrochemical etching from silver wires (see section 3.2.1) After discarding anomalous tips based on visual examination with a stereomicroscope (SMZ-2T, Nikon, Tokio, Japan), almost all tips gave TERS enhancement on a thiophenol self-assembled monolayer on gold. The prepared Ag tips were stored in plastic Petri dishes under normal laboratory conditions at a relative humidity of 50–60% and a temperature of 24–25°C.

For “revival”, the silver tips were inserted into small holes (Ø 250 µm) drilled into an aluminum block and immersed into a stirred 6 wt% $NaHCO_3$ (Merck) solution on a heating plate at 80°C. After 45 min, the tips were removed from the solution and thoroughly washed with milliQ water and ethanol. If, upon examination with the stereomicroscope, small crystals (probably $Al(OH)_3$) were visible, the tips were immersed in an acetic acid solution at pH 5 for 30 s to remove them. This treatment did not have a noticeable effect on the achieved signal enhancement and did not lead to additional (contamination) signals in the obtained Raman spectra. For storage, the silver tips were clamped between two aluminum plates and immersed in a 5 wt% $NaHCO_3$ solution at room temperature.

Gold substrates were prepared using a template stripping method described in section 3.3. These smooth surfaces ensure the absence of unwanted enhancement effects solely caused by the metallic substrate. The self-assembled monolayers of thiophenol were prepared by immersing a freshly cleaved gold substrate in a 5 mM ethanolic solution for 24 to 48 hours. The substrates were then thoroughly rinsed with ethanol and dried under a stream of N_2.

TERS measurements were performed using a combined scanning probe/Raman microscope (Ntegra Spectra Upright, NT-MDT, Zelenograd, Russia) described in more detail in section 3.1.1. The etched silver tips were brought into STM feedback with the sample surface (constant current mode, bias voltage of 0.1 V, setpoint of 0.1 nA) and a focused 632.8 nm HeNe laser was used for Raman excitation. To determine the tip enhancement, the laser focus was scanned across the apex (step size of 400 nm) and a spectrum was collected at every position. The spectrum from the most enhancing spot was then manually determined from this scan. All shown spectra were collected using an acquisition time of 0.5 s and a laser power of 550 µW on the sample stage. Position and height of Raman peaks were determined using Lorentzian peak fitting (Multipeak fit 2, IGOR Pro V6.35, WaveMetrics, Oregon, USA). The standard deviation of the noise was determined for each spectrum individually to calculate the signal-to-noise ratio.

All SEM images were acquired with a Gemini Leo 1530 (Zeiss, Oberkochen, Germany) at 5 kV. The morphology of silver tip surfaces were studied in an aberration corrected scanning transmission electron microscope (Cs-STEM, HD 2700, Hitachi, Japan) operated at 200 kV. The elemental composition analysis of the layers was performed by energy dispersive X-ray (EDX) spectroscopy of the Cs-STEM. Moreover, phase analyses were carried out from fast Fourier transform (FFT) patterns calculated from high resolution transmission electron microscope images.

4.3 Results and Discussion

Previous studies found that the plasmonic properties of silver nanostructures rapidly change with time.[130,149] McMahon et al. and Reed et al. showed that exposure to lab air leads to a significant redshift, broadening and weakening of the plasmon resonance peaks over the course of 36 hours and 30 days, respectively. McMahon et al. observed a linear resonance peak wavelength shift of 1.8 nm/h which translated to a significantly higher rate of corrosion in comparison to bulk silver. In our experiments, we follow a more practical route by directly investigating the influence of lab air exposure on the enhancement of Raman scattered light caused by a silver tip, which is known to be a direct consequence of the plasmon resonance at the tips nanometer sized apex. It is possible to measure the plasmon response of a single tip experimentally using dark-field scattering spectroscopy.[162] However, this approach would be challenging for our tip-to-substrate configuration. Figure 4.2 shows the signal-to-noise ratio for a characteristic Raman band of thiophenol collected with tips that have been exposed to lab air over different time periods prior to the measurement. Each point is an average from three tips, which were all used for measurements at three different sample positions. Since the measurements were all performed using the same parameters (acquisition time, laser power, bias voltage and current setpoint), a decrease in signal-to-noise ratio can directly be correlated with a decrease in Raman signal enhancement, if effects of the formed corrosion products on the STM feedback are neglected. The variance in the achieved signal-to-noise ratio is mainly caused by a high tip-to-tip variability, which can be attributed to differences in the corresponding plasmon resonance.[162] Otherwise, the graph shows that a major drop in enhancement happens within the first 48 h. After this, the trend is governed by the thiophenol signal intensity dropping below the limit of detection for some or all of the tips. Since thiophenol exhibits a fairly high Raman cross-section, we conclude that silver tips are essentially unusable for TERS experiments after the first 48 h, due to atmospheric corrosion.

The aforementioned redshift of the plasmon resonance as well as radiation and chemical interface damping are possible reasons for the drastic decrease in tip enhancement.[163] A redshift of the plasmon resonance can lead to a significant decrease in Raman intensity because the excitation wavelength (632.8 nm) used, will no longer lead to efficient excitation. However, since the different tip geometries will also lead to slightly different maxima in the plasmon resonance this could also lead to an increase in signal enhancement over time. However, this was not observed.

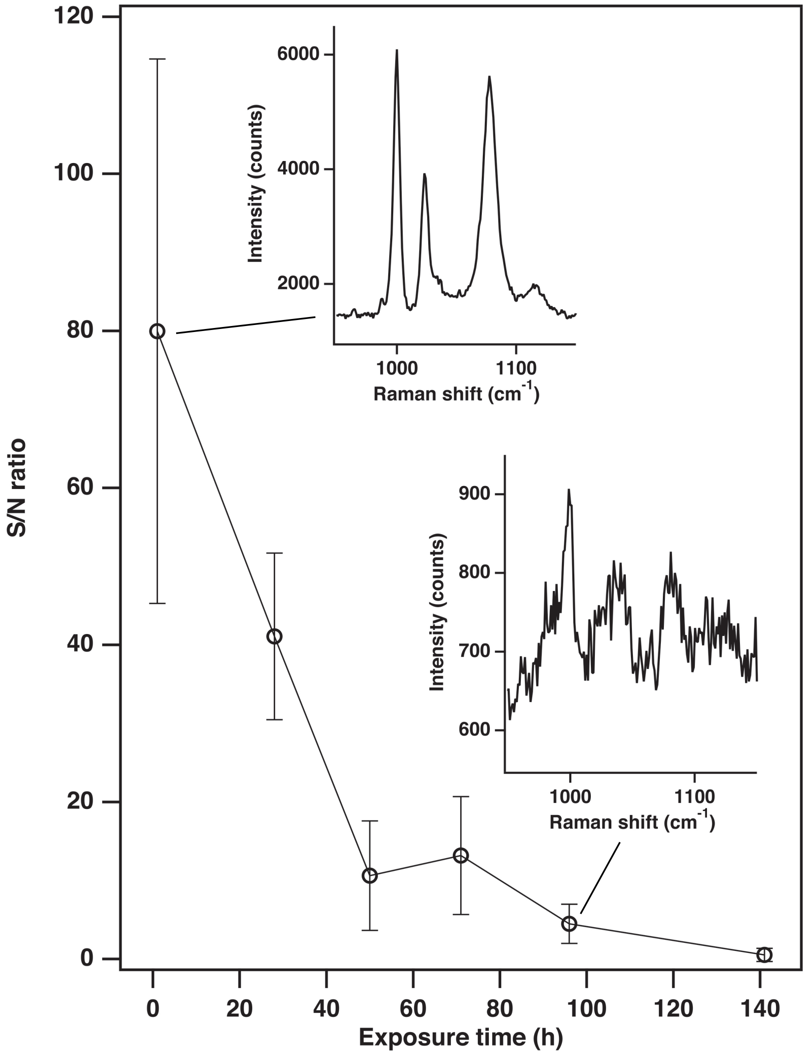

Figure 4.2: Observed signal-to-noise ratio of the ring breathing mode of thiophenol plotted against the time of exposure to laboratory air of the silver tips used. The insets show representative spectra after the indicated storage times. A major drop in enhancement is observed within the first 48 h. The error bars correspond to a 50% confidence interval. The lines are to guide the eye.

Therefore, the most likely explanation for the decrease in enhancement is damping of the resonance. The intensity drop to approx. 15% of the initial value within the first 48 h is comparable to the previously observed damping of the resonance without considering the effect of a redshift of the resonance peak.[130]

For the "revival" experiment, tips were first stored in lab air for 5 and 7 days, respectively. These storage times are long enough to not obtain any thiophenol

Raman signals using the tips with the previously applied measurement parameters (see Figure 4.2), but short enough to not severely affect the STM feedback. Figure 4.3 shows tip-enhanced Raman spectra acquired with a 7 days old tip from before and after the “revival” procedure. The lower trace does not show any prominent Raman signals besides the two broad features at <180 cm^{-1} (assigned to Ag phonon modes[164]) and 180–300 cm^{-1} (assigned to Ag_2S and/or Ag_2O[165,166]), which are almost always observed (even on freshly prepared tips). The same tip exhibits clear spectral features of thiophenol after the “revival” procedure (results for the other tips can be found in Appendix Figure B.1).[167,168] The signal-to-noise ratio reached 40, which is similar to values obtained with fresh silver tips (see Figure 4.2). The “revival” procedure was also effective for a 5.5 month old silver tip (see Appendix Figure B.2).

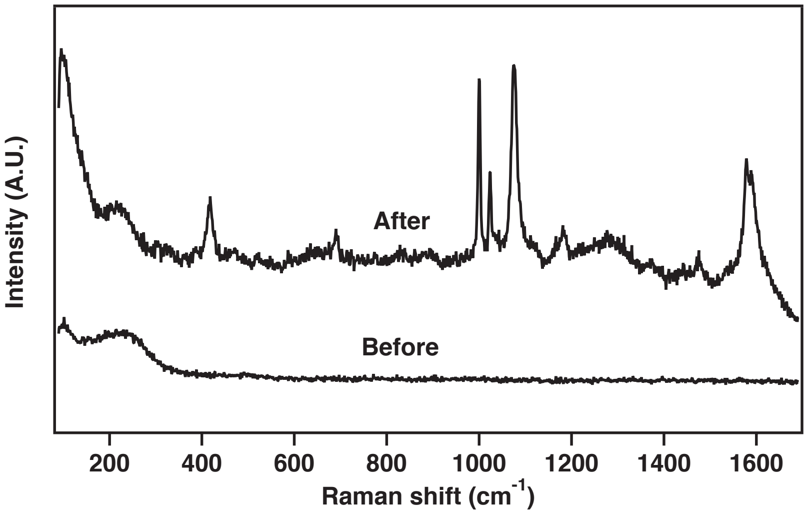

Figure 4.3: Tip-enhanced Raman spectra from a thiophenol self-assembled monolayer on gold using a 7 days old tip before and after “revival”. Whereas no Raman bands of thiophenol are obtained before “revival”, the known spectral features are clearly obtained after the procedure.

The strong enhancement observed in the above experiment suggests a successful reduction of the Ag_2S to elemental silver. However, it is not clear if morphological changes as observed by Reed et al.[149] on silver nanodisk arrays are also prevalent on the nanometer sized apex of the silver tips and what happens to the tips morphology upon “revival”. Figure 4.4 shows the SEM image of a freshly prepared silver TERS tip exhibiting a smooth surface. A pagoda-like structure is frequently observed,[169] although its origin is not known. Figure 4.5 shows close-up images from the same silver tip viewed from two angles that differ by 45° right after preparation (Figure 4.5a), one week after preparation (Figure 4.5b) and after the "revival" procedure (Figure 4.5c). The appearance of small grains in the size range of approx. 10 nm on the tip surface after one week of exposure to lab air is the most striking difference, which is in line with the SEM images shown by Reed et al. Since these small particles do not lead to a significant change in the tips radius of curvature, a geometric contribution to the rapid decrease of tip enhancement is unlikely. Changes in the optical properties caused by the formation of Ag_2S on the surface are expected to have a more pronounced effect. Most of the particles formed are still present after the "revival" procedure. Therefore, it seems that the "revival" procedure cannot fully recover the original morphology.

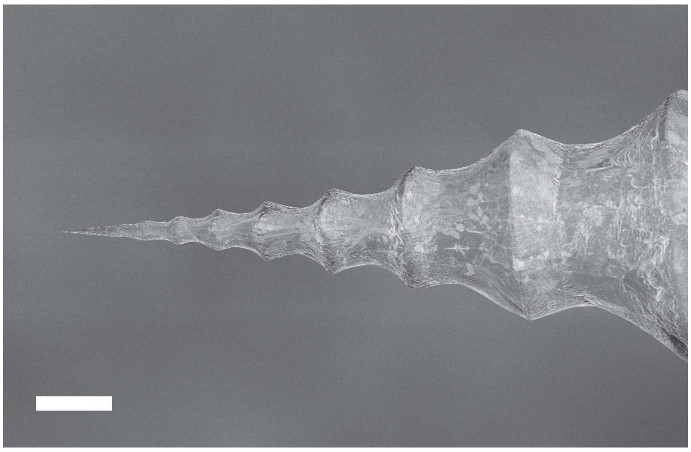

Figure 4.4: SEM image of a typical etched silver tip. The scale bar indicates 20 µm.

The identity of a bulge on the apex of an 8 days old silver tip was investigated using high resolution STEM. Figure 4.6a shows the very end of the tip were the bulge was observed. The brighter region within the bulge indicates a hollow space. The crystal lattice of the material is well resolved in the high-resolution TEM image. Thanks to that, FFT filtering could be performed to extract regions where the characteristic lattice planes of Ag and acanthite were exposed (see Figure 4.6b and c).[170] The distribution suggests that the bulge is solely comprised of crystalline Ag_2S, which is attached to the Ag tip surface. This finding was also confirmed by EDX mapping (see Figure 4.7b). The presence of sulfur not only within the extrusion, but also on the rest of the tip apex could indicate amorphous silver corrosion products or sulfur containing adsorbates. The EDX spectrum collected from the bulge (Figure 4.7b) indicated a close to 2:1 ratio between the silver and sulfur content, in agreement with the composition of Ag_2S. The carbon peak at low energy most likely originates

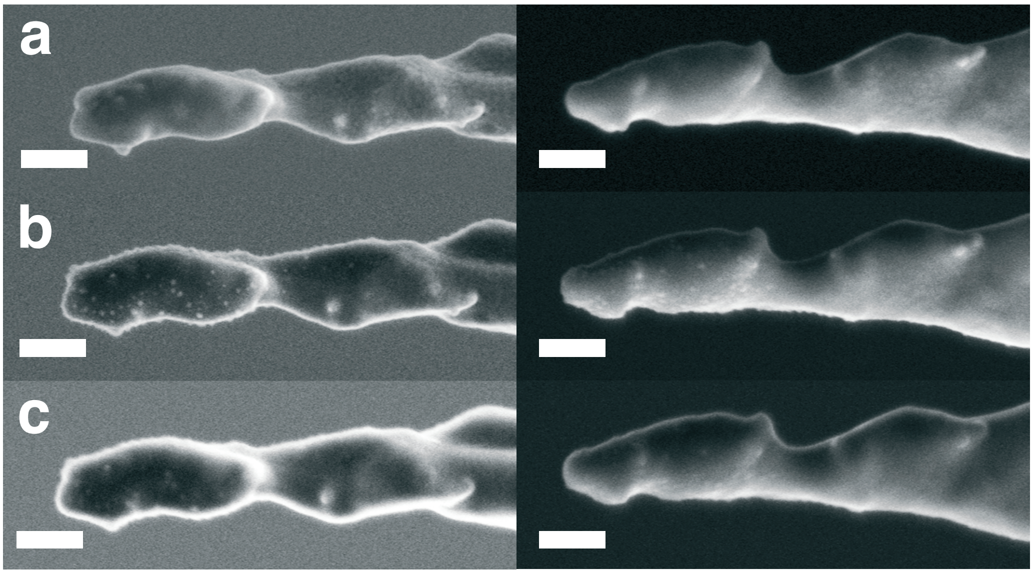

Figure 4.5: SEM image of a silver tip apex viewed from two different angles with a difference of 45° right after preparation (a), one week after preparation (b) and after the “revival” procedure (c). The scale bars indicate 200 nm.

from contaminations accumulated on the tip due to the electron irradiation during TEM imaging. The growth of acanthite in the form of extrusions makes sense, when considering its significantly lower density compared to silver.

The presence of the main corrosion product Ag_2S on silver tips stored in laboratory air over a period of several month was further demonstrated by means of cyclic voltammetry (see Appendix Figure B.4). Moreover, it was found that corrosion products can be directly characterized by means of Raman microscopic analysis. A study of early stage silver corrosion was recently presented by Martina et al., which found that Raman microscopy is very sensitive to detect adsorbates and small amounts of corrosion products.[166] Therefore, the presence of adsorbates and corrosion products on the tip surface should be visible in tip-enhanced Raman spectra collected with these tips. Figure 4.8 shows a Raman spectrum selected from a scan of the Raman laser across the tip apex of a 6 days old silver tip. The broad signal at lower wavenumbers can again be attributed to the main degradation product Ag_2S. The weak band at 615 cm^{-1} and the abundant peak at 960 cm^{-1} can be attributed to sulfate/sulfite ions and/or the respective silver salts.[166] These findings support the proposed corrosion pathways shown in Figure 4.1. The Raman signals of Ag_2SO_4 (or Ag_2SO_3) are not observed from the majority of the tips and sometimes only on certain positions on the tip apex. In agreement with the study by Martina et al.,

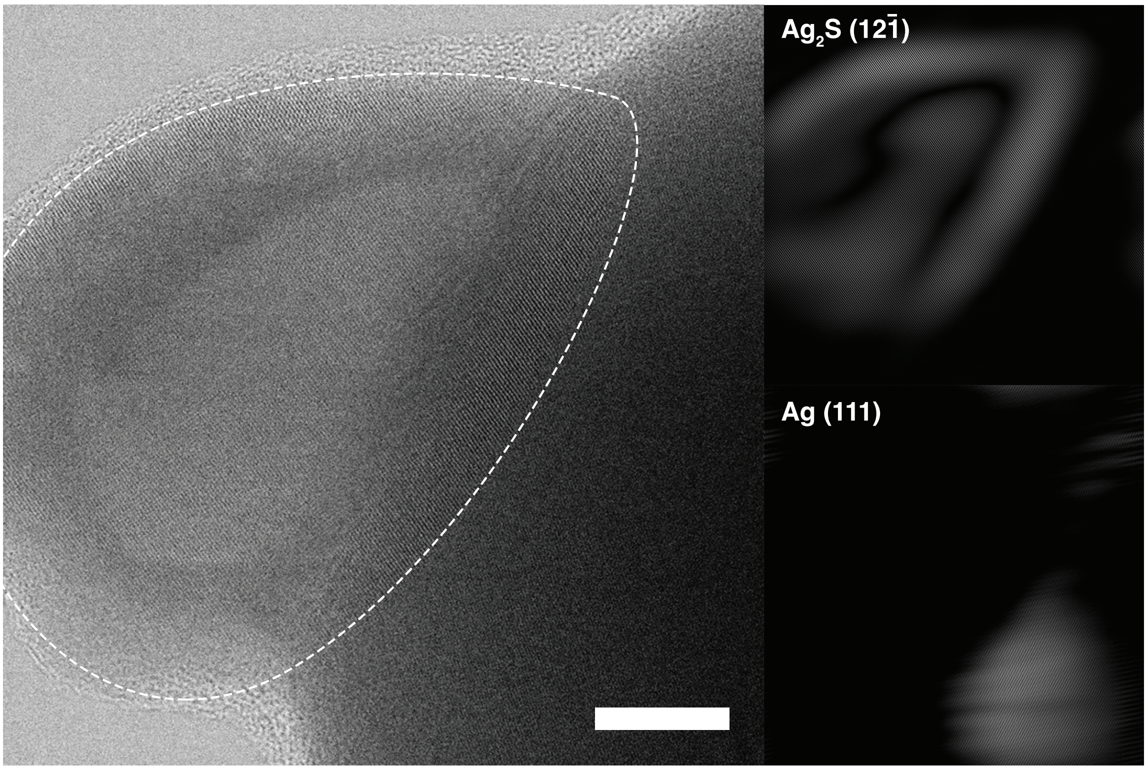

Figure 4.6: High resolution STEM image of the apex of a 8 days old Ag TERS tip with FFT filtered images of the indicated Ag (spacing of 2.3 Å) and the Ag_2S (spacing of 2.6 Å) lattice planes. The Ag_2S bulge is outlined with a dashed line in the unfiltered image and the scale bar indicates 10 nm.

these spectral features can, however, already appear within the first hours after tip production and interfere with lengthy imaging experiments.

The method of electrochemical reversal of silver tarnishing can also be used for storage of silver nanostructures. This can be accomplished by mounting the tip in an aluminum holder (sacrificial metal) and immersing it in a storage solution. Sacrificial metals are commonly used to protect boats and oil platforms from corrosion. Alternative methods to protect silver tips from atmospheric corrosion are vacuum storage and storage in inert gas. Vacuum storage could be effective, because the surface water layer can be fully removed preventing effective corrosion, especially when the probes are additionally heated. However, especially the shipment of silver nanostructures under high vacuum is complicated. Storage in dry inert atmosphere (e.g., Ar, N_2) effectively reduces the concentration of corrosive gases surrounding the tip.[171]

However, the surface water layer is still present and may already contain contaminants that can continue to react with the surface. The proposed method for storage

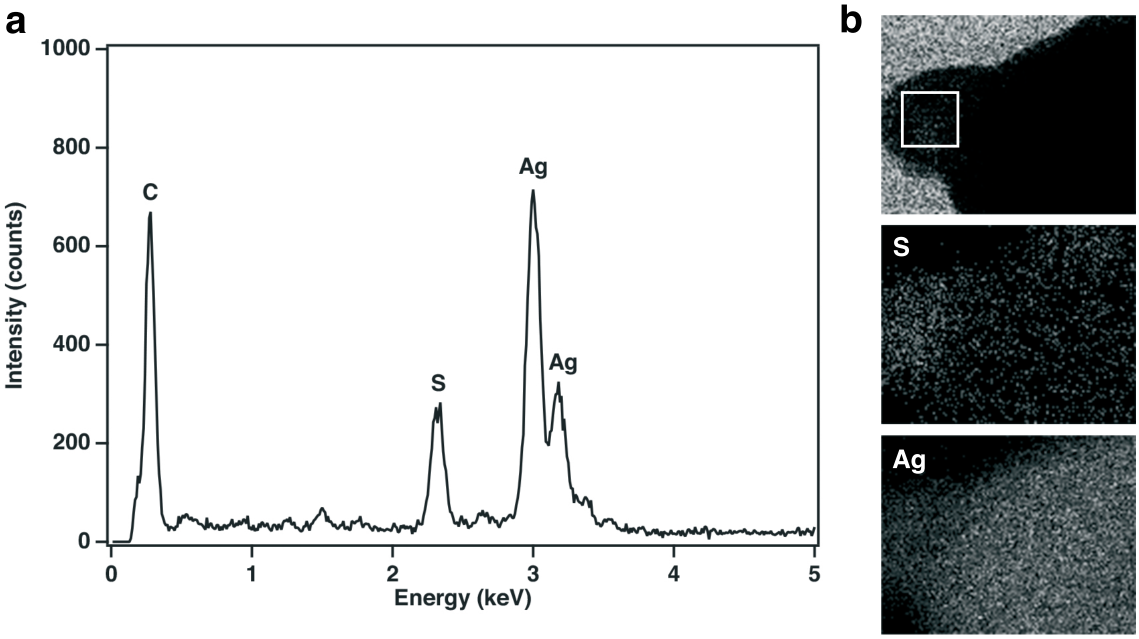

Figure 4.7: EDX spectrum from the indicated area on the Ag_2S bulge (a) and an EDX map from a slightly larger area showing the distribution of sulfur and silver at the tip apex.

relies on a cell, where silver corrosion is minimized by shifting the equilibrium of the following chemical reaction to the right side:

$$3Ag_2S + 2\,Al + 6\,H_2O \rightleftharpoons 6\,Ag + 2\,Al(OH)_3 + 3\,H_2S \tag{4.3}$$

The tips are stored in an aluminum holder and immersed into a 5 wt% $NaHCO_3$ solution at room temperature. This storage method is much less elaborate than vacuum storage or storage in an inert atmosphere and also allows for storage of individual tips. Prior to use, the tips are removed from the storage solution and rinsed with water and ethanol. To demonstrate successful longterm storage of the tips, two batches of tips were stored in lab air and in the storage solution, respectively. Figure 4.9 shows the achieved S/N ratio obtained for the ring breathing mode of thiophenol for tips from the storage solution and from lab air storage after a period of 45 and 54 days, respectively. Besides the fact that a high variability in the TERS intensity is observed for the tips from the storage solution, a significantly higher enhancement is observed in comparison to the tips stored in air.

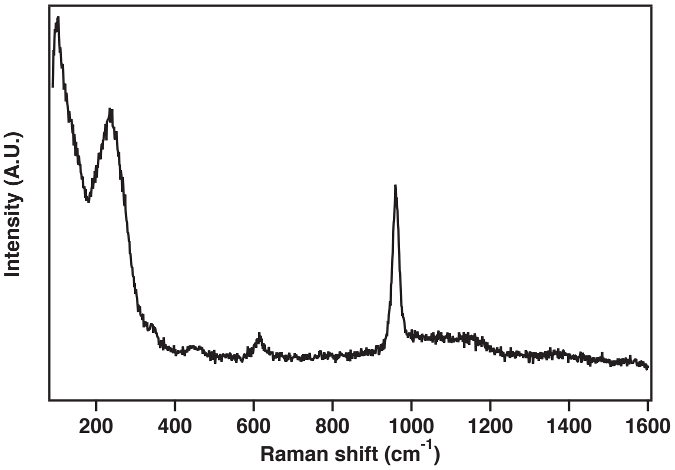

Figure 4.8: Tip-enhanced Raman spectrum from a 6 days old tip exhibiting Raman bands from typical degradation products. The broad band at 180–300 cm^{-1} can be attributed to the main degradation product(s) Ag_2S and/or Ag_2O. The bands at 615 and 960 cm^{-1} are signs of Ag_2SO_4 (or Ag_2SO_3).

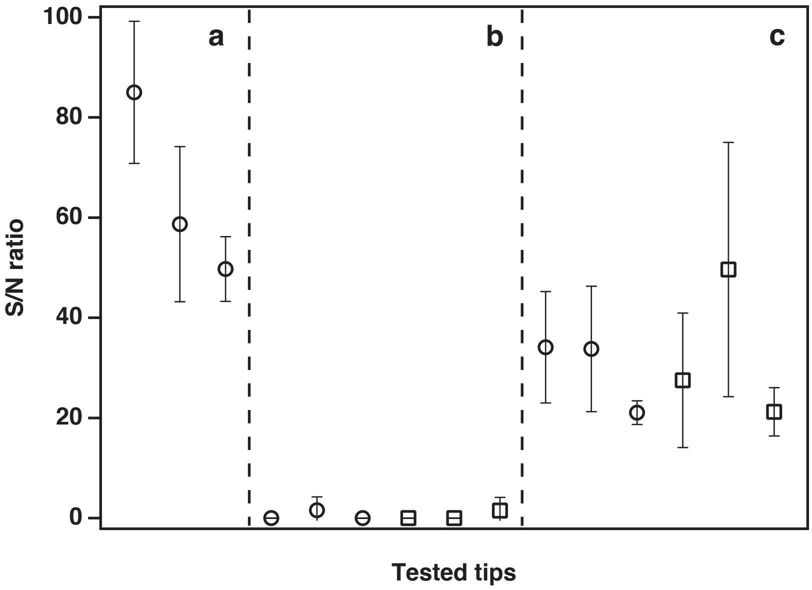

Figure 4.9: S/N ratio of the ring breathing mode of thiophenol obtained with freshly prepared silver tips (a), silver tips after storage in air for 45 (circle) and 54 (square) days (b) and tips from the storage solution after the same periods (c). The error bars show the standard deviation for the results from three measurements at different sample positions.

4.4 Conclusion and Outlook

In this chapter, the corrosion of silver TERS tips exposed to lab air was investigated. The presence of known corrosion products, namely Ag_2S and Ag_2SO_4, was confirmed by means of high-resolution TEM, EDX, cyclic voltammetry and Raman spectroscopic analysis. Minor morphological changes on the tip apex were observed after one week of exposure to laboratory air by means of scanning electron microscopy. A "revival" procedure based on electrochemical restoration of elemental silver was presented and applied successful to regain the original optical properties was demonstrated with tip-enhanced Raman spectroscopic measurements on a thiophenol SAM. Moreover, it was demonstrated that the electrochemical cell used for tip "revival" can also be used for long-term storage of tips. The procedure can also be adapted for the restoration and storage of other plasmonic structures as well as STM tips. The application of those methods to the widely used metallized AFM probes would be of particular interest, because their production is more time consuming compared with the etched tips making the possibility for "revival" even more attractive.

Chapter 5

Chemical Production of Thin Protective Coatings on Optical Nanotips for Tip-Enhanced Raman Spectroscopy

The enhancement by noble metal nanometer-sharp tips (especially the ones comprised of silver) used for TERS quickly fades, due to chemical degradation during storage and use. By covering the metal surface with an inert and thin dielectric layer, degradation can be slowed dramatically. To protect the metal surface against unwanted adsorption of analyte molecules or contaminants, and to avoid catalytic effects of the tip material in the investigated system, while keeping favorable optical properties, the protection layer must be very thin and pinhole-free. In this chapter, a method to produce strongly enhancing tips for TERS is introduced, which (in the case of silver) significantly exceed the typical lifetime of unprotected tips. This was achieved by chemical coating of a thin (<3 nm) silica shell on top of the enhancing noble metal nanostructures. The protective shell also has the advantage of allowing for non-invasive measurements on samples where the presence of a bare silver/gold surface can have unwanted effects. Additionally, it opens up various new functionalization methods commonly used for silica surfaces.

This chapter is adapted from:
L. Opilik, J.-F. Li, Ü. Dogan, B. Stephanidis, C. Blum, R. Zenobi: 'Chemical Production of Thin Protective Coatings on Optical Nanotips for Tip-Enhanced Raman Spectroscopy', in preparation.

5.1 Introduction

TERS is a nanoscale spectroscopic technique, where a very sharp metal or metallized tip is scanned across a sample surface and acts as a near-field light source for Raman spectroscopic measurements with a spatial resolution below the optical diffraction limit.[172] Silver and gold are the most commonly used materials for the nanotips used because of their unique optical properties. Au and Ag nanostructures show strong optical resonances in the visible part of the electromagnetic spectrum. Gold shows interband transitions in the blue and green part of the spectrum and is therefore limited in its applicability, whereas silver can be used for plasmonics over the whole visible range.[46] However, silver has the disadvantage of low chemical stability, which limits its usability under atmospheric conditions, whereas gold is chemically very inert. In TERS, the position of the metallic tip is controlled by means of a scanning probe microscope. A quick method to obtain TERS-active tips involves electrochemical etching of silver or gold wires. These tips can be readily used for TERS using STM feedback.[97,136] For TERS using AFM feedback, these tips either have to be glued to a tuning fork or need to be flattened and attached to a support.[89,115] Another more commonly used method to produce tips for AFM-TERS is to deposit the required metal (silver or gold) on commercial silicon or silicon nitride AFM tips, generally by physical vapor deposition.[71,173]

Silver tips have to be used within the first couple of days after production, because their lifetime is limited by the chemical instability of the silver coating (see chapter 4). It is known that silver reacts with sulfur compounds from the atmosphere (e.g., H_2S) resulting in a visible color change (tarnishing). Anti-tarnishing coatings are commonly used to prevent, e.g., silver jewelry from unwanted color changes.[150] Protective coatings would also be beneficial for silver nanostructures to maintain the enhancing optical properties of silver. The main difficulty in this case is the fact that the enhancement is a near-field effect, which rapidly decreases with increasing distance from the metal surface (it decays within the first 20 nm).[85] A protective coating therefore has to be very thin, but still uniform enough to effectively seal the whole silver surface. It was already demonstrated that a thin Al_2O_3 layer can improve the thermal stability and extend the shelf life of SERS active silver substrates.[151,174–176] An experimental study in 2009 by Barrios et al. demonstrating the suitability of Al_2O_3 for the protection of silver TERS tips.[114,127] However, the authors did not present sufficient experimental data to demonstrate the quality (uniformity and thickness) of their protective films and the enhancing effect of their probes was rather poor compared to what is nowadays commonly achieved.

The use of a dielectric coating on optical nanotips to tune their optical properties and at the same time protect them from mechanical wear and the ambient was first proposed by Cui et al. in 2008.[177] The idea developed from previous theoretical and experimental studies that demonstrated that dielectric materials with different optical properties in direct contact with the active metal film can be used to tune the resonance frequency of the localized surface plasmon resonance of the tip.[71,178]

Another advance in the direction of tip protection was presented by Schmid et al. in 2009.[179] They used silver coated AFM tips covered with a SAM of ethanethiol to effectively protect the tip from contaminants adsorbing to its surface when working in a liquid environment. However, self-assembled monolayers are known to be unstable against oxidation and thermally, which diminishes their usefulness as protective coatings.[180] In this chapter, we demonstrate a simple and cost-efficient method for more effective tip protection. It combines spontaneous assembly of an organic linker molecule (3-mercaptopropyltriethoxysilane) on the metal nanotip and subsequent growth of a silica shell. These protective coatings can be fabricated at ambient pressure and at relatively low temperatures. A similar method was recently presented by Li et al. for the preparation of shell-isolated nanoparticles for Raman spectroscopy to prevent nanoparticle agglomerates and to increase the substrate generality of SERS.[181] Experimental proof of the layer uniformity as well as the demonstration of extended lifetime of protected silver tips is provided.

5.2 Experimental Methods

Gold tips were prepared by electrochemical etching of gold wires (see section 3.2.2) and silver TERS tips were prepared by electrochemical etching of silver wires (Ø 0.25 mm, 99.99% purity, Sigma Aldrich). A 1:2 (v/v) mixture of perchloric acid (70%, Sigma Aldrich) and methanol (Merck) was used as etchant and a potential of 8.0 V was applied.

To protect gold TERS tips, they were immersed in a 1.0 mM 3-mercaptopropyltriethoxysilane (MPS, 95%, Alfa Aesar) solution for 1 h at room temperature. 1.0–4.0 ml of a 0.1 M HCl solution were mixed with 60 ml milliQ water (NANOpure Diamond, 18.2 MΩcm) and 6.4 ml of a 0.54% silicate solution (from sodium silicate solution, Sigma Aldrich) in a round bottom flask. The tips were then removed from the MPS solution and rinsed with ethanol before transferring them to the freshly prepared silicate solution. The tips were left there for 3 to 5 minutes at room temperature while stirring. After that, the flask with the silicate solution and the immersed tips was transferred to a water bath heated to 99°C and left to react for up to 2 h. The tips were then removed and washed with milliQ water. This procedure is similar to a previously described procedure for the preparation of thin silica shells on gold nanoparticles.[181]

To protect silver TERS tips, they were immersed in a 50 mM 3-mercaptopropyltriethoxysilane (MPS, 95%, Alfa Aesar) solution for 1–1.5 h at room temperature. The rest of the procedure was the same as for gold TERS tips.

TERS experiments were performed on a combined STM/AFM/Raman microscope (see section 3.1.1) using a 632.8 nm HeNe laser for excitation. Gold substrates were prepared by a template stripping method described in more detail in section 3.3. Self-assembled monolayers of thiophenol were prepared by immersing the substrate in a 5.0 mM ethanolic solution overnight. After rinsing them thoroughly with ethanol they were dried in a stream of nitrogen.

The morphology of gold and silver tip surfaces and the morphology of the protective layers were studied in an aberration corrected STEM instrument (Cs-STEM HD 2700, Hitachi, Tokyo, Japan) operated at 200 kV. The transmission electron (TE) and secondary electron (SE) detector imaging modes of the instrument were found to be most suitable for the visualisation of the very thin and light-element protective layer adjacent to the heavy-element tip material.

5.3 Results and Discussion

The method described for the protection of optical nanotips is based on a combined approach of thiol self-assembly and subsequent growth of a more robust, dense and chemically inert inorganic shell. In practice, this was accomplished by self-assembly of a linker molecule with both a thiol and a silane functionality, e.g., 3-mercaptopropyltriethoxysilane, (Figure 5.1a) and subsequent growth of a thin amorphous silica shell (Figure 5.1b).

In a first step, the procedure was demonstrated for etched gold wire tips. Figure 5.2a shows a transmission electron microscopy image from a silica protected Au tip with a thin (<3 nm) amorphous silica shell, which uniformly covers the darker metal surface. The controllability of the layer thickness was also confirmed by transmission electron microscopy of protected tips prepared using shorter reaction times (see Appendix Figure B.5).

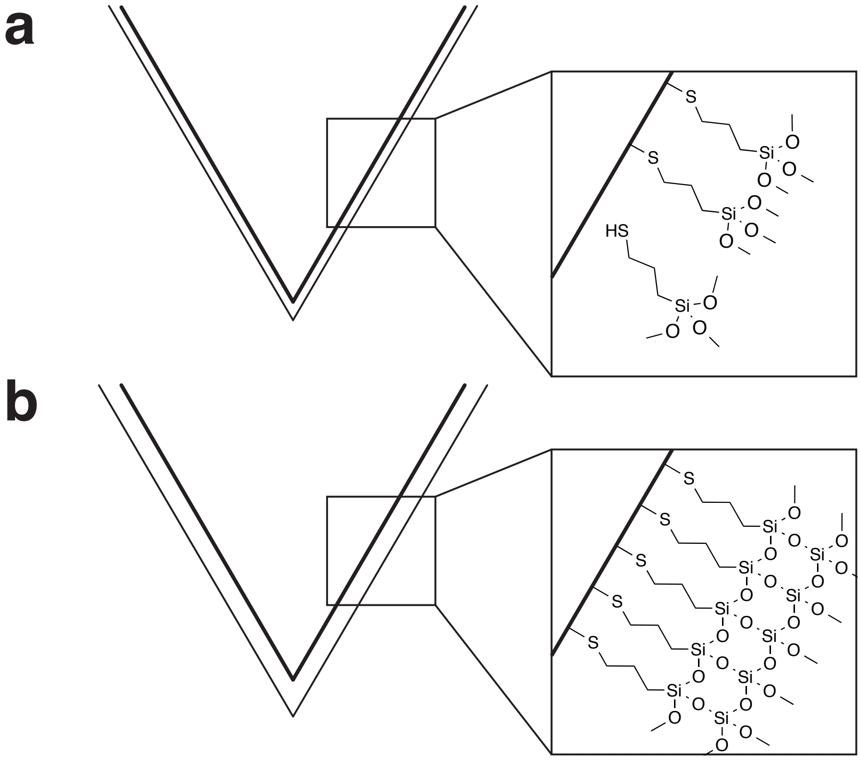

Figure 5.1: Scheme of the applied procedure for tip protection. Self-assembly of of 3-mercaptopropyltriethoxysilane on the tip surface (a) is followed by growth of a thin silica shell (b).

Only a small fraction of the protective layer formed can be imaged with TEM, which is not sufficient to rule out the presence of pinholes in the silica shell. The uniformity of the protective layer was therefore also checked with two complementary methods: cyclic voltammetry and tip-enhanced Raman spectroscopy. The cyclic voltammetry measurements (see Appendix Figure B.6) prove the uniformity of the silica protective layer by the absence of the characteristic oxidation and reduction peaks of gold in the first cycle. The TERS measurements were done as follows: a freshly prepared gold tip was dipped into an ethanolic thiophenol solution to allow chemisorption of thiophenol molecules onto exposed areas of the gold surface. The tip was then rinsed extensively with ethanol to remove physisorbed thiophenol molecules. The tip was then brought into STM feedback with a bare gold surface and Raman spectra were recorded to

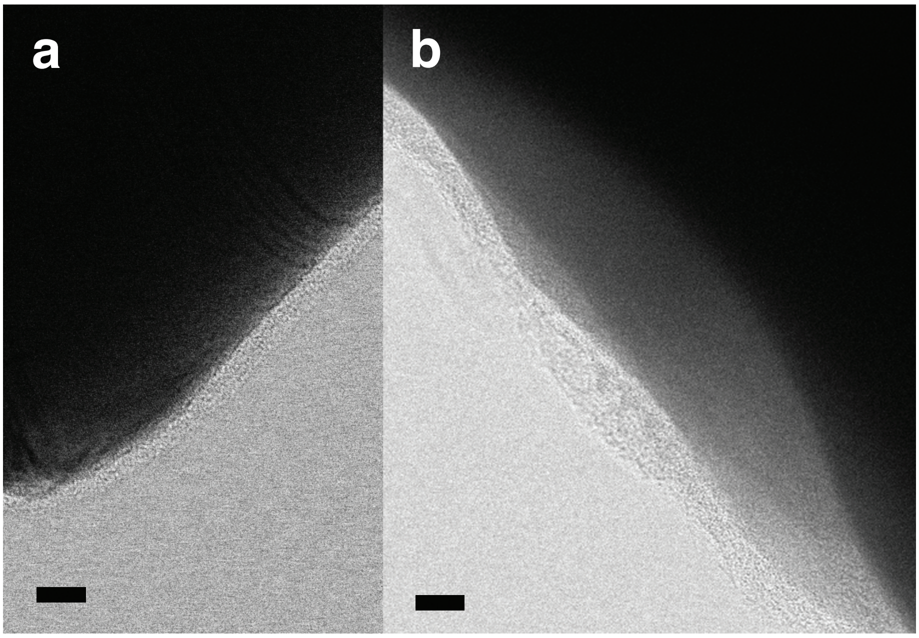

Figure 5.2: Transmission electron images from a region close to the apex of a silica protected Au tip (a) and a silica protected Ag tip (b) after a growth time of 2 h and 1 ml added 0.1 M HCl. A uniform, amorphous and thin (<3 nm) silica layer is visible on the Au tip surface. The silica layer on the Ag tip surface has a similar thickness, but seems to be less uniform. Scale bars are 5 nm.

check the tips cleanliness. Moreover, the enhancing capability of the tip was checked on a thiophenol SAM on gold using the same measurement parameters. The results for a silica protected gold tip after a growth time of 30 min and 1 ml added 0.1 M HCl are shown in Figure 5.3a and Figure 5.3b. The characteristic Raman signals of thiophenol are completely absent for the measurements on the bare gold surface (Figure 5.3b), whereas the characteristic pattern can be clearly obtained on the SAM (Figure 5.3a). Doing the same experiment with a tip having an incomplete silica shell (intentionally prepared by not adding 0.1 M HCl to the growth solution) results in an intense thiophenol spectrum already on the bare gold surface (see Figure 5.3c).

After these successful tests for the protective silica shell on gold, the procedure was adapted for Ag tips. This turned out to be challenging, because etched silver tips often exhibit a higher surface roughness compared to gold. Because the self-assembly of the linker molecule on the tip surface is a crucial step in obtaining pinhole free protective layers, a more concentrated solution of 3-mercaptopropyltriethoxysilane and longer assembly times were used. TEM reveals the presence of a thin protective silica coating on silver with a continuous, but slightly less uniform layer (see Figure 5.2b). The composition of the protective layer was confirmed by EDX spectroscopy measurements

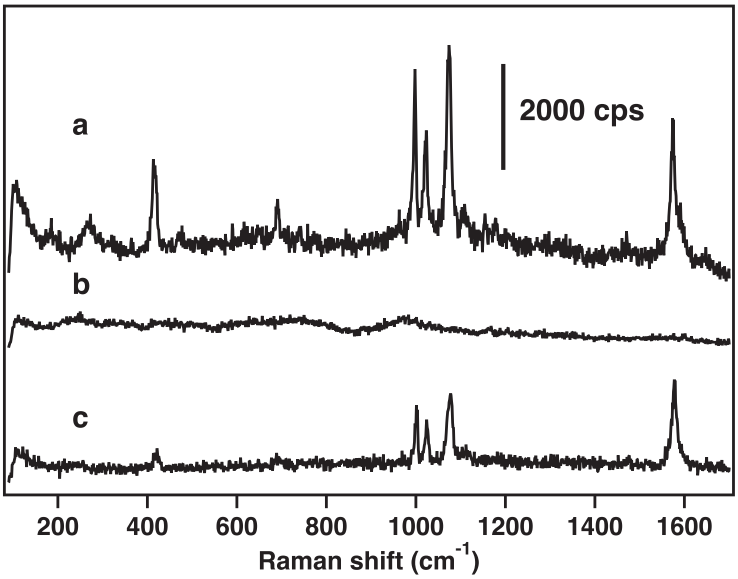

Figure 5.3: STM-TERS measurements using a protected Au tip on a PhS SAM on Au (a) and a bare Au substate (b) after dipping the tip into a PhS solution and extensive washing with ethanol. When using a non-optimized protection receipe that results in a non-uniform layers (with pinholes) the PhS spectrum is already visible on the bare Au substrate after dipping the tip into the PhS solution (c).

(see Appendix Figure B.7). Figure 5.4 shows the successful pinhole test for a silica protected silver tip after a growth time of 2 h and 4 ml added 0.1 M HCl, together with the result using a tip with an incomplete protective layer (0.1 M HCl was not added to the growth solution).

Because the enhancement achieved with the protected silver tips is comparable with the typical tip enhancement from various research groups, no major constraints for TERS experiments result.[182]

Because silver nanostructures quickly corrode under atmospheric conditions,[130] the thin protective layer should allow long-term storage of active TERS tips. A time-dependent comparison study of the TERS enhancement with protected and unprotected tips on a thiophenol SAM on gold was conducted, and the result is shown in Figure 5.5. The Raman intensity of the ring breathing mode of thiophenol is plotted for bare (circles) and silica protected (triangles) silver tips over the course of 20 days. The same growth conditions as for the tip, which successfully passed the pinhole test, were chosen for the protected tips used in this experiment. Each data point in the graph represents the averaged signal intensity from three tested

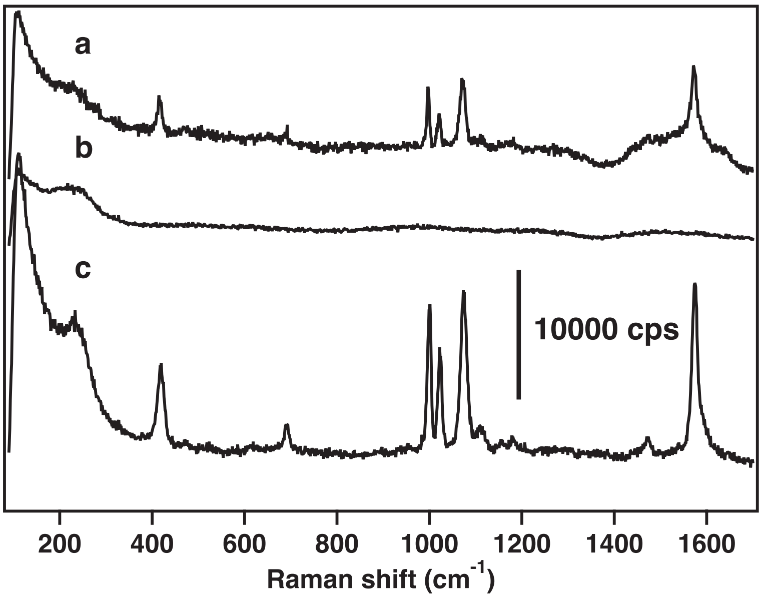

Figure 5.4: STM-TERS measurements with a protected Ag tip on a PhS SAM on Au (a) and a bare Au substate (b) after dipping the tip into a PhS solution and extensive washing with ethanol. When using a different protection receipe that results in non-uniform layers (with pinholes) the PhS spectrum is also visible on the bare Au substrate after dipping the tip into the PhS solution (c).

tips.[1] Each tip is only used once and contributes an average from three different sample positions. The tips were stored under normal lab conditions prior to use. For the bare tips, a significant decrease in Raman intensity was already visible after two days (similar to the trend observed in chapter 4), whereas the protected tips gave a more or less constant enhancement over the whole course of 20 days. The initially lower enhancement of the protected tips on the day of preparation could be caused by a shift of the plasmon resonance away from the excitation wavelength caused by the thin dielectric layer. However, on the second day, the protected tips gave an enhancement equivalent to that of bare silver tips, and they outperformed the unprotected tips from the third day on. The protective coating is therefore of great value, if a storage time of more than three days is required. It has to be noted that in the present study, the absence of spectral features of thiophenol in the Raman spectra does not mean that these tips are not active TERS probes anymore, it just means that the enhancement is too weak to reach the detection limit (thiophenol monolayers are too weak Raman scatterers to be observed without some kind of

---

[1] The last two data points for the unprotected silver tips stored after 11 and 20 days of storage represent the average of only two tips.

field enhancement). Since most applications require strongly enhancing TERS tips, Figure 5.5 demonstrates that storage of up to five days already renders unprotected tips unusable. Other lifetime studies on TERS tips observed a much slower decay, over the course of 40 days, however, based on much lower contrast values than in the present study.[114]

The applied dielectric coatings on the tips did not prevent successful STM feedback with these tips. Thicker tip coatings were found to lead to a visible crash of the tips upon approach. It is not yet fully understood how successful STM feedback was even possible with the relatively thin protective layers applied in this work and because the study was limit to point measurements no conclusions are yet possible on how these layers affect the STM performance during scans. A decrease in spatial resolution caused by the native oxide layer on a tungsten STM tip has been reported in the literature.[183] At this point, it cannot be excluded that the protective shell cracks open upon approach, exposing the bare tip surface. Another possible explanation for successful STM feedback is defect mediated leakage though the protective layer.[184] However, this would most probably require a considerably higher bias voltage than used in this work.

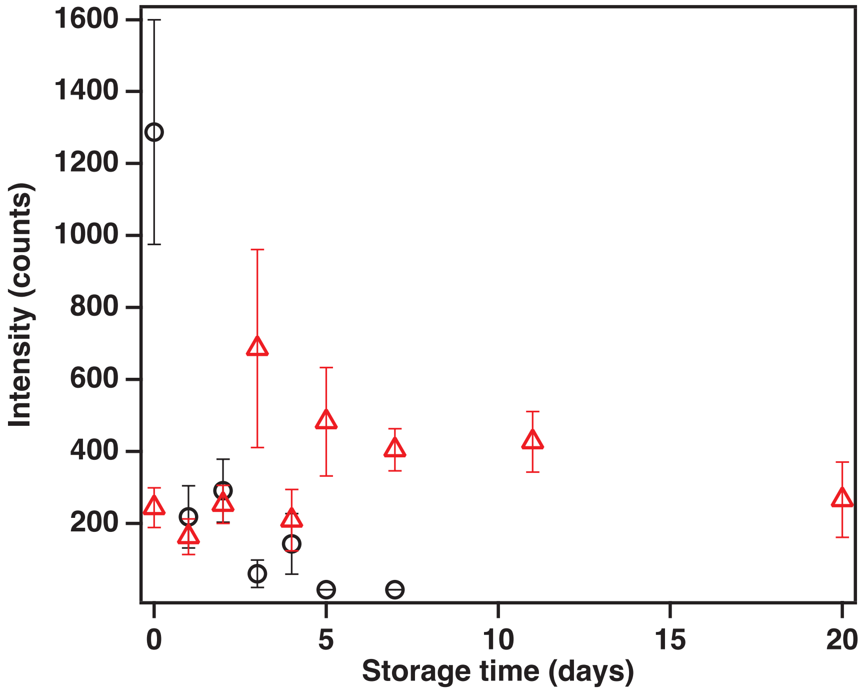

Figure 5.5: Direct comparison of the Raman intensity from TERS measurements on a thiophenol SAM performed after different storage times with unprotected (circles) and protected (triangles) tips. The error bars correspond to a 50% confidence interval.

5.4 Conclusion and Outlook

The experiments with silica protected gold and silver TERS tips indicate that the novel two-step coating procedure is an attractive option to fabricate highly enhancing, long-term stable TERS probes. It was shown that uniform protective silica coatings could be prepared on gold and silver tips with controllable thickness. The uniformity of the coating was demonstrated with transmission electron microscopy, cyclic voltammetry, and tip-enhanced Raman spectroscopy. Moreover, it was shown that the protected silver tips outperform bare silver tips after only three days. This is particularly interesting for their commercialization, where a certain shelf life is required. Moreover, the thiophenol dipping experiments demonstrate that the coating provides strong resistance against unwanted adsorbates, which should enable the application of TERS in liquid environments. This would make it possible to use TERS for studying biological systems in a native environment and for in-situ monitoring of catalytic processes on surfaces. Since various methods are available for the modification of silica surfaces, the coated tips could also serve as a nanoscale platform for various chemical modifications with specific interaction. Further studies are required, to clarify how the continuous thin protective coating affect the STM feedback (in particular during scans). Moreover, the novel two-step coating procedure is readily transferrable to AFM-TERS tips, where a protective coating does not adversely affect the feedback mechanism.

Chapter 6

Protective Layers – Other Approaches

Besides the method for tip protection described in the previous chapter, other approaches have been tested. This chapter starts with an overview of different methods to obtain thin protective layers on tips and some of the results from these attempts are summarized. At the end of the chapter, a test sample is introduced, which allows to assess the achieved optical contrast, spatial resolution and the tips stability during TERS imaging experiments.

Some of the data shown in this chapter (section 6.3.3 and 6.3.4) is the result of a close collaboration with Daniel Emmrich and Xianghui Zhang from the research group of Prof. Dr. Armin Gölzhäuser at Bielefeld University, Germany.

6.1 Introduction

Different approaches for production of thin protective layers on TERS tips have been reported in the literature[114,155,179] and additional methods have been tested in the course of this thesis. These attempts to prepare thin protective layers on tips are summarized in Figure 6.1 in a more general schematic form.

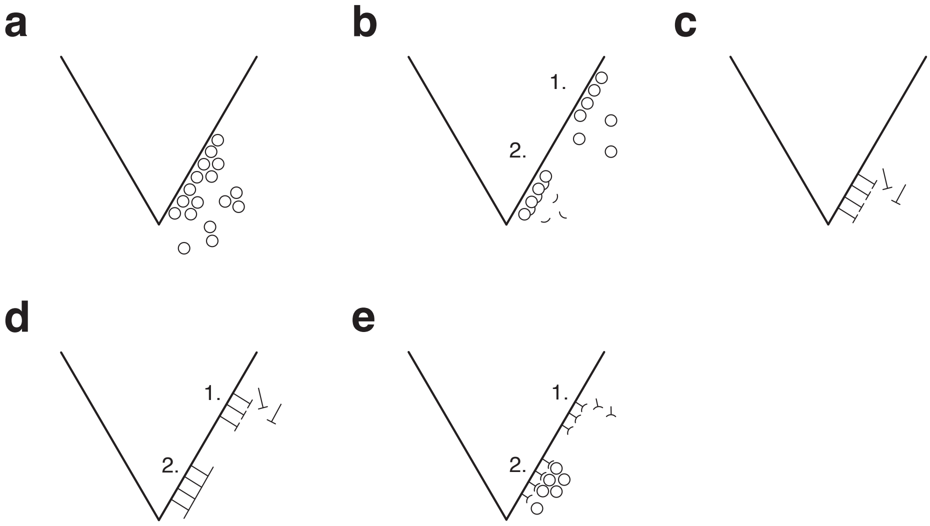

Figure 6.1: Schematic overview of tip protection methods, including physical vapor deposition (a), atomic layer deposition (b), molecular self assembly (c), molecular self assembly and subsequent cross-linking (d), molecular self assembly of linker molecules and subsequent surface-induced growth (e).

The use of physical vapor deposition to produce thin protective layers of Al_2O_3 and SiO_x was recently presented by Barrios et al.[114,155] This approach is rather simple, and since the enhancing silver layer is typically deposited with the same method, no additional instrumentation is necessary and the process can even be done without having to remove the tips from the reaction chamber in between deposition of the enhancing metal and the protective layer. However, exact thickness control is difficult and especially for rough tip surfaces, this method can lead to significant differences in layer thickness or even incomplete layers. Because complete coverage is required for an effective protection, and because already slight variations in film thickness can strongly affect the tips enhancement, we propose the use of atomic layer deposition (ALD) instead. ALD is known to result in very homogeneous oxide layers even on very rough surfaces with control on the monolayer level.[185] Commercial instruments for this procedure are available and suitable precursors for the deposition of, e.g., Al_2O_3

are well-known. Atomic layer deposition has previously been used for the protection of SERS substrates.[151,152,176] These studies demonstrated improved chemical and thermal stability.

A very different approach was presented by Schmid et al., who used self-assembled monolayers of an alkanethiol to protect TERS tips for their use in liquids.[179] The effective prevention of unwanted adsorption of analyte molecules and contaminants was successfully demonstrated. However, self assembled monolayers of thiols are prone to thermal decomposition and oxidation,[180] which does not render them good candidates for applications where stable protective layers are required. In the following, we therefore introduce two different methods to develop this approach further for the production of more stable protective layers. One key issue of the simple self-assembled monolayers approach is that the protective layer still consists of small individual molecules, which are easily exchanged and not very thermally stable. One approach to solve this issue is to cross-link self-assembled monolayers to produce a covalent monolayer on the tip surface, which is expected to show much higher resistivity to thermal effects and chemical reactions. One possibility to accomplish this in practice is the assembly of thiols with an aromatic chain and subsequent electron bombardment to form covalent bonds between the molecules.[186] These 'carbon nanomembranes' exhibit a significantly higher thermal stability and remain on the surface at temperatures above 700°C.[187] It was even demonstrated that an addition annealing step at higher temperatures can yield single-layer graphene from self-assembled monolayers.[188] Another approach to form more stable layers from self-assembled monolayers is the use of functionalized thiols and subsequent growth of silica layers to form continuous layers (see previous chapter).

The enhancement of a TERS tip can easily be tested on a homogeneous sample. (Sub-)monolayers of dye molecules,[9] thin polymer blends[114] and self-assembled monolayers[182] are commonly used for this purpose. However, these methods do not give any information on the field confinement achieved with the tip. This is an important characteristic for imaging applications, because it defines the achievable spatial resolution. Measuring the tip-sample distance dependence of the enhanced spectroscopic response by means of stepwise tip retraction[88] or multilayered samples[189] can yield the axial field confinement (along the tip axis) on laterally homogeneous samples. However, it is not possible to determine the lateral field confinement, and the stepwise retraction is not always possible (e.g., when using contact mode AFM feedback). In order to determine the lateral field confinement, a sample with nanoscale heterogeneity is required. The most common sample for this purpose are carbon nanotubes.[86,116] However, obtaining individual carbon nanotubes on a sample surface, preferentially in a particular orientation, is challenging.[190] In the last section of this chapter a novel approach to make a TERS standard sample based on patterned thiol SAMs is presented, which is inspired by optical resolution test targets (e.g., the test chart introduced by the United States Air Force in 1951).

6.2 Experimental

Silver-coated AFM tips were stored in a nitrogen flushed Schlenk tube for transport. ALD of Al_2O_3 was done using a Picosun Sunale R-150B reactor equipped with a trimethylaluminum and a water source. Up to 50 cycles (resulting in layer thicknesses of approx. 5 nm) were performed at a temperature of 120°C. In the standard method, one cycle consists of a 0.1 s trimethylaluminum pulse, 4s purging, a 0.1 s water pulse and 4 s purging. A modified method with multiple pulses and long purge times was introduced. In this case, one cycle consists of ten 0.1 s trimethylaluminum pulses. Each of them was followed by a 4 s purge. After a final 60 s of purging, ten 0.2 s water pulses followed. Each of them was followed by a 8 s purge. The cycle was then completed with 60 s purging.

The morphology of the protective layers were studied using a transmission electron microscope (Tecnai F30 FEG, FEI, Hillsboro, USA) operated at 300 kV. Elemental composition analysis of the layers was done by EDX spectroscopy.

Self-assembled monolayers of biphenyl-4-thiol (BPT) and 4'-nitro-1,1'-biphenyl-4-thiol (NBPT) were prepared as follows: Gold tips were immersed in a $\approx$ 10 mM solution of BPT or NBPT in dry and degassed dimethylformamide (DMF) kept under nitrogen atmosphere and left there for 72 hours. The tips were then rinsed with DMF and ethanol before drying them with dry nitrogen. Cross-linking was done at a chamber pressure of $<5 \times 10^{-7}$ mbar using an electron floodgun (SPECS, Berlin, Germany) at 100 eV and a typical dose of 50 mC/cm^2.

The same method was used for the preparation of the NBPT films on a UV-ozone cleaned gold substrate. The substrate was prepared by epitaxial growth of a 300 nm polycrystalline Au film on a mica substrate (Georg Albert Physical Vapor Deposition, Germany). The resolution target pattern was then written into the SAM by locally cross-linking the NBPT molecules by means of a focused helium ion beam (35 keV, 0.3 pA). This was done using a helium ion microscope (Orion Plus, Carl

Zeiss, Oberkochen) equipped with a pattern generator (resolution of 0.5 nm, Elphy MultiBeam, Raith, Dortmund, Germany).

6.3 Results and Discussion

6.3.1 Al_2O_3 Protected AFM-TERS Tips

Atomic layer deposition on silver coated AFM-TERS tips was done using the standard procedure described above using 25 cycles, which should result in an Al_2O_3 layer of approx. 1.5 to 2 nm. Quality control of the nanometer thin layers obtained was difficult, because the sample preparation for transmission electron microscopy includes breaking of the AFM cantilever from the bulky chip and transverse mounting on a copper ring or grid. Moreover, the rough silver coating and the low aspect ratio of the tips make it difficult to obtain a clear electron microscopy image of the nanometer thin protective layer. The preparation of thin cross-sections by means of focused ion beam (FIB) milling was tried, but led to drastic structural changes in the silver coating.

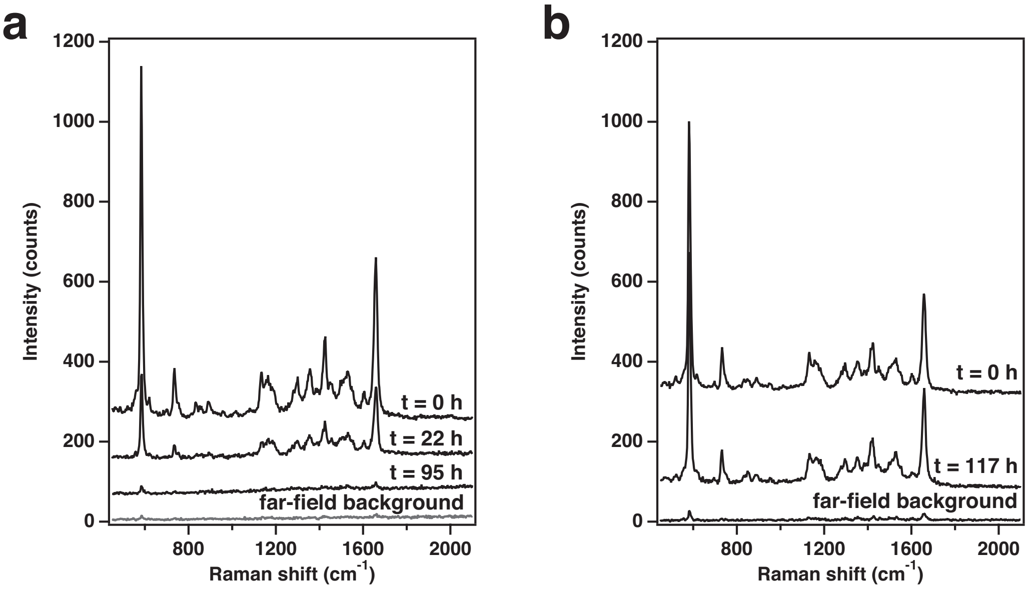

Figure 6.2: Selected tip-enhanced Raman spectra of spin-coated BCB on glass using freshly prepared unprotected (a) and Al_2O_3 protected (b) silver coated AFM-TERS tips after different storage times. A clear decrease in the contrast factor is obtained for the unprotected tips, whereas the contrast obtained with the protected tip is still almost unchanged after 117 hours.

The tips obtained were tested for their TERS enhancement on spin-coated BCB on glass using transmission illumination and detection. To evaluate their performance, the spectra obtained were directly compared to the results obtained with bare silver tips. Figure 6.2 shows selected Raman spectra obtained with a bare silver coated tip and an alumina protected silver coated AFM tip after different times of exposure to atmospheric conditions. A significant decrease in Raman band intensity already within the first 24 hours is observed in the case of the bare silver coated tip, whereas the Raman band intensity obtained with the alumina protected tip is practically unchanged after almost five days of air exposure. Figure 6.3 shows the change in the contrast factor obtained over the course of 5 days for the two previously mentioned tips. The decrease in enhancement of the bare silver tip is close to an exponential decrease, whereas high variations in enhancement between different storage times is observed with the protected tip. The fact that this variation is somehow higher than the standard deviation observed for different sample position could be explained by the fact that remounting of the cantilever for each experiment leads to a slightly different region at the tip apex interacting with the sample surface. This could be investigated further by increasing the statistical significance with a higher number of tested tips.

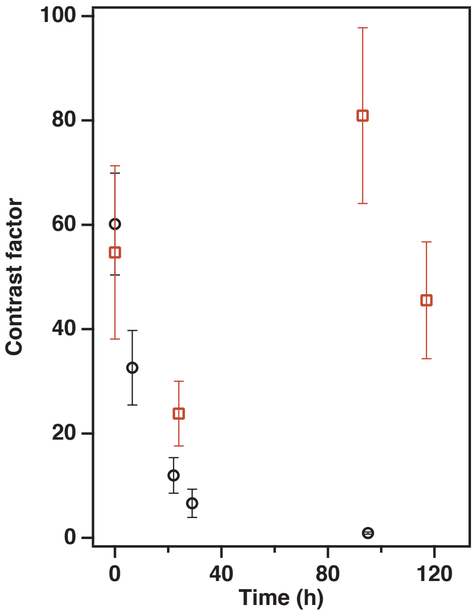

Figure 6.3: Contrast factor vs. storage time for an unprotected (circles) and an Al_2O_3 protected (squares) TERS tip used in contact-mode AFM feedback on spin-coated BCB on glass. Each data point is the mean contrast factor from three sample positions. The error bars represent ± the standard deviation.

Some shortcomings with the above approach were identified and will be described in the following. First, the above measurement were performed at a stage when the instrument used did not allow for slave scan acquisitions. This renders an unbiased determination of the contrast factor difficult and increases the measurement error. Second, because of the high variability in enhancement between different silver coated AFM-TERS tips including a considerable amount of non-enhancing tips, the same tips were used for all measurement points of the time-dependent study. The combination of chemical degradation and mechanical wear (especially during tip approach) increases the complexity of the study and makes it harder to draw reasonable conclusions. Third, pickup of BCB molecules is observed, which could affect subsequent chemical degradation of the tips. The use of other (fixed) test samples (e.g., thiols on transparent gold layers) was tested, but the higher requirements for strong signal enhancement to detect these samples, made it impossible to record time series.

6.3.2 Al_2O_3 Protected STM-TERS Tips

With the help of transmission electron microscopy, the ALD condition could be optimized for silver tips. It was found that the use of multiple pulses and long purge times resulted in the highest quality layers (see Figure 6.4a). The composition of the layer was confirmed by EDX spectroscopy (see Figure 6.5 below) However, it was often found that toward the high curvature of the tip apex, the layer delaminates from the underlying surface, which indicates that there is no covalent attachment (Figure 6.4b). This effect can probably be prevented by prior surface modifications like, e.g., plasma treatment[191] or self-assembled monolayers of a linker molecule.

The nucleation of dielectric layers on metal surfaces during the atomic layer deposition is not well understood.[192] It is, however, known that exposed hydroxyl groups on the surface are critical for the formation of high quality layers. Often, so-called interfacial layers are formed at the beginning of the deposition, where the growth rate is slightly higher than expected.[193] The thickness of such interfacial layers is strongly related to how easily a surface is oxidized. In the case of most nobel metals, initiation of the film growth is therefore difficult. Because the surface reactivity of silver is very complex, the exact mechanism of growth is not known. Plausible scenarios are direct growth from a thin native oxide layer or reaction of the precursor with the silver surface. Previous studies found a higher growth rate at the beginning, suggesting the formation of an intermediate layer.[194]

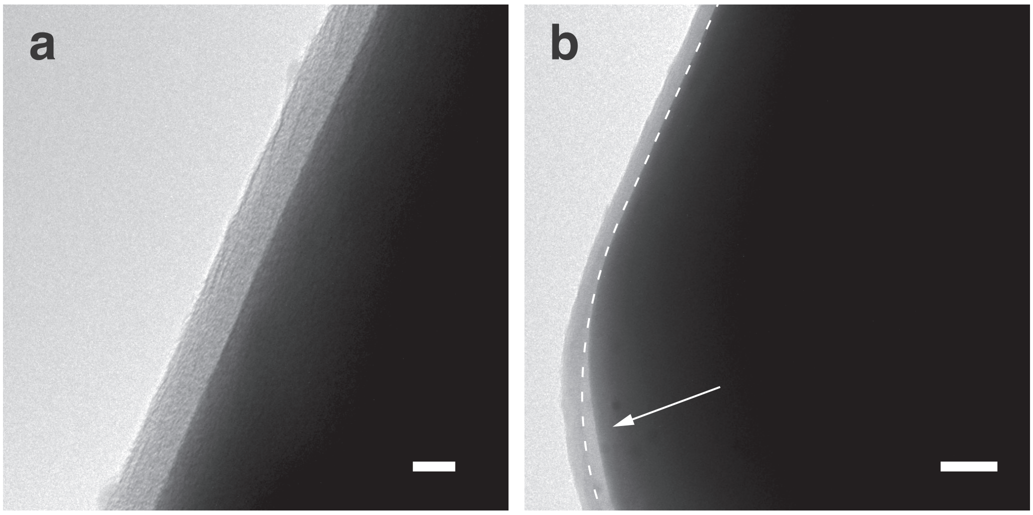

Figure 6.4: TEM images from an alumina protected tip (50 cycles, multiple pulses, long purges). The dashed line indicates the alumina layer boundary and the arrow points to a position where delamination occurred. The scale bars indicate 5 nm and 20 nm, respectively.

An insulating protective layer with a thickness of more than 1 nm can adversely affect the tunnelling current between tip and surface. It would therefore be beneficial to use conductive protective layers for STM-TERS tips. One possibility would be the use of thin films of conductive metal nitrides (e.g., TiN), which are readily prepared by atomic layer deposition.[185]

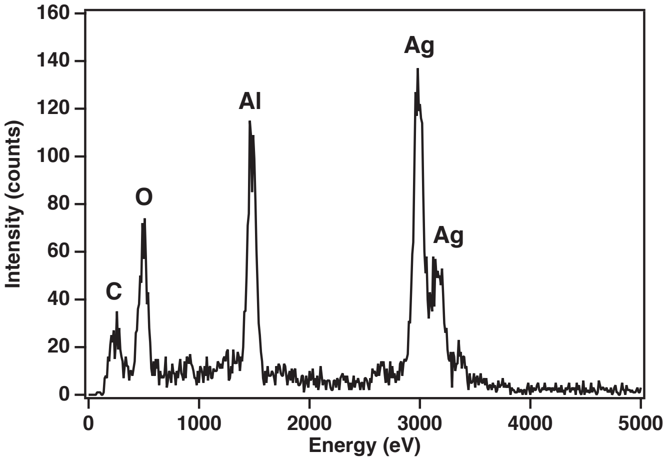

Figure 6.5: EDX spectrum of the Al_2O_3 protection layer shown in Figure 6.4.

6.3.3 Carbon-Membrane Protected STM-TERS Tips

An approach, where the protective layer thickness is predefined by the selected thiol, is the formation of cross-linked SAMs. Cross-linking of 1,1'-biphenyl-4-thiol SAMs on gold caused by bombardment with low energy electrons was first described in 1999.[186] The well-ordered BPT SAMs remained attached to the underlying gold surface during this procedure. Cross-linking is believed to be caused by electron-induced dehydrogenation and subsequent formation of covalent bonds between neighbouring biphenyls. This approach was used to prepare "carbon nanomembranes" on the surface of etched gold tips. A TEM image of the apex of such a tip is shown in Figure 6.6. An approx. 1 nm amorphous layer was found on the tip surface. However, it is impossible to get any insight into the degree of cross-linking based on transmission electron microscopy. Other methods to check the degree of cross-linking on the tip surface are therefore required.

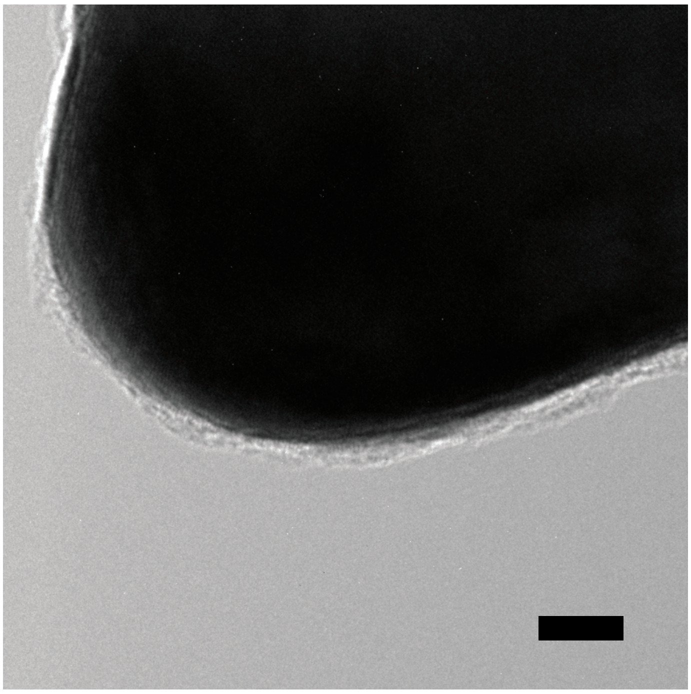

Figure 6.6: TEM images from a gold tip with a thin (approx. 1 nm) protective carbon membrane. The scale bar indicates 5 nm.

A recent study by Penner et al. demonstrated a significant difference in charge transport through BPT SAMs and carbon nanomembranes by approx. 1 order of magnitude.[195] It was therefore tested in a first step if an effect of the carbon membrane layer can be seen in I-V-curves acquired with a bare and a carbon nanomembrane protected gold tip in close proximity to a gold surface (see Figure 6.7). Both curves show almost Ohmic behavior with a slightly higher gap resistance for the carbon nanomembrane protected tip. However, since the exact tip-to-sample distance may have been slightly different for the two measurements, it is not possible to univocally ascribe this effect to the carbon membrane layer. A very clear distinction between the BPT SAM and the carbon nanomembrane is possible with tip enhanced Raman spectroscopy. Figure 6.8 shows tip enhanced Raman spectra collected from a bare gold surface using a BPT SAM covered tip and a carbon nanomembrane covered tip.

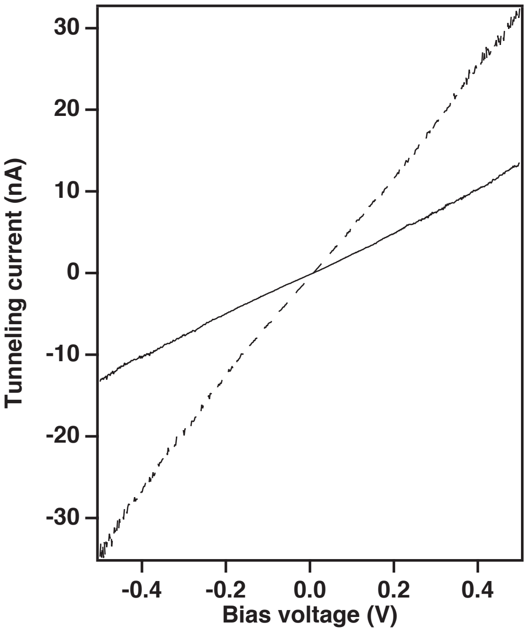

Figure 6.7: I-V curves collected with bare gold tips (dashed, starting at a setpoint of 0.6 nA and a bias voltage of 20 mV) and with cross-linked NBPT SAM gold tips (solid, starting at a setpoint of 0.3 nA and a bias voltage of 23 mV). Each curve is the average of five measurements (forward and backward traces).

Characteristic Raman bands of BPT are observed when the tip was not treated with an electron beam (Figure 6.8a), whereas the amorphous carbon nanomembrane is visible as two broad bands at 1360 cm^{-1} (D band) and 1580 cm^{-1} (G band). Because these broad bands are in a rather important wavenumber range for most applications, this can adversely affect TERS measurements with carbon nanomembrane protected tips.

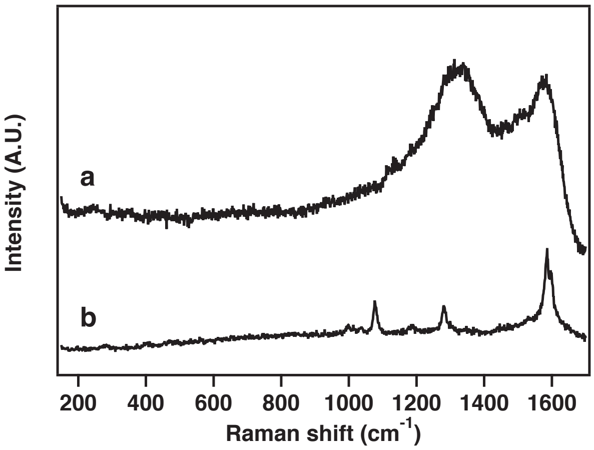

Figure 6.8: Tip-enhanced Raman spectra from a bare gold surface using a gold tip covered with cross-linked BPT SAM (a) and a untreated BPT SAM (b).

6.3.4 Development of a TERS Resolution Target

Figure 6.9 shows a scheme of the proposed resolution target. It consists of pairs of square blocks consisting of three lines with horizontal and vertical orientation. The gaps between the lines is the same as their width. The line width starts at 100 nm and decreases in steps of 2 nm along the spiral down to a final line width of 1 nm. The filled squares are guides and have the same dimension as the following pair of square blocks. The overall size of the resolution target is approx. 6x6 µm.

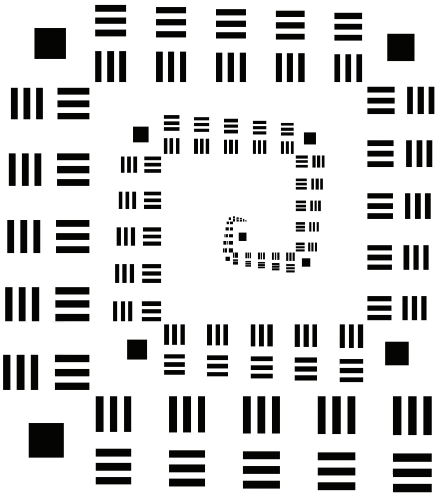

Figure 6.9: Scheme of the resolution target. The lines have a width of 1 to 100 nm and the line width of two neighboring triplet pairs along the spiral differs by 2 nm. The gaps between the lines have the same width as the lines.

These resolution targets were written into the SAM on the surface with respect to a scratch in the sample surface, which helped to find their location for TERS imaging. Because the molecular cross-linking is accompanied by a slight change in layer thickness, the target can also be found with an AFM scan. Characteristic Raman bands from NBPT are readily obtained at short acquisition times (≥0.1 s) and low laser power (≥30 µW), which allows for high pixel number scans with small step sizes. The beginning of a TERS map with a step size of 55 nm is shown in Figure 6.10. The topography image shows a negative contrast for the cross-linked areas, which can be attributed to the difference in charge transport through the carbon nanomembrane and the self-assembled monolayer mentioned above. The TERS contrast image shows a very homogeneous intensity on the NBPT SAM, with a gradual decrease towards the upper boundary of the image. Some of the line triplets are clearly resolved, but the gap appears narrower than the lines themselves. The tip is therefore found to be not very sharp. There is a slight distortion visible for some of the structures (most pronounced for the square on the left hand side). Unfortunately, there is a crack in the gold surface running though the target structure, which is probably the reason for the tip crash after the shown scan lines. A slightly brighter edge on the right side of the crack indicates the scan direction from left to right, because a slight increase in enhancement is observed when the tip hits the edge during the scan.

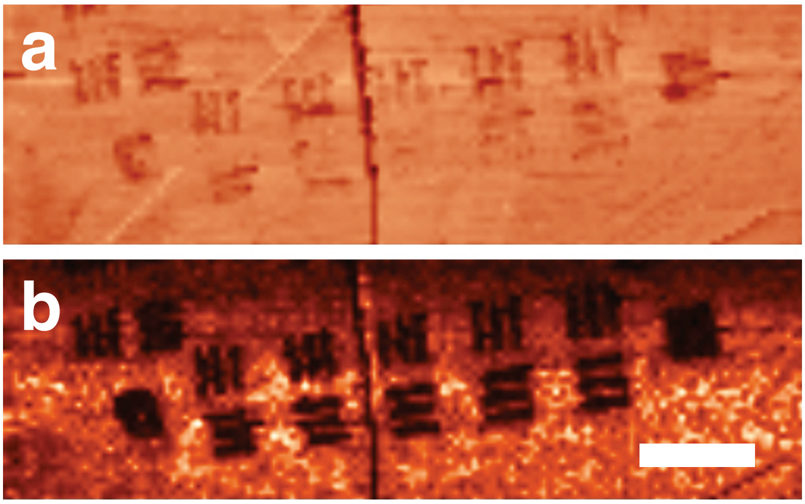

Figure 6.10: Beginning of a 128x128 tip-enhanced Raman map with a silver tip on the TERS resolution target written with 0.5 µC/cm^2. The STM height image (a) as well as the spectroscopic image (b) show clear contrast and most lines are resolved. The tip crashed after about 1/3 of the image, probably because of the huge crack in the gold surface visible in the middle of the image. An acquisition time of 0.1 s per pixel at a laser power of 30 µW at a wavelength of 632.8 nm was used. The scale bar indicates 1 µm.

Figure 6.11 shows a full TERS image from another copy of the resolution target on the sample surface using a fresh silver tip. In this case, a clearer contrast is observed for the topography image, whereas the TERS image shows poorer contrast with strong intensity variations. However, the spatial resolution seems to be higher compared with the previous map (probably caused by a sharper tip). Interestingly, the structures are also resolved in the elastic scattering image. However, no means of discrimination of the near-field scattered light from background scattering was applied and the true near-field nature of this observation still has to be confirmed.

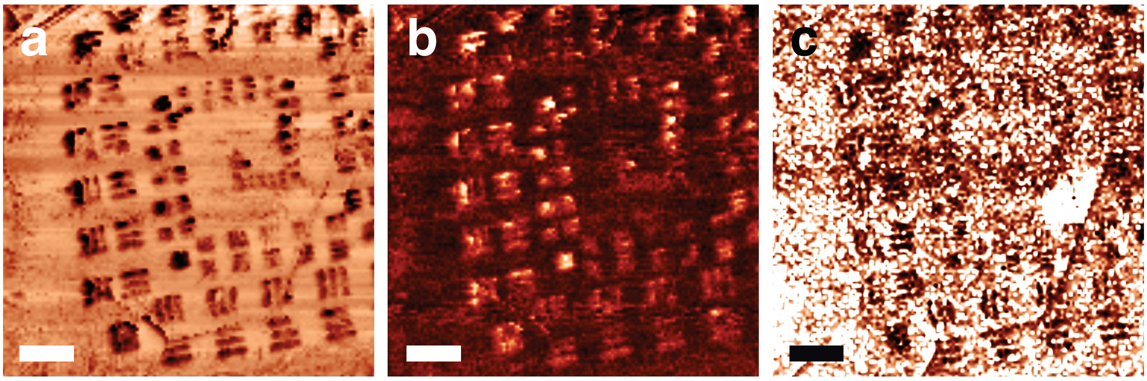

Figure 6.11: 128x128 tip-enhanced Raman map on the TERS with a silver tip resolution target written with 0.5 mC/cm^2. The STM height image (a), the elastic light scattering image (b) as well as the Raman spectroscopic image (c) show contrast and most lines are resolved. An acquisition time of 0.2 s per pixel at a laser power of 40 µW at a wavelength of 632.8 nm was used.The scale bars indicate 1 µm.

6.4 Conclusions and Outlook

Different approaches for the production of thin protective layers for near-field optical probes were presented. These include Al_2O_3 layers on silver coated AFM-TERS tips, where an extended measurement lifetime compared to unprotected tips was demonstrated. Because of the low aspect ratio and the high roughness of the coated tips, no transmission electron microscopy images of the thin layers could be obtained. However, a similar approach on etched silver wires allowed to check the quality of the obtained layers. An ALD recipe including multiple pulses and long purge times resulted in very uniform layers. However, the films do not seem to be covalently attached to the underlaying silver surface and detach from the surface at high radii of curvature (e.g., at the tip apex). Moreover, another tip protection method based on the cross-linking of SAMs was presented. The narrow Raman bands form the chemisorbed thiols were found to disappear upon electron bombardment and broad Raman bands characteristic for amorphous carbon appear, which are expected to interfere with the Raman bands from most analytes. At the end of the chapter, a first attempt for a TERS resolution target is presented based on the same cross-linking procedure used for tip protection. Two TERS imaging experiments on the target demonstrate that the sample allows conclusions concerning the tips' suitability for TERS imaging experiments.

Chapter 7

Nanoscale Chemical Imaging of Segregated Lipid Domains Using Tip-Enhanced Raman Spectroscopy

Lipid domains in supported lipid layers serve as a popular model to gain insight into the processes associated with the compartmentalization of biological membranes into so-called lipid rafts. In this chapter, reproducible tip-enhanced Raman spectra originating from a very small number of molecules in a lipid monolayer on a gold surface are presented. For the first time, large (128x128 pixels), high-resolution (<50 nm) tip-enhanced Raman images of binary lipid mixtures with full spectral information at each pixel are shown.

This chapter is reproduced by permission of the PCCP Owner Societies from:
L. Opilik, T. Bauer, T. Schmid, J. Stadler, R. Zenobi: "Nanoscale Chemical Imaging of Segregated Lipid Domains using Tip-Enhanced Raman Spectroscopy", *Phys. Chem. Chem. Phys.* **2011**, *13*, pp. 9978–9981.
doi: 10.1039/C0CP02832K

7.1 Introduction

According to the lipid raft concept, phase segregation into lipid domains is involved in processes like protein sorting and signaling in biological membranes.[196] Direct visualization of these small and highly dynamic domains in the complex environment of a cellular membrane is a very challenging task. Phase segregated giant vesicles[197,198] as well as supported lipid mono- and bilayers[199] with known chemical composition have therefore often been used as model systems. The size of the segregated phase domains ranges from tens of nanometers to several microns.

Fluorescence microscopy is a common technique for the visualization of coexisting domains in model membranes as well as cellular membranes.[197,198,200] However, epifluorescence and confocal fluorescence microscopy are diffraction limited and cannot be used to visualize domains with a size below 200 nm using light in the visible spectral range. The most common technique to visualize these very small lipid domains in supported membranes is atomic force microscopy.[201–203] This is mainly achieved by measuring the difference in height and friction force of coexisting phase domains in mixed mono- and bilayers. In contrast to spectroscopic methods, AFM yields no or very limited chemical information. For multicomponent mixtures with complex morphology, the purely topographic information is not sufficient to understand the distribution of all constituents within membrane leaflets.

Different attempts have been made to combine the high spatial resolution of SPM with the rich chemical information provided by spectroscopy. One such technique called aperture SNOM has already been used successfully to perform fluorescence microscopy on model[199] and biological membranes[204] with a typical lateral resolution of 50–100 nm. The main idea of the technique is to excite fluorophores with a confined light source at the end of a small-aperture optical probe, which can be scanned across the sample surface. However, in order to gain insight into the compartmentalization of biological membranes based on fluorescence microscopy, fluorescent probes with known partitioning preference for one of the coexisting phases are required. The phase preference for a given fluorescent probe can be different for different lipid systems and therefore has to be evaluated for each model system. Moreover, some of these fluorescent lipid analogues are known to perturb the phase behavior of lipid mixtures.[205] This also limits the application of other fluorescence-based high-resolution imaging techniques, such as STED, STORM and PALM.[5]

Methods based on Raman spectroscopy give the possibility for label-free chemical identification of coexisting lipid phases in membrane model systems under physiological conditions. The main challenge when working with spontaneous Raman scattering is the intrinsic weakness of the Raman scattering process. To counteract this, methods for enhanced Raman scattering have been developed. It has, for example, been shown that coherent anti-Stokes Raman scattering is sensitive enough to acquire lipid spectra from single mono- and bilayers[206,207] to allow for quantitative imaging on mixed lipid bilayers with a lateral resolution of 250 nm.[208] Another method resulting in an enhanced Raman scattering intensity is tip-enhanced Raman spectroscopy.[209] It is an apertureless near-field technique, where a metallic or metallized SPM tip is used to confine and enhance an electromagnetic field in close proximity to the sample surface. The main advantages compared to CARS are the better lateral resolution (15–40 nm)[82,104] and the fact that TERS allows for the collection of a full spectrum at each point, whereas CARS is restricted to one selected Raman band. Tip-enhanced Raman spectra in the fingerprint region ($<$1800 cm^{-1}) collected on a single spot on a mixed supported lipid bilayer have been recently shown.[210]

In this chapter, we demonstrate that it is possible to collect reproducible and strongly enhanced tip-enhanced Raman spectra from single lipid monolayers in the gap between a silver tip and a flat gold surface using top-illumination and STM feedback control.[104] This configuration can be employed to image the lateral distribution of the individual components in a monolayer composed of a binary mixture of phospholipids with chemical selectivity.

7.2 Experimental

The experiments were performed using a combined AFM/STM/Raman microscope described in more detail in section 3.1.1. A HeNe laser with a wavelength of 632.8 nm was used as excitation source. AFM was done using nose-type silicon tips (ATEC-NC from Nanosensors) in semi-contact mode. As STM tips electrochemically etched silver wires (diameter of 0.25 mm, 99.99% purity, Aldrich) were used. Template-stripped (TS) gold surfaces were used as substrate. The preparation procedure is described in section 3.3. After mechanical cleavage, the substrates were air-plasma treated for one minute to render the Au surface hydrophilic. Subsequently, they were directly immersed in Milli-Q water. 1,2-dioleoyl-sn-glycero-3-phosphocholine (DOPC), 1,2-di-palmitoyl-sn-glycero-3-phosphocholine (DPPC) and 1,2-di-palmitoyl(d62)-sn-glycero-3-phosphocholine (d62-DPPC) were purchased from Avanti Polar Lipids

(Alabaster, AL) and used without further purification. Binary lipid mixtures were prepared with a molar ratio of 1:1. Monolayers were prepared on a Langmuir-Blodgett (LB) trough (Minitrough, KSV, Finland) placed on an anti-vibration table in a dust-reduced environment, using milliQ water as the liquid phase. For every experiment, the deposition of the compounds was as follows: A 1 mg/mL $CHCl_3$ solution was spread onto the water and the solvent was allowed to evaporate for 10 min. The total amount of the used $CHCl_3$ solution was 25 µL for DPPC, DOPC and d62-DPPC, whereas 20 µL were used for the DPPC/DOPC and the d62-DPPC/DOPC mixture. The compression rate was set to 2 mm/min. The surface pressure was measured with a Wilhelmy balance with a precision of 0.01 mN/m. Structural annealing was performed by two compression/ expansion cycles between the final pressure (10 mN/m for DPPC, DOPC, the DPPC/DOPC mixture and 20 mN/m for the d62-DPPC/DOPC mixture) and 2 mN/m. Subsequently, the monolayers were transferred onto TS gold and mica via vertical Langmuir-Blodgett technique with 2 mm/min. All monolayer transfers were done at room temperature. DPPC (saturated fatty acid chains) and DOPC (unsaturated fatty acid chains) are immiscible at room temperature and at a surface pressure of 10 mN/m, DPPC is predominantly present in condensed phase domains protruding from a surrounding fluid phase that consists mainly of DOPC.[211]

7.3 Results and Discussion

A representative AFM topography image of a mixed LB monolayer of DPPC and DOPC deposited on freshly cleaved mica is shown in Figure 7.1a. The step height of approx. 1 nm at the domain edges (see the corresponding line cross-section) is consistent with the literature value.[211] The array of parallel stripe domains is most likely formed by shear force-induced alignment and coalescence during vertical transfer or substrate-mediated condensation.[212,213] Figure 7.1b shows the AFM topography of the same mixed monolayer transferred onto TS gold. In this case, the domains are not ordered, presumably due to the different surface properties compared to mica. The increased step height seen in the line cross-section could be the result of a higher stiffness difference between the two coexisting lipid phases resulting in a higher difference in penetration of the AFM tip at high oscillation damping (50%) in semi-contact mode. Such artifacts in AFM semi-contact imaging of lipid layers resulting in apparent topography differences that are affected by mechanical properties of the lipid agglomerate and tapping force are already described in the literature.[214] Monolayer deposition was only possible after air-plasma treatment of the TS gold surface, which shows the importance of removing residual organic impurities to ensure sufficient hydrophilicity of the gold surface.

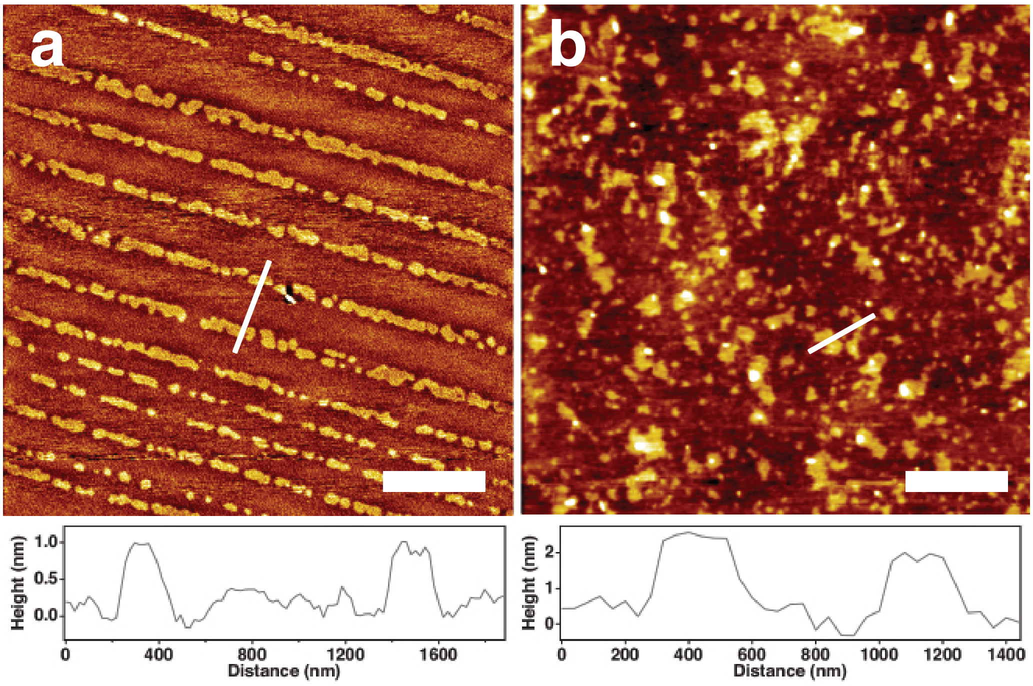

Figure 7.1: Semi-contact mode AFM topography images of a DPPC/ DOPC mixed monolayer (molar ratio of 1:1) transferred to mica (a) and TS gold (b) by Langmuir-Blodgett technique at room temperature. The scale bars indicate 2 µm and the cross-sections along the indicated lines are shown below the images.

Raman spectra of lipids show a strong band close to 2900 cm^{-1} corresponding to the methylene stretching vibrations of the long acyl chains which can be used as a marker band to visualize their distribution within a biological system.[215] Figure 7.2 shows Raman spectra of DPPC and DOPC powders over the full spectral range (a) and in the C-H stretching region (b). The C-H stretching region of DPPC is dominated by the symmetric and antisymmetric methylene stretching vibrations at 2848 cm^{-1} and 2883 cm^{-1}. The lower chain order of the DOPC molecules results in reduced signal intensity for the antisymmetric methylene stretching vibration (in direct comparison to the symmetric stretching vibration) and a shift of both peaks to higher wavenumbers.[206] The weak signal at 3005 cm^{-1} that is only observed in the spectrum of DOPC is assigned to the vinylic C-H vibrations. At a slightly higher Raman shift of 3033 cm^{-1} both spectra exhibit a band associated with the antisymmetric methyl stretch of the choline head group.[216]

Figure 7.2c shows tip-enhanced Raman spectra in the C-H stretching region collected at random tip positions on a pure DPPC and DOPC monolayer, respectively, deposited on TS gold. An acquisition time of 40x0.5 s was used for each spectrum, with an illumination laser power of 650 µW reaching the sample. The Raman bands at 2853 cm^{-1}, 2901 cm^{-1}, 2925 cm^{-1} and 2959 cm^{-1} are consistent with the bands from reference spectra. However, it is not possible to distinguish the two lipid compounds based on their C-H stretching vibrations.

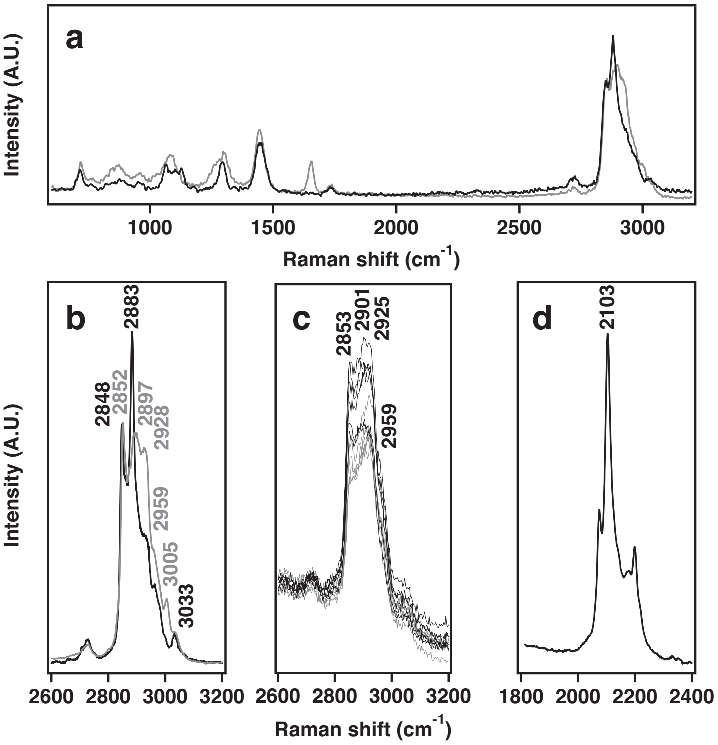

Figure 7.2: Raman spectra of DPPC (black) and DOPC (gray) powder over the full spectral range (a) and in the C-H stretching region (b). TER spectra (c) from 6 different tip positions on a pure DPPC (black) and DOPC (gray) monolayer show similarities with the reference Raman spectra. The bulk Raman spectrum of d62-DPPC in the C-D stretching region (d) shows a similar peak at lower wavenumbers. The spectral resolution of 4.4 cm^{-1} in (a) and (c) and of 0.8 cm^{-1} in (b) and (d) depends on the used spectrometer grating.

To improve spectroscopic contrast, DPPC was substituted by d62-DPPC with fully deuterated lipid chains, which results in a C-D Raman band at 2100 cm^{-1} (see Figure 7.2d), which is separated from any other lipid band. Due to the high degree of deuteration, the phase transition temperature of d62-DPPC is lowered by 5 °C compared to the protiated DPPC.[217] This alteration was taken into account by increasing the surface pressure in the LB experiment (see above and Appendix).

Figure 7.3a and 7.3b show the AFM phase images of the mixed LB monolayer of d62-DPPC and DOPC on mica and TS gold, respectively. The morphology of the d62-DPPC domains looks rather similar on the two substrates. Figure 7.3c shows a 26x64 pixels STM-TERS overview scan of a 6x15 µm^2 sample region (corresponding to a step size of 234 nm) and Figure 7.3d reveals a 128x128 pixels STM-TERS scan on the marked area with an edge length of 6 µm (step size of 47 nm). The brightness of each pixel reflects the ratio of the C-D and the C-H band intensity for a collection time of 0.5 s per point and a laser power of 150 µW (overview scan) and 300 µW (high-resolution scan), respectively. The bright pixels in both images therefore exhibit a predominance of d62-DPPC molecules directly underneath the tip. The observed concentration of these d62-DPPC dominated spots in micrometer-sized areas is in agreement with the known phase separation behavior of the binary system (see above). The high-resolution scan in the highlighted region of the overview scan shows a similarly shaped domain, clearly demonstrating the reproducibility of the technique as well as its non-destructive fashion. Figure 7.3e shows selected spectra from a bright pixel (gray) and from a dark pixel (black) extracted from the 128x128 pixels full spectrum scan illustrating the clear difference in band intensity of the two marker bands. Both marker bands are observed in almost every spectrum of the TERS map with a sufficient signal-to-noise ratio: in 95% of the cases the peak values of the bands are larger than six times the standard deviation of the observed noise level. By plotting the intensity ratio of the two Raman bands instead of individual signal intensities, local and temporal fluctuations in the TERS enhancement are eliminated. It can therefore be assumed that pixel-to-pixel intensity variations reflect true concentration differences of the two lipid compounds in the corresponding sample volume. Previous experiments with the same experimental setup[104] show that the used step size of 47 nm is well above the actual lateral resolution ($\leq$15 nm), which is given by the tip geometry and the gap size. From the surface pressure-area isotherm of the d62-DPPC/DOPC mixed monolayer at room temperature (see Figure B.10) it has been derived that at a transfer pressure of 20 mN/m, each molecule occupies an area of approx. 71 Å^2 on average. When we consider a lateral resolution of 15 nm we can estimate an average of 250 molecules contributing to each Raman spectrum. No reliable estimation for the achieved signal enhancement was possible, because no Raman bands could be obtained from a single lipid monolayer in the absence of the enhancing silver tip.

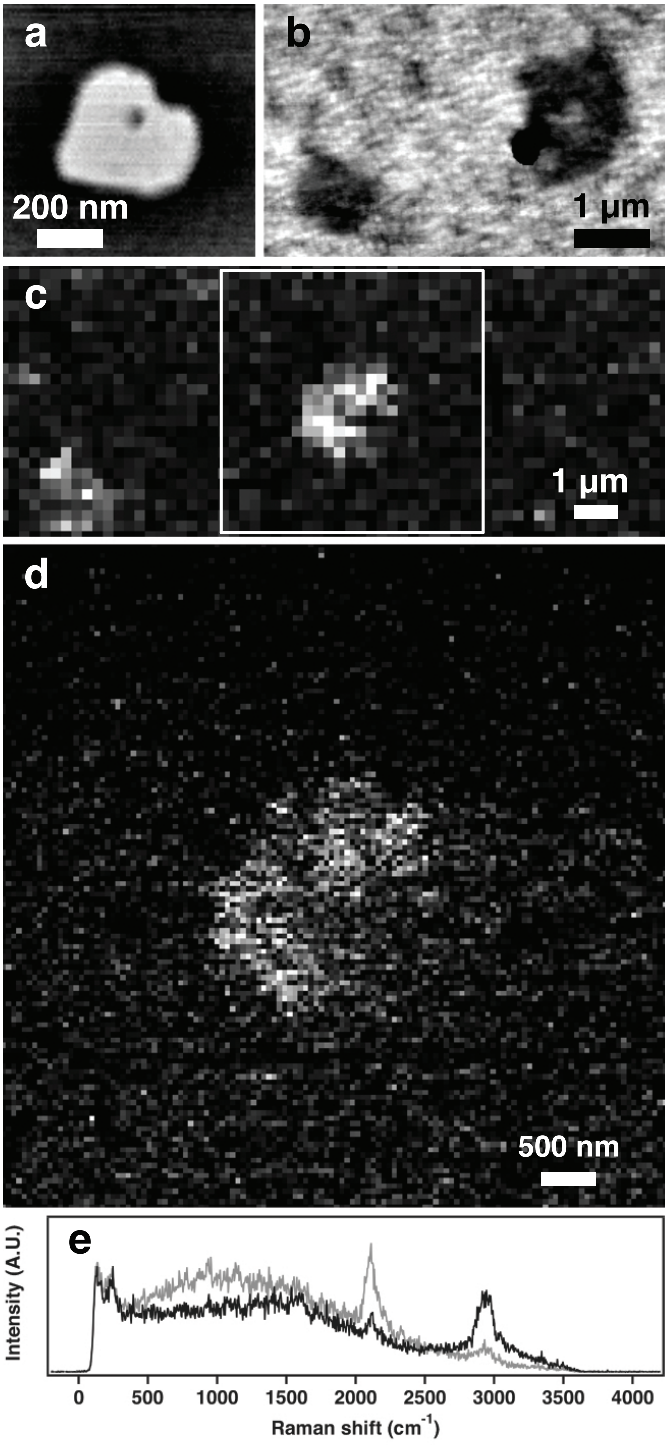

Figure 7.3: Semi-contact mode AFM phase images of a d62-DPPC/DOPC mixed monolayer (molar ratio of 1:1) transferred to mica (a) and TS gold (b) by Langmuir-Blodgett technique at room temperature. STM-TERS images with 26x64 pixels (c) and 128x128 pixels (d) from two consecutive raster scans in the same region (the area of (d) is indicated in (c) with a white box) on a mixed monolayer on TS gold reveal a micron-sized structure. The brightness of each pixel indicates the intensity ratio of the Raman band at 2100 cm^{-1} (C-D stretching vibrations) and 2900 cm^{-1} (C-H stretching vibrations). The Raman spectra from a dark (black) and a bright (gray) pixel of the high-resolution scan (e) illustrate the relative intensity change of the two mentioned Raman bands.

7.4 Conclusions and Outlook

In this work, we used TER spectra in the C-H stretching region for the first time to demonstrate that it is possible to obtain reproducible Raman bands from a very small number of lipid molecules. Moreover, the lipid distribution in a mixed supported lipid monolayer was directly measured with high lateral resolution resulting in the first full-spectral images on phase separated lipid domains. By plotting the ratio of the marker bands, we significantly improve image contrast by reducing variations in signal enhancement during TERS raster scanning. This evaluation method could be potentially applied to any other TERS mapping experiment. Future investigations could focus on TERS imaging using AFM feedback control, which would significantly widen the scope of possible lipid model systems because non-conducting substrates and thicker layers could be used. Scans with a step size of 15 nm or less could be carried out to confirm the lateral resolution limit of the method. Furthermore, we target similar experiments under physiological conditions supported by previous work from our group demonstrating the feasibility of AFM-TERS experiments in aqueous environments.[179]

Chapter 8

Ternary Lipid Mixtures – A Preliminary Study

Biological membranes do not simply consist of a mixture of different lipids, but are a complex structure comprised of various compounds. Incorporation of, e.g., cholesterol into the lipid bilayer seems to play a crucial role in domain formation. TERS is used to determine the distribution of cholesterol within mixed lipid layers, which is invisible to most other technique. Fluorescent labels are problematic because of the considerably small size of cholesterol compared to the available labels. We demonstrate that exchange of seven hydrogen atoms by deuterium makes cholesterol visible to TERS and potentially allows one to determine the spatial distribution within lipid layers.

Some of the data shown in this chapter was acquired by Idlir Liko during the course of a supervised research project and also appears in his report: 'Chemical Nano-Visualization of Cholesterol Propagation in Supported Lipid Domains Using Tip-Enhanced Raman Spectroscopy', 2011.

8.1 Introduction

Lipid domains can undergo phase transitions from a solid ordered phase to a liquid disordered phase dependent on temperature (defined by the compounds transition temperatures). High local concentrations of incorporated cholesterol can lead to a liquid ordered (l_o) phase co-existing with the liquid disordered (l_d) phase. Cholesterol is believed to be positioned between the hydrophic chains from neighbouring lipids, effectively shielding it from the hydrophilic head group. When the concentration of cholesterol is high enough, it has a condensing effect on the lipid layer, thus increasing the stability of the lipid layer. Because of its planar structure, cholesterol tends to incorporate better within groups of saturated lipids (e.g., DPPC) compared to groups of unsaturated lipids (e.g., DOPC).

Methods that have been applied to study the cholesterol driven liquid phase segregation within lipid membranes include pulsed-filed gradient NMR,[218] fluorescence microscopy[219] and atomic force microscopy.[220] AFM is well suited to study the effect of different membrane compositions on the size of the formed domains and it is even possible to study elastic properties of the membrane at particular positions. However, it is not possible to directly visualize the distribution of cholesterol within the lipid layers. Tip-enhanced Raman spectroscopy allows one to visualize the topographic features of the lipid layers, but also adds a spectroscopic contrast, which should allow to make the cholesterol distribution within the membrane visible. A previous study using pulsed field gradient NMR spectroscopy found cholesterol concentrations of 10–20 mol% in the l_d phase and concentrations of 30–40 mol% in the l_o phase.[221]

8.2 Experimental

DPPC, DOPC (25 mg/ml cholorform solution), cholesterol and cholesterol-D7 were all purchased from Avanti Polar Lipids (Alabaster, USA) and used without further purification.

Tapping-mode AFM images were collected with Concorde-type silicon probes (ATEC-NC, Nanosensors). Contact-mode AFM images in air were collected with silicon nitride cantilevers (force constant of 0.10 N/m, OMCL-RC800PSA-W, Olympus, Tokyo, Japan). Contact-mode AFM images in milliQ water were collected with silicon nitride cantilevers (force constant of 0.76 N/m, OMCL-RC800PSA-W, Olympus, Tokyo, Japan). Tapping-mode AFM images in milliQ water were collected with silicon nitride cantilevers (resonance frequency of ≈ 70 kHz, OMCL-RC800PSA-W, Olympus, Tokyo, Japan).

Binary/Ternary mixed bilayers of DPPC, DOPC (and cholesterol) with different molar ratios were prepared as follows: All compounds were dissolved in 300 µl chloroform in a test tube before the chloroform was evaporated under a constant flow of nitrogen. The lipid pellet that formed was then dispersed in milli Q water at 55°C and regular vortexing during 1 hour. 15 minutes of sonication then leads to a clear liposome dispersion. Deposition on mica was done by mechanical cleavage of mica to expose a fresh clean surface layer. A drop of a mixture of 10 µl of the liposome dispersion and 100 µl milliQ water is then placed on the surface and left there for 30 min before rinsing the surface ten times with 40 µl portions of milliQ water.

Ternary mixed monolayers of DPPC, DOPC and cholesterol/cholesterol-D7 were prepared by the Langmuir-Blodgett (LB) technique. The procedure was carried out on a mini trough equipped with a Wilhelmy balance (KSV, Finland). The required amounts were dissolved in chloroform with an overall concentration of 1 g/L. The monolayers were deposited on freshly cleaved mica or TS gold substrates. To ensure hydrophilicity of the gold surface, the substrates were air plasma cleaned for 1 minute and directly immersion into milliQ water. 25 µL of the lipid mixture was spread on the water surface in the Langmuir-trough and the chloroform was allowed to evaporate. Ten compression/expansion cycles (2 mm/min) were performed prior to the deposition by a vertical LB technique at the same rate.

8.3 Results and Discussion

The rupture and fusion of vesicles on a solid support is a very convenient method to prepare supported lipid bilayers. The mobility in these surface supported membranes is only slightly slower than in the case of giant vesicles[222] and they are therefore suitable model systems to study processes happening in biological membranes. Bilayers prepared by this method are only stable when submerged in water. A tapping mode AFM image of a submerged DPPC/DOPC (1:1, mol/mol) supported bilayer on mica is shown in Figure 8.1.

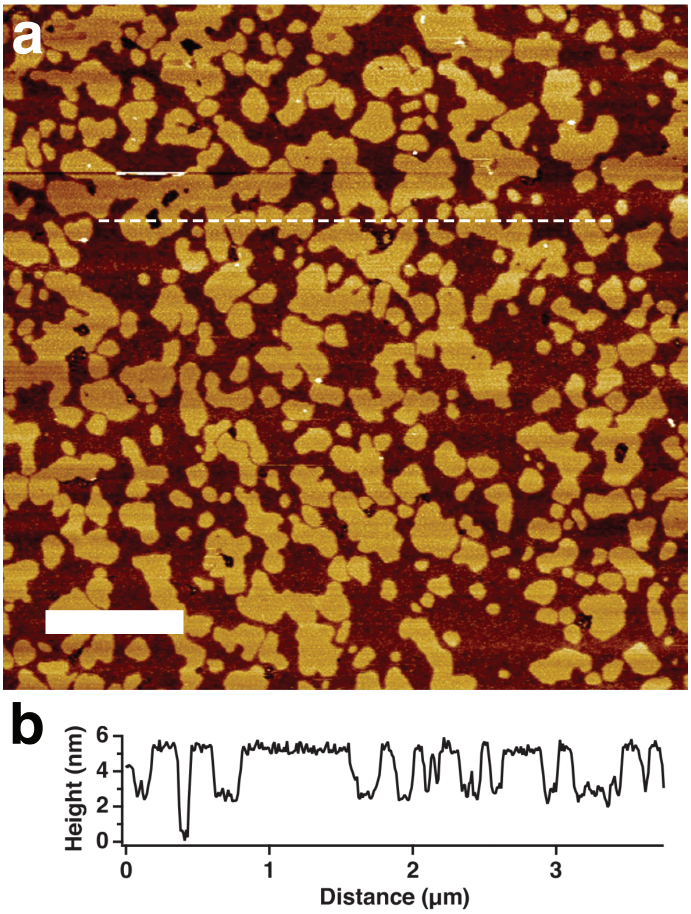

Figure 8.1: Tapping-mode AFM topography image (a) of a submerged mixed DPPC/DOPC (1:1, mol/mol) supported lipid bilayer on mica. Domain formation is observed. The indicated cross-section reveals a height difference of approx. 2 nm between the domains and the overall thickness of the lipid bilayer of 4 nm. The scale bar indicates 1 µm.

The coexistence of two phases is observed. The indicated cross-section shows a constant height difference between the DPPC dominated gel-phase or solid phase and the surrounding DOPC dominated liquid disordered phase. This is caused by an actual difference in bilayer thickness, but also by the mechanical properties of the layer. The overall thickness of the supported lipid bilayer is visible on the the left side of the cross-section where the tip reaches the mica surface through a hole in the lipid layer.

Different studies found that cholesterol can have a strong impact on the segregation properties (e.g., size, morphology) of supported lipid layers.[223,224] The effect of cholesterol on the domain formation was therefore first investigated by comparing contact-mode AFM images of submerged DPPC/DOPC (1:1, mol/mol) lipid bilayers with no cholesterol (Figure 8.2a) and with cholesterol added at a molar ratio of 0.5 (Figure 8.2b). The images look very similar, but the domains appear to have increased in size and exhibit narrow cracks and holes.

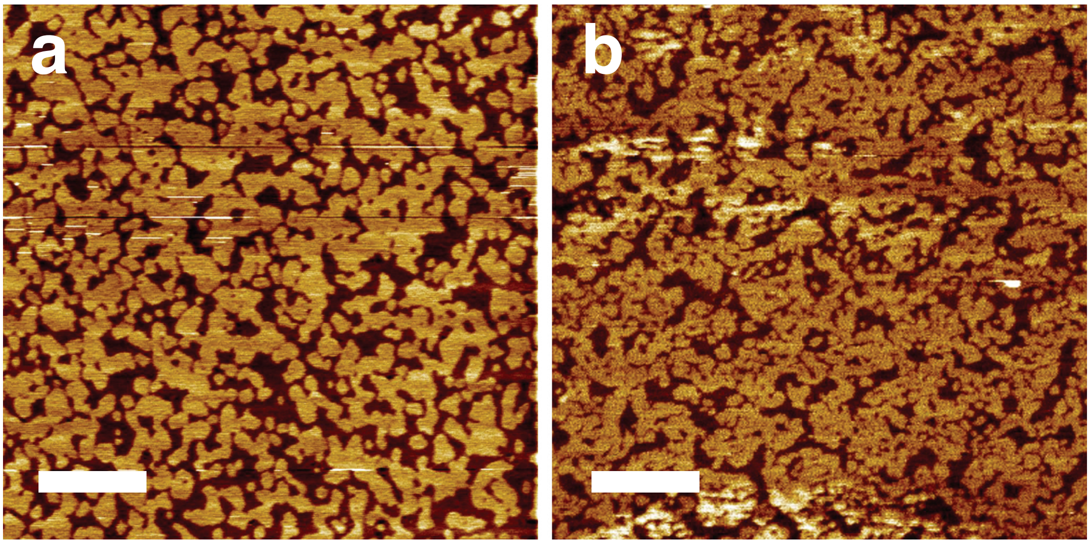

Figure 8.2: Contact-mode AFM topography image of a submerged mixed DPPC/DOPC (1:1) supported lipid bilayer on mica (a) and a submerged mixed DPPC/DOPC/Cholesterol (1:1:0.5) supported lipid bilayer on mica (b). Domain formation is observed in both images. The domain height difference of the lipid bilayer with incorporated cholesterol is 0.7 nm and the height difference in the case of the pure DPPC/DOPC supported lipid bilayer is 0.5 nm. The scale bars indicate 1 µm.

Because TERS measurements in liquids are not straightforward and only one proof-of-principle study exists so far,[179] no TERS experiments were tried on these submerged layers. Because the supported lipid layers prepared by rupture and fusion of vesicles on mica are not stable under dry conditions (see above), the Langmuir-Blodgett technique was used to prepare air-stable ternary mixed lipid monolayers on a mica and template-stripped gold. In oder to increase the spectroscopic contrast, some samples were prepared with d7-cholesterol (fully deuterated isopropyl group). Figure 8.3 shows a contact-mode AFM image of a DPPC/DOPC/Chol-D7 (1:1:0.5) monolayer transferred to mica at 10 mN/m. The image shows large elongated domains as well as small circular domains. The stripe pattern that appears in the image is most likely caused by shear-force induced alignment during the vertical transfer (see previous chapter). To confirm that the use of deuterated cholesterol has no significant influence on the domain formation, AFM measurements were also performed on samples prepared with non-deuterated cholesterol. These images did not exhibit significant morphological differences.

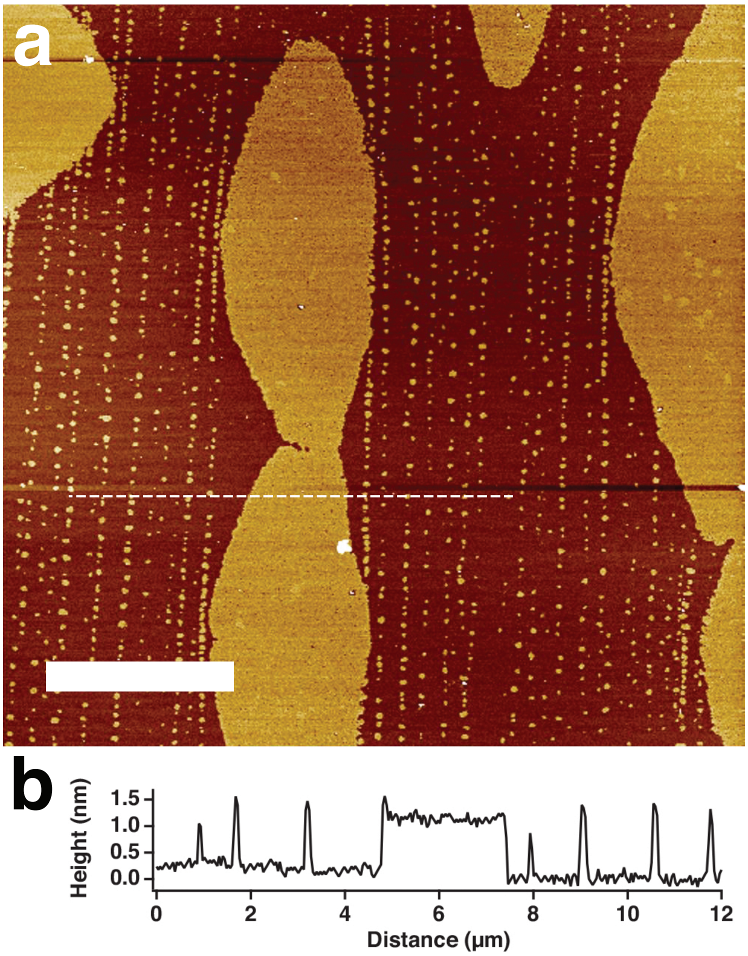

Figure 8.3: Contact-mode AFM topography image (a) of a mixed DPPC/DOPC/Chol-D7 (1:1:0.5) supported lipid monolayer on mica. Large oval domains as well as small round domains aligned in lines are observed. The indicated cross-section reveals a height difference of approx. 1 nm between the domains. The scale bar indicates 5 µm.

The same deposition method was then used to transfer the ternary mixtures onto template stripped gold surfaces suitable for STM-TERS measurements. However, the resulting domains were fractured. Increasing the surface pressure for the deposition to 20 mM/m resulted in intact, mostly circular domains of large diameters (up to 5 µm) shown in the AFM height and friction force images in Figure 8.4. Compared to the mica surfaces, the higher surface roughness of the gold surface leads to domains with fuzzy edges. Compared to the binary DPPC/DOPC mixtures (see previous chapter), the domains formed are significantly larger.

These samples were used for STM-TERS measurement with etched silver tips. Tip-enhanced Raman spectra from the ternary lipid monolayers show a broad Raman band close to 3000 cm^{-1} corresponding to the C-H stretching vibrations from the lipid chains and in some cases a weak peak at approx. 2130 cm^{-1} corresponding to one of the C-D stretching vibration from deuterated cholesterol (see Figure 8.5). These spectra demonstrate that TERS is sensitive enough to detect incorporated cholesterol molecules in lipid monolayers. The strong signal from the lipid chains can be used as an internal standard to correct for changes in enhancement. It was, however, not possible so far to detect differences in the C-D peak abundance, when performing a TERS imaging experiment across one of the domains.

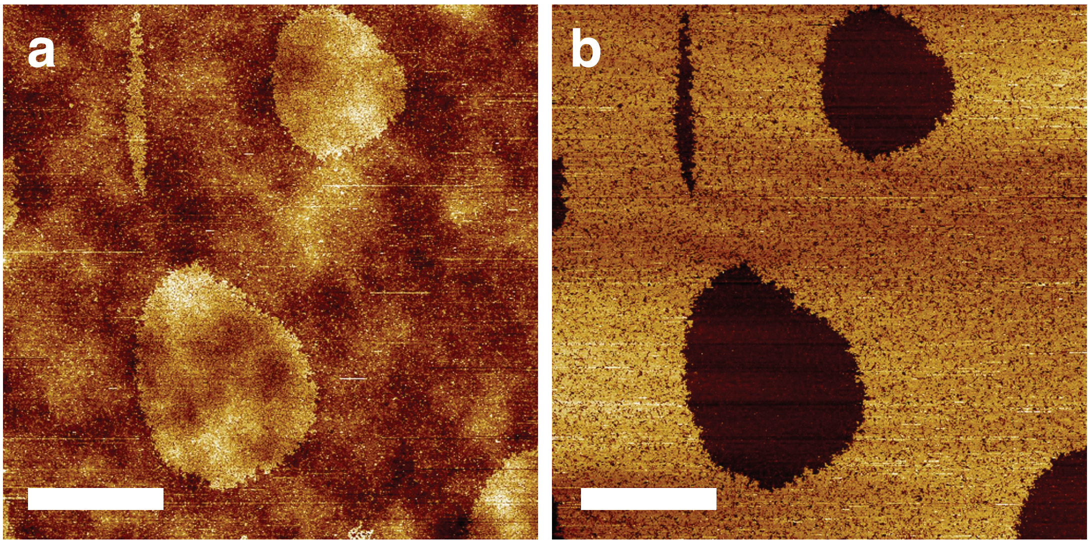

Figure 8.4: Contact-mode AFM topography (a) and friction force (b) image of a mixed DPPC/DOPC/Chol-D7 (1:1:0.5) supported lipid monolayer on TS gold. The domains have fuzzy edges, probably caused by the higher surface roughness of gold. The scale bars indicate 5 µm.

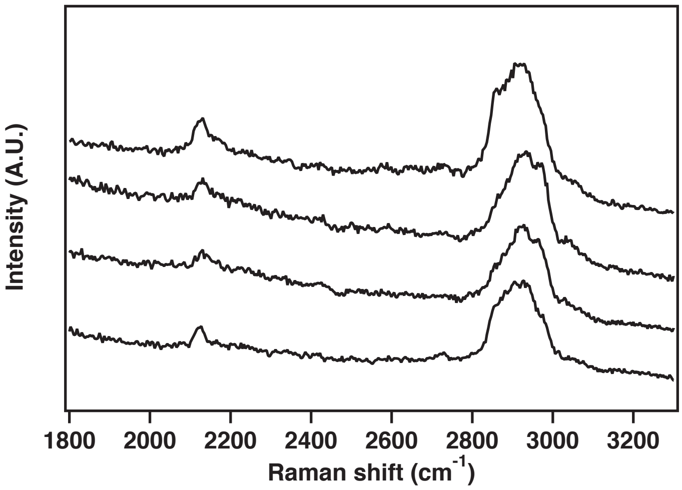

Figure 8.5: Tip-enhanced Raman spectra extracted form a map on a DPPC/DOPC/Chol-D7 (1:1:0.5) monolayer on TS gold. An etched silver tip in STM feedback was used for the map. An acquisition time of 4x0.5s at a laser power of 1.3 mW and a wavelength of 632.8 nm.

8.4 Conclusions and Outlook

In this chapter, the formation of ternary lipid mixtures prepared by rupture and fusion of lipid vesicles on mica was studied with AFM measurements in water. Preparation of more TERS compatible dry ternary lipid monolayers where then prepared on mica and gold surfaces. STM-TERS measurements on these samples did show a weak Raman band assigned to a C-D stretching mode of d7-cholesterol. However, this spectral feature was only observed in some of the acquired spectra. Measurements across domains did not allow any conclusion concerning the distribution of cholesterol between the segregated phases.

Direct TERS measurements of the distribution of cholesterol within submerged lipid bilayers prepared by rupture and fusion of lipid vesicles would be of particular interest, because these measurements would be much closer to real biological membranes. In order to makes such measurements a reality, additional efforts are required to make TERS measurements in an aqueous environment more accessible. This means in particular that robust TERS tips should be used, which still work when submerged in water without easily picking up contaminants.

Chapter 9

Minimally-Invasive Characterization of Covalent Monolayer Sheets Using Tip-Enhanced Raman Spectroscopy

Synthetic covalent monolayer sheets and their subclass, two-dimensional polymers, are of particular interest in materials science because of their special properties that differ from any three-dimensional material. However, structural analysis of such entities is rather challenging, and there is a clear need for additional analytical methods. This chapter demonstrates how TERS can be performed on monomer monolayers and the covalent sheets prepared by [4+4]-cycloaddition to explore rather complex structural and mechanistic issues. The high spatial resolution (<60 nm) and the significantly improved sensitivity (contrast factor of >4000) compared to confocal Raman microscopy provides new insights into the structure of this new and exciting material, namely significant consumption of the reactive units (anthracenes) and exclusion of the alternative [4+2]-cycloaddition. Moreover, due to the high lateral resolution, it is possible to find a first spectroscopic hint for step growth as the dominant mechanism in the formation of these novel monolayer sheets. In addition, TERS was used to get first insights into the phase behavior of a comonomer mixture.

This chapter is adapted and reproduced with permission from:
L. Opilik, P. Payamyar, J. Szczerbiński, A. P. Schütz, M. Servalli, T. Hungerland, A. D. Schlüter, R. Zenobi: "Minimally Invasive Characterization of Covalent Monolayer Sheets Using Tip-Enhanced Raman Spectroscopy", *ACS Nano* **2015**, *9*, pp. 4252–4259.
doi: 10.1021/acsnano.5b00629

9.1 Introduction

Methods to obtain single sheets of layered inorganic materials (graphene, MoS_2, etc.) are, e.g., micromechanical cleavage of the layered crystals[225] or chemical vapor deposition (CVD) on heated surfaces.[226] Even though thermolytic synthesis can result in large sheets,[227] it lacks the control of an organic synthesis approach, in particular in terms of functionality on the molecular level. Bottom-up synthesis of large one-repetition-unit thin sheets is challenging and doing it in a controlled fashion would open up new possibilities to tailor their properties for different purposes, e.g., as molecular sieves,[228] pressure sensors[229] or 2D scaffolds for molecular ordering. The first experimental realizations were based on photochemical solid state polymerisation in preordered monomer crystals.[230,231] Because synthetic molecular sheets obtained after delamination from these crystals are not larger than a few micrometers, the synthesis of more extended covalent monolayers requires another approach. Recently, it was demonstrated that this can be accomplished by anthracene dimerization of compressed amphiphilic monomer units (see Figure 9.1) at an air-water interface.[232,233] The procedure can be carried out at room temperature and results in extended free-standing sheets. However, compared to the crystal approaches, suitable analytical methods to investigate the internal structure of these individual sheets are scarce. Powerful methods such as high resolution transmission electron microscopy,[230] scanning probe microscopy,[230,234,235] X-ray diffraction,[230,234,235] solid state NMR spectroscopy,[235] IR spectroscopy[231,234,235] and Raman spectroscopy[234] that can be used for crystal analysis are normally not suitable for the analysis of single molecular sheets. Some dedicated methods with single-sheet sensitivity exist, such as, e.g., grazing incidence X-ray diffraction (GIXD) and infrared reflection-absorption (IRRA) spectroscopy;[236–238] however these methods only provide limited lateral information. Electron microscopy and scanning probe microscopy are powerful methods to visualize structures that are far beyond the resolving power of an optical microscope. However, these methods do not give much information on the chemical composition. Moreover, the molecularly thin organic sheets are particularly sensitive to electron beam irradiation, restricting the acquisition of high resolution transmission electron microscopy images. Confocal Raman spectroscopy can give detailed spectroscopic information with a lateral resolution down to approx. 200 nm at optical frequencies. Unfortunately, the typically low Raman cross sections of most materials require strong laser irradiation and/or very long measurement times, which in the cases of molecular thin sheets makes it almost impossible to obtain a spectrum at all. When combined with scanning probe microscopy using a metal or metallized tip (tip-enhanced Raman spectroscopy) orders of magnitudes stronger Raman responses as well as a lateral resolution below 20 nm can be reached.[104,239] This gives the possibility to obtain Raman spectra from very few or even single molecules[15] and to localize nanometer sized structural differences (e.g., defects in single-layer graphene) with high precision.[13]

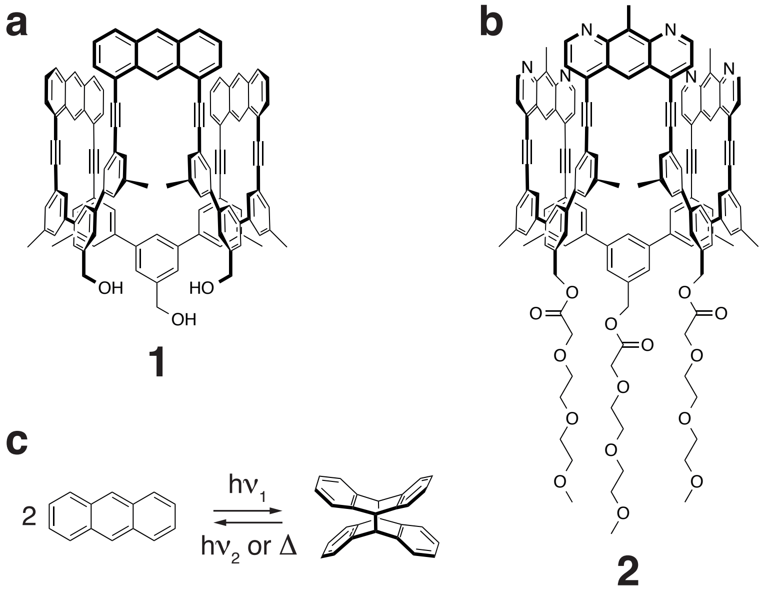

Figure 9.1: Amphiphilic and shape-persistent trifunctional monomer 1 (a) and monomer 2 (b). The photochemically reactive sites (anthracene moieties) are ideally positioned at an angle of 120° with respect to each other. The reaction scheme (c) shows the reversible photochemical anthracene dimerization (UV radiation with $\lambda_1 = c/\nu_1 > 300$ nm leads to dimerization, whereas UV radiation with $\lambda_2 = c/\nu_2 < 300$ nm leads to photodissociation).

In this chapter, TERS is used to probe the internal structure of novel covalent monomolecular sheets produced at the air-water interface by photoinduced anthracene dimerization between trifunctional monomers (see Figure 9.1). High quality vibrational spectra from single/few layers of a synthetic covalent monomolecular sheets are obtained. The spectra indicate that a significant fraction of the anthracene is consumed and potential side reactions can be excluded (e.g., [4+2]-cycloaddition between anthracene and alkyne). The spatial information from the TERS imaging experiments indicates that the remaining Raman intensity from unreacted anthracenes cannot be attributed to islands of unreacted monomers, but is more or less homogeneously distributed (down to a lateral resolution of approximately 100 nm). Moreover, a first attempt was made to investigate mixed monolayers in two dimensions by this method.

9.2 Experimental Methods

A Langmuir trough (Minitrough, KSV, Finland) was used to create monomer monolayers at the air-water interface. A platinum Wilhelmy balance allowed us to monitor the surface pressure. In-plane polymerization was induced at a pressure of 20 mN/m by irradiating a circluar area (Ø 1–2 cm) of the monolayer with a fiber-coupled 455 nm light emitting diode (300 mW, LEDOD OEM, Omicron-Laserage Laserprodukte GmbH, Germany) for up to 18 hours. Two different methods were used to transfer monomer monolayers and polymer sheets onto gold and 300 nm SiO_2/Si substrates at a surface pressure of 20 mN/m and a transfer speed of 1 mm/min. First, samples were produced by three consecutive vertical Langmuir-Blodgett transfers. The threefold deposition is done to increase the surface coverage because the film easily breaks apart. Second, substrates were pulled through the molecular film on the water surface at an angle of approximately 45°, which results in almost full surface coverage with one layer at most. Coverage of the substrate is typically checked using a reflected light differential interference contrast (DIC) microscope (DM4000 M, Leica Microsystems). Flat gold substrates were prepared by a template stripping method described in more detail in section 3.3.

TERS measurements were performed on a combined AFM/STM/Raman microscope (see section 3.1.1) using a 632.8 nm HeNe laser for Raman excitation. Silver tips were prepared by electrochemical etching of a silver wire (diam. 0.25 mm, 99.99% purity, Sigma Aldrich). A 2:1 (v/v) mixture of methanol (p.a., Sigma Aldrich) and perchloric acid (70%, VWR) was used as etchant. TERS spectra were collected after focusing the excitation laser on the apex of a silver tip in scanning tunnelling feedback (constant current mode) with the sample surface. Imaging was performed by moving the piezo sample stage in x,y and z directions while keeping the relative laser-to-tip position fixed. An acquisition time of 3 s was used for all shown spectra. A fairly low laser power of 30 µW on the sample stage was chosen in order to minimize photoinduced reactions/decomposition of the sample molecules.

Theoretical Raman activity spectra were calculated using Gaussian 09 (Gaussian, Wallingford, USA). Optimization of the molecular structures was performed by means of density functional theory (DFT). The Becke, three parameter, Lee-Yang-Parr

(B3LYP) exchange-correlation functional with the 6-311G(d) basis set was used for all atoms. The vibrational modes were assigned based on visual inspection in GaussView 5. All calculated frequencies were scaled with a factor of 0.970.

Accumulated spectra from each map were fitted with a third-order polynomial baseline fit and with Lorentzians for the main peaks (up to ten for the monomer mixtures) and for all other spectral features. The spatial map shown is based on the peak area determined from fits to individual spectra with the constraints of fixed peak positions and full width at half maxima from the fit of the accumulated spectra. The peak heights were determined by means of an automatic peak finder based on Gaussian filtering of the spectra (Mathematica 10, Wolfram Research, Oxfordshire, UK) and an individual threshold for each spectrum (after baseline substraction) corresponding to a three times noise criterion. The determined peak ratios with their uncertainties are calculated as mean ± two standard deviations for the spectra that fulfill the aforementioned criterion.

9.3 Results and Discussion

In order to evaluate the expected changes in the vibrational fingerprint spectrum upon polymerization, DFT calculations of two model compounds were carried out (see Figure 9.2). A strong Raman band close to 2200 cm^{-1} corresponding to the triple bond stretching vibrations is observed for both model compounds, but is omitted for better visibly of the spectral range below 1800 cm^{-1}. Raman bands that could be used for clear spectroscopic differentiation are marked with dashed lines. It is apparent that the two most prominent peaks in the Raman spectrum for the unreacted monomer model compound (Figure 9.2a) at 1362 cm^{-1} and 1546 cm^{-1} can be assigned to anthracene C=C stretching vibrations, whereas these modes are absent in the spectrum of the dimer model compound. Also the other indicated modes at 817 cm^{-1}, 1027 cm^{-1} and 1433 cm^{-1} are dominated by anthracene vibrations. All these modes are clearly absent in the Raman spectrum of the dimer model (Figure 9.2b) and are therefore expected to disappear upon polymerization.

The DIC microscopy image in Figure 9.3 shows the typical surface coverage of the covalent monolayer on gold after the threefold deposition described above. It is possible to discern the covalent monolayers because of the clear contrast at the edges. The surface coverage is fairly high, and large sheets with a size in the range of a few hundred micrometers are observed. Few areas with a slightly darker appearance most

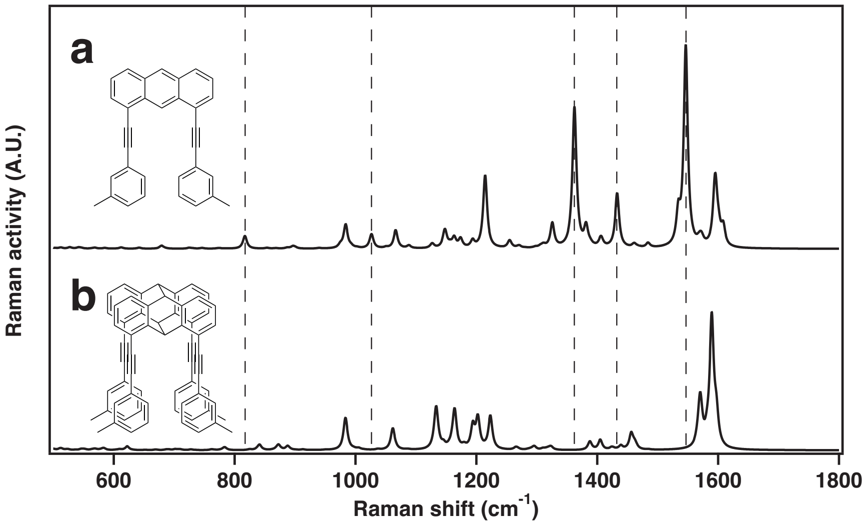

Figure 9.2: Theoretical Raman spectra of the indicated model compounds for the monomer molecule with intact anthracene moieties (a) and the covalent monolayer with dimerized anthracene moieties (b).

likely indicate multilayers. Similar surface coverages were observed in the case of unreacted monomer layer deposition.

Confocal Raman spectra from single/few-layers on 300 nm SiO_2/Si substrates before and after irradiation only exhibit weak spectral features, even for an acquisition time of 30 min at 1.7 mW using 632.8 nm excitation, which does not allow any spectroscopic differentiation of the sheets before and after reaction because anthracene vibrational modes are almost completely missing in both cases (see Appendix Figure B.13). However, with a freshly prepared sharp silver tip in close proximity to the sample surface (maintained by STM feedback), Raman spectra exhibiting the characteristic peaks (including anthracene vibrational modes) were observed with a much lower laser power (30 µW) and a collection time of only 3 s. Figure 9.4 shows a typical tip-enhanced Raman spectrum from a non-irradiated monomer monolayer obtained after threefold deposition on gold. Direct comparison of the intensity of the triple bond stretching vibration in a representative tip-enhanced Raman and a confocal Raman spectrum taking the different laser powers and acquisition times into account gives a contrast factor of >4000.

By scanning the tip across extended areas of the sample surface, spectroscopic images of the transferred monomer layers can be obtained. Figure 9.5a shows the sum of 1024 spectra from a 16x16 µm^2 TERS map performed on a non-irradiated monomer layer on gold. The spectrum shows high resemblance with the theoretical

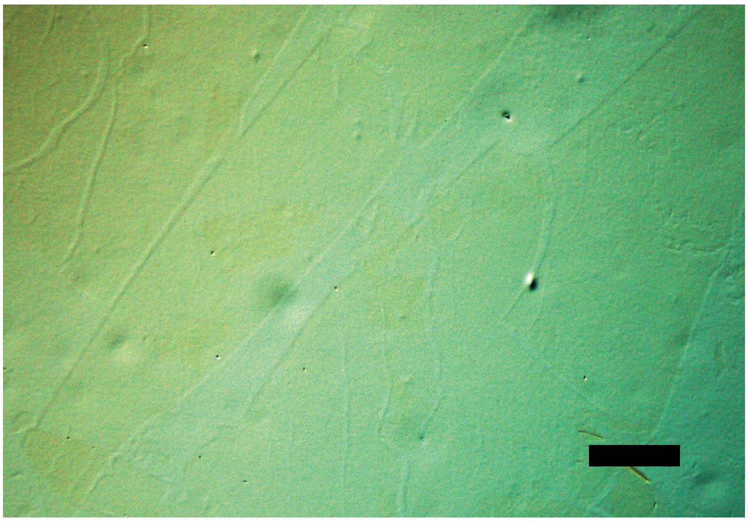

Figure 9.3: Differential interference contrast microscopy image of a covalent monolayer sheet after transfer to a gold substrate. Individual layers can be recognized due to the clear change in contrast at the edges. The scale bar indicates 100 µm.

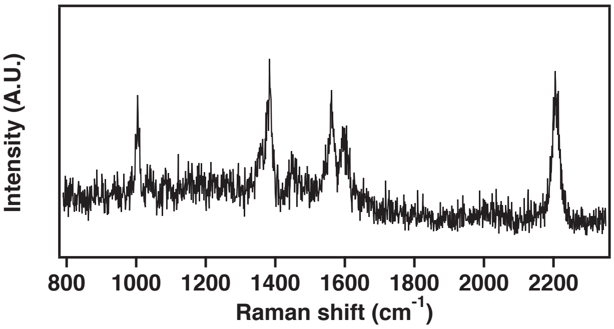

Figure 9.4: Tip-enhanced Raman spectrum from the transferred monomer film on gold. The observed spectral features correspond well to the theoretical spectra obtained from DFT calculations.

Raman spectrum (see Figure 9.2). The high abundance of the peaks at 1383 cm^{-1} and 1562 cm^{-1} corresponding to anthracene vibrations indicate that the tightly packed monomers carry intact anthracene moieties.

This result is conflicting with the results form the abovementioned confocal Raman measurements, where the anthracene modes were hardly observable. The reason could be that the high incident power and long acquisition time required to obtain the confocal Raman spectra alters the sample. It could, for example, be that despite the fact that the excitation wavelength of 632.8 nm is far away from the absorption band of the monomer,[232] the high energy flux leads to an anthracene dimerization or possible side reaction (e.g., reaction with dioxygen[240]). This finding is a clear indication that TERS is a less invasive analytical method for investigation of covalent monolayers than confocal Raman microscopy. In other words, TERS does not alter the specimen as much as Raman microscopy does, and consequently allows to probe these delicate molecule layers in a state close to native. Various examples where the applied analytical technique can cause changes in the investigated sample are known.[241,242] Moreover, the peaks at 1004 cm^{-1} (benzene ring breathing mode) and 2207 cm^{-1} (triple bond stretch) indicate integrity of the transferred molecules.

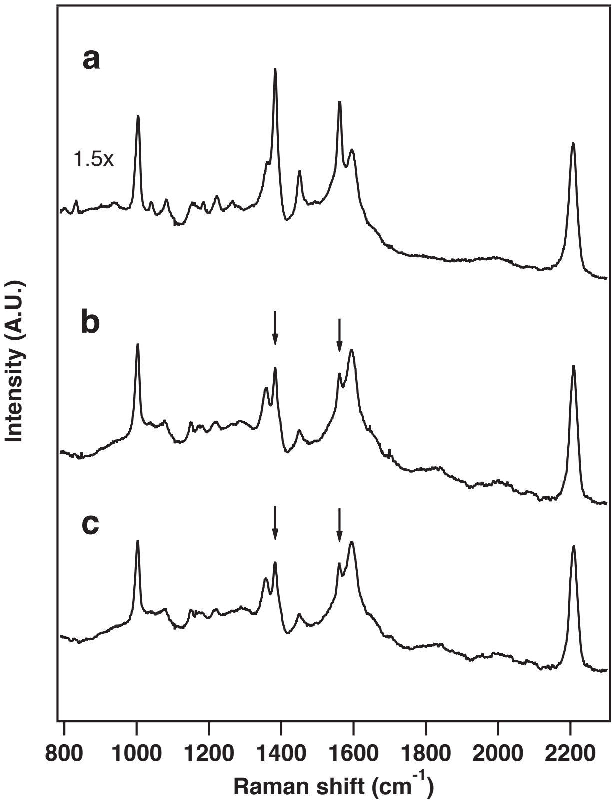

Figure 9.5: Accumulated spectrum from a TERS map of a non-irradiated monomer layer on gold (a) and accumulated spectra from two TERS maps of a monomer layer after irradiation with a 455 nm LED for 18 h (c,d). The arrows indicate the decrease in relative intensity of the most abundant anthracene vibrational modes. All maps have a size of 32x32 pixels and were performed on 16x16 µm^2 and 20x20 µm^2 areas, respectively. The spectra are offset for better visibility and spectrum a was scaled in intensity with a factor of 1.5 for better comparability.

Dimerization of neighbouring molecules was induced by irradiation of a packed monomer monolayer with a 455 nm LED for 18 hours directly on the Langmuir trough. This was followed by transfer to a gold substrate (see Figure 9.3). Raman imaging experiments on the sheets were performed the same way as for the unreacted monomer layers. The accumulated tip-enhanced Raman spectra (1024 individual spectra) from two different sample positions are shown in Figure 9.5b and 9.5c. A significant decrease in relative peak intensity for the characteristic anthracene bands at 1383 cm^{-1} and 1562 cm^{-1} was observed (indicated with arrows in Figure 9.5) . Additional changes include a decrease in relative peak intensity for the anthracene ring breathing mode at 833 cm^{-1}, the anthracene C–H scissoring mode at 1040 cm^{-1} and the anthracene C–H rocking/C=C stretching vibration at 1450 cm^{-1}. These observations are in agreement with the expected changes highlighted in the calculated spectra (see Figure 9.2). The residual intensity for the anthracene vibrational modes indicates the presence of unreacted anthracene units within the formed sheets. Payamyar et al. recently observed complete disappearance of the red-shifted anthracene fluorescence after 2 h irradiation at $\lambda = 373$ nm based on in situ measurements at the air/water interface.[232] This discrepancy is most likely caused by the two orders of magnitude lower photon flux used in the present study resulting in an incomplete photochemical reaction even after 18 h irradiation. A well-known competitive reaction to anthracene dimerization is its oxidation through a [4+2] photoaddition. With the evidence that netpoint formation even occured at high oxygen levels, Payamyar et al. showed that the oxygen product is not competitive with photodimerization.[232] Spectroscopic analysis would in principle allow a more quantitative evaluation of the dimer to oxide ratio. For TERS, a spectral signature of the oxidation product is expected at approximately 1650 cm^{-1} (C=O stretching vibration) and was not observed. However, it could be obstructed by the broad peak at 1595 cm^{-1} (benzene C=C stretching vibration). The possible competing light-induced [4+2] cycloaddition between anthracene and the alkyne functionality[230] can be excluded, because the relative triple bond peak intensity is essentially unchanged after irradiation. The preference for the [4+4] cycloaddition is most likely of steric nature and caused by the close stacking of the anthracene moieties on the Langmuir trough (supported by the observation of excimer fluorescence[232]). No vibrational modes related with the newly formed bonds between the two anthracene moieties (expected at 892 and 841 cm^{-1}) were observed. One possible reason could be that the sheets formed are amorphous, which would imply that no discrete vibrational mode for the newly formed C–C bonds would be expected. Another reason could be that the vibrational modes of these newly formed bonds oriented parallel to the sample surface are not as effectively enhanced as modes, which are oriented perpendicular to the surface and thus more prominent in the spectra. A similar finding was recently reported on single-layer graphene imaged with the same

TERS configuration.[13]

In a next step, we used the spatial information encoded in TERS maps. To prove that tip-enhanced Raman spectroscopic imaging on the covalent monolayers actually probes the local chemical composition, an imaging experiment was conducted at the edge of one of the covalent sheets. A Raman intensity image (32x32 pixels, 4x4 µm^2) evaluated for the triple bond stretching vibration is shown in Figure 9.6. The distance between two subsequent points is 129 nm. The immediate drop in Raman intensity at the edge (from one point to the next) indicates that the actual lateral resolution is below the optical diffraction limit at the used wavelength (a spectroscopic image across the film edge with an even smaller step size of 60 nm is shown in the Appendix Figure B.14).

In order to investigate the spatial distribution of the residual anthracene moieties indicated by the residual peak intensity at 1383 cm^{-1} and 1562 cm^{-1} in the accumulated spectrum in Figure 9.5c, the ratio of the two neighbouring peaks at 1562 cm^{-1} and 1595 cm^{-1} was analyzed at every position of the map, only taking into account peaks with an intensity above the three times noise criterion. A well-defined Gaussian distribution of the peak ratio of 0.75±0.18 was found (for the 18 h irradiated sample), which is significantly below the ratio of 1.29±0.40 found for the non-irradiated monomer monolayer (see Appendix Figure B.15 and B.17). This finding suggests a homogeneous consumption of anthracene within the sheet. To look into this in more detail, a TERS map with a smaller step size (103 nm) was performed on a layer (one-time transfer) that had only been irradiated for 20 minutes at 455 nm. The observed peak ratio distribution was again found to be well-approximated by a Gaussian function with a value of 0.94±0.24 (see Appendix Figure B.16). The fact that the anthracene consumption is reflected in well-defined peak ratio distributions at all investigated stages of the reaction is an indication that the formation of the covalent sheets happens with a step-growth mechanism. In the case of a chain-growth mechanism, a less defined intensity distribution would be expected (if the lateral resolution is high enough) with more values at the initial peak ratio of the unreacted monomer. However, a reliable examination would require spectroscopic analysis down to the single molecule level which has not been possible so far.

An example where the spatial information provided by tip-enhanced Raman imaging is of particular value is the spectroscopic analysis of mixed monomer monolayers. When considering a binary mixture of monomers 1 and 2 (see Figure 9.1), the phase behavior on the Langmuir trough will predetermine the structure of the resulting

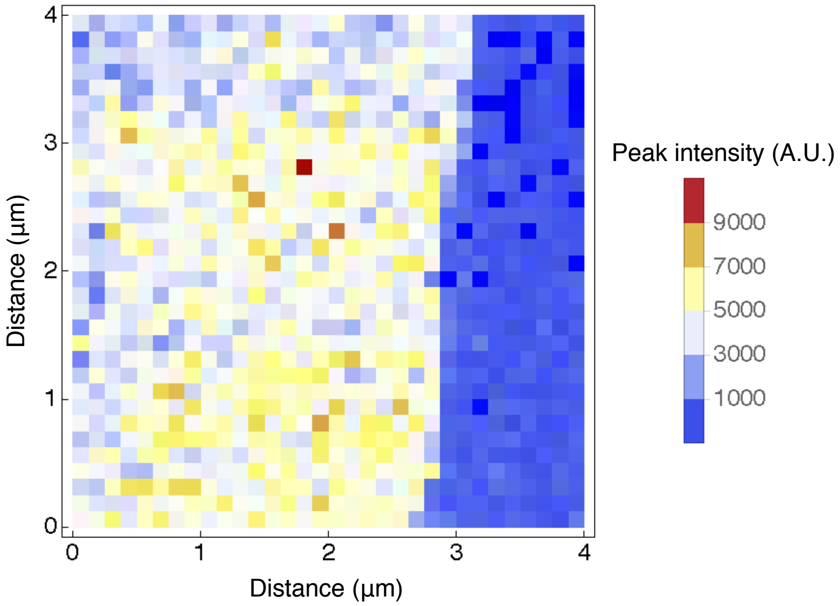

Figure 9.6: Raman intensity image of the intensity of the triple bond stretching vibration across the edge of a polymer film.

two-dimensional copolymer.[233] We made a first attempt to study a binary mixtures of monomers 1 and 2 in a molar ratio of 1:1 by performing a tip-enhanced Raman imaging experiment on a premixed monomer layer prepared on a Langmuir trough and transferred to a gold substrate by one-time transfer.

Figure 9.7 shows the predicted Raman spectra of the corresponding model compounds. Spectroscopic contrast is given by a shift of one of the anthracene C=C (respectively C=N) stretching vibrations to a lower wavenumber (namely 1325 cm^{-1}) because of strong involvement of the nitrogen atoms. Differentiation is also possible based on the additional peak at 1455 cm^{-1}, which correspond to a vibrational mode with strong involvement of the additional methyl group at the 9-position of anthracene.

TERS imaging on a 1:1 mixed monolayer of monomers 1 and 2 was performed on a 20x20 µm^2 area (32x32 pixels), and the resulting accumulated spectrum is shown in Figure 9.8b. Direct comparison to the accumulated spectrum from the pure monomer 1 layer (Figure 9.8a) indicates a significant decrease in intensity of the two anthracene C=C stretching vibrational modes. Moreover, additional modes are observed at 1330, 1341 and 1462 cm^{-1}, which can be assigned to monomer 2 vibrations (see Figure 9.7).

It is again possible to perform a spatial analysis similar to the one applied for the

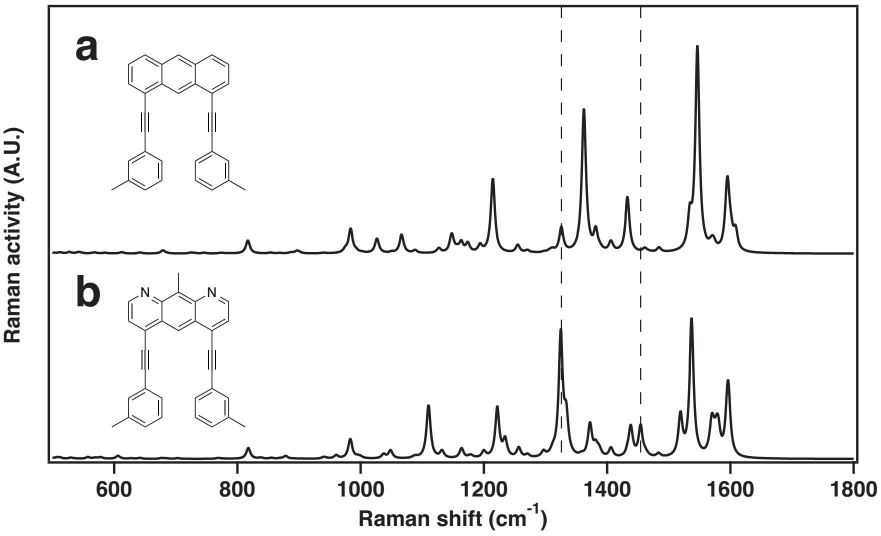

Figure 9.7: Theoretical Raman spectra of model compounds for the two premixed monomers with an anthracene (a) and an 1,8-diazaanthracene (b) moiety, respectively.

pure monomer layers. The intensity ratio of the peaks at 1562 cm^{-1} and 1595 cm^{-1} shows a well-defined distribution of 0.83±0.11 (see Appendix B.18). The significantly lower ratio compared to the pure layer of monomer 1 can be explained by the fact that the two monomers appear to be homogeneously mixed on the sample surface (within the resolution limit). In the case of a heterogeneous distribution, ratios as observed for the pure monomer 1 layers would appear more frequently. Interestingly, some spectra exhibit a particularly intense peak at 1330 cm^{-1}, which can be attributed to a characteristic vibrational mode of monomer 2 (see above and Figure 9.9). However, these spectra did not show any significant decrease in band intensity for the anthracene modes at 1383 cm^{-1} and 1562 cm^{-1}. The particularly high peak intensity of the 1,8-diazaanthracene C=C/C=N stretch vibration at 1330 cm^{-1} could be a result of a direct interaction of the nitrogen lone pair with silver atoms of the tip. This additional enhancement effect is known as chemical enhancement in the surface-enhanced Raman spectroscopy literature.[49] Work by Hayazawa et al. even reported splitting of the ring-breathing mode of adenine crystals caused by direct interaction between the atoms of a silver tip and the nitrogen atoms.[129]

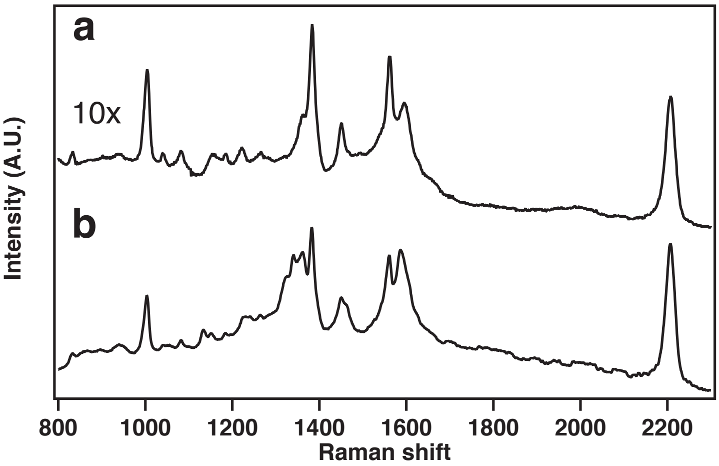

Figure 9.8: Accumulated spectrum from a TERS map with 32x32 pixels on an 20x20 µm^2 area of a 1:1 mixed monolayer of monomers 1 and 2 (b) compared to the accumulated spectrum of a pure threefold deposited monomer 1 layer (a). The spectra are offset for better visibility and spectrum a was scaled in intensity with a factor of 10 for better comparability.

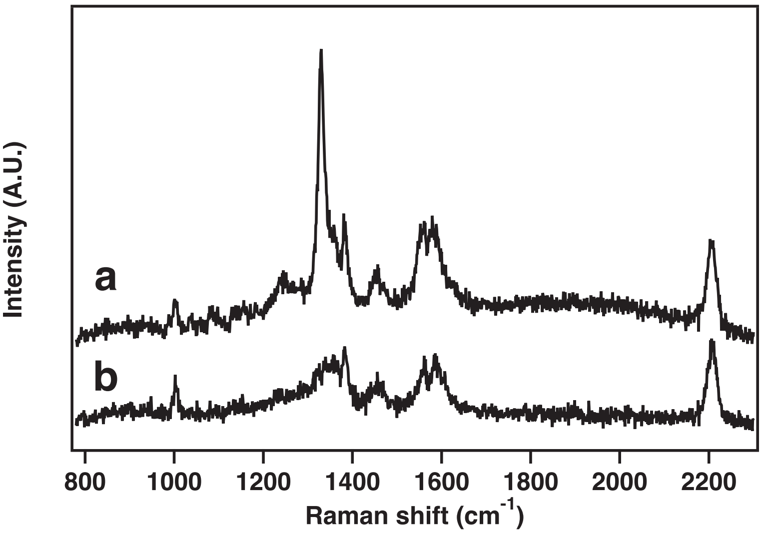

Figure 9.9: Tip-enhanced Raman spectra extracted from the map underlying the accumulated spectrum in Figure 9.8. Few spectra show a particularly strong peak at 1330 cm^{-1} (a), whereas in the other spectra (b), this peak is only of moderate intensity. The spectra are offset for better visibility.

9.4 Conclusion and Outlook

In the present study, TERS was used for the first time to obtain high signal-to-noise Raman spectra from single/few layers of a synthetic covalent sheet. The orders of magnitudes higher sensitivity compared to confocal Raman microscopy allows to use acquisition times of a few seconds and laser powers in the low microwatt range, which significantly reduces invasiveness of the analytical method in the case of susceptible samples.

A clear intensity decrease of the characteristic anthracene vibrations indicates successful dimerization of neighbouring monomers within compressed layers on the Langmuir trough. The potential side reaction of a [4+2] cycloaddition could be excluded based on the rich spectroscopic information. The laterally resolved spectroscopic data shows a well-defined distribution of unreacted monomer units within a partially reacted layer based on individual spectra from <5000 monomers collected from sample positions separated by approx. 100 nm. No domains were found on the investigated length scale. Since the formation of covalent nanosheets would be favoured in the case of a chain growth mechanism, this finding indicates that the polymerization in two dimensions probably happens with a step-growth mechanism. However, a more reliable examination would require to push the lateral resolution further towards the single/few-molecule level. Moreover, a first attempt towards the high-resolution spectroscopic mapping of two-dimensional copolymers was made. The possibility to image the lateral molecular distribution with high resolution could allow to shine light on the processes involved in the formation of two-dimensional molecular films, especially in the case of copolymerization. The differentiation of gradient and random copolymers, for example, is only possible on the molecular or close to molecular level.[243] A possibility would also be to use the tip enhancement not as an analytical tool, but to produce nanoscale covalent sheets with a predefined shape. This could, for example, be realized by using plasmonic aluminum tips with UV irradiation to locally induce anthracene dimerization.

Chapter 10

Raman Analysis of 2D Analogues of Copolymers Synthesized by Site-to-Site Transmetalation of Organometallic Monolayer Sheets

Methods to exchange integral parts of monolayer sheets without changing the overall structure would be of great interest in material science. One method to do this is site-to-site transmetalation within metal-organic sheets. A recent approach demonstrated transmetalation within substrate supported sheets at random positions as well as at predetermined patterns defined by photolithography. It is shown that Raman microscopy can be used to follow the transmetalation reaction in real time and to visualize patterns in two-dimensional copolymers. In the last part of this chapter, first TERS measurements on these metal-organic sheets are presented.

Parts of this chapter are adapted and reproduced with permission from::
Z. Zheng, L. Opilik, F. Schiffmann, W. Liu, G. Bergamini, P. Ceroni, L.-T. Lee, A. Schütz, J. Sakamoto, R. Zenobi, J. VandeVondele, A. D. Schlüter: 'Synthesis of Two-Dimensional Analogues of Copolymers by Site-to-Site Transmetalation of Organometallic Monolayer Sheets', *J. Am. Chem. Soc.* **2014**, *136*, pp. 6103–6110.
doi: 10.1021/ja501849y

10.1 Experimental

Raman spectra were acquired on two different instruments. Spectra of sheets on SiO_2/Si substrates were acquired on a NTEGRA Spectra Upright Instrument (NT-MDT, Zelenograd, Russia) using a 532 nm diode pumped solid-state laser (MLL532, CNILaser, Changchun, China) for Raman excitation. Spectra of sheets prepared on borosilicate glass were acquired on an inVia Raman spectrometer (Renishaw, Gloucestershire, UK) connected to an inverted microscope (IX70, Olympus, Tokyo, Japan). A 532 nm diode pumped solid-state laser (Ventus, Laser Quantum, Germany) was focused on the sample surface using an oil-immersion objective (PlanApo, 60x, NA 1.4, Olympus, Tokyo, Japan) and the back-scattered light was collected with the same objective. The instrument is equipped with a piezo tip/tilt-mirror (S-334, Physik Instrumente, Karlsruhe, Germany) for beam steering. To reduce the risk of sample decomposition, the spectra shown were acquired while scanning the excitation laser across an area of 32x32 μm^2 with approx. 10 s/frame. The peak area plotted in Figure 10.3 was determined by fitting a Lorentzian to the peak in every spectrum of the time series.

10.2 Results and Discussion

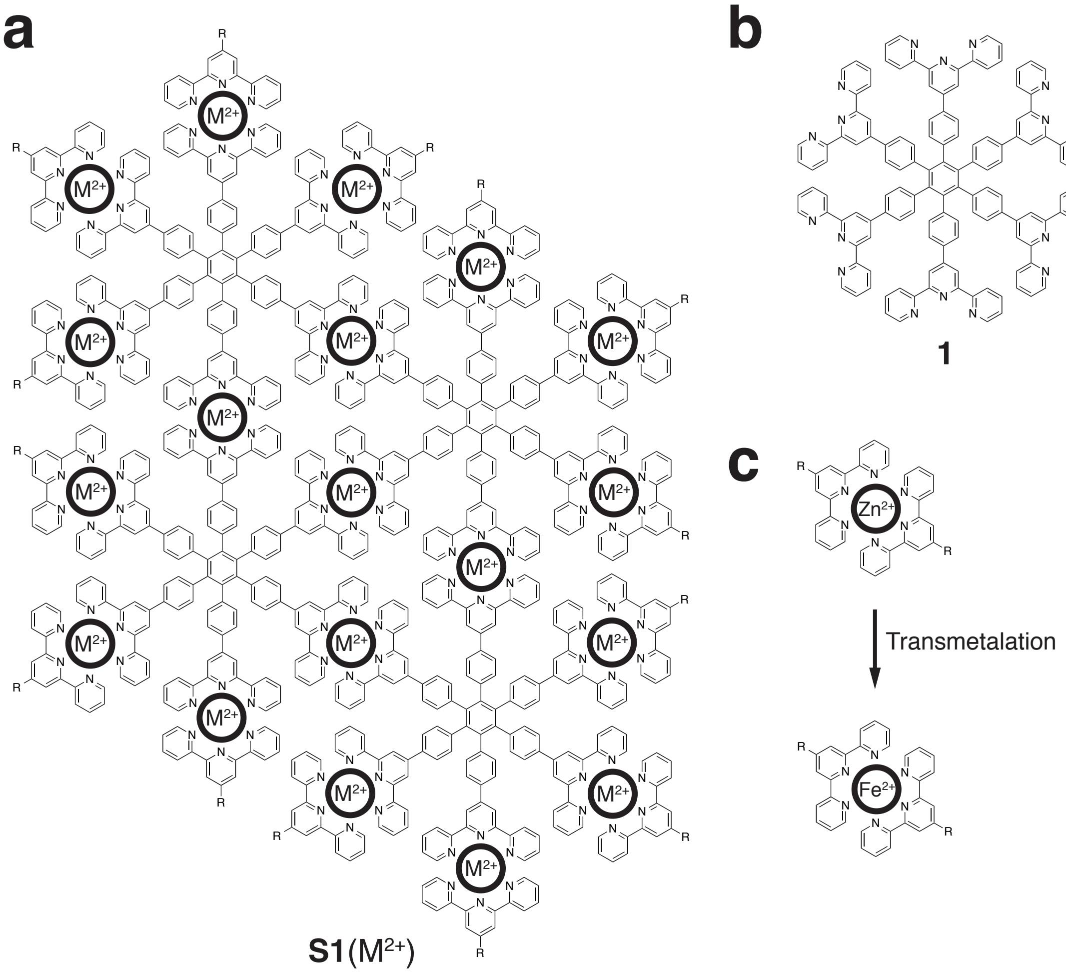

Figure 10.1: Idealized chemical structure of the metal-organic sheets **S1**(M^{2+}) (a). The hexafunctional terpyridine monomers **1** (b) are connected by the transition metal ions M^{2+} (Zn^{2+} or Fe^{2+}). Two coordinated terpyridines are probably orthogonal to each other. During transmetalation the metal ion is exchanged from Zn^{2+} to Fe^{2+} (c).

Figure 10.1a shows the idealized chemical structure of the organometallic monolayer sheets comprised of a hexafunctional terpyridine monomer (see Figure 10.1b) interconnected by transition metal ions. Transmetalation of Zn^{2+} by Fe^{2+} (see Figure 10.1c) is possible while the sheet is supported on borosilicate glass or 285 nm SiO_2/Si.[244] Figure 10.2 compares the Raman spectra in transmission mode of **S1**(Zn^{2+}) and the proposed product sheet **S1**(Fe^{2+}). Raman and resonance Raman spectroscopy of bis-tpy complexes (metal ions: Fe^{2+}, Ru^{2+}, Zn^{2+}) is the topic of various publications.[245–251] The Fe^{2+} and Ru^{2+} complexes show metal-to-ligand charge transfer (MLCT) transitions in the visible part of the electromagnetic spectrum. When the Raman excitation wavelength (532 nm in the present case) is in the same range as these electronic transitions, Franck-Condon active vibrations become enhanced (resonance Raman effect).[252] In contrast, Zn^{2+} has d^{10} configuration (full electron shell) and does not show MLCT transitions.[248]

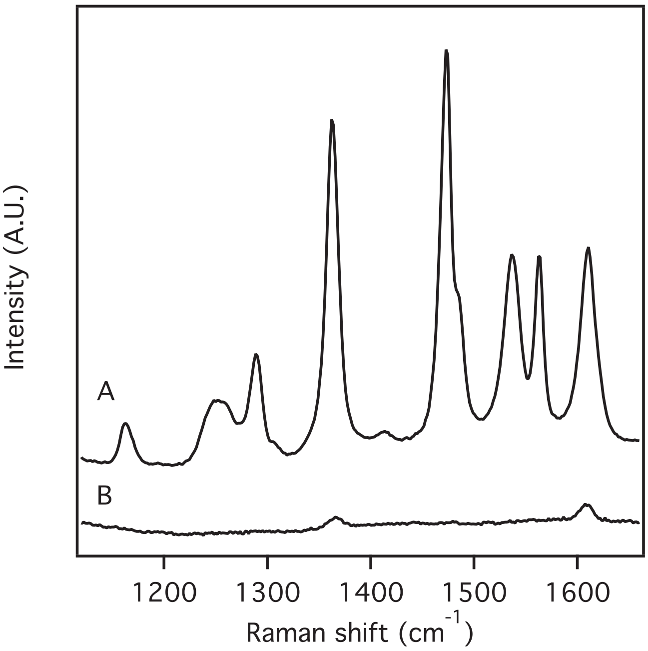

Figure 10.2: Raman spectra of the starting (B) and product sheet (A) on thin borosilicate glass slides in transmission mode.

The aromatic in-plane vibration at 1610 cm^{-1} and the tpy ring breathing mode ν(phenyl-tpy) at 1367 cm^{-1} are the only Raman bands observed for **S1**(Zn^{2+}). The resonance Raman spectrum of the **S1**(Fe^{2+}) additionally shows strong bands at 1473 and 1163 cm^{-1} (assigned to tpy vibrations) as well as at 1532 and 1363 cm^{-1} (assigned to vibrations, with significant involvement of the benzene ring attached to the 4'-position of the tpy ligand). This indicates delocalization of the MLCT excited state over the connected ring. The ν(phenyl-tpy) mode is slightly shifted to 1363 cm^{-1}. Since this mode involves strong phenyl-tpy bond stretching, its position can be shifted depending on the binding situation to the metal center.[248] More detailed band assignments for similar resonant and nonresonant Raman spectra of Ru(II) and Zn(II) complexes can be found in the literature.[246,248,250] Moreover, a series of Raman spectra were acquired after placing a drop of freshly prepared Fe salt solution (approximately 0.05 mL, 60'000-fold molar excess) on a sheet **S1**(Zn^{2+}) on glass with an acquisition time of 10 s per spectrum. The intensities of the Raman bands reached their maximum at approximately 30 min. Figure 10.3 shows the time-dependent evolution of the transmetalation based on the peak area of the ν(phenyl-tpy) mode. These measurements are in good agreement with XPS measurements after different times of exposure.[244] Because Raman microscopy allows on-line monitoring of the exchange, the experiment can be stopped at any reaction conversion, which opens the door to study conversion-dependent properties of the nanosheets. Note that this cannot be realized with sheets synthesis at an air-water interface.

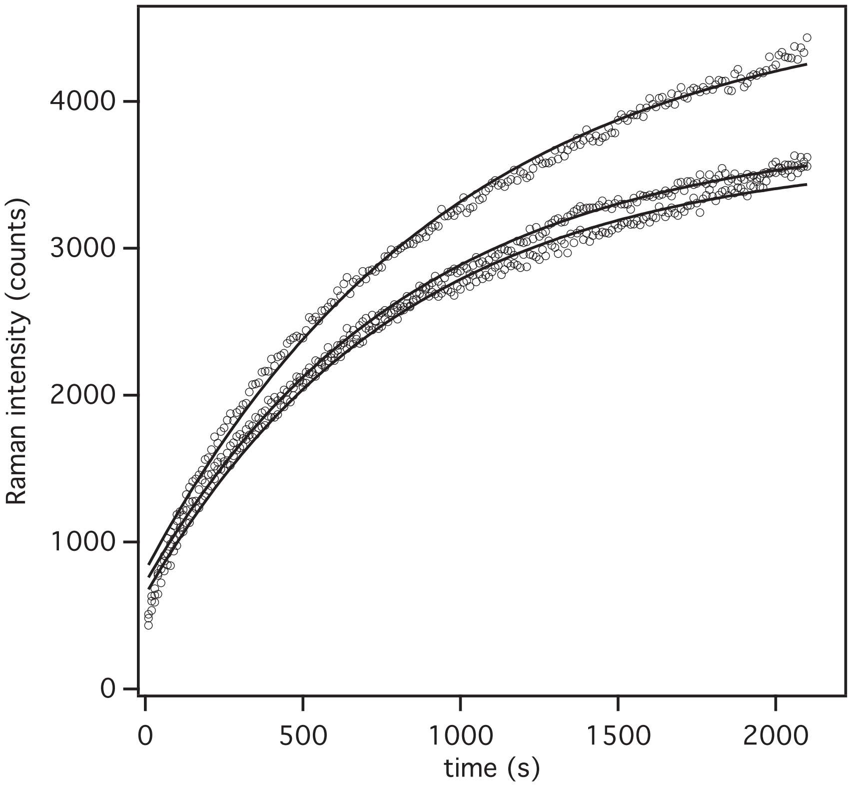

Figure 10.3: Change of the peak area of the ν(phenyl-tpy) Raman mode during surface transmetalation. The same measurement was repeated three times on different samples to demonstrate the reproducibility of the measurement. An exponential fit (solid line) is shown with each series of data points (circles).

The above described transmetalation was also used to make a two-dimensional analogue of a block copolymer (2DBP). This was accomplished by first generating a pattern of photoresist on a **S1**(Zn^{2+}) sheet and subsequent exposure to a Fe salt solution. Dissolving the photoresist then exposes the patterned 2DPB. The chemical compositions of a stripe patterned 2DPB was confirmed by a Raman imaging experiment. The Raman spectra of the **S1**(Zn^{2+}) and **S1**(Fe^{2+}) resemble the ones of **S1**(Zn^{2+}) and **S1**(Fe^{2+}) prepared at the air-water interface, validating the netpoint assignments. The Raman intensity image for the band at 1473 cm^{-1} in Figure 10.4 was obtained when scanning the excitation laser across one of the stripes.

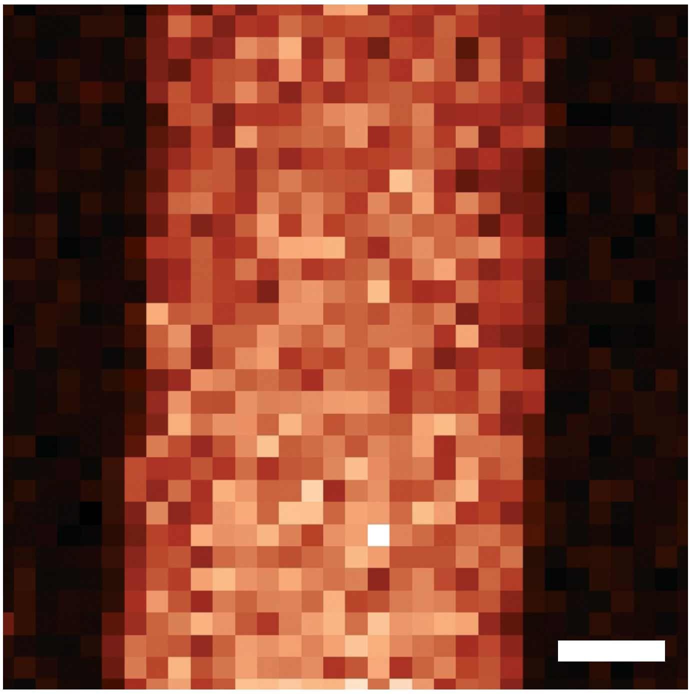

Figure 10.4: Raman microscopy image across a stripe of a 2DBP on 285 nm SiO_2/Si showing the intensity of the Raman band at 1473 cm^{-1}. The scale bare indicates 5 µm.

Because individual **S1**(Fe^{2+}) sheets are easily detected with confocal Raman spectroscopy, these layers would qualify as standard sample to determine TERS contrast factors. Moreover, monitoring of the transmetalation described above by means of TERS would allow one to investigate local kinetics of the metal ion exchange. Therefore, AFM-TERS measurements with silver coated AFM tips were performed on individual layers of **S1**(Fe^{2+}) on glass. Unfortunately, only very low contrast was obtained so far (see Figure 10.5). A reason for this could be the intrinsic property of most two-dimensional materials, namely, that characteristic chemical bonds (and therefore the corresponding vibrational modes) are in-plane and only weakly enhanced by the TERS tip. This was recently hypothesized by Stadler et al. for the case of graphene, where the strongest TERS enhancement was observed for deviations from the two-dimensional structure.[13]

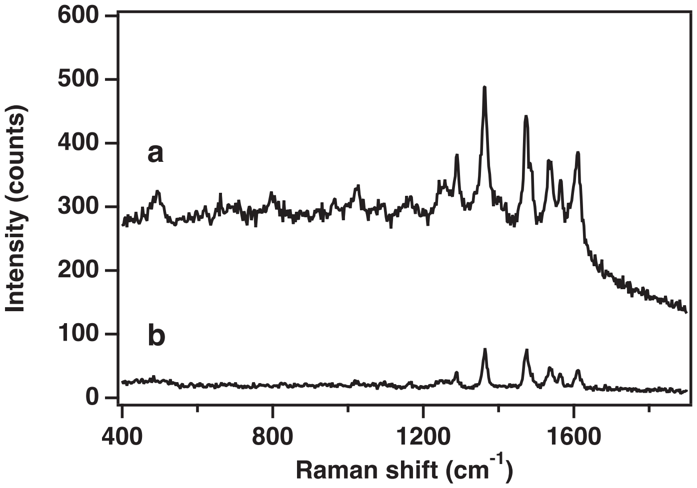

Figure 10.5: Raman spectrum of an S1(Fe^{2+}) layer on glass with an AFM-TERS tip in contact (a) and retracted (b). Both spectra were collected with an acquisition time of 5 s and with a 532 nm laser at a power of 230 µW.

Chapter 11

Summary and Outlook

11.1 Summary

In a first part, this thesis approaches one of the main limitations of tip-enhanced Raman spectroscopy, which is the production of robust, long-term stable and highly enhancing tips. With the focus on full-metal silver tips, methods for restoration, storage and protection were presented. Successful electrochemical restoration of the enhancement of atmospherically corroded TERS tips and long-term storage (≥54 days) of tips under atmospheric conditions were presented. These methods allow one to re-use particularly good tips and to safely ship tips to other researchers who do not have the possibility to prepare TERS active tips themselves. Other approaches, where thin protective coatings were applied to TERS tips, not only aimed at effective prevention from atmospheric corrosion during storage, but also at higher chemical and mechanical stability during imaging experiments. Effective protection from analyte/contaminant adsorption and atmospheric corrosion by means of a thin protective coating was demonstrated experimentally. This approach involved self-assembly of a linker molecule, allowing subsequent growth of a thin, uniform and robust amorphous silica layer on the tip surface.

In a second part of this thesis, TERS imaging experiments on Langmuir-Blodgett monolayers of amphiphilic molecules were presented. The main difficulty with these samples was the fact that the molecules used are intrinsically weak Raman scatterers and for a monolayer coverage can only be detected with highly enhancing TERS tips. Moreover, these molecules are particularly prone to decomposition under laser irradiation and care had to taken that the TERS measurement did not change/influence the sample under investigation. In a first study, TERS was used for the imaging of segregated lipid monolayers. A clear spectroscopic differentiation of the two mixed phospholipids was not possible because of their very similar chemical structure. To increase the specificity, a common Raman label (deuterium) was therefore used, which leads to a characteristic shift of the CH vibrational modes if hydrogen is substituted by deuterium. With this approach, it was possible to study the aforementioned segregated binary lipid mixture on the nanoscale. For the first time, subsequent TERS maps on the same sample region proved the non-invasiveness of the method. Moreover, by evaluating the peak ratio of the two compounds, common TERS imaging artefacts (e.g., sudden changes in overall Raman intensity from one line to the next) could beavoided. A preliminary study on ternary lipid mixtures demonstrated that TERS imaging can also be used to locate deuterated cholesterol incorporated in lipid monolayers.

A very different task was then tackled, namely the spectroscopic analysis of the formation of covalent monolayers and two-dimensional coordination polymers. Recent approaches towards the controlled synthesis of highly structured two dimensional materials came with new challenges for analytical scientists. Structural information needs to be combined with high spatial resolution preferably on a single one-atom/one-molecule thin layer. In this thesis, high-quality Raman spectra of single/few layers of a novel covalent monolayer sheet were presented. It was demonstrated that, compared to confocal Raman microscopy, TERS is a less invasive analytical method for the analysis of the radiation-sensitive monomer monolayers because of the significantly lower laser power and acquisition time necessary. It was shown that the high-quality spectroscopic data obtained by TERS imaging can give valuable insights into the mechanisms involved in the formation of these novel material.

11.2 Outlook

Overall, TERS has matured since its first demonstration in 2000. However, the technique still requires dedicated laboratories and highly trained users, and is still far away from being a routine analytical technique. Nonetheless, TERS is already a valuable high resolution spectroscopic imaging tool for the analysis of molecular monolayers and heterogeneous surfaces. Unfortunately, at the moment there is no method which fills the wide gap between the diffraction limited resolution achieved with confocal Raman microscopy and the near-field optical resolution achieved with tip-enhanced Raman spectroscopy. A smart solution using a ‘continuous zoom’ could probably fill this gap. But even if this would be possible, the sequential nature of both methods limits their use for large-scale imaging. Widefield Raman spectroscopy has a lot of potential for strong Raman scatterers (as, e.g., graphene) and serves as a high-throughput alternative for confocal Raman microscopy.[253] However, if the signal enhancement and high spatial resolution of TERS is required, there is so far no high-throughput alternative for sequential TERS imaging with a single enhancing tip in SPM feedback with the sample surface. A first attempt to achieve sub-diffraction spatial resolution ($\geq$100 nm) without scanning was based on a SERS imaging array at the end of a coherent optical fiber bundle.[254] Such an approach, however, is only applicable to very flat sample surfaces. Developing new TERS modifications with the aim of high-throughput imaging with sub-diffraction spatial resolution of large sample areas would be of great value for, e.g., quality control of semiconductor surfaces.

Other important task for the future include attempts to bring TERS more to a metrological level. This means, for example, the introduction of a suitable standard test sample for the evaluation of TERS tips and instruments. Samples with predefined nanometer-sized patterns that can be prepared reproducibly and within clear specifications allow better lab-to-lab comparability. The first attempt in this direction presented in this thesis should be further developed. Such a sample should, e.g., be compatible with any of the existing TERS configurations. Moreover, such a standard sample should be robust enough to be reusable. This would reduce costs and allow to test the repeatability of high resolution imaging experiments. The used of inorganic materials instead of molecular monolayers would, e.g., be a more stable alternative. However, testing the achievable spatial resolution with a particular TERS tip is not enough. Determining the optical response of each individual tip would be beneficial for better tip quality control.[162] This would allow to adjust the tip preparation procedure or the used excitation wavelength for maximum near-field coupling.

Most results shown in this thesis were acquired with TERS tips in STM feedback with a gold substrate. This approach has the advantage of particularly high field enhancement without requiring direct contact between tip and sample surface, which makes it particularly useful for TERS imaging. However, this configuration is restricted to conductive samples and thin molecular layers that can be deposited on a conductive substrate (preferably gold). Moreover, the thin dielectric layers applied for tip protection in this thesis can have an adverse effect on the tunnelling current and lead to unstable feedback or tip crashes. Therefore, the approaches towards top-illumination AFM-TERS presented in this thesis, should be further developed. This could allow high-resolution Raman spectroscopic imaging of opaque non-conductive samples, including, for example, CVD grown WS_2 sheets (or nanotubes) directly on the oxide surface (e.g., alumina) where they were prepared.[255] Simultaneous near-field analysis of the room-temperature photoluminescence characteristic of WS_2 sheets would be of particular relevance. The unique electronic and optical properties of WS_2 make it a good candidate for, e.g., photovoltaic devices[256] and anode materials for Li-Ion batteries.[257] Other non-conductive and opaque samples, where top-illumination AFM-TERS imaging could give valuable insights are inorganic solar cell materials. To reveal the crystalline forms of commonly used absorber materials on the nanoscale could give valuable insights that would allow to design new absorber materials with particularly high light gathering characteristics.[258]

The full-metal TERS tips presented in this thesis can be used in STM and AFM feedback using an in-house modified tip holder. This would allow to study differences in TERS spectra caused by the used feedback mechanism (e.g., effects caused by the tunnelling of electrons through the tip-sample gap in STM feedback). Combination of shear-force AFM and STM feedback control was used recently for precise position control over a wide distance range to study the effect of quantum coupling on the observed field enhancement.[259]

An urgently needed development is the possibility to perform TERS imaging experiments in a liquid environment. Combinations of atomic force microscopy and Raman microscopes which are fully compatible with submerged samples are available nowadays. The main limitation is again the TERS tip. Particularly when working in buffer solution, protection of the metallic surface of the tip agains chemical degradation and contamination is challenging. Different protective coatings for TERS tips should be tested for their ability to withstand submersion in an aqueous solution. The possibility to routinely perform TERS imaging in water or any other liquid would allow to investigate biological membranes in a more native environment and various catalytic processes could be studied on the nanoscale. Moreover, TERS could be used to study dynamic processes (e.g., single-molecule dynamics, chemical reactions) on the nanoscale by parking the tip at a desired position on the sample surface and recording time series of Raman spectra. The main limitation of this approach is probably the achievable temporal resolution, which is limited by the intrinsic weakness of Raman scattering. Nevertheless, tip-enhanced Raman spectra from resonant molecules using picosecond excitation were recently presented.[260] With the possibility to obtain spectra with high temporal resolution, it would also be of great interest to implement TERS with high-speed AFM instruments,[261] which would allow video rate spectroscopic analysis of dynamic processes on nanometer-sized areas (e.g., membrane-mediated protein-protein interactions). A smart interconnection of spectral acquisition and the cantilever tapping amplitude would be required for this approach.

References

1. G. B. Airy, “On the diffraction of an object-glass with circular aperture”, *Trans. Camb. Phil. Soc.* **1835**, *5*, 283–291.
2. E. Abbe, “Beiträge zur Theorie des Mikroskops und der mikroskopischen Wahrnehmung”, *Archiv f. mikrosk. Anatomie* **1873**, *9*, 413–418.
3. H. Helmholtz, “Die theoretische Grenze für die Leistungsfähigkeit der Mikroskope”, *Pogg. Ann. Jubelband* **1874**, 557–584.
4. L. Rayleigh, “On the manufacture and theory of diffraction-gratings”, *Phil. Mag.* **1874**, *47*, 81–93.
5. S. W. Hell, “Far-field optical nanoscopy.”, *Science* **2007**, *316*, 1153–1158.
6. W. Heisenberg, “Über den anschaulichen Inhalt der quantentheoretischen Kinematik und Mechanik”, *Z. Phys.* **1927**, *43*, 172–198.
7. L. Novotny, B. Hecht, *Principles of nano-optics*, Cambridge University Press, Cambridge, UK, 1st edition, **2006**.
8. A. Hartschuh, “Tip-enhanced near-field optical microscopy”, *Angew. Chem. Int. Ed.* **2008**, *47*, 8178–8191.
9. R. M. Stöckle, Y. D. Suh, V. Deckert, R. Zenobi, “Nanoscale chemical analysis by tip-enhanced Raman spectroscopy”, *Chem. Phys. Lett.* **2000**, *318*, 131–136.
10. M. S. Anderson, “Locally enhanced Raman spectroscopy with an atomic force microscope”, *Appl. Phys. Lett.* **2000**, *76*, 3130–3132.
11. N. Hayazawa, Y. Inouye, Z. Sekkat, S. Kawata, “Metallized tip amplification of near-field Raman scattering”, *Opt. Commun.* **2000**, *183*, 333–336.
12. L. G. Cancado, A. Hartschuh, L. Novotny, “Tip-enhanced Raman spectroscopy of carbon nanotubes”, *J. Raman Spectrosc.* **2009**, *40*, 1420–1426.
13. J. Stadler, T. Schmid, R. Zenobi, “Nanoscale chemical imaging of single-layer graphene”, *ACS Nano* **2011**, *5*, 8442–8448.
14. M. D. Sonntag, J. M. Klingsporn, L. K. Garibay, J. M. Roberts, J. A. Dieringer, T. Seideman, K. A. Scheidt, L. Jensen, G. C. Schatz, R. P. Van Duyne, “Single-molecule tip-enhanced Raman spectroscopy”, *J. Phys. Chem. C* **2012**, *116*, 478–483.
15. R. Zhang, Y. Zhang, Z. C. Dong, S. Jiang, C. Zhang, L. G. Chen, L. Zhang, Y. Liao, J. Aizpurua, Y. Luo, J. L. Yang, J. G. Hou, “Chemical mapping of a single molecule by plasmon-enhanced Raman scattering.”, *Nature* **2013**, *498*, 82–86.
16. M. Minsky, “Microscopy apparatus”, **1961**, *US Patent No. 3013467*.
17. O. Shimomura, F. H. Johnson, Y. Saiga, “Extraction, purification and properties of aequorin, a bioluminescent protein from the luminous hydromedusan, *Aequorea.*”, *J. Cell. Comp. Physio.* **1962**, *59*, 223–239.
18. M. Chalfie, Y. Tu, G. Euskirchen, W. W. Ward, D. C. Prasher, “Green fluorescent protein as a marker for gene expression”, *Science* **1994**, *263*, 802–805.
19. J. Juhasz, J. H. Davis, F. J. Sharom, “Fluorescent probe partitioning in giant unilamellar vesicles of ’lipid raft’ mixtures”, *Biochem. J.* **2010**, *430*, 415–423.

20. T. Chernenko, R. R. Sawant, M. Miljkovic, L. Quintero, M. Diem, V. Torchilin, “Raman microscopy for noninvasive imaging of pharmaceutical nanocarriers: intracellular distribution of cationic liposomes of different composition”, *Mol. Pharmaceutics* **2012**, *9*, 930–936.
21. N. L. Garrett, A. Lalatsa, D. Begley, L. Mihoreanu, I. F. Uchegbu, A. G. Schätzlein, J. Moger, “Label-free imaging of polymeric nanomedicines using coherent anti-stokes Raman scattering microscopy”, *J. Raman Spectrosc.* **2012**, *43*, 681–688.
22. M. Li, D. P. Canniffe, P. J. Jackson, P. A. Davison, S. FitzGerald, M. J. Dickman, J. G. Burgess, C. N. Hunter, W. E. Huang, “Rapid resonance Raman microspectroscopy to probe carbon dioxide fixation by single cells in microbial communities”, *ISME J.* **2012**, *6*, 875–885.
23. H. Yamakoshi, K. Dodo, M. Okada, J. Ando, A. Palonpon, K. Fujita, S. Kawata, M. Sodeoka, “Imaging of EdU, an alkyne-tagged cell proliferation probe, by Raman microscopy”, *J. Am. Chem. Soc.* **2011**, *133*, 6102–6105.
24. X. Zhang, M. B. J. Roeffaers, S. Basu, J. R. Daniele, D. Fu, C. W. Freudiger, G. R. Holtom, X. S. Xie, “Label-free live-cell imaging of nucleic acids using stimulated Raman scattering microscopy.”, *Chem. Phys. Chem.* **2012**, *13*, 1054–1059.
25. C. V. Raman, K. S. Krishnan, “A new type of secondary radiation”, *Nature* **1928**, *121*, 501–502.
26. P. Larkin, *Infrared and Raman spectroscopy: principles and spectral interpretation*, Elsevier, Waltham, MA, **2011**.
27. J. R. Ferraro, K. Nakamoto, C. W. Brown, *Introductory Raman spectroscopy*, Academic Press, Waltham, MA, 2nd edition, **2002**.
28. E. Smith, G. Dent, *Modern Raman spectroscopy: a practical approach*, Wiley, Chichester, UK, **2005**.
29. D. A. Long, *The Raman effect: a unified treatment of the theory of Raman scattering by molecules*, Wiley, Chichester, UK, 1st edition, **2002**.
30. S. D. Rassat, E. J. Davis, “Temperature measurement of single levitated microparticles using Stokes/anti-Stokes Raman intensity ratios”, *Appl. Spectrosc.* **1994**, *48*, 1498–1505.
31. E. Hecht, *Optics*, Pearson, Harlow, UK, 4th edition, **2014**.
32. R. W. Boyd, *Nonlinear optics*, Academic Press, 3rd edition, **2008**.
33. E. J. Woodbury, W. K. Ng, “Ruby laser operation in the near IR”, *Proc. IRE* **1962**, *50*, 2367.
34. P. D. Maker, R. W. Terhune, “Study of optical effects due to an induced polarization third order in electric field strength”, *Phys. Rev.* **1965**, *137*, A801–A818.
35. A. Zumbusch, G. R. Holtom, X. S. Xie, “Three-dimensional vibrational imaging by coherent anti-Stokes Raman scattering”, *Phys. Rev. Lett.* **1999**, *82*, 4142–4145.
36. W. Min, C. W. Freudiger, S. Lu, X. S. Xie, “Coherent nonlinear optical imaging: beyond fluorescence microscopy”, *Annu. Rev. Phys. Chem.* **2011**, *62*, 507–530.
37. C. L. Evans, X. S. Xie, “Coherent anti-Stokes Raman scattering microscopy: chemical imaging for biology and medicine”, *Annu. Rev. Anal. Chem.* **2008**, *1*, 883–909.
38. A. Silve, N. Dorval, T. Schmid, L. M. Mir, B. Attal-Tretout, “A wide-field arrangement for single-shot CARS imaging of living cells”, *J. Raman Spectrosc.* **2012**, *43*, 644–650.

39. H. Segawa, M. Okuno, H. Kano, P. Leproux, V. Couderc, H.-o. Hamaguchi, “Label-free tetra-modal molecular imaging of living cells with CARS, SHG, THG and TSFG (coherent anti-Stokes Raman scattering, second harmonic generation, third harmonic generation and third-order sum frequency generation)”, *Opt. Express* **2012**, *20*, 9551–9557.
40. C. W. Freudiger, W. Min, G. R. Holtom, B. Xu, M. Dantus, X. S. Xie, “Highly specific label-free molecular imaging with spectrally tailored excitation-stimulated Raman scattering (STE-SRS) microscopy”, *Nat. Photonics* **2011**, *5*, 103–109.
41. D. Fu, F.-K. Lu, X. Zhang, C. Freudiger, D. R. Pernik, G. Holtom, X. S. Xie, “Quantitative chemical imaging with multiplex stimulated Raman scattering microscopy”, *J. Am. Chem. Soc.* **2012**, *134*, 3623–3626.
42. D. L. Jeanmaire, R. P. Van Duyne, “Surface Raman spectroelectrochemistry: part I. heterocyclic, aromatic, and aliphatic amines adsorbed on the anodized silver electrode”, *J. Electroanal. Chem.* **1977**, *84*, 1–20.
43. M. Fleischmann, P. J. Hendra, A. J. McQuillan, “Raman spectra of pyridine adsorbed at a silver electrode”, *Chem. Phys. Lett.* **1974**, *26*, 163–166.
44. J. Wessel, “Surface-enhanced optical microscopy”, *J. Opt. Soc. Am. B* **1985**, *2*, 1538–1541.
45. P. L. Stiles, J. A. Dieringer, N. C. Shah, R. P. Van Duyne, “Surface-enhanced Raman spectroscopy”, *Annu. Rev. Anal. Chem.* **2008**, *1*, 601–626.
46. E. C. Le Ru, P. G. Etchegoin, *Principles of surface-enhanced Raman spectroscopy and related plasmonic effects*, Elsevier, Amsterdam, 1st edition, **2009**.
47. *Tip Enhancement*, (Eds.: S. Kawata, V. M. Shalaev), Elsevier, 1st edition, **2007**.
48. M. Moskovits, “Surface-enhanced Raman spectroscopy: a brief retrospective”, *J. Raman Spectrosc.* **2005**, *36*, 485–496.
49. A. Campion, P. Kambhampati, “Surface-enhanced Raman scattering”, *Chem. Soc. Rev.* **1998**, *27*, 241–250.
50. *Raman microscopy: developments and applications*, (Eds.: G. Turrell, J. Corset), Elsevier, London, **1996**.
51. S. Schlücker, M. D. Schaeberle, S. W. Huffman, I. W. Levin, “Raman microspectroscopy: a comparison of point, line, and wide-field imaging methodologies”, *Anal. Chem.* **2003**, *75*, 4312–4318.
52. J. Zhao, “Raman Spectroscope”, **2006**, *US Patent No. 7102746.*
53. R. Bennett, J. C. C. Day, G. M. Meaden, “Spectroscopy Apparatus and Method”, **2006**, *US Patent No. 7139071.*
54. N. J. Everall, “Confocal Raman microscopy: performance, pitfalls, and best practice.”, *Appl. Spectrosc.* **2009**, *63*, 245A–262A.
55. E. H. Synge, “XXXVII. A suggested method for extending microscopic resolution into the ultra-microscopic region”, *Philosoph. Mag. Ser.* **1928**, *6*, 356–362.
56. D. W. Pohl, W. Denk, M. Lanz, “Optical stethoscopy: image recording with resolution $\lambda/20$”, *Appl. Phys. Lett.* **1984**, *44*, 651–653.
57. A. Lewis, M. Isaacson, A. Harootunian, A. Muray, “Development of a 500 angstrom spatial resolution light microscope: I. light is efficiently transmitted through $\lambda/16$ diameter apertures”, *Ultramicroscopy* **1984**, *13*, 227–231.

58. L. Neumann, Y. Pang, A. Houyou, M. L. Juan, R. Gordon, N. F. van Hulst, "Extraordinary optical transmission brightens near-field fiber probe", *Nano Lett.* **2011**, *11*, 355–360.
59. T.-a. Yano, P. Verma, Y. Saito, T. Ichimura, S. Kawata, "Pressure-assisted tip-enhanced Raman imaging at a resolution of a few nanometres", *Nat. Photonics* **2009**, *3*, 473–477.
60. S. Berweger, J. M. Atkin, R. L. Olmon, M. B. Raschke, "Adiabatic tip-plasmon focusing for nano-Raman spectroscopy", *J. Phys. Chem. Lett.* **2010**, *1*, 3427–3432.
61. F. Keilmann, R. Hillenbrand, "Near-field microscopy by elastic light scattering from a tip", *Phil. Trans. R. Soc. Lond. A* **2004**, *362*, 787–806.
62. M. B. Raschke, C. Lienau, "Apertureless near-field optical microscopy: tip–sample coupling in elastic light scattering", *Appl. Phys. Lett.* **2003**, *83*, 5089–5091.
63. F. De Angelis, G. Das, P. Candeloro, M. Patrini, M. Galli, A. Bek, M. Lazzarino, I. Maksymov, C. Liberale, L. C. Andreani, E. Di Fabrizio, "Nanoscale chemical mapping using three-dimensional adiabatic compression of surface plasmon polaritons", *Nat. Nanotechnol.* **2010**, *5*, 67–72.
64. P. Drude, "Zur Elektronentheorie der Metalle, I. Teil", *Ann. Phys.* **1900**, *1*, 566–613.
65. P. Drude, "Zur Elektronentheorie der Metalle, II. Teil", *Ann. Phys.* **1900**, *3*, 369–402.
66. E. D. Palik, *Handbook of optical constants of solids III*, Academic Press, New York, **1998**.
67. C. F. Bohren, D. R. Huffman, *Absoption and scattering of light by small particles*, Wiley, New York, **1983**.
68. J. Stadler, T. Schmid, R. Zenobi, "Developments in and practical guidelines for tip-enhanced Raman spectroscopy", *Nanoscale* **2012**, *4*, 1856–1870.
69. Z. Yang, Q. Li, Y. Fang, M. Sun, "Deep ultraviolet tip-enhanced Raman scattering", *Chem. Commun.* **2011**, *47*, 9131–9133.
70. A. Taguchi, N. Hayazawa, K. Furusawa, H. Ishitobi, S. Kawata, "Deep-UV tip-enhanced Raman scattering", *J. Raman Spectrosc.* **2009**, *40*, 1324–1330.
71. B.-S. Yeo, T. Schmid, W. Zhang, R. Zenobi, "Towards rapid nanoscale chemical analysis using tip-enhanced Raman spectroscopy with Ag-coated dielectric tips", *Anal. Bioanal. Chem.* **2007**, *387*, 2655–2662.
72. N. Hayazawa, T.-a. Yano, S. Kawata, "Highly reproducible tip-enhanced Raman scattering using an oxidized and metallized silicon cantilever tip as a tool for everyone", *J. Raman Spectrosc.* **2012**, *43*, 1177–1182.
73. M. Fleischer, A. Weber-Bargioni, M. V. P. Altoe, A. M. Schwartzberg, P. J. Schuck, S. Cabrini, D. P. Kern, "Gold nanocone near-field scanning optical microscopy probes", *ACS Nano* **2011**, *5*, 2570–2579.
74. J. A. Schuller, E. S. Barnard, W. Cai, Y. C. Jun, J. S. White, M. L. Brongersma, "Plasmonics for extreme light concentration and manipulation", *Nat. Mater.* **2010**, *9*, 193–204.
75. A. Ermushev, B. V. Mchedlishvili, V. Oleinikov, A. Petukhov, "Surface enhancement of local optical fields and the lightning-rod effect", *Quantum Electron.* **1993**, *23*, 435–440.
76. R. Esteban, R. Vogelgesang, K. Kern, "Simulation of optical near and far fields of dielectric apertureless scanning probes", *Nanotechnology* **2006**, *17*, 475–482.
77. L. Novotny, N. van Hulst, "Antennas for light", *Nat. Mater.* **2011**, *5*, 83–90.

78. N. Marquestaut, D. Talaga, L. Servant, P. Yang, P. Pauzauskie, F. Lagugné-Labarthet, "Imaging of single GaN nanowires by tip-enhanced Raman spectroscopy", *J. Raman Spectrosc.* **2009**, *40*, 1441–1445.
79. Y. Ogawa, T. Toizumi, F. Minami, A. V. Baranov, "Nanometer-scale mapping of the strain and Ge content of Ge/Si quantum dots using enhanced Raman scattering by the tip of an atomic force microscope", *Phys. Rev. B* **2011**, *83*, 081302.
80. B. R. Wood, E. Bailo, M. A. Khiavi, L. Tilley, S. Deed, T. Deckert-Gaudig, D. McNaughton, V. Deckert, "Tip-enhanced Raman scattering (TERS) from hemozoin crystals within a sectioned erythrocyte", *Nano Lett.* **2011**, *11*, 1868–1873.
81. P. Hermann, M. Hecker, D. Chumakov, M. Weisheit, J. Rinderknecht, A. Shelaev, P. Dorozhkin, L. M. Eng, "Imaging and strain analysis of nano-scale SiGe structures by tip-enhanced Raman spectroscopy", *Ultramicroscopy* **2011**, *111*, 1630–1635.
82. N. Anderson, A. Hartschuh, L. Novotny, "Chirality changes in carbon nanotubes studied with near-field Raman spectroscopy", *Nano Lett.* **2007**, *7*, 577–582.
83. C. Williams, D. Roy, "Fabrication of gold tips suitable for tip-enhanced Raman spectroscopy", *J. Vac. Sci. Technol. B* **2008**, *26*, 1761–1764.
84. S. S. Kharintsev, G. G. Hoffmann, P. S. Dorozhkin, G. d. With, J. Loos, "Atomic force and shear force based tip-enhanced Raman spectroscopy and imaging", *Nanotechnology* **2007**, *18*, 315502.
85. T.-a. Yano, T. Ichimura, A. Taguchi, N. Hayazawa, P. Verma, Y. Inouye, S. Kawata, "Confinement of enhanced field investigated by tip-sample gap regulation in tapping-mode tip-enhanced Raman microscopy", *Appl. Phys. Lett.* **2007**, *91*, 121101.
86. L. G. Cancado, A. Jorio, A. Ismach, E. Joselevich, A. Hartschuh, L. Novotny, "Mechanism of near-field Raman enhancement in one-dimensional systems", *Phys. Rev. Lett.* **2009**, *103*, 186101.
87. M. Böhmler, A. Hartschuh, "Tip-enhanced near-field optical microscopy of quasi-1D nanostructures.", *Chem. Phys. Chem.* **2012**, *13*, 927–929.
88. C. C. Neacsu, S. Berweger, M. B. Raschke, "Tip-enhanced Raman imaging and nanospectroscopy: sensitivity, symmetry, and selection rules", *Nanobiotechnol.* **2007**, *3*, 172–196.
89. C. C. Neacsu, J. Dreyer, N. Behr, M. Raschke, "Scanning-probe Raman spectroscopy with single-molecule sensitivity", *Phys. Rev. B* **2006**, *73*, 193406.
90. L. Novotny, S. J. Stranick, "Near-field optical microscopy and spectroscopy with pointed probes", *Annu. Rev. Phys. Chem.* **2006**, *57*, 303–331.
91. B. Pettinger, K. Domke, D. Zhang, R. Schuster, G. Ertl, "Direct monitoring of plasmon resonances in a tip-surface gap of varying width", *Phys. Rev. B* **2007**, *76*, 113409.
92. R. Roth, N. Panoiu, M. Adams, R. Osgood, C. C. Neacsu, M. B. Raschke, "Resonant-plasmon field enhancement from asymmetrically illuminated conical metallic-probe tips", *Opt. Express* **2006**, *14*, 2921–2931.
93. B. Pettinger, K. F. Domke, D. Zhang, G. Picardi, R. Schuster, "Tip-enhanced Raman scattering: influence of the tip-surface geometry on optical resonance and enhancement", *Surf. Sci.* **2009**, *603*, 1335–1341.
94. B. Pettinger, G. Picardi, R. Schuster, G. Ertl, "Surface enhanced Raman spectroscopy: towards single molecular spectroscopy", *Electrochemistry* **2000**, *68*, 942–949.

95. M. S. Anderson, W. T. Pike, “A Raman-atomic force microscope for apertureless-near-field spectroscopy and optical trapping”, *Rev. Sci. Instrum.* **2002**, *73*, 1198–1203.
96. M. Motohashi, N. Hayazawa, A. Tarun, S. Kawata, “Depolarization effect in reflection-mode tip-enhanced Raman scattering for Raman active crystals”, *J. Appl. Phys.* **2008**, *103*, 034309.
97. W. Zhang, B. S. Yeo, T. Schmid, R. Zenobi, “Single molecule tip-enhanced Raman spectroscopy with silver tips”, *J. Phys. Chem. C* **2007**, *111*, 1733–1738.
98. D. Mehtani, N. Lee, R. D. Hartschuh, A. Kisliuk, M. D. Foster, A. P. Sokolov, J. F. Maguire, “Nano-Raman spectroscopy with side-illumination optics”, *J. Raman Spectrosc.* **2005**, *36*, 1068–1075.
99. R. Wang, J. Wang, F. Hao, M. Zhang, Q. Tian, “Tip-enhanced Raman spectroscopy with silver-coated optical fiber probe in reflection mode for investigating multiwall carbon nanotubes”, *Appl. Opt.* **2010**, *49*, 1845–1848.
100. K. F. Domke, D. Zhang, B. Pettinger, “Toward Raman fingerprints of single dye molecules at atomically smooth Au(111)”, *J. Am. Chem. Soc.* **2006**, *128*, 14721–14727.
101. G. Picardi, M. Chaigneau, R. Ossikovski, C. Licitra, G. Delapierre, “Tip enhanced Raman spectroscopy on azobenzene thiol self-assembled monolayers on Au(111)”, *J. Raman Spectrosc.* **2009**, *40*, 1407–1412.
102. B. Pettinger, B. Ren, G. Picardi, R. Schuster, G. Ertl, “Nanoscale probing of adsorbed species by tip-enhanced Raman spectroscopy”, *Phys. Rev. Lett.* **2004**, *92*, 096101.
103. W. X. Sun, Z. X. Shen, “A practical nanoscopic Raman imaging technique realized by near-field enhancement”, *Mater. Phys. Mech.* **2001**, *4*, 17–21.
104. J. Stadler, T. Schmid, R. Zenobi, “Nanoscale chemical imaging using top-illumination tip-enhanced Raman spectroscopy”, *Nano Lett.* **2010**, *10*, 4514–4520.
105. J. Steidtner, B. Pettinger, “High-resolution microscope for tip-enhanced optical processes in ultrahigh vacuum”, *Rev. Sci. Instrum.* **2007**, *78*, 103104.
106. J. Steidtner, B. Pettinger, “Tip-enhanced Raman spectroscopy and microscopy on single dye molecules with 15 nm resolution”, *Phys. Rev. Lett.* **2008**, *100*, 236101.
107. C. Stanciu, M. Sackrow, A. J. Meixner, “High NA particle- and tip-enhanced nanoscale Raman spectroscopy with a parabolic-mirror microscope.”, *J. Microsc.* **2008**, *229*, 247–253.
108. J. Stadler, B. Oswald, T. Schmid, R. Zenobi, “Characterizing unusual metal substrates for gap-mode tip-enhanced Raman spectroscopy”, *J. Raman Spectrosc.* **2013**, *44*, 227–233.
109. B. Knoll, F. Keilmann, “Enhanced dielectric contrast in scattering-type scanning near-field optical microscopy”, *Opt. Commun.* **2000**, *182*, 321–328.
110. T. Deckert-Gaudig, V. Deckert, “Ultraflat transparent gold nanoplates-ideal substrates for tip-enhanced Raman scattering experiments”, *Small* **2009**, *5*, 432–436.
111. T. Deckert-Gaudig, F. Erver, V. Deckert, “Transparent silver microcrystals: synthesis and application for nanoscale analysis”, *Langmuir* **2009**, *25*, 6032–6034.
112. B. Pettinger, G. Picardi, R. Schuster, G. Ertl, “Surface-enhanced and STM-tip-enhanced Raman spectroscopy at metal surfaces”, *Single Molecules* **2002**, *3*, 285–294.

113. B. Pettinger, P. Schambach, C. J. Villagómez, N. Scott, “Tip-enhanced Raman spectroscopy: near-fields acting on a few molecules”, *Annu. Rev. Phys. Chem.* **2012**, *63*, 17.
114. C. A. Barrios, A. V. Malkovskiy, A. M. Kisliuk, A. P. Sokolov, M. D. Foster, “Highly stable, protected plasmonic nanostructures for tip enhanced Raman spectroscopy”, *J. Phys. Chem. C* **2009**, *113*, 8158–8161.
115. V. Snitka, R. D. Rodrigues, V. Lendraitis, “Novel gold cantilever for nano-Raman spectroscopy of graphene”, *Microelectron. Eng.* **2011**, *88*, 2759–2762.
116. D. Roy, J. Wang, C. Williams, “Novel methodology for estimating the enhancement factor for tip-enhanced Raman spectroscopy”, *J. Appl. Phys.* **2009**, *105*, 013530.
117. A. Weber-Bargioni, A. Schwartzberg, M. Cornaglia, A. Ismach, J. J. Urban, Y. Pang, R. Gordon, J. Bokor, M. B. Salmeron, D. F. Ogletree, P. Ashby, S. Cabrini, P. J. Schuck, “Hyperspectral nanoscale imaging on dielectric substrates with coaxial optical antenna scan probes”, *Nano Lett.* **2011**, *11*, 1201–1207.
118. L. Opilik, T. Bauer, T. Schmid, J. Stadler, R. Zenobi, “Nanoscale chemical imaging of segregated lipid domains using tip-enhanced Raman spectroscopy”, *Phys. Chem. Chem. Phys.* **2011**, *13*, 9978–9981.
119. J. Stadler, T. Schmid, L. Opilik, P. Kuhn, P. S. Dittrich, R. Zenobi, “Tip-enhanced Raman spectroscopic imaging of patterned thiol monolayers”, *Beilstein J. Nanotechnol.* **2011**, *2*, 509–515.
120. T. Ichimura, H. Watanabe, Y. Morita, P. Verma, S. Kawata, Y. Inouye, “Temporal fluctuation of tip-enhanced Raman spectra of adenine molecules”, *J. Phys. Chem. C* **2007**, *111*, 9460–9464.
121. E. Bortchagovsky, T. Schmid, R. Zenobi, “Internal standard for tip-enhanced Raman spectroscopy”, *Appl. Phys. Lett.* **2013**, *103*, 043111.
122. E. G. Bortchagovsky, U. C. Fischer, T. Schmid, “Possibilities of functionalized probes in optical near-field microscopy”, *Phys. Scr.* **2014**, *T162*, 014005.
123. N. P. W. Pieczonka, R. F. Aroca, “Inherent complexities of trace detection by surface-enhanced Raman scattering”, *Chem. Phys. Chem.* **2005**, *6*, 2473–2484.
124. J. C. Tsang, J. E. Demuth, P. N. Sanda, J. R. Kirtley, “Enhanced Raman-scattering from carbon layers on silver”, *Chem. Phys. Lett.* **1980**, *76*, 54–57.
125. A. Kudelski, B. Pettinger, “SERS on carbon chain segments: monitoring locally surface chemistry”, *Chem. Phys. Lett.* **2000**, *321*, 356–362.
126. A. Kudelski, “Role of O_2 in inducing intensive fluctuations of surface-enhanced Raman scattering spectra”, *J. Phys. Chem. B* **2006**, *110*, 12610–12615.
127. R. L. Agapov, A. V. Malkovskiy, A. P. Sokolov, M. D. Foster, “Prolonged blinking with TERS probes”, *J. Phys. Chem. C* **2011**, *115*, 8900–8905.
128. K. F. Domke, D. Zhang, B. Pettinger, “Enhanced Raman spectroscopy: single molecules or carbon?”, *J. Phys. Chem. C* **2007**, *111*, 8611–8616.
129. N. Hayazawa, H. Watanabe, Y. Saito, S. Kawata, “Towards atomic site-selective sensitivity in tip-enhanced Raman spectroscopy”, *J. Chem. Phys.* **2006**, *125*, 244706.
130. M. D. McMahon, R. Lopez, H. M. Meyer III, L. C. Feldman, R. F. Haglund Jr., “Rapid tarnishing of silver nanoparticles in ambient laboratory air”, *Appl. Phys. B* **2005**, *80*, 915–921.
131. J. Liu, J. K. Notbohm, R. W. Carpick, K. T. Turner, “Method for characterizing nanoscale wear of atomic force microscope tips”, *ACS Nano* **2010**, *4*, 3763–3772.

132. R. L. Agapov, A. P. Sokolov, M. D. Foster, “Protecting TERS probes from degradation: extending mechanical and chemical stability”, *J. Raman Spectrosc.* **2013**, *44*, 710–716.
133. K. L. Norrod, K. L. Rowlen, “Removal of carbonaceous contamination from SERS-active silver by self-assembly of decanethiol”, *Anal. Chem.* **1998**, *70*, 4218–4221.
134. T. W. Johnson, Z. J. Lapin, R. Beams, N. C. Lindquist, S. G. Rodrigo, L. Novotny, S.-H. Oh, “Highly reproducible near-field optical imaging with sub-20-nm resolution based on template-stripped gold pyramids”, *ACS Nano* **2012**, *6*, 9168–9174.
135. *CRC Handbook of Chemistry and Physics*, (Ed.: W. M. Haynes), CRC Press, Boca Raton, FL, 95th edition, **2014**.
136. B. Ren, G. Picardi, B. Pettinger, “Preparation of gold tips suitable for tip-enhanced Raman spectroscopy and light emission by electrochemical etching”, *Rev. Sci. Instrum.* **2004**, *75*, 837–841.
137. J. Stadler, *Analytical chemistry on the nanometer scale: tip-enhanced Raman spectroscopy in the top-illumination geometry*, PhD Thesis, ETH Zurich, Switzerland, **2012**.
138. A. Kikuchi, S. Baba, A. Kinbara, “Measurement of the adhesion of silver films to oxidized silicon”, *Thin Solid Films* **1988**, *164*, 153–156.
139. R. D. Rodriguez, E. Sheremet, S. Müller, O. D. Gordan, A. Villabona, S. Schulze, M. Hietschold, D. R. T. Zahn, “Compact metal probes: a solution for atomic force microscopy based tip-enhanced Raman spectroscopy”, *Rev. Sci. Instrum.* **2012**, *83*, 123708.
140. H.-J. Butt, B. Cappella, M. Kappl, “Force measurements with the atomic force microscope: technique, interpretation and applications”, *Surf. Sci. Rep.* **2005**, *59*, 1–152.
141. E. A. Weiss, G. K. Kaufman, J. K. Kriebel, Z. Li, R. Schalek, G. M. Whitesides, “Si/SiO$_2$-templated formation of ultraflat metal surfaces on glass, polymer, and solder supports: their use as substrates for self-assembled monolayers”, *Langmuir* **2007**, *23*, 9686–9694.
142. N. Hayazawa, A. Tarun, Y. Inouye, S. Kawata, “Near-field enhanced Raman spectroscopy using side illumination optics”, *J. Appl. Phys.* **2002**, *92*, 6983–6986.
143. R. Ossikovski, Q. Nguyen, G. Picardi, “Simple model for the polarization effects in tip-enhanced Raman spectroscopy”, *Phys. Rev. B* **2007**, *75*, 045412.
144. R. Dorn, S. Quabis, G. Leuchs, “Sharper focus for a radially polarized light beam”, *Phys. Rev. Lett.* **2003**, *91*, 233901.
145. C. Chen, N. Hayazawa, S. Kawata, “A 1.7 nm resolution chemical analysis of carbon nanotubes by tip-enhanced Raman imaging in the ambient”, *Nat. Commun.* **2014**, *5*, 3312.
146. C. Georgi, A. Hartschuh, “Tip-enhanced Raman spectroscopic imaging of localized defects in carbon nanotubes”, *Appl. Phys. Lett.* **2010**, *97*, 143117.
147. P. R. West, S. Ishii, G. V. Naik, N. K. Emani, V. M. Shalaev, A. Boltasseva, “Searching for better plasmonic materials”, *Laser Photonics Rev.* **2010**, *4*, 795–808.
148. T. E. Graedel, “Corrosion mechanisms for silver exposed to the atmosphere”, *J. Electrochem. Soc.* **1992**, *139*, 1963–1970.
149. J. C. Reed, H. Zhu, A. Y. Zhu, C. Li, E. Cubukcu, “Graphene-enabled silver nanoantenna sensors”, *Nano Lett.* **2012**, *12*, 4090–4094.

150. L. Paussa, L. Guzman, E. Marin, N. Isomaki, L. Fedrizzi, “Protection of silver surfaces against tarnishing by means of alumina/titania-nanolayers”, *Surf. Coat. Technol.* **2011**, *206*, 976–980.
151. X. Zhang, J. Zhao, A. V. Whitney, J. W. Elam, R. P. Van Duyne, “Ultrastable substrates for surface-enhanced Raman spectroscopy: Al_2O_3overlayers fabricated by atomic layer deposition yield Improved anthrax biomarker detection”, *J. Am. Chem. Soc.* **2006**, *128*, 10304–10309.
152. S. M. Mahurin, J. John, M. J. Sepaniak, S. Dai, “A reusable surface-enhanced Raman scattering (SERS) substrate prepared by atomic layer deposition of alumina on a multi-layer gold and silver film”, *Appl. Spectrosc.* **2011**, *65*, 417–422.
153. E. Angelini, S. Grassini, M. Parvis, “Silver artefacts: plasma deposition of SiO_x protective layers and tarnishing evolution assessment”, *Corros. Eng. Sci. Technol.* **2010**, *45*, 334–340.
154. E. Angelini, S. Grassini, G. M. Ingo, D. Mombello, F. Fracassi, F. Palumbo, “Surface analysis of SiO_2-like high-barrier thin films for protection of silver artefacts”, *Surf. Interface Anal.* **2010**, *42*, 666–670.
155. C. A. Barrios, A. V. Malkovskiy, R. D. Hartschuh, A. M. Kisliuk, A. P. Sokolov, M. D. Foster, “Extending lifetime of plasmonic silver structures designed for high-resolution chemical imaging or chemical and biological sensing”, *Proc. of SPIE* **2008**, *6954*, 69540C.
156. T. Baše, Z. Bastl, V. Havránek, K. Lang, J. Bould, M. G. S. Londesborough, J. Macháček, J. Plešek, “Carborane–thiol–silver interactions. A comparative study of the molecular protection of silver surfaces”, *Surf. Coat. Technol.* **2010**, *204*, 2639–2646.
157. M. C. Bernard, E. Dauvergne, M. Evesque, M. Keddam, H. Takenouti, “Reduction of silver tarnishing and protection against subsequent corrosion”, *Corros. Sci.* **2005**, *47*, 663–679.
158. C. Liang, C. Yang, N. Huang, “Tarnish protection of silver by octadecanethiol self-assembled monolayers prepared in aqueous micellar solution”, *Surf. Coat. Technol.* **2009**, *203*, 1034–1044.
159. C. H. Liang, C. J. Yang, N. B. Huang, B. Wu, “Comparison of four antitarnishing self-assembled monolayers on silver coin”, *Surf. Eng.* **2011**, *27*, 199–204.
160. M. E. Ayhan, G. Kalita, S. Sharma, M. Tanemura, “Chemical vapor deposition of graphene on silver foil as a tarnish-resistant coating”, *Phys. Status Solidi RRL* **2013**, *7*, 1076–1079.
161. J. A. Dieringer, A. D. McFarland, N. C. Shah, D. A. Stuart, A. V. Whitney, C. R. Yonzon, M. A. Young, X. Zhang, R. P. Van Duyne, “Surface enhanced Raman spectroscopy: new materials, concepts, characterization tools, and applications”, *Faraday Discuss.* **2006**, *132*, 9–26.
162. C. C. Neacsu, G. A. Steudle, M. B. Raschke, “Plasmonic light scattering from nanoscopic metal tips”, *Appl. Phys. B* **2005**, *80*, 295–300.
163. U. Kreibig, M. Vollmer, *Optical properties of metal clusters*, Springer, Berlin, **1995**.
164. W. Akemann, A. Otto, H. R. Schober, “Raman scattering by bulk phonons in microcrystalline silver and copper via electronic surface excitations”, *Phys. Rev. Lett.* **1997**, *79*, 5050–5053.

165. B. Minceva-Sukarova, M. Najdoski, I. Grozdanov, C. J. Chunnilall, “Raman spectra of thin solid films of some metal sulfides”, *J. Mol. Struct.* **1997**, *410-411*, 267–270.
166. I. Martina, R. Wiesinger, M. Schreiner, “Micro-Raman investigations of early stage silver corrosion products occurring in sulfur containing atmospheres”, *J. Raman Spectrosc.* **2013**, *44*, 770–775.
167. D. W. Scott, J. P. McCullough, W. N. Hubbard, J. F. Messerly, I. A. Hossenlopp, F. R. Frow, G. Waddington, “Benzenethiol - thermodynamic properties in the solid, liquid and vapor states - internal rotation of the thiol group”, *J. Am. Chem. Soc.* **1956**, *78*, 5463–5468.
168. C. G. Tetsassi Feugmo, V. Liégeois, “Analyzing the vibrational signatures of thiophenol adsorbed on small gold clusters by DFT calculations”, *Chem. Phys. Chem.* **2013**, *14*, 1633–1645.
169. C. Zhang, B. Gao, L. G. Chen, Q. S. Meng, H. Yang, R. Zhang, X. Tao, H. Y. Gao, Y. Liao, Z. C. Dong, “Fabrication of silver tips for scanning tunneling microscope induced luminescence.”, *Rev. Sci. Instrum.* **2011**, *82*, 083101.
170. R. Chen, N. T. Nuhfer, L. Moussa, H. R. Morris, P. M. Whitmore, “Silver sulfide nanoparticle assembly obtained by reacting an assembled silver nanoparticle template with hydrogen sulfide gas”, *Nanotechnology* **2008**, *19*, 455604.
171. H. E. Bennett, R. L. Peck, D. K. Burge, J. M. Bennett, “Formation and growth of tarnish on evaporated silver films”, *J. Appl. Phys.* **1969**, *40*, 3351.
172. T. Schmid, L. Opilik, C. Blum, R. Zenobi, “Nanoscale chemical imaging using tip-enhanced Raman spectroscopy: a critical review”, *Angew. Chem. Int. Ed.* **2013**, *52*, 5940–5954.
173. E. M. van Schrojenstein Lantman, T. Deckert-Gaudig, A. J. G. Mank, V. Deckert, B. M. Weckhuysen, “Catalytic processes monitored at the nanoscale with tip-enhanced Raman spectroscopy”, *Nat. Nanotechnol.* **2012**, *7*, 583–586.
174. J. F. John, S. Mahurin, S. Dai, M. J. Sepaniak, “Use of atomic layer deposition to improve the stability of silver substrates for in situ, high-temperature SERS measurements”, *J. Raman Spectrosc.* **2010**, *41*, 4–11.
175. J. Sung, K. M. Kosuda, J. Zhao, J. W. Elam, K. G. Spears, R. P. VanDuyne, “Stability of silver nanoparticles fabricated by nanosphere lithography and atomic layer deposition to femtosecond laser excitation”, *J. Phys. Chem. C* **2008**, *112*, 5707–5714.
176. A. V. Whitney, J. W. Elam, P. C. Stair, R. P. VanDuyne, “Toward a thermally robust operando surface-enhanced Raman spectroscopy substrate”, *J. Phys. Chem. C* **2007**, *111*, 16827–16832.
177. X. Cui, D. Erni, W. Zhang, R. Zenobi, “Highly efficient nano-tips with metal – dielectric coatings for tip-enhanced spectroscopy applications”, *Chem. Phys. Lett.* **2008**, *453*, 262–265.
178. X. Cui, W. Zhang, B.-S. Yeo, R. Zenobi, C. Hafner, D. Erni, “Tuning the resonance frequency of Ag-coated dielectric tips.”, *Opt. Express* **2007**, *15*, 8309–8316.
179. T. Schmid, B.-S. Yeo, G. Leong, J. Stadler, R. Zenobi, “Performing tip-enhanced Raman spectroscopy in liquids”, *J. Raman Spectrosc.* **2009**, *40*, 1392–1399.
180. L. Srisombat, A. C. Jamison, T. R. Lee, “Stability: a key issue for self-assembled monolayers on gold as thin-film coatings and nanoparticle protectants”, *Colloid Surface A: Physicochem. Eng. Aspects* **2011**, *390*, 1–19.

181. J.-F. Li, Y. F. Huang, Y. Ding, Z.-L. Yang, S. B. Li, X.-S. Zhou, F. R. Fan, W. Zhang, Z. Y. Zhou, D.-Y. Wu, B. Ren, Z. L. Wang, Z.-Q. Tian, “Shell-isolated nanoparticle-enhanced Raman spectroscopy”, *Nature* **2010**, *464*, 392–395.
182. C. Blum, L. Opilik, J. M. Atkin, K. Braun, S. B. Kämmer, V. Kravtsov, N. Kumar, S. Lemeshko, J.-F. Li, K. Luszcz, T. Maleki, A. J. Meixner, S. Minne, M. B. Raschke, B. Ren, J. Rogalski, D. Roy, B. Stephanidis, X. Wang, D. Zhang, J.-H. Zhong, R. Zenobi, “Tip-enhanced Raman spectroscopy - an interlaboratory reproducibility and comparison study”, *J. Raman Spectrosc.* **2014**, *45*, 22–31.
183. S. Heike, T. Hashizume, “Atomic resolution noncontact atomic force/scanning tunneling microscopy using a 1 MHz quartz resonator”, *Appl. Phys. Lett.* **2003**, *83*, 3620–3622.
184. H. Watanabe, K. Fujita, M. Ichikawa, “Observation and creation of current leakage sites in ultrathin silicon dioxide films using scanning tunneling microscopy”, *Appl. Phys. Lett.* **1998**, *72*, 1987–1989.
185. S. M. George, “Atomic layer deposition: an overview”, *Chem. Rev.* **2010**, *110*, 111–131.
186. W. Geyer, V. Stadler, W. Eck, M. Zharnikov, A. Gölzhäuser, M. Grunze, “Electron-induced crosslinking of aromatic self-assembled monolayers: negative resists for nanolithography”, *Appl. Phys. Lett.* **1999**, *75*, 2401–2403.
187. A. Turchanin, M. El-Desawy, A. Gölzhäuser, “High thermal stability of cross-linked aromatic self-assembled monolayers: nanopatterning via selective thermal desorption”, *Appl. Phys. Lett.* **2007**, *90*, 053102.
188. D. G. Matei, N.-E. Weber, S. Kurasch, S. Wundrack, M. Woszczyna, M. Grothe, T. Weimann, F. Ahlers, R. Stosch, U. Kaiser, A. Turchanin, “Functional single-layer graphene sheets from aromatic monolayers”, *Adv. Mater.* **2013**, *25*, 4146–4151.
189. N. Kumar, A. Rae, D. Roy, “Accurate measurement of enhancement factor in tip-enhanced Raman spectroscopy through elimination of far-field artefacts”, *Appl. Phys. Lett.* **2014**, *104*, 123106.
190. N. Geblinger, A. Ismach, E. Joselevich, “Self-organized nanotube serpentines”, *Nat. Nanotechnol.* **2008**, *3*, 195–200.
191. C.-H. Chang, Y.-K. Chiou, C.-W. Hsu, T.-B. Wu, “Hydrous-plasma treatment of Pt electrodes for atomic layer deposition of ultrathin high-k oxide films”, *Electrochem. Solid-State Lett.* **2007**, *10*, G5–G7.
192. M. D. Groner, J. W. Elam, F. H. Fabreguette, S. M. George, “Electrical characterization of thin Al_2O_3 films grown by atomic layer deposition on silicon and various metal substrates”, *Thin Solid Films* **2002**, *413*, 186–197.
193. A. J. Elliot, G. Malek, L. Wille, R. Lu, S. Han, J. Z. Wu, J. Talvacchio, R. M. Lewis, “Probing the nucleation of Al_2O_3 in atomic layer deposition on aluminum for ultrathin tunneling barriers in Josephson junctions”, *IEEE Trans. Appl. Supercond.* **2013**, *23*, 1101405.
194. A. V. Whitney, J. W. Elam, S. Zou, A. V. Zinovev, P. C. Stair, G. C. Schatz, R. P. Van Duyne, “Localized surface plasmon resonance nanosensor: a high-resolution distance-dependence study using atomic layer deposition”, *J. Phys. Chem. B* **2005**, *109*, 20522–20528.

195. P. Penner, X. Zhang, E. Marschewski, F. Behler, P. Angelova, A. Beyer, J. Christoffers, A. Gölzhäuser, “Charge rransport through carbon nanomembranes”, *J. Phys. Chem. C* **2014**, *118*, 21687–21694.
196. K. Simons, E. Ikonen, “Functional rafts in cell membranes”, *Nature* **1997**, *387*, 569–572.
197. J. Korlach, P. Schwille, W. W. Webb, G. W. Feigenson, “Characterization of lipid bilayer phases by confocal microscopy and fluorescence correlation spectroscopy”, *Proc. Natl. Acad. Sci. U.S.A.* **1999**, *96*, 8461–8466.
198. S. L. Veatch, S. L. Keller, “Separation of liquid phases in giant vesicles of ternary mixtures of phospholipids and cholesterol”, *Biophys. J.* **2003**, *85*, 3074–3083.
199. L. J. Johnston, “Nanoscale imaging of domains in supported lipid membranes”, *Langmuir* **2007**, *23*, 5886–5895.
200. K. Gaus, E. Gratton, E. Kable, A. S. Jones, I. Gelissen, L. Kritharides, W. Jessup, “Visualizing lipid structure and raft domains in living cells with two-photon microscopy”, *Proc. Natl. Acad. Sci. U.S.A.* **2003**, *100*, 15554–15559.
201. Y. F. Dufrene, W. R. Barger, J.-B. D. Green, G. U. Lee, “Nanometer-scale surface properties of mixed phospholipid monolayers and bilayers”, *Langmuir* **1997**, *13*, 4779–4784.
202. F. Tokumasu, A. J. Jin, G. W. Feigenson, J. A. Dvorak, “Nanoscopic lipid domain dynamics revealed by atomic force microscopy”, *Biophys. J.* **2003**, *84*, 2609–2618.
203. M.-C. Giocondi, D. Yamamoto, E. Lesniewska, P.-E. Milhiet, T. Ando, C. Le Grimellec, “Surface topography of membrane domains”, *Biochim. Biophys. Acta* **2010**, *1798*, 703–718.
204. T. S. van Zanten, J. Gómez, C. Manzo, A. Cambi, J. Buceta, R. Reigada, M. F. Garcia-Parajo, “Direct mapping of nanoscale compositional connectivity on intact cell membranes”, *Proc. Natl. Acad. Sci. U.S.A.* **2010**, *107*, 15437–15442.
205. S. L. Veatch, S. S. W. Leung, R. E. W. Hancock, J. L. Thewalt, “Fluorescent Probes Alter Miscibility Phase Boundaries in Ternary Vesicles”, *J. Phys. Chem. B* **2007**, *111*, 502–504.
206. G. W. H. Wurpel, J. M. Schins, M. Müller, “Direct measurement of chain order in single phospholipid mono- and bilayers with multiplex CARS”, *J. Phys. Chem. B* **2004**, *108*, 3400–3403.
207. E. O. Potma, X. S. Xie, “Direct visualization of lipid phase segregation in single lipid bilayers with coherent anti-Stokes Raman scattering microscopy.”, *Chem. Phys. Chem.* **2005**, *6*, 77–79.
208. L. Li, H. Wang, J.-X. Cheng, “Quantitative coherent anti-Stokes Raman scattering imaging of lipid distribution in coexisting domains”, *Biophys. J.* **2005**, *89*, 3480–3490.
209. B.-S. Yeo, J. Stadler, T. Schmid, R. Zenobi, W. Zhang, “Tip-enhanced Raman spectroscopy. Its status, challenges and future directions”, *Chem. Phys. Lett.* **2009**, *472*, 1–13.
210. R. Böhme, M. Richter, D. Cialla, P. Rösch, V. Deckert, J. Popp, “Towards a specific characterisation of components on a cell surface-combined TERS-investigations of lipids and human cells”, *J. Raman Spectrosc.* **2009**, *40*, 1452–1457.

211. O. Coban, J. Popov, M. Burger, D. Vobornik, L. J. Johnston, “Transition from nanodomains to microdomains induced by exposure of lipid monolayers to air”, *Biophys. J.* **2007**, *92*, 2842–2853.
212. P. Moraille, A. Badia, “Highly parallel, nanoscale stripe morphology in mixed phospholipid monolayers formed by Langmuir-Blodgett transfer”, *Langmuir* **2002**, *18*, 4414–4419.
213. X. Chen, N. Lu, H. Zhang, M. Hirtz, L. Wu, H. Fuchs, L. Chi, “Langmuir-Blodgett patterning of phospholipid microstripes: effect of the second component”, *J. Phys. Chem. B* **2006**, *110*, 8039–8046.
214. P. Moraille, A. Badia, “Spatially directed protein adsorption by using a novel, nanoscale surface template.”, *Angew. Chem. Int. Ed.* **2002**, *41*, 4303–4306.
215. C. W. Freudiger, W. Min, B. G. Saar, S. Lu, G. R. Holtom, C. He, J. C. Tsai, J. X. Kang, X. S. Xie, “Label-free biomedical imaging with high sensitivity by stimulated Raman scattering microscopy.”, *Science* **2008**, *322*, 1857–1861.
216. F. Lhert, D. Blaudez, C. Heywang, J. M. Turlet, “Free-standing black films: an alternative to Langmuir monolayers for the study by Raman spectroscopy of peptide-phospholipid interaction in ultrathin films”, *Langmuir* **2002**, *18*, 512–518.
217. D. D. Baldyga, R. A. Dluhy, “On the use of deuterated phospholipids for infrared spectroscopic studies of monomolecular films: a thermodynamic analysis of single and binary component phospholipid monolayers”, *Chem. Phys. Lipids* **1998**, *96*, 81–97.
218. A. Filippov, G. Orädd, G. Lindblom, “Domain formation in model membranes studied by pulsed-field gradient-NMR: the role of lipid polyunsaturation”, *Biophys. J.* **2007**, *93*, 3182–3190.
219. L. A. Bagatolli, “To see or not to see: lateral organization of biological membranes and fluorescence microscopy”, *Biochim. Biophys. Acta* **2006**, *1758*, 1541–1556.
220. K. El Kirat, S. Morandat, Y. F. Dufrêne, “Nanoscale analysis of supported lipid bilayers using atomic force microscopy”, *Biochim. Biophys. Acta* **2010**, *1798*, 750–765.
221. G. Orädd, P. W. Westerman, G. Lindblom, “Lateral diffusion coefficients of separate lipid species in a ternary raft-forming bilayer: a pfg-NMR multinuclear study”, *Biophys. J.* **2005**, *89*, 315–320.
222. M. Przybylo, J. Sykora, J. Humpolickova, A. Benda, A. Zan, M. Hof, “Lipid diffusion in giant unilamellar vesicles is more than 2 times faster than in supported phospholipid bilayers under identical conditions”, *Langmuir* **2006**, *22*, 9096–9099.
223. H. A. Rinia, M. M. E. Snel, J. P. J. M. van der Eerden, B. de Kruijff, “Visualizing detergent resistant domains in model membranes with atomic force microscopy”, *FEBS Lett.* **2001**, *501*, 92–96.
224. R. M. A. Sullan, J. K. Li, C. Hao, G. C. Walker, S. Zou, “Cholesterol-dependent nanomechanical stability of phase-segregated multicomponent lipid bilayers”, *Biophys. J.* **2010**, *99*, 507–516.
225. K. S. Novoselov, D. Jiang, F. Schedin, T. J. Booth, V. V. Khotkevich, S. V. Morozov, A. K. Geim, “Two-dimensional atomic crystals”, *Proc. Natl. Acad. Sci. U.S.A.* **2005**, *102*, 10451–10453.

226. A. Reina, X. Jia, J. Ho, D. Nezich, H. Son, V. Bulovic, M. S. Dresselhaus, J. Kong, “Large area, few-layer graphene films on arbitrary substrates by chemical vapor deposition”, *Nano Lett.* **2009**, *9*, 30–35.
227. S. Bae, H. Kim, Y. Lee, X. Xu, J.-S. Park, Y. Zheng, J. Balakrishnan, T. Lei, H. R. Kim, Y. Il Song, Y.-J. Kim, K. S. Kim, B. Özyilmaz, J.-H. Ahn, B. H. Hong, S. Iijima, “Roll-to-roll production of 30-inch graphene films for transparent electrodes”, *Nat. Nanotechnol.* **2010**, *5*, 574–578.
228. K. Celebi, J. Buchheim, R. M. Wyss, A. Droudian, P. Gasser, I. Shorubalko, J.-I. Kye, C. Lee, H. G. Park, “Ultimate permeation across atomically thin porous graphene”, *Science* **2014**, *344*, 289–292.
229. A. D. Smith, S. Vaziri, F. Niklaus, A. C. Fischer, M. Sterner, A. Delin, M. Östling, M. C. Lemme, “Pressure sensors based on suspended graphene membranes”, *Solid-State Electron.* **2013**, *88*, 89–94.
230. P. Kissel, R. Erni, W. B. Schweizer, M. D. Rossell, B. T. King, T. Bauer, S. Götzinger, A. D. Schlüter, J. Sakamoto, “A two-dimensional polymer prepared by organic synthesis.”, *Nat. Chem.* **2012**, *4*, 287–291.
231. R. Bhola, P. Payamyar, D. J. Murray, B. Kumar, A. J. Teator, M. U. Schmidt, S. M. Hammer, A. Saha, J. Sakamoto, A. D. Schlüter, B. T. King, “A two-dimensional polymer from the anthracene dimer and triptycene motifs”, *J. Am. Chem. Soc.* **2013**, *135*, 14134–14141.
232. P. Payamyar, K. Kaja, C. Ruiz-Vargas, A. Stemmer, D. J. Murray, C. J. Johnson, B. T. King, F. Schiffmann, J. VandeVondele, A. Renn, S. Götzinger, P. Ceroni, A. Schütz, L.-T. Lee, Z. Zheng, J. Sakamoto, A. D. Schlüter, “Synthesis of a covalent monolayer sheet by photochemical anthracene dimerization at the air/water interface and its mechanical characterization by AFM indentation”, *Adv. Mater.* **2014**, *26*, 2052–2058.
233. P. Payamyar, M. Servalli, T. Hungerland, A. P. Schütz, Z. Zheng, A. Borgschulte, A. D. Schlüter, “Approaching two-dimensional copolymers: photoirradiation of anthracene- and diaza-anthracene-bearing monomers in Langmuir monolayers”, *Macromol. Rapid Commun.* **2015**, *36*, 151–158.
234. P. Kissel, D. J. Murray, W. J. Wulftange, V. J. Catalano, B. T. King, “A nanoporous two-dimensional polymer by single-crystal-to-single-crystal photopolymerization”, *Nat. Chem.* **2014**, *6*, 774–778.
235. M. J. Kory, M. Wörle, T. Weber, P. Payamyar, S. W. van de Poll, J. Dshemuchadse, N. Trapp, A. D. Schlüter, “Gram-scale synthesis of two-dimensional polymer crystals and their structure analysis by X-ray diffraction”, *Nat. Chem.* **2014**, *6*, 779–784.
236. V. M. Kaganer, H. Möhwald, P. Dutta, “Structure and phase transitions in Langmuir monolayers”, *Rev. Mod. Phys.* **1999**, *71*, 779–819.
237. J. B. Peng, G. T. Barnes, I. R. Gentle, “The structures of Langmuir-Blodgett films of fatty acids and their salts”, *Adv. Colloid Interface Sci.* **2001**, *91*, 163–219.
238. S. Schrettl, C. Stefaniu, C. Schwieger, G. Pasche, E. Oveisi, Y. Fontana, A. F. i. Morral, J. Reguera, R. Petraglia, C. Corminboeuf, G. Brezesinski, H. Frauenrath, “Functional carbon nanosheets prepared from hexayne amphiphile monolayers at room temperature”, *Nat. Chem.* **2014**, *6*, 468–476.
239. N. Anderson, A. Hartschuh, S. Cronin, L. Novotny, “Nanoscale vibrational analysis of single-walled carbon nanotubes”, *J. Am. Chem. Soc.* **2005**, *127*, 2533–2537.

240. W. Fudickar, T. Linker, “Novel anthracene materials for applications in lithography and reversible photoswitching by light and air”, *Langmuir* **2010**, *26*, 4421–4428.

241. G. J. Puppels, J. H. F. Olminkhof, G. M. J. Segers-Nolten, C. Otto, F. F. M. DeMul, J. Greve, “Laser irradiation and Raman spectroscopy of single living cells and chromosomes: sample degradation occurs with 514.5 nm but not with 660 nm laser light”, *Exp. Cell Res.* **1991**, *195*, 361–367.

242. R. F. Egerton, P. Li, M. Malac, “Radiation damage in the TEM and SEM”, *Micron* **2004**, *35*, 399–409.

243. J. Sakamoto, J. van Heijst, O. Lukin, A. D. Schlüter, “Two-dimensional polymers: just a dream of synthetic chemists?”, *Angew. Chem. Int. Ed.* **2009**, *48*, 1030–1069.

244. Z. Zheng, L. Opilik, F. Schiffmann, W. Liu, G. Bergamini, P. Ceroni, L.-T. Lee, A. Schütz, J. Sakamoto, R. Zenobi, J. VandeVondele, A. D. Schlüter, “Synthesis of two-dimensional analogues of copolymers by site-to-site transmetalation of organometallic monolayer sheets”, *J. Am. Chem. Soc.* **2014**, *136*, 6103–6110.

245. P. W. Jensen, L. B. Jorgensen, “Resonance Raman-spectra of some iron(II) imine complexes”, *J. Mol. Struct.* **1982**, *79*, 87–92.

246. P. W. Hansen, P. W. Jensen, “Vibrational studies on bis-terpyridine-ruthenium(II) complexes”, *Spectrochim. Acta* **1994**, *50A*, 169–183.

247. B. J. Coe, D. W. Thompson, C. T. Culbertson, J. R. Schoonover, T. J. Meyer, “Synthesis and photophysical properties of mono(2,2’,2”-terpyridine) complexes of ruthenium(II)”, *Inorg. Chem.* **1995**, *34*, 3385–3395.

248. M. Presselt, B. Dietzek, M. Schmitt, J. Popp, A. Winter, M. Chiper, C. Friebe, U. S. Schubert, “Zinc(II) bisterpyridine complexes: the influence of the cation on the π-conjugation between terpyridine and the lateral phenyl substituent”, *J. Phys. Chem. C* **2008**, *112*, 18651–18660.

249. K. Heinze, K. Hempel, S. Tschierlei, M. Schmitt, J. Popp, S. Rau, “Resonance Raman studies of bis(terpyridine)ruthenium(II) amino acid esters and diesters”, *Eur. J. Inorg. Chem.* **2009**, *2009*, 3119–3126.

250. A. Winter, C. Friebe, M. Chiper, U. S. Schubert, M. Presselt, B. Dietzek, M. Schmitt, J. Popp, “Synthesis, characterization, and electro-optical properties of Zn^{II} complexes with π-conjugated terpyridine ligands”, *Chem. Phys. Chem.* **2009**, *10*, 787–798.

251. R. Siebert, F. Schlütter, A. Winter, M. Presselt, H. Görls, U. S. Schubert, B. Dietzek, J. Popp, “Ruthenium(II)-bis(4’-(4-ethynylphenyl)-2,2’:6’,2”-terpyridine). A versatile synthon in supramolecular chemistry. Synthesis and characterization”, *Cent. Eur. J. Chem.* **2011**, *9*, 990–999.

252. A. B. Myers, “Resonance Raman intensities and charge-transfer reorganization energies.”, *Chem. Rev.* **1996**, *96*, 911–926.

253. R. W. Havener, S.-Y. Ju, L. Brown, Z. Wang, M. Wojcik, C. S. Ruiz-Vargas, J. Park, “High-throughput graphene imaging on arbitrary substrates with widefield Raman spectroscopy”, *ACS Nano* **2012**, *6*, 373–380.

254. M. E. Hankus, H. Li, G. J. Gibson, B. M. Cullum, “Surface-enhanced Raman scattering-based nanoprobe for high-resolution, non-scanning chemical imaging”, *Anal. Chem.* **2006**, *78*, 7535–7546.

255. Y. Zhang, Y. Zhang, Q. Ji, J. Ju, H. Yuan, J. Shi, T. Gao, D. Ma, M. Liu, Y. Chen, X. Song, H. Y. Hwang, Y. Cui, Z. Liu, “Controlled growth of high-quality

monolayer WS_2layers on sapphire and imaging its grain boundary", *ACS Nano* **2013**, *7*, 8963–8971.

256. M. Bernardi, M. Palummo, J. C. Grossman, "Extraordinary sunlight absorption and one nanometer thick photovoltaics using two-dimensional monolayer materials", *Nano Lett.* **2013**, *13*, 3664–3670.
257. R. Bhandavat, L. David, G. Singh, "Synthesis of surface-functionalized WS_2 nanosheets and performance as Li-ion battery anodes", *J. Phys. Chem. Lett.* **2012**, *3*, 1523–1530.
258. A. Chirilă, P. Reinhard, F. Pianezzi, P. Bloesch, A. R. Uhl, C. Fella, L. Kranz, D. Keller, C. Gretener, H. Hagendorfer, D. Jaeger, R. Erni, S. Nishiwaki, S. Buecheler, A. N. Tiwari, "Potassium-induced surface modification of $Cu(In,Ga)Se_2$ thin films for high-efficiency solar cells", *Nat. Mater.* **2013**, *12*, 1107–1111.
259. V. Kravtsov, S. Berweger, J. M. Atkin, M. B. Raschke, "Control of plasmon emission and dynamics at the transition from classical to quantum coupling", *Nano Lett.* **2014**, *14*, 5270–5275.
260. J. M. Klingsporn, M. D. Sonntag, T. Seideman, R. P. Van Duyne, "Tip-enhanced Raman spectroscopy with picosecond pulses", *J. Phys. Chem. Lett.* **2014**, *5*, 106–110.
261. T. Ando, T. Uchihashi, N. Kodera, "High-speed AFM and applications to biomolecular systems", *Annu. Rev. Biophys.* **2013**, *42*, 393–414.

A Abbreviations

AFM	atomic force microscopy
ALD	atomic layer deposition
BCB	brilliant cresyl blue
BPT	biphenyl-4-thiol
CARS	coherent anti-Stokes Raman scattering
CCD	chage-coupled device
CVD	chemical vapor deposition
DFT	density functional theory
DIC	differential interference contrast
DMF	dimethylformamide
DOPC	1,2-di-palmitoyl-sn-glycero-3-phosphocholine
DPPC	1,2-dioleoyl-sn-glycero-3-phosphocholine
DPSS	diode-pumped solid-state
EDX	energy-dispersive X-ray
EMCCD	electron-multiplying charge-coupled device
EtOH	ethanol
FFT	fast Fourier transform
FIB	focused ion beam
FWHM	full width at half maximum
GFP	green fluorescent protein
IR	infrared
ITO	indium tin oxide
LB	Langmuir-Blodgett
LED	light-emitting diode
LSPR	localized surface plasmon resonance
MeOH	methanol
MLCT	metal-to-ligand charge transfer
MPS	3-mercaptopropyl-triethoxysilane

NA	numerical aperture
NBPT	4’-nitro-1,1’-biphenyl-4-thiol
NMR	nuclear magnetic resonance
PALM	photoactivated localization microscopy
PMT	photomultiplier tube
PVD	physical vapor deposition
QCM	quartz crystal microbalance
SAM	self-assembled monolayer
SEM	scanning electron microscopy
SERS	surface-enhanced Raman scattering
SNOM	scanning near-field optical microscopy
SPM	scanning probe microscopy
SRS	stimulated Raman scattering
STED	stimulated emission depletion
STEM	scanning transmission electron microscopy
STM	scanning tunneling microscopy
STORM	stochastic optical reconstruction microscopy
TEM	transmission electron microscopy
TERS	tip-enhanced Raman spectroscopy
TS	template stripped
UV	ultraviolet
XPS	X-ray photoelectron spectroscopy

B Supporting Figures

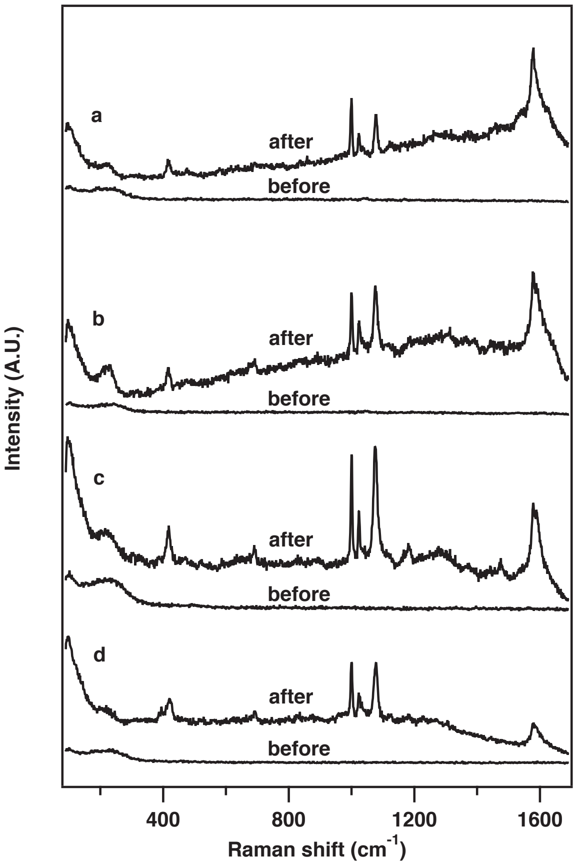

Figure B.1: Tip-enhanced Raman spectra from a thiophenol self-assembled monolayer on gold using 5 days (b,d) and 7 day (a,c) old tips before and after “revival”. Whereas no Raman bands of thiophenol are obtained before “revival”, the known spectral features are clearly obtained after the procedure.

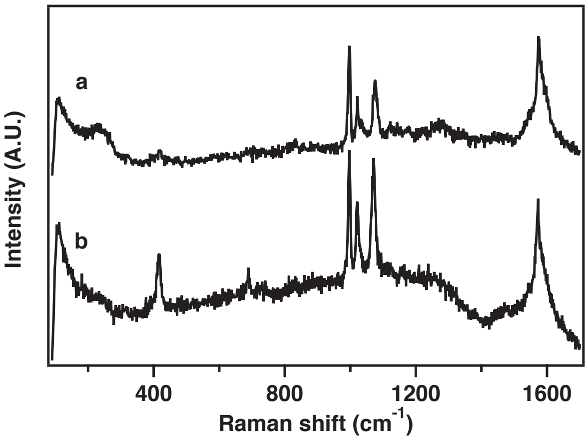

Figure B.2: STM-TER spectra from a thiophenol self-assembled monolayer on gold using a 5.5 month old silver tip after “revival” (a) and a fresh Ag tip (b).

Optical microscope images were collected through the same objective (100x, NA 0.7, Mitutoyo, Kawasaki, Japan) as that used for Raman measurements. The tip was moved across the focal plane of the objective by means of a micrometer translational stage. Sample illumination is achieved with white light directed though the objective using a 45° beamsplitter between the objectives back aperture and the camera sensor. To increase the images depth of field, image stacking was performed using Adobe Photoshop CS6. Additionally, dust spots in the image were manually removed for aesthetic reasons.

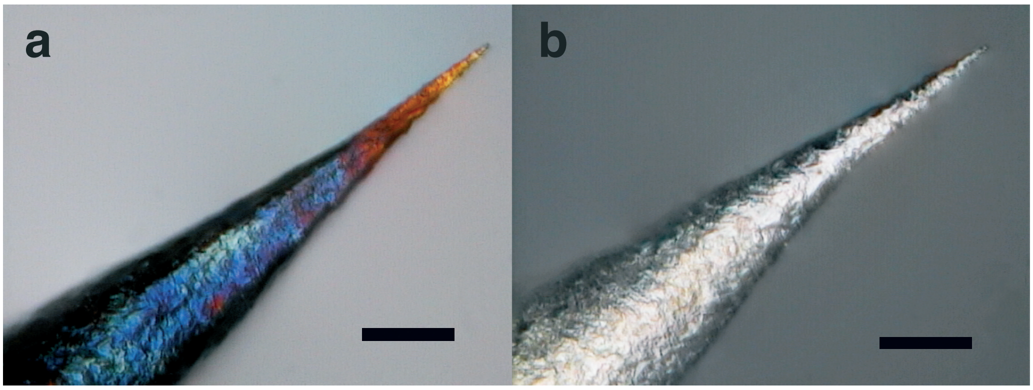

Figure B.3: Optical microscope image of the apex of a four month old silver tip before (a) and after (b) “revival”. The different colors (blue, red and yellow) on the tip shaft before “revival” can be explained by the formation of a Ag_2S layer leading to thin layer interference. The disappearance of the interference colors as well as the increase in reflectivity (the image brightness had to be adjusted) after “revival” is a clear indication for a successful recovery of elemental silver. The difference in shape is caused by the fact that the image after “revival” shows the tip from a different side. The scale bars are 20 µm.

Cyclic voltammetry (CV) measurements were conducted in a three electrode system (PGSTAT 128N, Metrohm Autolab, Utrecht, Netherlands) in 0.1 M $LiClO_4$ (Fluka) solution in acetonitrile (≥99.5%, Sigma Aldrich) at 25±1°C. The silver tip of interest was used as working electrode, a platinum wire as counter electrode and a silver wire as pseudo-reference electrode. Fresh silver tips were artificially tarnished by dipping them into a 0.1 mM $Na_2S \cdot 9\,H_2O$ (≥98%, Sigma Aldrich) solution for 3 minutes.

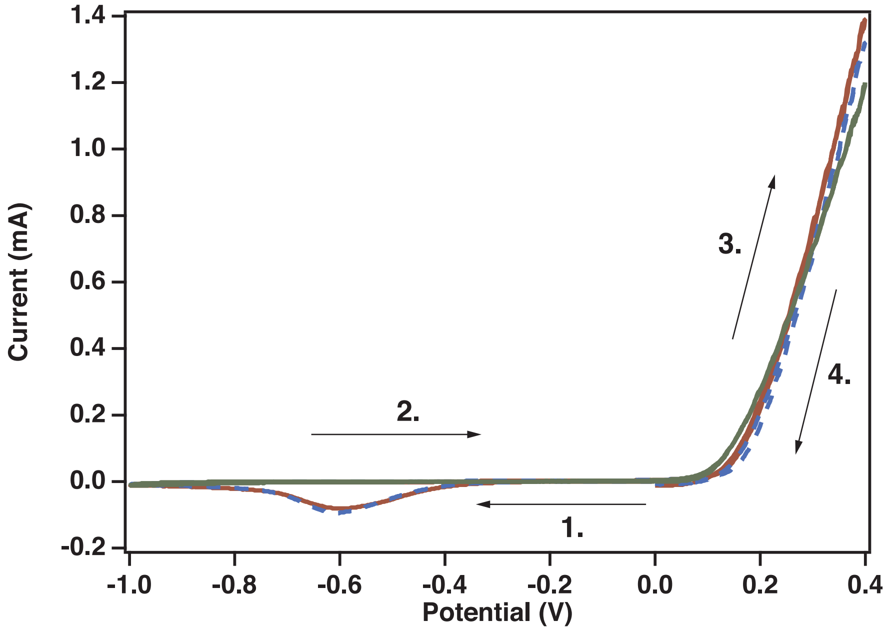

Figure B.4: Cyclic voltammograms of a freshly prepared silver tip (green), a tip stored in lab air over a period of 7 month (red) and a fresh silver tip artificially tarnished in a solution of Na_2S (blue). The peak at approx. -0.6 V, which is not observed for the fresh silver tip, can be attributed to reduction of Ag_2S formed on the silver surface during atmospheric and artificial tarnishing. The arrows indicate the direction of the potential scan. Starting and end point are at 0 V.

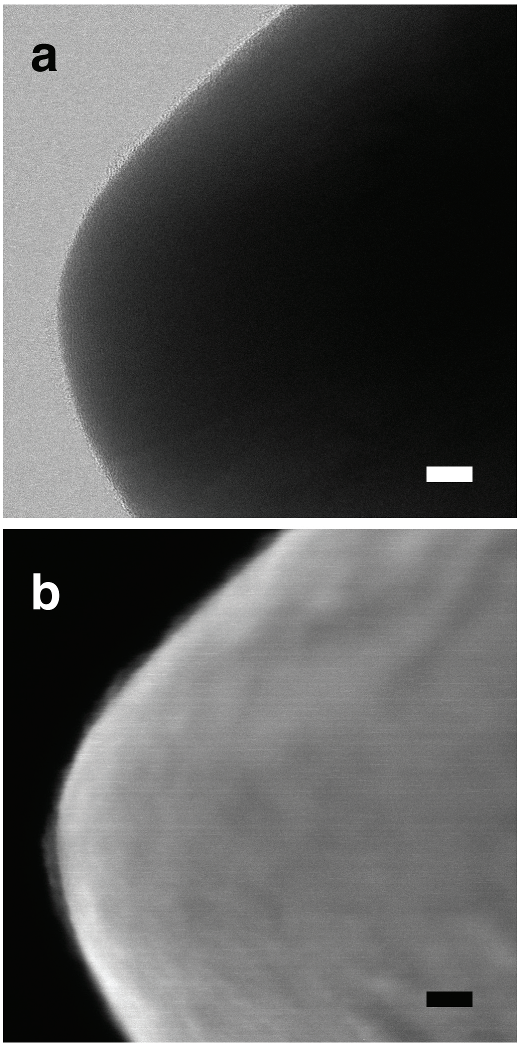

Figure B.5: Transmission electron (a) and secondary electron (b) images from the apex of a silica protected Au tip after a growth time of 30 min and 1 ml added 0.1 M HCl. A thin (<1.5 nm) layer on the tip surface is visible in the secondary electron image, whereas the amorphous character of the layer is apparent in the transmission electron image. The scale bars indicate 5 nm.

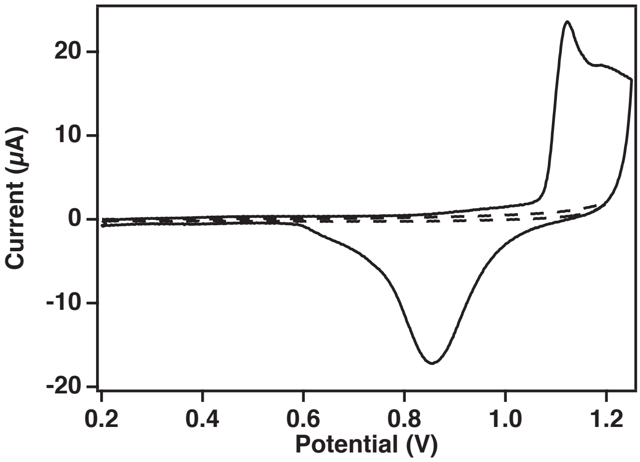

Figure B.6: Cyclic votammogram for a bare gold tip (solid line) and a silica protected gold tip (dashed line). The experiment was performed in a 0.1 M H_2SO_4 solution and a scan rate of 0.1 V/s was used. The characteristic oxidation and and reduction peaks (vs. a saturated calomel reference electrode) of gold are only visible for the bare tip.

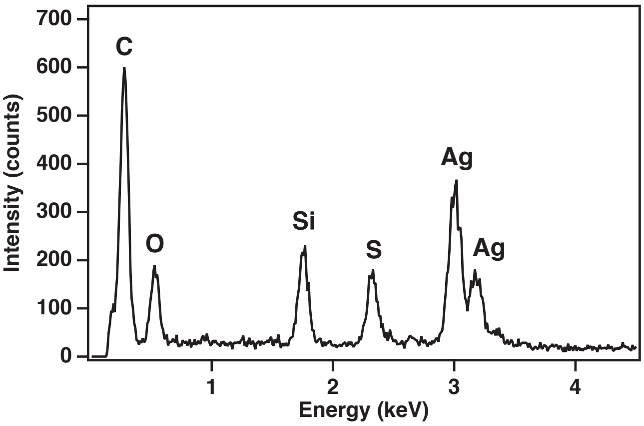

Figure B.7: EDX spectrum from a thicker region of the amorphous layer on the Ag tip surface shown in Figure 5.2.

Figure B.8 shows the Raman spectra of DPPC and DOPC powders. Spectral differences can be found in the fingerprint region (600–1800 cm^{-1}) as well as in the C-H stretching region (2800–3100 cm^{-1}). The two cis double bonds in the oleoyl chains of DOPC show up as a sharp Raman band at 1654 cm^{-1} representing the C=C stretching vibration. This band is absent in the spectrum of DPPC, which has two saturated acyl chains. The three distinct peaks at 1066 cm^{-1}, 1102 cm^{-1} and 1128 cm^{-1} in the DPPC spectrum represent the carbon backbone vibrations, which appear as one broad signal in the DOPC spectrum.

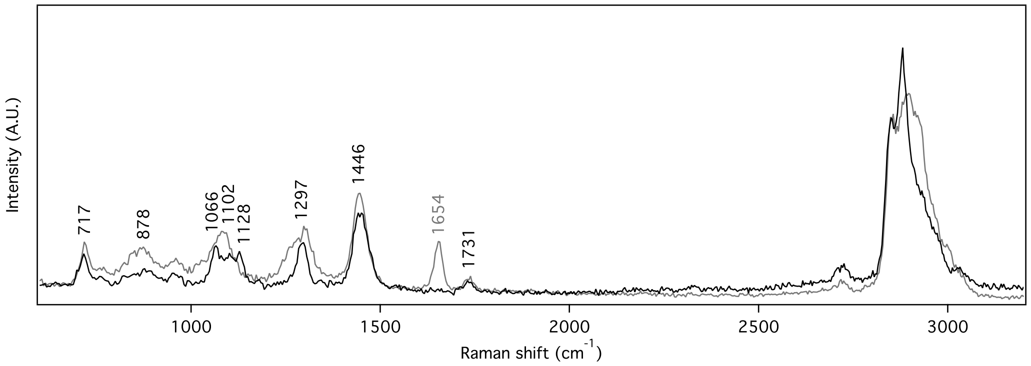

Figure B.8: Extended version of Figure 7.2. Raman spectra of DPPC (black) and DOPC (gray) over the full spectral range.

Figure B.9 shows the surface pressure-area isotherms for a pure DPPC and a pure d62-DPPC monolayer at the air-water interface. The step observed for both isotherms is caused by a phase transition from the liquid-expanded to the liquid-condensed phase (S. L. Duncan and R. G. Larson, *Biophys J*, 2008, **94**, 2965.) The isotherm for the d62-DPPC monolayer is shifted to lower packing densities at any given surface pressure and the phase transition occurs at a higher surface pressure compared to the DPPC monolayer. Thus, the deuteration of the two acyl chains of DPPC has a significant influence on the molecular interaction within the lipid monolayer. We take this into account by using a higher surface pressure for transfer to the substrate when substituting DPPC by d62-DPPC in the mixed monolayer to ensure clear phase separation.

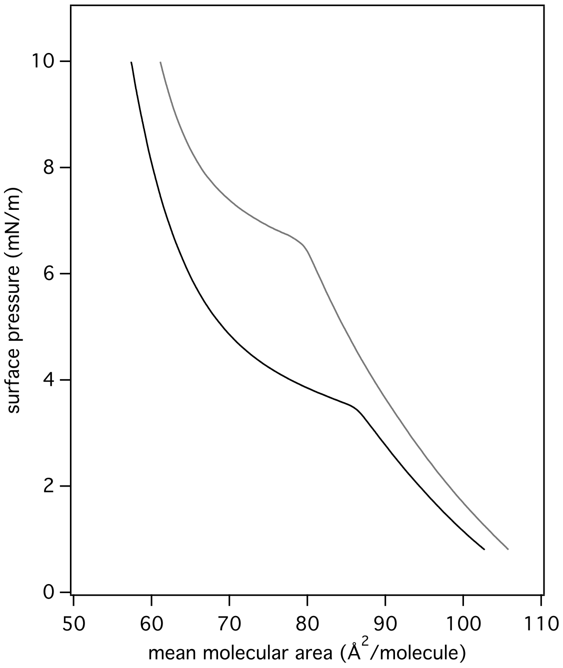

Figure B.9: Surface pressure-area isotherm for a pure monolayer of DPPC (black) and d62-DPPC (gray) at room temperature. The observed plateau present in both curves is caused by a phase transition occurring at the corresponding surface pressures.

Figure B.10 shows the surface pressure-area isotherm for the d62-DPPC/DOPC mixture (molar ratio of 1:1) up to a surface pressure of 20 mN/m used for transfer to the substrate. The mean molecular area achieved at this pressure is 71 Å^2/molecule (corresponding value on the x-axis).

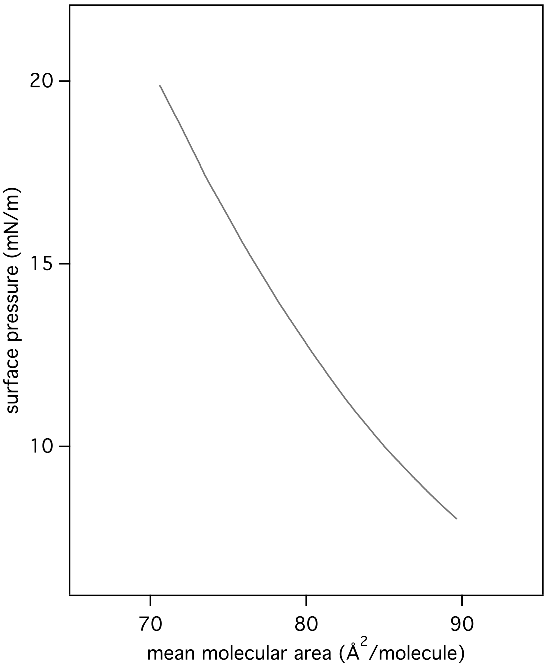

Figure B.10: Surface pressure-area isotherm for d62-DPPC/DOPC (molar ratio of 1:1) at room temperature. Only the last compression before transfer to the substrate is shown.

Figure B.11 shows three different stages during processing of the collected data from the 128x128 pixels raster scan. The scan direction was from bottom left to top right. In the first image, the brightness represents the background corrected intensity of the Raman band at 2100 cm^{-1} extracted from the full spectrum associated with each pixel. Doing the same for the Raman band at 2900 cm^{-1}, yields the second image. If we combine these two data sets by taking the ratio of the two peaks, we end up with the third image. It can be noted that this procedure leads to a significant improvement of the image contrast. This is because overall variations of the signal enhancement (e.g., due to differences in tip-sample distance) are eliminated. For example the sudden drop of the overall intensity seen in the middle of image (a) and (b) is successfully removed.

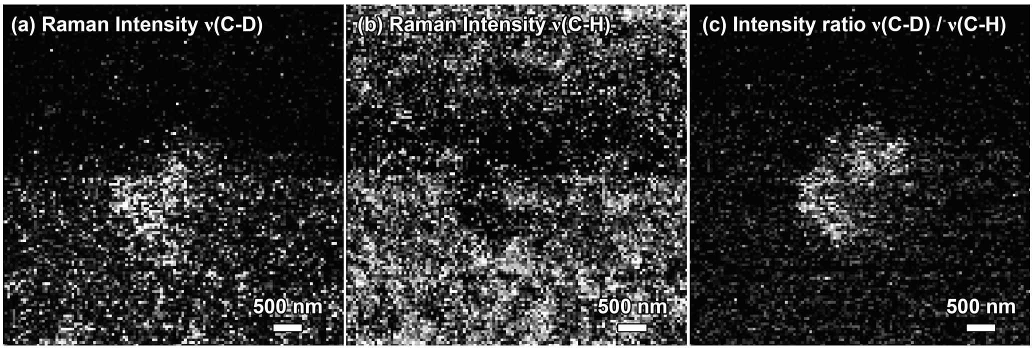

Figure B.11: Intensity maps for the Raman band at 2100 cm^{-1} (a), the Raman band at 2900 cm^{-1} (b) and the ratio of both (c). Intensities in (a) and (b) are given in counts. The images were generated and processed using the NOVA software (NT-MDT, Russia).

Figure B.12 shows the constant current mode STM image acquired during the 128x128 pixels TERS raster scan shown in Figure 7.3 and Figure B.11. The condensed phase domain is visible as a darker area in the middle of the image, which is due to a lower tip position to maintain the tunnel current. This could be due to the higher molecular density of the condensed phase domain leading to a higher insulation. An exact value for the step size in z direction cannot be determined because of the low signal-to-noise ratio. However, the difference in tip-sample distance does not affect the spectral information used for the TERS image, because each pixel represents an intensity ratio of two Raman bands and is therefore not affected by changes in the overall enhancement.

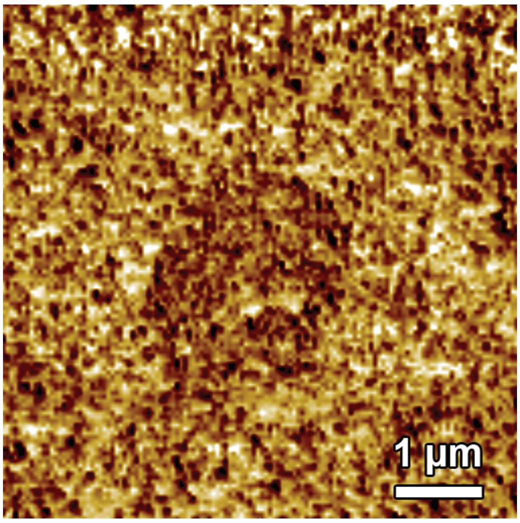

Figure B.12: Constant current mode STM image measured during the 128x128 pixels TERS raster scan. A bias voltage of 200 mV was applied between silver tip and gold surface and the tunnel current was set to 0.1 nA. The dark region (lower tip position) in the middle of the image matches the condensed phase domain observed in the TERS raster scan.

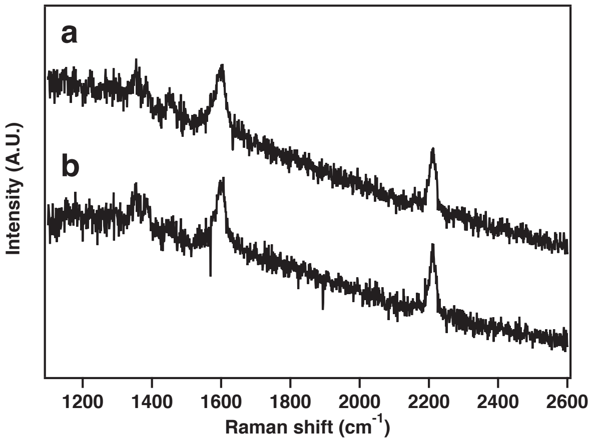

Figure B.13: Confocal Raman spectra from single/few layers of monomer 1 before (a) and after (b) irradiation. Both spectra were obtained after 60 times accumulation of spectra collected with an acquisition time of 30 s at an incident laser power of 1.7 mW and after subtracting a background spectrum from an empty area on the substrate.

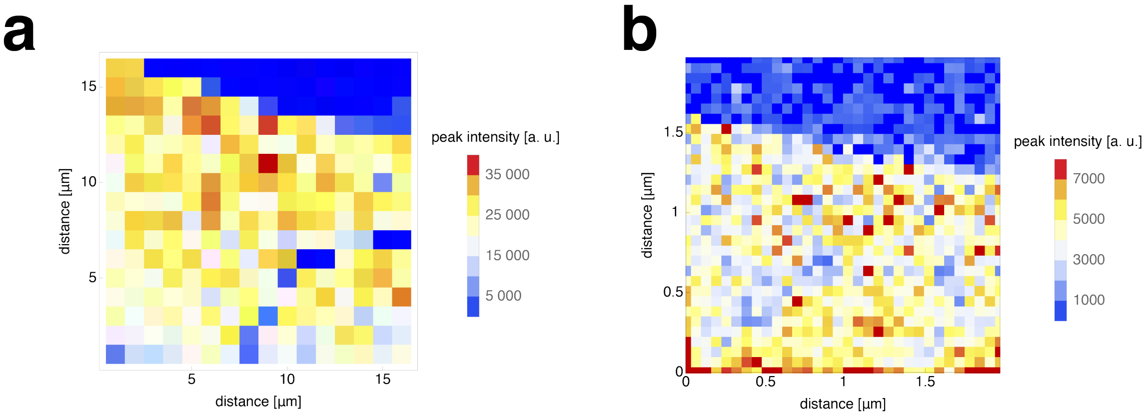

Figure B.14: Tip-enhanced Raman images showing the intensity of the peak at 2207 cm^{-1} corresponding to the triple bond stretch vibration. The first image (a) has a step size of 1 µm, whereas the high-resolution map (b) has a step size of 60 nm.

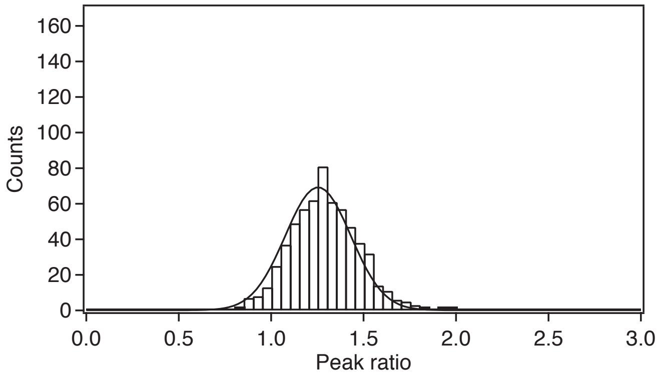

Figure B.15: 1562 cm^{-1}/1595 cm^{-1} peak ratio distribution (with Gaussian fit) for a tip-enhanced Raman image on a non-irradiated monomer layer. Only spectra where both peaks fulfilled the three times noise criterion were considered. This was the case for 625 of 1024 spectra.

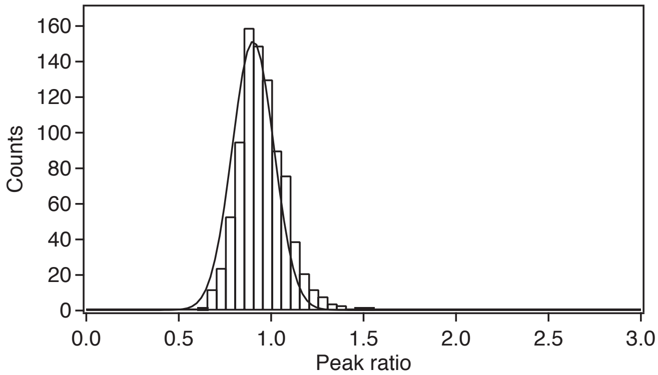

Figure B.16: 1562 cm^{-1}/1595 cm^{-1} peak ratio distribution (with Gaussian fit) for a tip-enhanced Raman image on a 20 min irradiated monomer monolayer. Only spectra where both peaks fulfill the three times noise criterion were considered. This was the case for 881 of 1024 spectra.

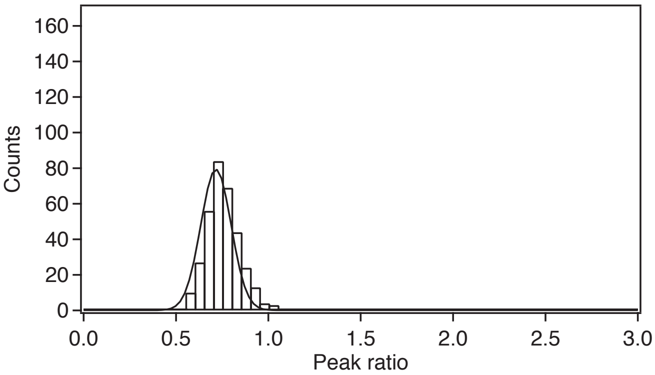

Figure B.17: 1562 cm^{-1}/1595 cm^{-1} peak ratio distribution (with Gaussian fit) for a tip-enhanced Raman image on a 18 h irradiated monomer layer. Only spectra where both peaks fulfilled the three times noise criterion were considered. This was the case for 337 of 1024 spectra. If the criterion is lowered to two times the noise level, 588 spectra are considered, which leads to a more pronounced tail on the left side of the histogram.

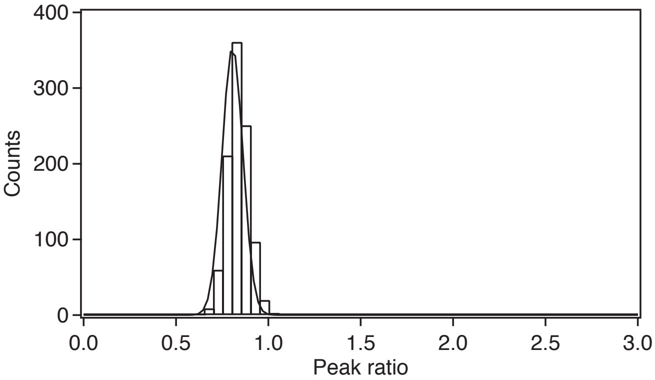

Figure B.18: 1562 cm^{-1}/1595 cm^{-1} peak ratio distribution (with Gaussian fit) for a tip-enhanced Raman image on a non-irradiated 1:1 mixed monolayer of monomer 1 and monomer 2.

C Contributions

Publications

L. Opilik, P. Payamyar, J. Szczerbiński, A. P. Schütz, M. Servalli, T. Hungerland, A. D. Schlüter, and R. Zenobi: *"Minimally Invasive Characterization of Covalent Monolayer Sheets Using Tip-Enhanced Raman Spectroscopy"*, ACS Nano, **2015**, 9, 4252, doi: 10.1021/acsnano.5b00629.

Z. Zheng, **L. Opilik**, F. Schiffmann, W. Liu, G. Bergamini, P. Ceroni, L. T. Lee, A. Schütz, J. Sakamoto, R. Zenobi, J. VandeVondele, and A. D. Schlüter: *"Synthesis of Two-Dimensional Analogues of Copolymers by Site-to-Site Transmetalation of Organometallic Monolayer Sheets"*, Journal of the American Chemical Society, **2014**, 136, 6103, doi: 10.1021/ja501849y.

C. Blum, **L. Opilik**, J. M. Atkin, K. Brown, S. B. Kaemmer, V. Kravtsov, N. Kumar, S. Lemeshko, J. F. Li, K. Luszcz, T. Maleki, A. J. Meixner, S. Minne, M. B. Raschke, B. Ren, J. Rogalski, D. Roy, B. Stephanidis, X. Wang, D. Zhang, J. H. Zhong, and R. Zenobi: *"Tip-Enhanced Raman Spectroscopy - An Interlaboratory Reproducibility and Comparison Study"*, Journal of Raman Spectroscopy, **2014**, 45, 22, doi: 10.1002/jrs.4423.

M. Paulite, C. Blum, T. Schmid, **L. Opilik**, K. Eyer, G. C. Walker, and R. Zenobi: *"Full Spectroscopic Tip-Enhanced Raman Imaging of Single Nanotapes Formed from beta-Amyloid (1-40) Peptide Fragments"*, ACS Nano, **2013**, 7, 911, doi: 10.1021/nn305677k.

L. Opilik, T. Schmid, and R. Zenobi: *"Modern Raman Imaging: Vibrational Spectroscopy on the Micrometer and Nanometer Scales"*, Annual Reviews in Analytical Chemistry, **2013**, 6, 379, doi: 10.1146/annurev-anchem-062012-092646.

T. Schmid, **L. Opilik**, C. Blum, and R. Zenobi: *"Nanoscale Chemical Imaging Using Tip-Enhanced Raman Spectroscopy: A Critical Review"*, Angewandte Chemie: International Edition, **2013**, 52, 5940, doi: 10.1002/anie.201203849.

C. Blum, T. Schmid, **L. Opilik**, S. Weidmann, S. R. Fagerer, and R. Zenobi: *"Understanding Tip-enhanced Raman Spectra of Biological Molecules: A Combined Raman, SERS and TERS Study"*, Journal of Raman Spectroscopy, **2012**, 43, 1895, doi: 10.1002/jrs.4099.

C. Blum, T. Schmid, **L. Opilik**, N. Metanis, S. Weidmann, and R. Zenobi: *"Missing Amide I Mode in Tip-Enhanced Raman Spectra of Proteins?"*, Journal of Physical Chemistry C, **2012**, 116, 23061, doi: 10.1021/jp306831p.

J. Stadler, T. Schmid, **L. Opilik**, P. Kuhn, P. Dittrich, and R. Zenobi: *"Tip-Enhanced Raman Spectroscopic Imaging of Patterned Thiol Monolayers"*, Beilstein Journal of Nanotechnology, **2011**, 2, 509, doi: 10.3762/bjnano.2.55.

L. Opilik, T. Bauer, T. Schmid, J. Stadler, and R. Zenobi: *"Nanoscale Chemical Imaging of Segregated Lipid Domains Using Tip-Enhanged Ramsn Spectroscopy"*, Physical Chemistry Chemical Physics, **2011**, 13, 9978, doi: 10.1039/C0CP02832K.

T. Schmid, A. Sebesta, J. Stadler, **L. Opilik**, R. M. Balabin, and R. Zenobi: *"Tip-Enhanced Raman Spectroscopy and Related Techniques in Studies of Biological Materials"*, Proceedings of SPIE, **2010**, 7586, 758603, doi: 10.1117/12.845471.

C. Haisch, **L. Opilik**, M. Hays, and R. Niessner: *"Photo-Thermophoresis as a New Tool for Aerosol Characterization"*, Journal of Physics: Conference Series, **2010**, 214, 012011, doi: 10.1088/1742-6596/214/1/012011.

Selected Conference Contributions

L. Opilik, P. Payamyar, A. Schütz, C. Blum, J. Sakamoto, A. D. Schlüter, and R. Zenobi: *"Structure Determination of a Novel Covalent Monolayer on the Nanometer Length Scale Using Tip-Enhanced Raman Spectroscopy"*, 7th International Conference on Advanced Vibrational Spectroscopy, Kobe/Japan, August 25–30, 2013 (Poster Presentation).

L. Opilik, P. Payamyar, A. Schütz, C. Blum, J. Sakamoto, A. D. Schlüter, and R. Zenobi: *"Structural Determination of a Novel Covalent Monolayer on the Nanometer Length Scale Using Tip-Enhanced Raman Spectroscopy"*, 3rd Meeting on Tip-Enhanced Raman Spectroscopy, Zurich/Switzerland, August 19–20, 2013 (Oral Presentation).

L. Opilik, T. Schmid, C. Blum, and R. Zenobi: *"Long-Term Stable and Strongly Enhancing Near-Field Optical Probes for Tip-Enhanced Raman Spectroscopy"*, 12th International Conference on Near-Field Optics, Nanophotonics and Related Techniques, San Sebastian/Spain, September 3–7, 2011 (Poster Presentation).

L. Opilik, M. Spergl, T. Schmid, T. Bauer, Z. Zheng, J. Sakamoto, A. D. Schlüter, and R. Zenobi: *"Imaging of 2D Polymer Films Below the Optical Diffraction Limit"*, 23rd International Conference on Raman Spectroscopy, Bangalore/India, August 12–17, 2011 (Poster Presentation).

L. Opilik, T. Schmid, T. Bauer, I. Liko, J. Stadler, and R. Zenobi: *"Spectroscopic Imaging of Segregated Lipid Domains below the Diffraction Limit using Tip-Enhanced Raman Spectroscopy"*, Annual Meeting of the Swiss Working Group for Surface and Interface Science, Fribourg/Switzerland, January 27, 2012 (Oral Presentation).

L. Opilik, T. Schmid, T. Bauer, I. Liko, J. Stadler, and R. Zenobi: *"Nanoscale Chemical Imaging of Segregated Lipid Domains using Tip-Enhanced Raman Spectroscopy"*, 2nd Center for Imaging Science and Technology Zurich-Paris Young Scientists Symposium, Zurich/Switzerland, October 6–7, 2011 (Oral Presentation).

L. Opilik, T. Schmid, T. Bauer, I. Liko, J. Stadler, and R. Zenobi: *"Nanoscale Chemical Imaging of Segregated Lipid Domains using Tip-Enhanced Raman Spectroscopy"*, Swiss Chemical Society Fall Meeting, Lausanne/Switzerland, September 9, 2011 (Oral Presentation).